Dynamical Phase-Change Phenomena

Seyedfarzad Ahmadi

Dissertation submitted to the Faculty of the
Virginia Polytechnic Institute and State University
in partial fulfillment of the requirements for the degree of

Doctor of Philosophy
in
Engineering Mechanics

Jonathan B. Boreyko, Chair
Nicole T. Abaid
Sunghwan Jung
Saad A. Ragab
Pengtao Yue

May 13, 2019
Blacksburg, Virginia

Keywords: traffic flow, superhydrophobic, anti-frosting, anti-icing, bubbles

Dynamical Phase-Change Phenomena

S. Farzad Ahmadi

(ABSTRACT)

Matter on earth exists mostly in three different phases of solid, liquid, and gas. With extreme amounts of energy, temperature, or pressure, a matter can be changed between the phases. Six different types of phase-change phenomena are possible: freezing (the substance changes from a liquid to a solid), melting (solid to liquid), condensation (gas to liquid), vaporization (liquid to gas), sublimation (solid to gas), and desublimation (gas to solid). Another form of phase change which will be discussed here is the wetting or dewetting transitions of a superhydrophobic surface, in which the phase residing within the surface structure switches between vapor and liquid. Phase transition phenomena frequently occur in our daily life; examples include: a "liquid" to "solid" transition when cars decrease their distance at a traffic light, solidification of liquids droplets during winter months, and the dancing of droplets on a non-sticking pan. In this dissertation we will address seven different phase-change problems occurring in nature. We unveil completely new forms of phase-change phenomena that exhibit rich physical behavior. For example, during traffic flow, drivers keep a large distance from the vehicle in front of them to ensure safe driving. When vehicles come to a stop, for example at a red light, drivers voluntarily induce a "phase transition" from this "liquid phase" to a close-packed "solid phase". This phase transition is motivated by the intuition that traveling as far as possible before stopping will minimize the overall travel time. However, we are going to investigate this phase-change process and show that this long standing intuition is wrong. Phase-change of solidification will be discussed for different problems. Moreover, the complex physics of oil as it wicks up sheets of frost and freezing of bubble unveil completely new forms of multiphase flows that exhibit rich physical behavior. Finally, the "Cassie" to "Wenzel" transition will be investigated for layered nano-textured surfaces. These phenomena will be modeled using thermodynamics and fluid mechanics equations.

This work received support from the National Science Foundation (CBET-1604272), 3M Company (Grant #26296337), and the Department of Biomedical Engineering and Mechanics at Virginia Tech.

Dynamical Phase-Change Phenomena

S. Farzad Ahmadi

(GENERAL AUDIENCE ABSTRACT)

The main focus of this dissertation is on the dynamical phase change phenomena occurring in nature. First, we study the solid to liquid phase change of group of people moving from rest. We show that increasing the packing density of vehicles at a stop-and-go motion (e.g., vehicles at a traffic light) would not increase the efficiency of the flow once it is resumed. Second, we present a passive anti-frosting surfaces just by using the chemistry of ice. We show how the in-plane frost growth can be passively suppressed by patterning arrays of microscopic ice stripes across a surface. Third, we elucidate how bubbles deposited on a chilled and icy substrate freeze in different ambient conditions. We reveal the various phenomena that govern how soap bubbles freeze and produce a variety of beautiful effects. Fourth, we will study oil-ice interactions which are important for the emerging science of using oil-impregnated surfaces for anti-icing and anti-frosting applications, where oil drainage from the surface due to wicking onto ice is a pressing issue. We observe oil as it wicks up sheets of frost grown on aluminum surfaces of varying wettability: superhydrophilic, hydrophilic, hydrophobic, and superhydrophobic. Fifth, we study the effect of topography of the nanopillars on dynamics of jumping droplets. The critical diameter for jumping to occur was observed to be highly dependent on the height and diameter of the nanopillars, with droplets as small as $2\,\mu$m jumping on the surface with the tallest and most slender pillars. Sixth, we show that micrometric condensate spontaneously launches several millimeters from a wheat leaf's surface, taking adhered pathogenic spores with it. We quantify spore liberation rates of order 10 cm^{-2} hr^{-1} during a dew cycle. Finally, inspired by duck feathers, two-tier porous superhydrophobic surfaces were fabricated to serve as synthetic mimics with a controlled surface structure. We show the effect of layers of feathers on energy barrier for the wetting transition.

تقدیم به پدرومادر عزیزم

Dedicated to my dear parents . . .

Acknowledgements

Over the course of my studies, I have been fortunate enough to be surrounded by amazing people. I strove to learn from each and every one of them, and that is why I have tried to listen more and speak less. While it's difficult to thank everyone, I'll do my best:

I would first like to express my gratitude to my amazing advisor, a good friend, a wonderful person, and a great teacher, Prof. Jonathan Boreyko. Thank you, Jonathan! Thanks for everything you gave me over the past four and a half years. It means a lot to me that you gave me lots of opportunities, a great level of flexibility, and responsibility during my PhD career. You taught me the joy of my life. You taught me experiments. I was really fortunate to begin my PhD career at the same time as you started your tenure track at VT as we learned lots of things together. I was lucky to be the last one to join your group in 2014 and to be your first PhD student now. I will miss your optimism, our writing workshops, our brainstorming, your lovely children and their beautiful drawings. There has not been a single time when I came to your office and you were sad or disappointed. You have always had a warm smile, and have taken the time to help me with my research.

Thanks, as well, to all my committee members, Prof. Saad Ragab, Prof. Nicole Abaid, Prof. Sunny Jung, and Prof. Pengtao Yue. Thanks to Prof. Ragab for all he taught me in the viscous flow course. He changed the way I was looking at fluid mechanics problems. I am also grateful to Prof. Abaid who taught me perturbation methods. It was an honor for me to work with her on my project of the phase change phenomena in traffic. I loved Prof. Jung's enthusiasm for research, and his experimental and analytical skills. I especially enjoyed our meetings when we brainstormed crazy and sophisticated ideas. Finally, I want to thank Prof. Yue who has listened patiently to my ideas and shown me the correct direction. Pengtao, you are an amazing teacher; although I have not taken any courses with you, our endless conversations on different problems taught me a lot.

One of the best event happened during my PhD was getting to know an amazing researcher, a younger brother, and a great friend, Saurabh Nath. Indeed, I was really lucky to work with this amazing researcher as a labmate. He is one of the most brilliant persons that I have ever seen.

NIFI was not just a lab to me; it was a home! I am grateful for all the help and friendship given me by my awesome labmates: Ranit, Hyunggon, Weiwei, Kevin, Viverjita, Pranav, and Mohammad. I have been so fortunate to work with most of my labmates. Ranit, thank you for always being available to discuss and provide assistance on problems. Hyunggon, thank you for helping me prepare my set up and take beautiful images; you are an amazing experimentalist. Moreover, during my PhD, I have had a great opportunity to mentor lots of awesome undergrads, Andrew, Christian, Corey, Julia, Katherine, Lance, Megan, and Zaara. Although I was supposed to mentor them, I must admit that I have also learned a lot from them. Indeed, I enjoyed working with them and I will miss them a lot. I already missed Austin, Grady, Daniel, Josh, Matt, and Ziad. I also missed conversations with Bailey and Brian.

Thanks, as well, to the National Science Foundation (NSF), 3M Company for funding my research, and the Department of Biomedical Engineering and Mechanics at VT for their financial support. Special thanks go to all ESM/BEAM staff, especially Jessica, Melissa, Beverly, Darrell, and Dave, without whom I could not go to any conferences or purchase any parts for my experiments.

Finally, my PhD studies would not have been possible without the lifetime support and encouragement of my father, mother, sisters, brother and my amazing friend, Barb. Special thanks to my brother, Farid, who has supported and encouraged me all the time and without whose help I would not be in academia. Although I have not had the chance to visit my sisters and brother since the beginning of my PhD, they have always been in my heart and mind. Last but not least, a big thank goes to Aida, Flor, and Rahim who have always stood by my side in my most difficult time and supported me no matter what!

Contents

List of Figures

List of Abbreviations and Symbols

Symbols

a	Sensitivity (Chapter 2)
a	Fixed contact radius of the liquid/ice interface (Chapter 4)
A	Total cross-sectional area substrates (Chapter 3)
A	Peak amplitude (Chapter 7)
b	Slip length
b_f	Inflection point in the Optimal Velocity Function
b_c	Critical lower limit of the headway distance
c_{i}	Vapor concentrations of ice (Chapter 3)
c_{i}	Specific heat capacity of ice (Chapter 4)
c_{w}	Vapor concentrations of water
c_{∞}	Vapor concentrations of ambient
d	Average pillar diameter
D	Diffusivity of water vapor in air
D_c	Critical size of droplet departure
e_0	Bubble thickness
f	Estimated frost thickness atop the fins (Chapter 3)
f	Imposed frequency (Chapter 7)
F_{acc}	Acceleration force acting on the car
F_{dec}	Deceleration force acting on the car

h	Height of the top of the micro-fins relative to the floor (Chapter 3)
h	Height of the liquid dome (Chapter 4)
h	Frost thickness (Chapter 5)
h_e	Effective height of the ice stripes with respect to the floor
I_c	Critical embryo formation rate
I_0	Kinetic constant
J_e	Liquid droplet's evaporation flux
J_c	Liquid droplet's condensation flux
k	Boltzmann constant (Chapter 3)
k	Height of nanopillars (Chapter 6)
K	Total kinetic energy of the system
k_l	Thermal conductivity of liquid
k_i	Thermal conductivity of ice
l	Characteristic groove spacing (Chapter 5)
l	Center-to-center pitch of nanopillars (Chapter 6)
L	Latent heat of fusion (Chapter 4)
L	Displacement of the liquid front over time (Chapter 5)
l_c	Car length
M	Mass of cars
Ma	Marangoni number
p	Center-to-center pitch of two adjacent ice stripes (Chapter 3)
p	Pore radius (Chapter 4)
p_avg	Average pore diameter
P	Relevant saturation pressure
P_w	Saturated vapor pressure corresponding to the wall temperature (Chapter 3)

P_{w}	Water pressure (Chapter 8)
P_{g}	Pressure of the entrapped gas pockets
P_{∞}	Ambient partial pressure of water vapor
r	Roughness ratio
R	Radius of bubble (Chapter 4)
R	Radius of curvature of the droplet (Chapters 6 and 7)
R	Radius of curvature of the meniscus (Chapter 8)
R_{i}	Ice radius
R_{p}	Thermal plume radius
RH	Relative Humidity
r_p	Pinned contact radius
r_s	Spore radius
$\bar{R}$	Gas constant of water vapor
$\overline{R}$	Universal gas constant
R_{s}	Specific gas constant (Chapter 4)
R_{s}	Spore-laden droplet's radius of curvature (Chapter 7)
R_f	Post-merged radius
R_{eff}	Effective pore radius
Re	Reynolds number
S	Supersaturation (Chapter 3)
S	Arc length of the growing freeze front (Chapter 4)
S^*	Non-dimensional supersaturation
S^*_{Cr}	Critical supersaturation
SSD	Supersaturation degree
t	Time
t_{d}	Drainage time scale

T	Temperature
T_{t}	Temperature top of bubbles
T_{m}	Melting temperature
T_{w}	Substrate temperature
T_{∞}	Ambient temperature
U	Total interaction potential of the vehicles (Chapter 2)
U	Wind velocity (Chapter 7)
v	Velocity of a car (Chapter 2)
v	Growth of coarsening of the ice stripes (Chapter 3)
v	Jumping velocity (Chapter 7)
v_{b}	Bursting velocity
v_{v}	Vibrational speed
v_{i}	Velocity of the i-th car (Chapter 2)
v_{i}	Velocity of freeze front (Chapter 4)
V_{max}	Speed limit of the road
V_{M}	Marangoni velocity
V_{opt}	Optimal velocity
w	Width of an ice stripe
w_{ad}	Work of adhesion
α_{l}	Thermal diffusivity of liquid
α_{i}	Thermal diffusivity of ice
α_{v}	Thermal diffusivity of water/vapor with respect to air
τ	Delay time
τ_{D}	Thermal diffusion time scale
τ_{f}	Time scale of the freeze front motion
δ	Edge-to-edge distance between water and ice (Chapter 3)

δ	Length scale of the temperature gradient (Chapter 4)
δ_{Cr}	Steady-state dry zone length
δ_j	Jamming length
δ_s	Bumper-to-bumper spacing
γ	Liquid-vapor surface tension
$\gamma_{\mathrm{i,l}}$	Interfacial energy of ice with respect to water
$\gamma_{\mathrm{i,v}}$	Interfacial energy of ice with respect to vapor
Δx_i	The headway distance between the $(i+1)$-th and i-th cars
κ^{-1}	Capillary length of water
μ	Viscosity of liquid
$\phi(x)$	Interaction potential function
ϕ	Solid fraction
ρ	Density of liquid
ρ_{air}	Density of air
ζ	Height of the concentration boundary layer of water vapor (Chapter 3)
ζ	Thermal boundary layer (Chapter 4)
ν	Molar volume of water/ice (Chapter 3)
ν	Ratio of the thermal diffusivity of ice to the water (Chapter 4)
ν	Air's kinematic viscosity (Chapter 7)
ν_{i}	Poisson's ratio of ice
σ	Surface tension of water/ice
θ_{a}	Advancing intrinsic contact angle
θ_{A}	Advancing apparent contact angle
θ_{r}	Receding intrinsic contact angle
θ_{R}	Receding apparent contact angle

Ω	Volume of air enclosed by soap film
ψ_0	Fixed angular coordinate of the bubble's contact line
ψ	Angular coordinate of the evolving freeze front
$\forall$	Volume of the liquid spherical cap
ϵ	Emissivity coefficient (Chapters 4 and 5)
ϵ	Degree of asymmetry between merging two droplets (Chapter 7)

Abbreviations

ESEM	Environmental scanning electron microscope
SDS	Solium dodecyl sulfate
SEM	Scanning electron microscope
HPB	Hydrophobic (water-repellent surface)
HPL	Hydrophilic (water-absorbant surface)
SHPB	Superhydrophobic (ultra water-repellent surface)
SHPL	Superhydrophilic (ultra water-absorbant surface)

1

Introduction

1.1 Background information and motivation

The goal of this work is to discover and characterize novel types of phase-change phenomena happening in our daily life. We are interested in the dynamic response of various systems as they undergo melting, condensation, desublimation, or freezing. Specifically, we desire to probe six types of phase-change problems here that are currently under-explored or not even known at all. Problems will be modeled using thermodynamics and fluid mechanics equations.

1.1.1 Latent heat of traffic moving from rest

Rear-end crashes are the most common accident at work zones and tailgating is the leading cause of traffic fatalities in the U.S. [2]. Given the increased safety risk, close-packing at queues can only be justified if it significantly improves the efficiency of traffic flow; it is therefore surprising that there have been virtually no studies on the effects of spacing on the efficiency of group motion from rest. In Chapter 2, we show both experimentally and theoretically how the physics of group motion from rest are governed by the thermodynamic concept of latent heat. Two different types

of experiments were conducted: one with ten cars stopped at a red light and a second with pedestrians queued in a single-file line, where the initial separation between each car/person was varied and the resulting movement through the intersection/line was captured with a drone/motion-capture.

1.1.2 Anti-frosting surfaces using arrays of ice patterns

Ice and frost accumulating on energy and transportation infrastructure results in economic losses amounting to tens of billions of dollars each year [3]. Frost accretion compromises the mechanical integrity and/or energy efficiency of marine structures, power grids, wind turbines, HVAC systems, and aircraft [4]. For example, frost can result in up to a 75% reduction in the efficiency of refrigerators and heat exchangers [5], or a 25% reduction in lift and 90% increase in drag for aircraft [6]. In Chapter 3, we develop a passive anti-frosting surface that can remain 90% dry indefinitely without requiring any input of heat or mechanical forces. The mechanism, ironically enough, uses ice itself. Ice stripes patterned into an array of micro-stripes across a surface, either by using chemical patterns or physical wicking patterns that preferentially attract all nearby moisture from the air due to their hygroscopic nature. Unlike all other hygroscopic materials, ice cannot become diluted as it harvests moisture, so these overlapping dry zones do not collapse over time. Theoretically, we use a rich blend of analytical and computational methods to gain a comprehensive understanding of how the overlapping dry zones depend upon all system parameters.

1.1.3 Freezing soap bubbles

Particularly in the past decade, the kinetics of freezing sessile droplets has been carefully studied. Features of interest include the tendency for ice nucleation to initiate at the three-phase contact line [7], the universal tip singularity that forms at the end of freezing [8], the ability to provoke homogeneous ice nucleation near

the liquid-air interface via evaporative cooling [9], and the formation of explosive frost halos due to recalescence-induced evaporation [10]. Yet almost shockingly, the freezing of bubbles has never been reported in the academic literature despite the fact that bubbles are a popular subject of study [11]. In Chapter 4, as a bubble freezes, we discover that depending on the ambient conditions, two distinct modes of freezing for the ice crystals. The first mode, occurring for isothermally supercooled bubbles, generates a strong Marangoni flow that entrains growing ice crystals to produce a swirling effect that is visually reminiscent of a snow globe. The second mode occurs when the ambient is warmer than the melting temperature, resulting in a bottom-up freeze front that eventually halts due to poor conduction along the bubble. Blending experiments, scaling analysis, and numerical methods, the dynamics of the freeze fronts and Marangoni flows are characterized.

1.1.4 Ice wicking

For offshore and onshore drilling in cold regions, understanding how oil interacts with ice and snow is important from both environmental and economic standpoints. As an interesting example, perhaps the slow rate of oil spreading across ice compared to open water could be better exploited to maximize production yield while minimizing leaks and spills. Oil-ice interactions are also important for the emerging science of using oil-impregnated surfaces for anti-icing and anti-frosting applications, where oil drainage from the surface due to wicking onto ice is a pressing issue. It is therefore quite surprising that, to date, nobody has characterized the physics of oils wicking across ice, frost, or snow on a fundamental level. In Chapter 5, we observe oil as it wicks up sheets of frost grown on aluminum surfaces of varying wettability. Simple scaling arguments are conducted to elucidate the capillary action of a liquid wicking across the surface of ice.

1.1.5 Effect of nanostructures on jumping-droplet condensation

It is now well known that a superhydrophobic surface exhibiting nano-scale roughness is the key requirement to enabling jumping-droplet condensation [12, 13]. To date all experimental studies of jumping-droplet condensation that have explicitly reported the critical departure diameter (D_c) for jumping have only used one [14, 15] or two [16] types of nano-structures. Furthermore, these nano-structures were either hierarchical [14, 15] or highly disordered [16], making it extremely difficult to correlate the incipient growth and inflation of droplets to a simple theoretical model. In Chapter 6, we try to use single-tier, vertically aligned, ordered nano-roughness whose geometrical parameters are systematically varied. In this manner, the experimental values of D_c can be explored over a much wider parameter space than ever before. Both experimentally and theoretically, we try to directly correlate the critical jumping diameter to the topology of the underlying surface structure.

1.1.6 'Sneezing' plants

Wheat provides roughly one quarter of the world's food supply [17], but its total yield is significantly compromised by the spread of diseases such as Fusarium Head Blight (FHB) [18–21] and leaf rusts [22, 23]. The dispersal of plant pathogens is a multifaceted process that involves liberation (discharge from surface), drift (horizontal transport), and deposition (descent and landing) [24, 25]. The drift and deposition of pathogens in the wind has been extensively researched for decades [25–27]. However, for pathogen dispersal in the wind to even be possible, spores must first be ejected a sufficient distance from their plant surface to clear the laminar boundary layer. To our knowledge, condensation has not been considered previously as a spore liberation mechanism. In Chapter 7, we will show that condensation plays a major role in the liberation of fungal spores from wheat plants, both on the heads and on the leaves of the plant. We present our observation that jumping droplet condensation occurs

on the leaves of common wheat plants.

1.1.7 Robust superhydrophobicity using multiple feathers

To date, the wetting and dewetting characteristics of a single superhydrophobic surface have been well established [28–30]. It has been shown that for a single superhydrophobic surface, water initially in the suspended ("Cassie") wetting state can become irreversibly impaled in the "Wenzel" state under a variety of practical conditions such as mechanical compression, underwater submersion beyond a critical hydrostatic pressure, electrowetting, evaporation to a higher Laplace pressure, drop impact, mechanical vibration or deceleration during drop deposition [1, 31–33]. To date no one has studied how the wettability of porous superhydrophobic surfaces is affected by stacking multiple layers together. In nature, virtually every large animal that travels extensively across the free surface of water exhibits multiple layers of feathers, suggesting an adaptational advantage. Considering that naval ships are the engineering equivalent to waterfowl traveling atop water, in Chapter 8, we therefore propose that adding synthetic feathered coatings to ships has the potential to maximize their travel efficiency while also minimizing hull fouling. We quantitatively characterize the critical pressure required for water to impale both natural and synthetic duck feathers. We will develop model to reveal mechanism of the "layer effect."

1.2 Intellectual merit

This dissertation will characterize the dynamics of various phase-change phenomena, and in some cases even reveal entirely new phenomena. Historically, systems undergoing phase changes have been considered as fixed boundaries and/or fixed boundary conditions in terms of their dynamic motion. For example, the classical case of filmwise condensation on an inclined substrate exhibits a steady liquid profile.

As another example, virtually all prior studies of freezing droplets have deposited sessile (i.e. motionless) droplets on a chilled substrate. However, we argue that many real-life phase-change systems are more dynamical in nature. To return to the condensation example, we explore here how a condensing droplet can not only dynamically grow within a surface structure in a thermodynamically complex fashion, but even jump from the surface upon coalescence. This philosophy of bringing out the dynamic nature of phase-change systems can be encapsulated in one final example. To date, traffic studies have only characterized the steady-state motion of vehicles through a traffic light. In contrast, we capture the transient dynamics upon the initiation of the green light, where the packing density of the cars has to melt from a close-packed "solid" phase into a more open "liquid" phase. Surprisingly, we found that the lag inherent to such phase changes made the transient flow rate independent of the initial packing density at the queue. In other words, there is no practical purpose (and often danger) by coming to a stop close to the car in front of you. By looking beyond the static or steady simplifications that represent the bulk of historical scholarship, we can reveal rich and complex dynamical phenomena lurking underneath seemingly mundane phase-change processes.

1.3 Practical applications

Understanding the complex phase-change phenomenon at a traffic light would result in an optimal space between vehicles at stoppages for a safer driving. The anti-frosting technology which merely uses the unique chemistry of ice, can be the only efficient and practical way to passively halt the frost propagation on a surface without using any active energy. The complex physics of freezing of bubbles unveil completely new forms of multiphase flows that exhibit rich physical behavior. The effect of superhydrophobic nanostructures on jumping-droplet condensation of water helps us to fabricate more efficient condensers. Finally, understanding why layered

structures delay the onset of the Cassie to Wenzel wetting transition in superhydrophobic coatings helps us to engineer robust and durable antifouling coatings for ships and submarine which may yield a dramatic decrease in drag force.

2

Latent Heat of Traffic Flow

Moving From Rest

"Nature does not hurry, yet everything is accomplished."

−Lao Tzu

The content of this chapter was previously published as a journal manuscript in [34], and reproduced here with minor modifications. In this chapter we are trying to understand how the physics of group motion from rest are governed by the thermodynamic concept of latent heat.

2.1 Introduction

Any driver knows the unspoken rule that vehicles should increase their packing density at stoppages such as red lights or traffic jams. However, this "liquid-to-solid" phase transition can be a source of accidents. For instance, rear-end crashes are the most common accident at work zones, due to the tailgating inherent to the frequent

stop-and-go phase transitions [35, 36]. More generally, it was estimated that over a quarter of all car crashes were rear-end collisions, which almost always occur due to short headways between vehicles [2]. Given the increased safety risk, close-packing at queues can only be justified if it significantly improves the efficiency of traffic flow; it is therefore surprising that there have been virtually no studies on the effects of spacing on the efficiency of group motion from rest. It is not necessarily a given that inducing phase transitions at stoppages increases flow efficiency, as reverting back into the liquid phase when motion is resumed is analogous to the input of "latent heat," which produces significant lag.

Various types of nonphysical systems including traffic and granular flows or economic, social, and biological systems have been modeled by employing statistical physics, nonlinear dynamics, and thermodynamical considerations [37–42]. Similar modeling techniques have also been used to model the social interactions and collective behavior of various animal species [43–46]. For the specific context of vehicular traffic flow, several models have been developed that are macroscopic (fluid dynamics) [47,48], microscopic (follow-the-leader) [49,50], or mesoscopic (Lattice gas automata) [51, 52].

Perhaps the most impactful traffic model is the Optimal Velocity Model (OVM) pioneered by Bando et al., where the acceleration and deceleration forces of each individual car are a function of the spacing between cars, the speed limit of the road, and the sensitivity of the drivers [49, 50, 53–57]. The OVM has been correlated with experiments of single-lane traffic on circuits [58, 59] or freeways [60–64], but nearly always in the context of beginning with flow in the liquid phase and identifying critical conditions for jamming to occur. To the best of our knowledge, the reverse situation of cars moving from rest has not been considered, aside from some brief mentions in purely theoretical implementations of OVM [65, 66].

Weber and Mahnke have recently expanded the OVM to develop expressions for

the internal energy and kinetic energy of the traffic system [67]. This thermodynamical approach was used to calculate the theoretical change in energy for a liquid-to-solid phase transition [68]. While these works were an important first step toward conceptualizing the thermodynamics of phase transitions, no experiments were done to test the model and only the liquid-to-solid phase transition was considered, not the reverse case of solid-to-liquid.

The dynamics of pedestrian traffic are analogous to vehicles, except that flow is two-dimensional and the preferred direction of the pedestrians has to be considered [69]. As with traffic studies, most models of pedestrians focus on beginning with the liquid phase and identifying bottlenecks that cause jamming [70–74], not the latent heat associated with motion from rest.

Here, for the first time we show both experimentally and theoretically how the physics of group motion from rest are governed by the thermodynamic concept of latent heat. Two different types of experiments were conducted: one with ten cars stopped at a red light and a second with pedestrians queued in a single-file line, where the initial separation between each car/person was varied and the resulting movement through the intersection/line was captured with a drone/motion-capture. Correlating the results to the OVM revealed a universal trend that the interaction potential of a group at rest must go to zero in order for group motion to fully resume, resulting in the latent heat (lag time) inherent to group motion from rest. For the slow-moving pedestrian system, the intuition to close-pack in a queue is correct, as the increase in lag time is minor relative to the savings in displacement. However, the importance of latent heat for vehicles was profound: the time required for cars to cross the intersection did not vary even as the initial spacing between cars was increased by a factor of 20. Hence, the current rule of thumb that vehicles should become close-packed at stoppages does not appear to be sensible, as safer spacings can be maintained with no reduction in the departure flow rate.

2.2 Car motion through a traffic light

2.2.1 Smart road experiments

Ten volunteer drivers conducted a study on the closed-circuit Smart Road located at the Virginia Tech Transportation Institute (Figure 2.1A). Each driver was provided a Chevy Impala (LS Sedan 4D, 2011-2012) of identical dimensions that was rented from Virginia Tech Fleet Services and insured for the study. The Smart Road includes a traffic light located in the middle of a flat, straight road with single lanes and a speed limit of 35 mph (15.6 m/s). The traffic light was initially set to red and all ten volunteer drivers were instructed to line up in a queue. Using radio transmitters and approved safety protocols (IRB #15-484), each driver came to a stop at a fixed bumper-to-bumper spacing (δ_s) from the car ahead (see section 2.5.1). Spacings were measured by fixing a tape measure between two tall traffic cones; one cone was placed at the rear bumper of a car already stopped in "Park," while another car was instructed to slowly approach the second cone until its front bumper made contact. For any given trial, all cars in the queue exhibited an identical value of δ_s, which was varied to be either 1.25 ft (0.38 m), 3 ft (0.91 m), 6 ft (1.8 m), 12 ft (3.6 m), 25 ft (7.6 m), or 50 ft (15 m).

Once all ten cars were queued at the red light with the appropriate spacing, a drone helicopter (DJI Inspire 1) was programmed to hover over the intersection at a fixed elevation of 200 ft (61 m) with respect to the road. The drone included a digital video camera attached to a gimbal (DJI Zenmuse X3) to obtain controlled bird's-eye-view footage of the traffic. All drivers could see the traffic signal and they were instructed to accelerate in a normal and comfortable fashion up to the road's speed limit of 35 mph when the light turned green. It was strongly emphasized that the bumper-to-bumper spacing initially imposed at the red light does not need to be maintained once flow resumed. Three trials were captured for each car spacing, with

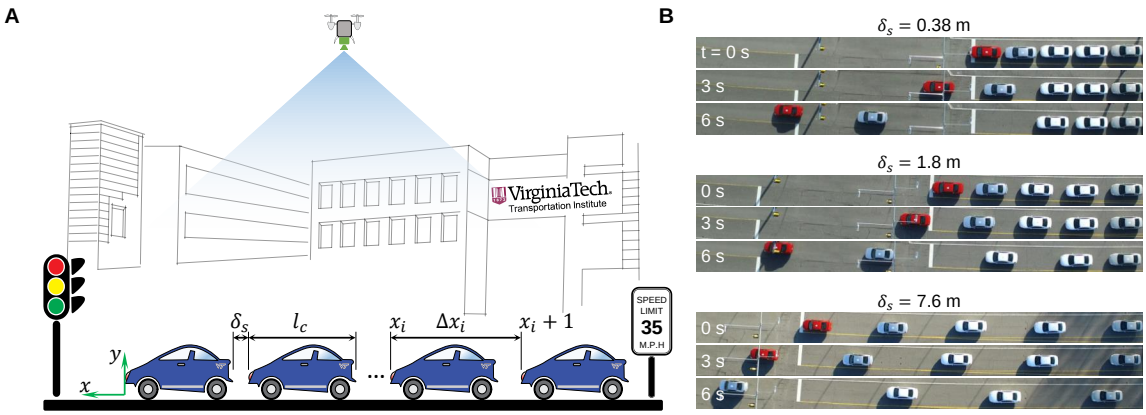

FIGURE 2.1: Setup of experiment performed on a Smart Road. A) Schematic of the experiment performed on a Smart Road, where ten volunteer drivers with identical Chevy Impalas (length $l_c = 5.0\,\text{m}$) were queued at a red light with a controlled bumper-to-bumper spacings (δ_s). When the light turned green, a drone flying overhead captured the acceleration of the cars through the intersection as a function of δ_s. B) Drone footage revealed that it takes more time for cars to begin to move for small values of δ_s (bottom images) compared to larger values, which can be conceptualized as the latent heat of transitioning from a solid phase to a liquid phase. Time zero for all figures corresponds to the leading car's onset of motion, as the drone could not see exactly when the light turned green.

the order of the drivers changing for each trial. For consistency, the three different driver orders chosen for the three trials were kept the same for all six car spacings. When the cars and drone were all in place, the drivers were instructed to put their cars in "Drive" and proceed through the intersection when the light turned green. Once all drivers confirmed via radio that they were idling and ready to go, the traffic light was turned to green using a Smart phone interfaced with the Smart light.

The drone footage showed that it takes more time for cars to begin to accelerate with decreasing δ_s (Figure 2.1B). For example, when $\delta_s = 0.38\,\text{m}$ (top images), the third car in the queue is not moving even after 6 s from when the first car began to accelerate through the intersection. This is because of the long delay time required for each car to regain a safe distance to the car ahead before readily accelerating (latent heat). In contrast, when $\delta_s = 7.6\,\text{m}$, the latent heat is reduced and even the fifth car is able to move within the initial 6 s.

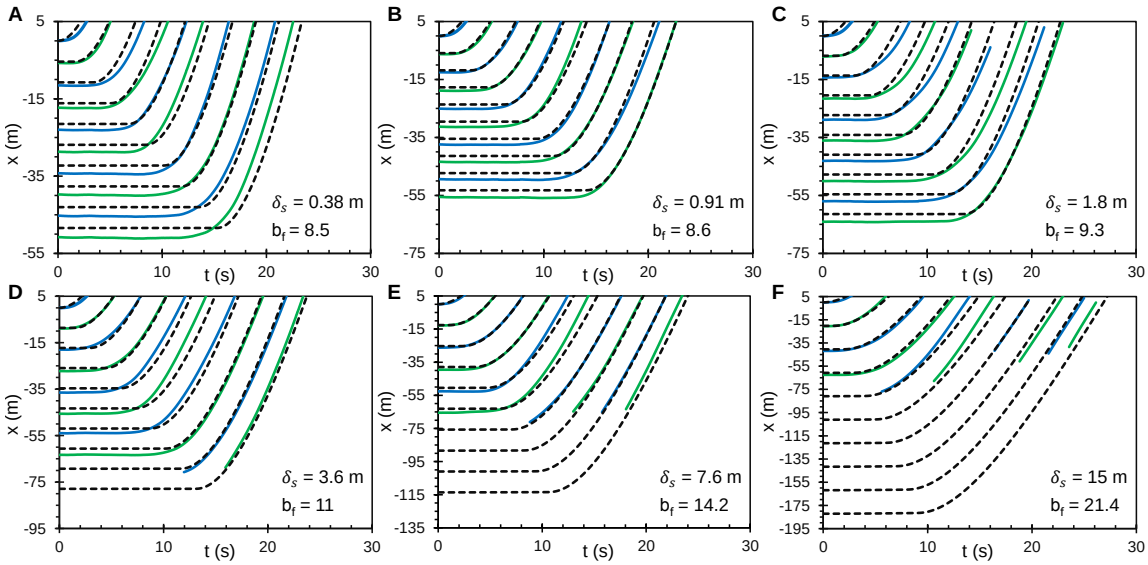

FIGURE 2.2: Displacements of cars driving from rest. Experimental (solid lines) and theoretical (dashed lines) displacements of ten cars driving from rest through a traffic light. The initial location of the lead car's front bumper is defined as $x = 0$ and each vehicle effectively clears the intersection upon reaching $x = 5$ m. The initial bumper-to-bumper spacings of the cars was (A) $\delta_s = 1.25$ ft (0.38 m), (B) $\delta_s = 3$ ft (0.91 m), (C) $\delta_s = 6$ ft (1.8 m), (D) $\delta_s = 12$ ft (3.6 m), (E) $\delta_s = 25$ ft (7.6 m), (F) $\delta_s = 50$ ft (15 m). Experimental lines represent an average of 3 trials and the alternating blue and green colors are to help guide the eye. The black dashed lines represent the Optimal Velocity Model, where b_f is a fitting parameter representing the inflection point of the Optimal Velocity Function that will be discussed fully in Section 2.2.2. For visualization purposes, the y-axis is not scaled the same for graphs A – F.

An open-source software (Tracker) was used to convert the drone footage to displacement plots for each car. Solid lines in Figure 2.2 show the displacements of the front bumpers of all ten cars over time for each value of δ_s, with all values being averaged from the 3 separate trials to mitigate effects of driver variability. Remarkably, the time required for all ten cars to cross the intersection remained fixed at 23.0 ± 1.1 s for all spacings ranging from $\delta_s = 0.38$ m up to $\delta_s = 7.6$ m (Figure 2.5A), even though in the latter case δ_s is larger by a factor of 20 and the vehicles are traveling twice as far to cross the intersection (Figure 2.2A,E). This balance between reduced lag and increased displacement is eventually lost, but only for the extreme

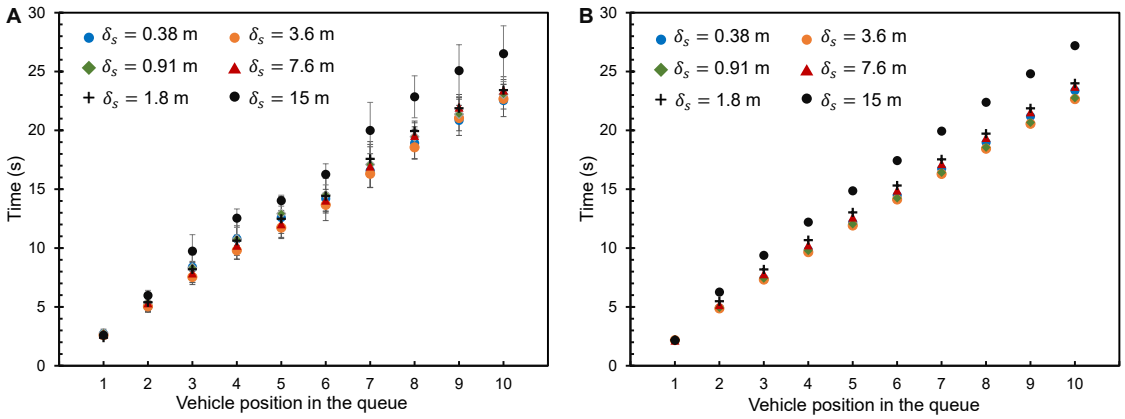

FIGURE 2.3: Time required for each vehicle to pass the intersection. Experimental (A) and theoretical (B) time required for each vehicle to pass the intersection vs. vehicle position in the queue for different static bumper-to-bumper spacings. Error bars show one standard deviation between the three trials.

case where δ_s exceeds the minimum spacing required for comfortable driving (analogous to a "gas phase"). For example, the cars required a slightly larger time of $27 \pm 3\,\mathrm{s}$ for $\delta_s = 15\,\mathrm{m}$ (Figure 2.5A). Moreover, as it is depicted in Figure 2.3 A, the time required for each car to cross the intersection was found independent of the static bumper-to-bumper spacing as δ_s varies from 0.38 m to 7.6 m.

It is already well known that the saturation flow rate of vehicles passing through a green light is generally fixed around 1500–1800 vphg (vehicles per hour of green) over a wide variety of natural driving conditions [75–77]. However, this is because the saturation flow rate only considers the steady-state case of cars that are already crossing the intersection with a constant liquid-phase headway (Figure 2.4A) [78, 79], thus ignoring the initial start-up lost time where the solid-to-liquid transition actually occurs. Our focus here is therefore not on the saturation flow rate, but on the start-up lost time (i.e. departure flow rate) which considers the time required for the first four cars in the queue to cross the intersection when the light first turns green. By breaking up the total time required for all 10 cars to cross the intersection into the transient and steady times, we observe that both the departure flow rate and

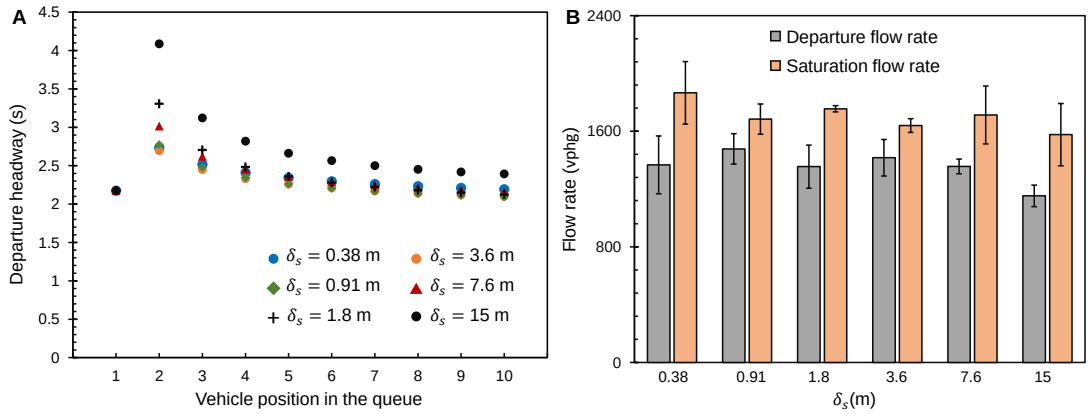

FIGURE 2.4: Departure headway and saturation flow rates. (A) Departure headway vs. vehicle position in the queue for different static bumper-to-bumper spacings (δ_s). The saturation headway is the steady-state headway which was (approximately) obtained after the fourth car in the queue, and was about 2 s for all cases except the "gas phase" of $\delta_s = 15$ m. Values are based off the theoretical model that was best-fit to the experimental results; the departure headway for the first car is artificially low because the reaction time of the driver to the light turning green was not included. (B) Experimental departure and saturation flow rates for different values of δ_s, in terms of the vehicles per hour of green light (vphg) that cross the intersection. The departure flow rate corresponds to the start-up lost time of the first four vehicles crossing the intersection during the initial transient, while the saturation flow rate corresponds to steady-state headway conditions.

the saturation flow rate are insensitive to δ_s for all solid and liquid-phase packing densities (Figure 2.5A, Figure 2.4B). By definition, it is obvious that the saturation flow rate is independent of δ_s, so we emphasize that our surprising finding is that even the start-up lost time is invariant with δ_s due to the effect of latent heat. Previous reports have characterized how the start-up lost time can be affected by inclement weather [80], countdown timers [81, 82], the time of day or speed limit [83], and distracted drivers [84, 85]. However, we could not find a single study in the traffic literature where the effects of the initial (static) car spacing on the start-up lost time were investigated, which is the novelty of our present work.

2.2.2 Theoretical model

The above results show the pronounced effect of latent heat on group motion from rest, which will now be examined analytically using the OVM. The development of a theoretical model will be especially useful for extrapolating the displacement curves of the experiments done with large spacings ($\delta_s \geq 3.6\,\mathrm{m}$), where the drone's field-of-view could not capture the initial position and acceleration of several cars at the back of the queue (see Figure 2.2D−F). Recall that the OVM is a semi-empirical microscopic model and can be used to develop theoretical displacement curves to match the experiments. The equation of motion for the i-th car with mass M and velocity v_i is [65]:

$$M\frac{dv_i}{dt} = F_{\mathrm{acc}}(v_i) + F_{\mathrm{dec}}(\Delta x_i), \tag{2.1}$$

where F_{acc} and F_{dec} are the acceleration and deceleration forces acting on the car, respectively, and Δx_i is the headway distance between the $(i+1)$-th and i-th cars ($\Delta x_i = x_{i+1} - x_i$).

The acceleration and deceleration functions are defined as:

$$F_{\mathrm{acc}}(v_i) = \frac{M}{\tau}(V_{\max} - v_i) \geq 0, \tag{2.2}$$

$$F_{\mathrm{dec}}(\Delta x_i) = \frac{M}{\tau}(V_{\mathrm{opt}}(\Delta x_i) - V_{\max}) \leq 0, \tag{2.3}$$

where τ is the delay time and defined as the inverse of drivers' sensitivity ($\tau = 1/a$). The higher the sensitivity of a driver, the faster the driver will accelerate or decelerate to reach the optimal velocity. The value of a is typically chosen to fit the model to the experimental displacement curves; here, a constant value of $a = 0.15\,\mathrm{s}^{-1}$ was assigned to all drivers. The V_{max} term in Equation 2.2 corresponds to the speed limit of the road (15.6 m/s). In Equation 2.3, $V_{\mathrm{opt}}(\Delta x_i)$ represents the optimal velocity desired by each car at any moment in time as a function of the headway distance, and is

represented by the Optimal Velocity Function (OVF) [49]:

$$V_{\text{opt}}(\Delta x_i) = v_0\big[\tanh\left(m(\Delta x_i - b_f)\right) - \tanh\left(m(b_c - b_f)\right)\big], \tag{2.4}$$

where the four parameters v_0, m, b_f and b_c are constants obtained from the experiments. Specifically, v_0 is a velocity term solved from boundary conditions, m is a fitting parameter, b_f is the inflection point in the OVF, and b_c is the critical lower limit of the headway distance that represents jamming. Note that while there are alternate expressions for the OVF in the literature [67], we found that Equation 2.4 resulted in the best fit with the experimental data.

To obtain the value of b_c, let us define the actual length of the car as l_c, which is approximately 5 m for the Chevy Impalas used in this study. Obviously, even in traffic jams each driver must maintain a headway distance larger than the actual car length to avoid crashing. Therefore the effective length of each car (b_c) must include a minimal bumper-to-bumper spacing (typically $\delta_j = 2\,\text{m}$), such that $b_c = l_c + \delta_j = 7\,\text{m}$. Note that for the controlled experiments performed here, the parameter space deliberately included $\delta_s < \delta_j$ (by virtue of using traffic cones and spotters) to probe the full extent of latent heat. A solution for v_0 can be obtained by considering the limiting case of $\Delta x_i \to \infty$, where the optimal velocity of each car will simply be the speed limit ($V_{\text{opt}}(\infty) = V_{\text{max}}$) and $\tanh(m(\Delta x_i - b_f)) \to \tanh(\infty) = 1$. This simplifies Equation 2.4 to $v_0 = V_{\text{max}}/[1 - \tanh(m(b_c - b_f))]$, where here $m = 2\,\text{m}^{-1}$ for each spacing. Finally, the inflection point of the OVF is defined as $b_f = l_c + B$ in which $V_{\text{opt}}(b_f) = V_{\text{max}} - v_0$ and B is a fitting parameter to be determined from the experimental data. In Equation 2.3, the deceleration force reaches to its maximum value when $V_{\text{opt}}(b_c) = 0$ and it goes to zero as Δx_i goes to infinity. In summary, we utilize a constant value for τ, V_{max}, l_c, δ_j, b_c, and m for all trials, such that only B and by extension b_f and v_0 are varying with δ_s. For a given trial, all of these terms are the same for all ten drivers. Despite the fact that $\delta_s < \delta_j$ for some of the

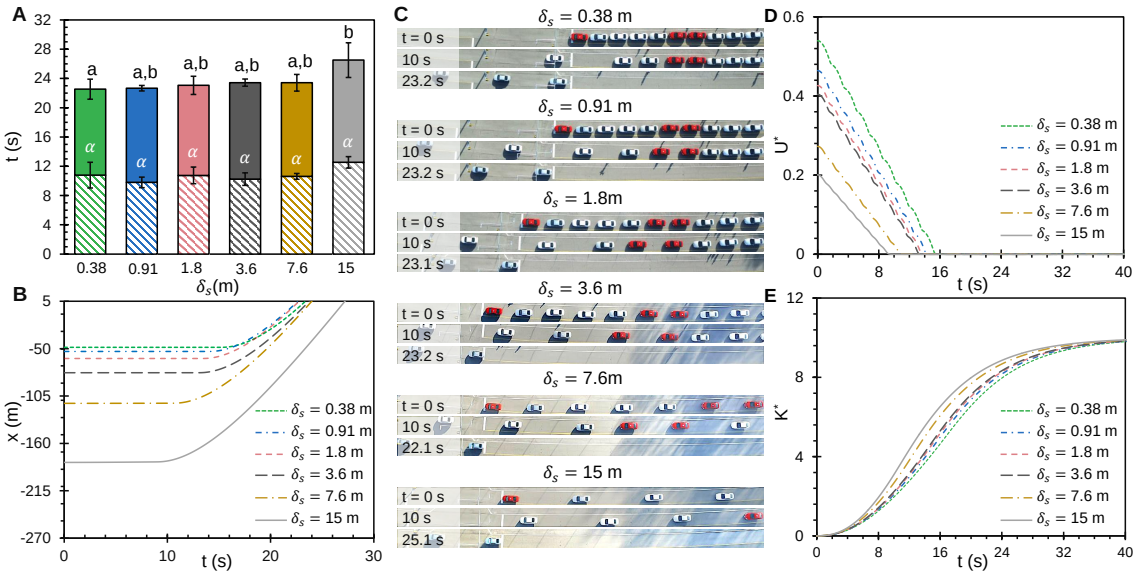

FIGURE 2.5: Vehicular motion through a traffic light. A) Mean total time required for all ten cars to drive through the intersection. Time zero corresponds to when the lead car begins to move. The hashed region depicts the start-up lost time, which by convention is the time for the first four cars to pass the intersection. Error bars show one standard deviation between the three trials. The effect of condition is statistically significant for the total time and start-up lost time, using two one-way ANOVAs (JMP Pro 11 software, $p < 0.09$ for significance). Conditions sharing the same superscript letters are not significantly different in terms of Tukey post hoc tests ($p > 0.10$). There is no statistically significant difference in the start-up lost time for all six spacings, despite a variance in the bumper-to-bumper spacing by a factor of 40; only the conditions with smallest and largest initial spacings show statistically significant differences for the total time. B) Displacement vs. time of the last (tenth) car in the line for different static bumper-to-bumper spacings. C) Drone imaging of the vehicular flow dynamics for all the six spacings at $t = 0$ s, 10 s, and the time when the last car crosses the finished-line. D,E) Non-dimensionalized interaction potential and kinetic energy of the system versus time.

experiments here ($\delta_s = 0.38\,\mathrm{m}$ and $\delta_s = 0.91\,\mathrm{m}$), fitting B to the experimental data ensures that $V_{\mathrm{opt}}(\Delta x_i) \geq 0$ over the entire parameter space even when modeling the initial motion from rest (Figure 2.6).

The governing differential equations of the system can be found by substituting

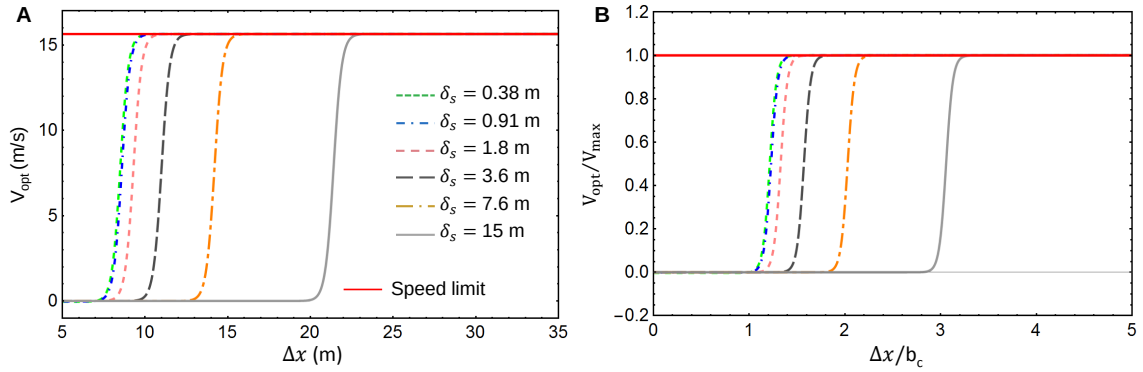

FIGURE 2.6: Optimal Velocity Function. (A) Dimensionalized and (B) non-dimensionalized Optimal Velocity Function (OVF) vs. headway distance for all of the static bumper-to-bumper spacings. The horizontal red line corresponds to the speed limit of 15.6 m/s. Even for the highly-packed case of $\delta_s = 0.38$ m, it can be seen that the OVF is zero until the headway distance becomes larger than b_c to ensure safe driving. The OVF is either zero or positive over the entire parameter space, showing that the nonphysical case of a negative velocity does not occur.

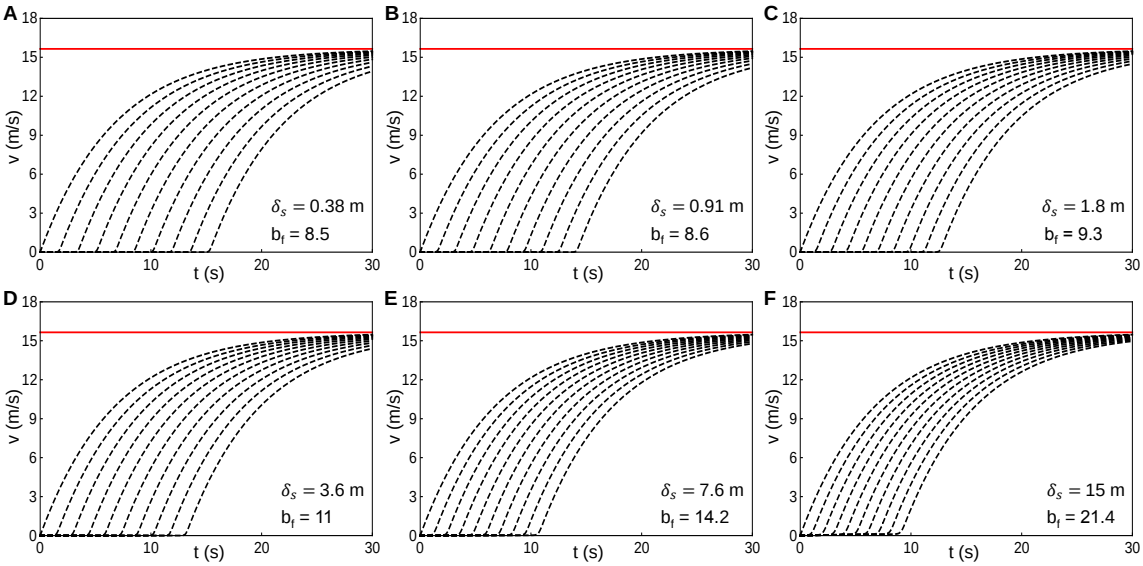

FIGURE 2.7: Velocity of vehicles driving from rest. Theoretical velocities of ten cars driving from rest through a traffic light for: (A) $\delta_s = 0.38$ m, (B) $\delta_s = 0.91$ m, (C) $\delta_s = 1.8$ m, (D) $\delta_s = 3.6$ m, (E) $\delta_s = 7.6$ m, and (F) $\delta_s = 15$ m. The red line represents the speed limit ($V_{\max} = 15.6$ m/s).

Equation 2.2 and Equation 2.3 into Equation 2.1 [49]:

$$\frac{dx_i}{dt} = v_i, \tag{2.5}$$

$$\frac{dv_i}{dt} = a(V_{\text{opt}}(\Delta x_i) - v_i). \tag{2.6}$$

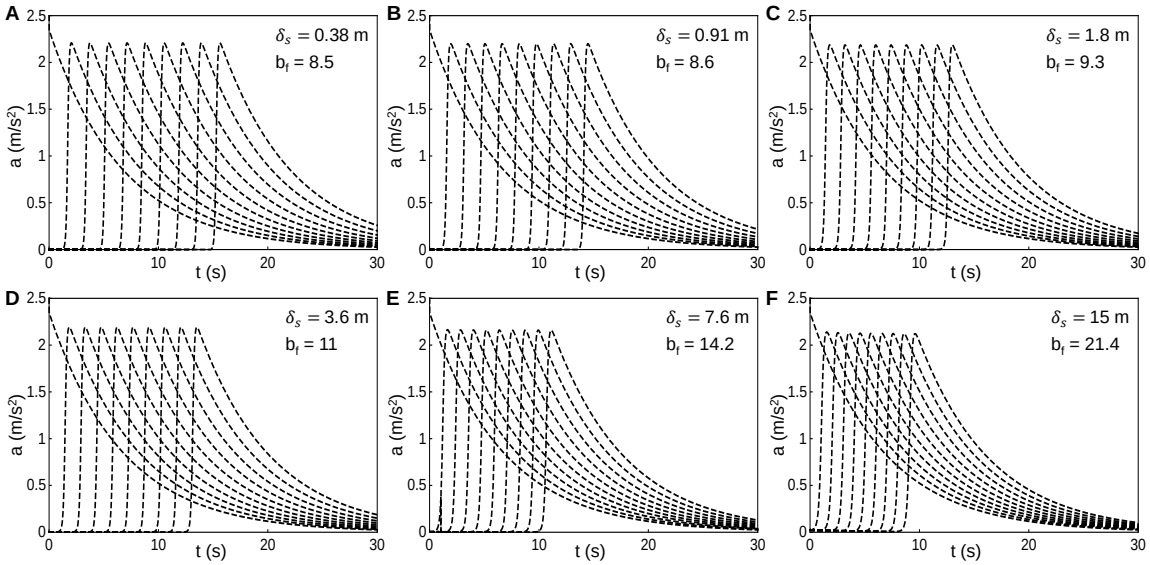

FIGURE 2.8: Acceleration of vehicles driving from rest. Theoretical accelerations of ten cars driving from rest through a traffic light for: (A) $\delta_s = 0.38\,\text{m}$, (B) $\delta_s = 0.91\,\text{m}$, (C) $\delta_s = 1.8\,\text{m}$, (D) $\delta_s = 3.6\,\text{m}$, (E) $\delta_s = 7.6\,\text{m}$, and (F) $\delta_s = 15\,\text{m}$.

We have used Mathematica to integrate the coupled equations of motion, Equations 2.5 and 2.6, in order to determine the position and velocity of each car at every time moment. The dashed black lines in Figure 2.2 show the theoretical displacement curves, which agree with their experimental counterparts within the experimental uncertainty for all times (Figure A.1). Therefore, we can use the theoretical solution to extract all of the velocity and acceleration curves for each spacing (Figures 2.7 and 2.8). Note that minor differences in the initial positions of the cars are due to imperfections in aligning the cars experimentally compared to the perfectly consistent values of δ_s used in the model.

By plotting the theoretical displacement curves of the final (tenth) car in the line for each value of δ_s, it can be seen that the increased travel distance required for liquid phase queues is perfectly compensated for by a reduced lag in acceleration compared to solid phase queues (Figure 2.5B). This is also evident by looking at the drone footage for each value of δ_s (Figure 2.5C). As mentioned before, the time

required to clear the intersection does finally increase for the largest ("gas phase") spacing of $\delta_s = 15\,\mathrm{m}$, where the increase in required displacement finally becomes greater than the reduction in lag. The theoretical time required for each of the ten cars to cross the intersection is in excellent agreement with the experimental results (Figure 2.3).

As δ_s increases, the delay time required until each vehicle begins to move with respect to the car in front of it will be decreased (Figures 2.7 and 2.8). For example, 20 s after the first car begins to move, the average velocity of the tenth car increased by 49 % when comparing $\delta_s = 0.9\,\mathrm{m}$ to $\delta_s = 7.6\,\mathrm{m}$.

To characterize the lag of vehicular motion in terms of the concept of latent heat, we first need to develop an expression for the internal energy of the system. The total interaction potential of the vehicles is [67]:

$$U = \sum_{i=1}^{n} \phi(\Delta x_i), \tag{2.7}$$

where $\phi(\Delta x_i)$ is the interaction potential function which represents the interaction between the $(i+1)$-th car and the i-th car ahead. The interaction potential function can be obtained from the integration of the deceleration force function with respect to Δx_i. The interaction potential function can be found from the deceleration force as:

$$\frac{d\phi(x)}{dx} = F_{\mathrm{dec}}(x), \tag{2.8}$$

$$\phi(x) = \int F_{\mathrm{dec}}(x)dx, \tag{2.9}$$

where the deceleration force (F_{dec}) is defined as:

$$F_{\mathrm{dec}}(x) = \frac{M}{\tau}\left(V_{\mathrm{opt}}(\Delta x_i) - V_{\max}\right). \tag{2.10}$$

Recall that V_{opt} is the Optimal Velocity Function, which is defined as:

$$V_{\text{opt}}(x) = \frac{V_{\max}}{1 - \tanh(m(b_c - b_f))}\Big(\tanh(m(x - b_f)) - \tanh(m(b_c - b_f))\Big), \quad (2.11)$$

and the terms on the right hand side of Equation 2.11 are already defined in the main paper. Substituting (2.10) and (2.11) into (2.9) yields:

$$\phi(x) = \frac{MV_{\max}}{\tau}\int \frac{1 + \tanh(m(b_f - x))}{\tanh(m(b_c - b_f)) - 1}dx. \quad (2.12)$$

To find the analytical solution of (2.12) let us define $m(b_f - x) = \bar{x}$ so that $dx = -d\bar{x}/m$. Using the trigonometric identity

$$1 + \tanh(x) = \frac{2e^{2x}}{1 + e^{2x}}, \quad (2.13)$$

(2.12) is simplified to:

$$\phi(\bar{x}) = \frac{-MV_{\max}}{\tau[\tanh(m(b_c - b_f)) - 1]}\int \left(\frac{2e^{2\bar{x}}}{1 + e^{2\bar{x}}}\right)\frac{d\bar{x}}{m}, \quad (2.14)$$

whose integration yields the following solution:

$$\phi(\bar{x}) = \frac{-MV_{\max}}{\tau m[\tanh(m(b_c - b_f)) - 1]}\log(1 + e^{2\bar{x}}) + C, \quad (2.15)$$

where C is the constant of the integration. Using the boundary condition of $\phi(\bar{x}) \to 0$ as $\bar{x} \to -\infty$, the interaction potential energy between two particles is found as:

$$\phi(\Delta x_i) = \frac{MV_{\max}\log(1 + e^{2m(b_f - \Delta x_i)})}{\tau m[1 - \tanh(m(b_c - b_f))]}, \quad (2.16)$$

Figure 2.5D plots the total non-dimensionalized interaction potential, $U^* = U/(1/2MV_{max}^2)$, vs. time for each value of δ_s. As expected, the interaction potential of the system is dramatically larger with decreasing δ_s, for example the potential for $\delta_s = 0.38$ m

(smallest spacing) is nearly three times larger than for $\delta_s = 15$ m (biggest spacing). Interestingly, the interaction potential is completely reduced to zero well before the cars are able to cross the intersection, which reveals that drivers do not feel comfortable reaching even moderate velocities under the presence of internal energy. This explains the significant lag time of close-packed queues of vehicles upon resumption of flow, where the interaction potentials are dramatically increased relative to loose-packed systems. We therefore define the latent heat of fusion as equivalent to the queue's total interaction potential at rest. To our knowledge, this is the first such definition of latent heat with regards to group motion from rest.

The total kinetic energy of the system is:

$$K = \sum_{i=1}^{n} \frac{M v_i^2}{2}, \tag{2.17}$$

which can be non-dimensionalized by the maximum kinetic energy($1/2MV_{max}^2$) and plotted vs. time for each car spacing (Figure 2.5E). Looking at Figure 2.5D,E together, one can conclude that the kinetic energy of the system cannot come close to its maximum value until the interaction potential goes to zero. Trying to accelerate cars packed in a solid-phase is somewhat analogous to trying to heat a bucket of ice water. Just as the energy input into the ice water cannot be converted to sensible heat until all ice has melted by the latent heat of fusion, the cars cannot readily increase their "temperature" (kinetic energy) until the solid phase has "melted" into the liquid phase.

2.3 Pedestrians emptying a line

2.3.1 Motion-capture experiments

It is now clear that latent heat plays a major role in the dynamics of vehicular motion starting from rest. But how general are these findings? In the preceding

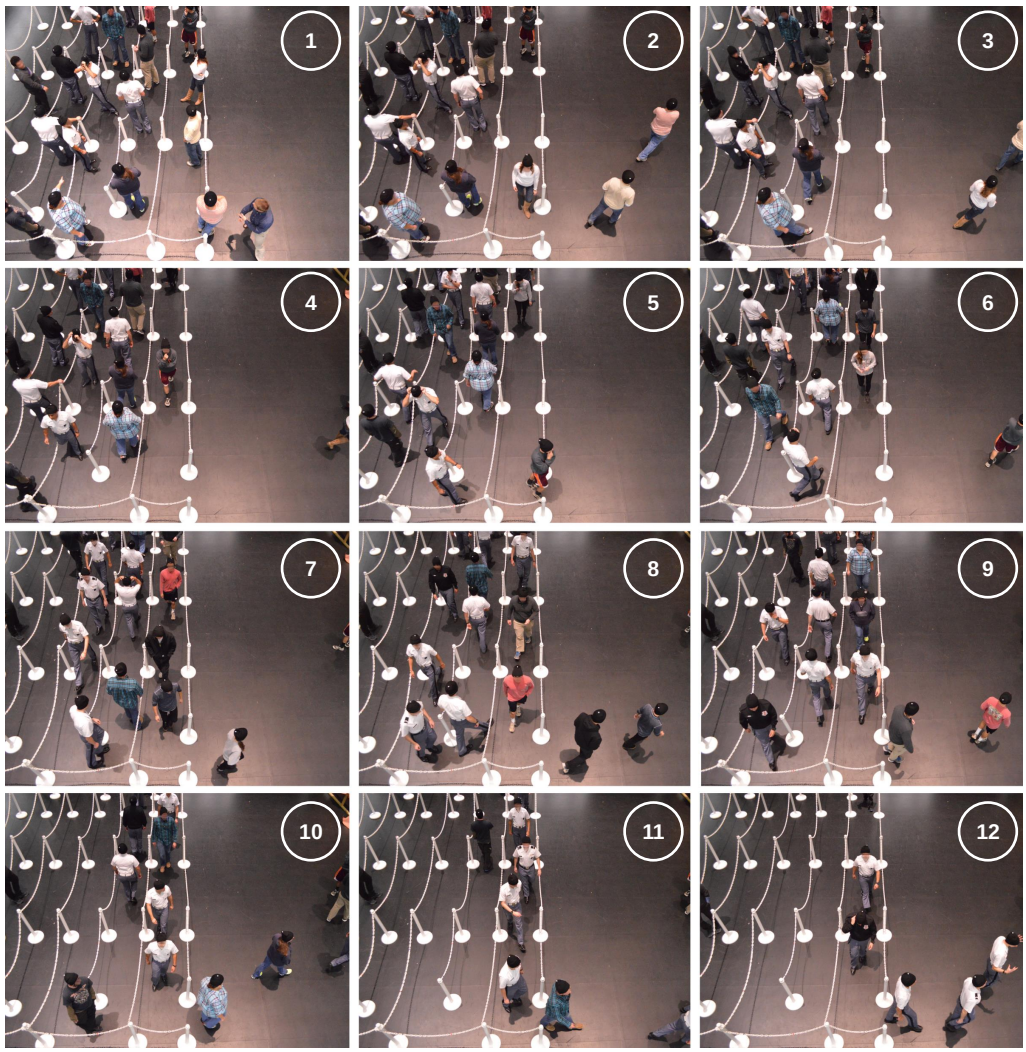

FIGURE 2.9: Experimental setup of a motion-capture room. Snapshots of the experiment in the motion-capture room which shows the motion of pedestrians exiting a line when the initial period between people is $\delta_s = 1.8\,\mathrm{m}$. As it is shown in Figure 2.10, the required time for the 16^{th} person to exit the line is about 25.5 s.

section, we defined the latent heat as equivalent to the total interaction potential of the queue at rest: $U_i = U(0)$. According to the OVM model, the value of U_i is dependent upon system parameters such as the maximum speed (V_{max}) and the sensitivity ($a = 1/\tau$) of each moving body (Equations 2.7 and 2.16). Therefore it

is possible that, for systems where moving bodies are slow and/or able to quickly accelerate, the latent heat becomes less significant and it may no longer be desirable to avoid phase transitions at stoppages. To test this hypothesis, a second set of experiments were performed to study the effects of latent heat on the group motion of pedestrians, who move slowly and accelerate quickly relative to vehicles. The experiment was performed at the Moss Arts Center at Virginia Tech in a motion-capture room called 'The Cube.' Using approved protocols (IRB #14-914), a group of 27 volunteers were asked to form a one-dimensional line that was defined by velvet ropes suspended between stanchions (Figures. 2.10A and 2.9). As with the vehicles, the spacing between pedestrians at rest in the line was systematically varied and 3 trials were performed for each spacing. In one set of experiments the subjects were instructed to pack together as close as possible (average period of 0.37 m), while subsequent experiments fixed the person-to-person spacing at 3 ft (0.91 m), 6 ft (1.8 m), and 12 ft (3.6 m).

The person at the front of the line was adjacent to a detachable rope, which was removed to initiate group motion once all 27 pedestrians were in place. The volunteers were instructed in advance to proceed from the line into an adjacent open space by walking at a normal pace without any passing. Each pedestrian wore a black hat containing a white motion-capture tracer bead, whose displacement was captured using 24 synchronized cameras surrounding the walls that were interfaced to a software package (Qualisys). Analogous to the Smart Road study, the Tracker software was used to generate the displacement plots (solid lines in Figure A.2A-D). Displacements were only analyzed for the first 16 pedestrians in the line, as this was the maximum number of people who were able to fit inside of the line for the largest spacing.

In contrast to the vehicular flows, Figure 2.10B shows that the required time for all pedestrians to empty the line increases significantly with increasing δ_s. Note that

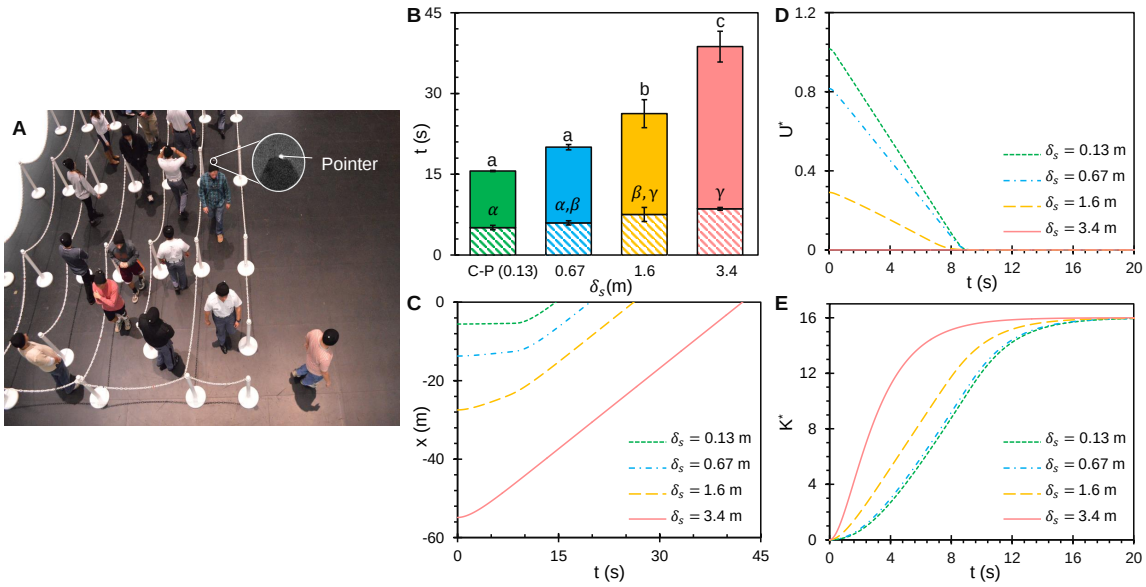

FIGURE 2.10: Characterizing pedestrian motion. A) Experiments with queues of pedestrians used motion-capture facilities to characterize the flow out of a line as a function of initial packing densities. B) Mean total time required for the first 16 pedestrians to exit the line increased with increasing spacings, revealing that latent heat is not as important for pedestrians as for vehicles. The hashed region shows the start-up lost time required for the fourth pedestrian to exit the line. Error bars show one standard deviation between the three trials. The effect of condition is statistically significant for the total time and start-up lost time, using two one-way ANOVAs (JMP Pro 11 software, $p < 0.01$). Conditions sharing the same superscript letters are not significantly different in terms of Tukey post hoc tests ($p > 0.10$). Both the start-up lost time and the total evacuation time are increasing with larger initial spacings by a statistically significant amount, with possible overlap between adjacent values of δ_s. C) Displacement vs. time of the last last person in the line for each spacing. D,E) Non-dimensionalized interaction potential and kinetic energy of the pedestrian traffic.

for the minimal value of δ_s tested, the pedestrians were instructed to pack as close together as possible, so our observation of increasing flow rates with decreasing δ_s held true even for the maximal possible amount of latent heat.

2.3.2 Theoretical model

The one-dimensional configuration of the pedestrian flow enables the use of the OVM to quantify these findings in a manner similar to the vehicular study. The maximum

velocity of the pedestrian traffic was measured to be approximately $V_{max} \approx 1.37\,\mathrm{m/s}$, in agreement with the literature [73]. The actual length of each person has been assumed as $l_c \approx 0.24\,\mathrm{m}$. The jamming length of $\delta_j \approx 0.12\,\mathrm{m}$ was found from the trials where the volunteers were instructed to pack together as comfortably as possible. To fit the model to the experiments, the sensitivity of the pedestrians was found to be $a \approx 0.45\,\mathrm{s}^{-1}$ and $m = 12$ for all spacings. Dashed lines in Figure A.2 A−D show the theoretical displacement vs. time for different static spacings which have a good agreement with the experimental data. Moreover, the velocity and acceleration of all individuals were extrapolated from the x-t plot (Figures A.2E,F and A.3).

Analogous to the vehicular motion, we have also found the departure vs. saturation flow rates of the pedestrian motion (Figure A.4). Both the departure flow rate and saturation flow rate decrease as δ_s increases, in sharp contrast to the vehicular experiments. This confirms our hypothesis that for systems with low velocities and fast accelerations, it now becomes favorable to change to a solid phase at stoppages. This is because the lag time due to latent heat of the close-packed system is now minor relative to the benefit of the increased initial displacement.

Figure 2.10C graphs the modeled displacement of the last (16^{th}) person in line; the required time for this last person to exit the line increases significantly with increasing δ_s. There is still some latent heat, for example the last person is able to begin moving nearly 10 s earlier for $\delta_s = 3.4\,\mathrm{m}$ compared to $\delta_s = 0.13\,\mathrm{m}$. However, the last pedestrian required only 5 s of walking for $\delta_s = 0.13\,\mathrm{m}$ compared to roughly 40 s of walking for $\delta_s = 3.4\,\mathrm{m}$, more than offsetting the comparatively minor lag of the latent heat. This can be more explicitly quantified by again considering the system's interaction potential, which can be dissipated considerably faster than with the vehicular traffic (Figures 2.5D and 2.10D). When comparing the minimum δ_s of the pedestrians to the vehicles, U_i was dissipated after only 9 s for pedestrians while requiring 16 s, which is 78% longer. Finally, note that for the largest pedestrian

spacing ($\delta_s = 3.4$ m) the interaction potential was completely negligible, compared to a much larger spacing with vehicles ($\delta_s = 15\,\mathrm{m}$) which still exhibited a nonzero potential.

2.4 Conclusions

Using a drone camera and drivers queued at a red light on a Smart Road, we have shown that vehicles jamming into a "solid phase" at stoppages do not increase the efficiency of resumed flow due to the latent heat inherent to the reverse phase-transition back to the "liquid phase." Counterintuitively, the larger bumper-to-bumper spacings that cars maintain when driving at speed can therefore be largely preserved at stoppages to minimize the risk of rear-end collisions with no loss in travel efficiency. Latent heat becomes less important when considering slow moving systems such as pedestrian traffic, as demonstrated by motion-capture experiments where lines of people could empty more efficiently with increasing packing density. As a queue's packing density is increased, we conclude that how the cost of the lag time (latent heat) compares with the savings of increased initial displacement depends upon the optimal velocity and sensitivity of the system.

Our findings with the Smart Road experiments suggest that future policy should discourage close-packing for vehicles during certain stop-and-go scenarios. Because gridlock is often a concern for traffic intersections and city driving, these findings are expected to be more relevant for stop-and-go traffic on highways. A practical challenge is the difficulty of changing the entrenched habit of drivers to induce phase transitions at stoppages. Another open question is whether the dangers of high packing densities at queues will eventually be removed via advances in adaptive cruise control and autonomous vehicles. We hope that our study will inspire the analysis of other aspects of latent heat on traffic, for example on lane merges/splits on a freeway.

2.5 Materials and methods

2.5.1 IRB approval and recruiting procedure

Since this research involved human subjects, the protocols of the study (for both the vehicular and pedestrian traffic) were reviewed and approved by the Institutional Review Board (IRB #15-484 for vehicular experiments and IRB #14-914 for pedestrians). After receiving IRB approval, volunteers were recruited for the pedestrian experiment by on-campus advertising (flyers and class announcements), while volunteers for the vehicular experiment were recruited by both on-campus and off-campus advertising (flyers). Each volunteer read and signed the informed consent form which provided the study procedures, risks, compensations, etc. To avoid any risk of bias in the participants' behavior, volunteers were not told the hypothesis of the studies. For the vehicular experiment, all participants had a background check of their driving record by the Department of Human Resources and were required to pass vision and hearing tests at the consent signing. All vehicles used were rented from the Virginia Tech Fleet Services Department with insurance to cover the study.

3

Passive Anti-Frosting Technology

"He who cannot put his thoughts on ice should not enter into the heat of dispute."

—Friedrich Nietzsche

The content of this chapter was previously published as journal manuscripts in [86, 87], and reproduced here with minor modifications. In this chapter we are trying to introduce a passive anti-frosting surface technology, where the majority of a chilled substrate stays completely dry from dew and frost under highly supersaturated conditions.

3.1 Introduction

There are two primary strategies for dealing with unwanted ice and frost: anti-icing, which aims to prevent ice from forming in the first place [88–90], and deicing, which removes existing ice via the input of chemicals, heat, or mechanical forcing [91–98]. A passive anti-icing method known as icephobicity has recently been introduced, where a superhydrophobic surface can delay ice nucleation long enough to dynamically shed

impacting water before it freezes [99–101]. However, it was discovered that this approach could not translate to anti-frosting, because of an unavoidable inter-droplet ice-bridging phenomenon that spreads frost from frozen condensate to nucleating liquid condensate [4,102,103]. Recent reports have demonstrated the passive dislodging of supercooled liquid droplets from nonwetting substrates as they freeze [104, 105], but this required a low-pressure vacuum or a chilled gas flow. Another approach to anti-frosting is to use hygroscopic chemicals such as salts or glycols that attract nearby moisture to inhibit ice nucleation on the surrounding surface [106–109]. Of course, as the hygroscopic chemicals harvest water, they become diluted and needs continual replacement. For example, over 20 million tons of salt are used annually for deicing highways in the United States alone [110], which has long-term environmental consequences for soil and water [111, 112]. In summary, existing methods of anti-icing are either not translatable to anti-frosting (superhydrophobic surfaces), not conducive to ambient environments (self-dislodging), or require large quantities of hygroscopic chemicals that become diluted.

Regarding the deicing of already-formed ice/frost sheets, one approach is to apply chemicals to melt the ice but this is quite costly. An illustrative example: up to 4,000 L of antifreeze are required for the deicing of a single large aircraft, and the resulting runoff causes aquatic toxicity [113]. A more attractive approach is to tune the surface properties of the substrate to greatly reduce the adhesion strength of ice sheets (down to $\tau_{\text{ice}} \approx 10\,\text{kPa}$), such that even passive forcing from gravity or wind could periodically remove the ice. The reduced stiffness of soft elastomeric coatings has been shown to reduce ice adhesion, particularly when interfacial slippage is enabled by adding uncross-linked polymeric chains [91, 95, 114]. Ice adhesion can also be reduced by impregnating a porous substrate with a lubricating oil [115–117], although over time the oil tends to drain by wicking into the forming ice [118]. Superhydrophobic surfaces can trap air pockets beneath supercooled droplets by

virtue of their micro/nano-roughness; these air pockets are well known to reduce the ice adhesion strength when this water freezes over [3]. Recently, this concept of trapping air pockets underneath "Cassie" ice has been extended to frost [92, 119, 120], as properly designed superhydrophobic nanotextures can even suspend condensation in a Cassie state [13, 121] prior to freezing over into frost. However, such an approach requires a thin hydrophobic coating that is conformally applied to a fine nanostructure, which is simply not durable for practical systems such as airplanes or outdoor infrastructure [122].

Here, we develop a passive anti-frosting surface that can remain 90% dry indefinitely without requiring any input of chemicals, heat, or mechanical forces. The mechanism, ironically enough, uses ice itself. First, water was patterned into an array of micro-stripes across a surface, either by using chemical patterns or physical wicking patterns. Under subfreezing conditions, the water freezes into ice stripes that preferentially attract all nearby moisture from the air due to their hygroscopic nature. Thus, the intermediate surface areas between the sacrificial ice stripes remain dry from both condensation and frost, even under highly supersaturated conditions. Unlike all other hygroscopic materials, ice cannot become diluted as it harvests moisture, so these overlapping dry zones do not collapse over time. The sacrificial ice stripes themselves of course will continue to coarsen over time. However, when we elevated the ice stripes atop micro-fins, the coarsening occurs above the surface resulting in a growth rate an order of magnitude slower than frost growing directly on the solid substrate. The suspended state of the coarsened ice is analogous to Cassie frost on superhydrophobic surfaces, but no longer requires a fragile nanostructure or hydrophobic coating. In short, our surface technology offers complementary benefits: at early time scales, the majority of the projected area remains dry to enable anti-frosting, while at late time scales, the air trapped underneath the coarsened frost will serve to minimize its adhesive strength to facilitate deicing.

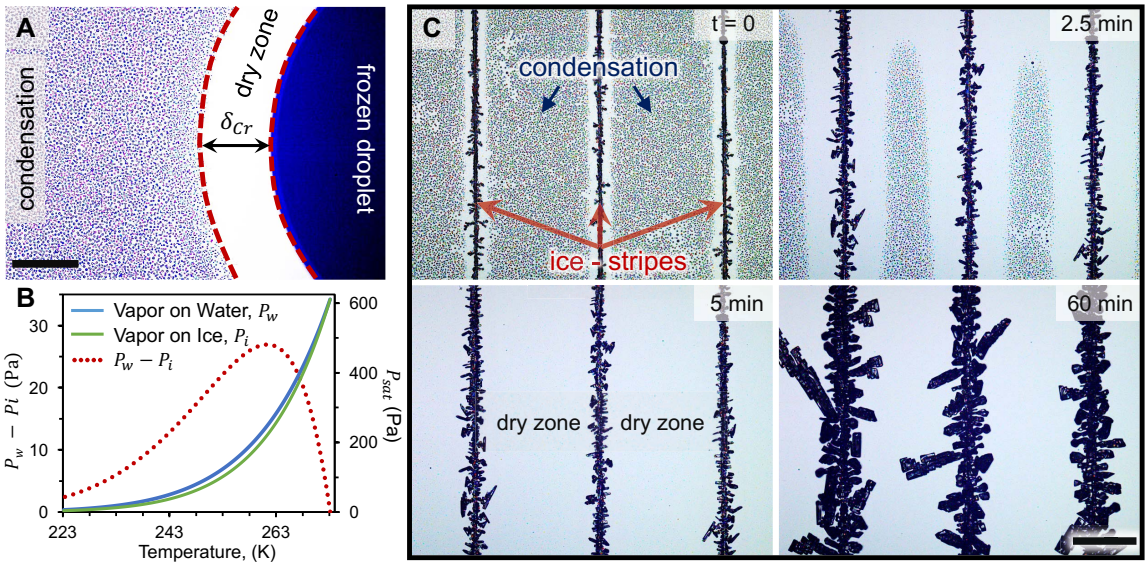

FIGURE 3.1: Generating overlapping dry zones between patterned ice stripes. A) A frozen water droplet creates a steady-state dry zone between itself and the surrounding condensation and frost. Here, a dry zone of length $\delta_{Cr} = 513\,\mu$m was obtained for a surface temperature of $T_w = -10\,^{\circ}$C and supersaturation of $S = 2.6$. B) The mechanism of the dry zone about ice is its depressed saturation vapor pressure (green curve, right y-axis) compared with supercooled water (blue curve, right y-axis) at the same temperature. The vapor pressure difference (dashed red, left y-axis) peaks at $T_w = -12.5\,^{\circ}$C. C) Time-lapse photography of frost growing on chemically patterned silicon at $T_w = -8\,^{\circ}$C and $S = 1.2$, where an array of $10\,\mu$m-wide hydrophilic stripes were used to pattern and selectively freeze condensed water. The overlapping dry zones produced by the ice stripes resulted in the complete evaporation of supercooled water condensing in the intermediate hydrophobic regions. However, in-plane coarsening of the ice stripes did intrude upon the dry zones over time. Scale bars represent $500\,\mu$m.

3.2 Results

3.2.1 Dry zones about ice

When supercooled condensation forms on a chilled substrate that already contains a frozen droplet, an annular dry zone forms between the frozen droplet and the surrounding condensate (Figure 3.1A). This dry zone, free of dew or frost, is caused by the depressed vapor pressure of ice [123] which preferentially attracts nearby water vapor from both the supersaturated ambient and any nearby liquid droplets

(Figure 3.1B). Unlike all other hygroscopic materials, which become diluted from the harvested water leading to dry zone collapse [107, 109, 124], ice cannot become diluted and the dry zone is quite stable over time.

The length of the steady-state dry zone (δ_{Cr}) can be modeled by considering the competition between a liquid droplet's in-plane evaporation flux due to the ice and its out-of-plane condensation flux due to the supersaturated ambient [107]. The liquid droplet's evaporation flux can be expressed as $J_e \sim D(c_\mathrm{w} - c_\mathrm{i})/\delta$ while its condensation scales as $J_c \sim Dc_\infty/\zeta$ [125], where D is the diffusivity of water vapor in air, δ is the edge-to-edge distance between water and ice, ζ is the height of the concentration boundary layer of water vapor, and c_w, c_i, and c_∞ are the vapor concentrations of water, ice and the ambient, respectively (see Figure B.1). Note that the numerical values of the various concentrations are readily obtained from $c = P/\bar{R}T$ where P is the relevant saturation pressure (for water or ice) or partial pressure (ambient), T is either the surface temperature or air temperature, and $\bar{R} = 461.5\,\mathrm{J/kg{\cdot}K}$ is the gas constant of water vapor. For purely diffusive systems, the length of a dry zone corresponds to a critical separation between water and ice where J_e balances J_c [125]:

$$\delta_{Cr} \sim \frac{\zeta(c_\mathrm{w} - c_\mathrm{i})}{c_\infty}, \tag{3.1}$$

where the concentration mismatch between water and ice scales as $(c_w - c_i) \sim 10^{-4}$ kg/m^3 for moderate subfreezing temperatures ($T_\mathrm{w} \approx -10\,^\circ\mathrm{C}$), while $c_\infty \sim 10^{-3}$ kg/m^3 for moderate supersaturations ($S = 1$–2). Supersaturation is a ratio of the ambient partial pressure of water vapor (P_∞) to the saturated vapor pressure corresponding to the wall temperature (P_w), such that $S = P_\infty/P_w$. Plugging into Equation 3.1 results in typical steady-state dry zone lengths of $\delta_{Cr} \approx 1\,\mathrm{mm}$ when the boundary layer scales as $\zeta \sim 1\,\mathrm{cm}$ on small substrates ($A \sim 1\,\mathrm{cm}^2$).

3.2.2 Anti-frosting with chemical patterns

The obvious limitation with a single dry zone is that condensation frosting is still free to occur beyond the millimetric dry zone. Here, we create a passive anti-frosting surface that is scalable by patterning an array of microscopic ice stripes across a substrate. Consider any two adjacent ice stripes separated by a center-to-center pitch (p). A small droplet located in the middle of the intermediate surface is a distance $\delta \sim p/2$ from both ice stripes. The evaporative flux of the droplet is now doubled due to the dual humidity sinks: $J_e \sim 2D(c_\mathrm{w} - c_\mathrm{i})/(p/2)$. When balancing J_e with the same J_c as before, the critical pitch becomes:

$$p_\mathrm{Cr} \sim \frac{4\zeta(c_\mathrm{w} - c_\mathrm{i})}{c_\infty} \sim 4\delta_{Cr}, \tag{3.2}$$

where δ_{Cr} refers to the length of a single dry zone from Equation 3.1. In other words, when the pitch between adjacent ice stripes is smaller than this critical value, the dry zones overlap to keep the entire intermediate surface dry. Technically the design criteria is $(p-w) < 4\delta_{Cr}$, where w is the width of an ice stripe, as the dry zones extend from the edges of the ice stripes. However, this is well approximated by $p < 4\delta_{Cr}$ for $p \gg w$, which is the case here.

For our initial proof-of-concept, we microfabricated chemical patterns onto a silicon chip comprised of hydrophilic SiO_2 stripes against a hydrophobic backdrop (see Materials and Methods section). To ensure that the dry zones would overlap while also maximizing the percentage of the surface that remained dry, the hydrophilic stripes exhibited widths of only $w = 10$ μm while the pitch was $p = 1\,\mathrm{mm}$. The surface was primed by chilling to $T_\mathrm{w} = -10\,^\circ\mathrm{C}$ on a Peltier stage inside of a supersaturated humidity chamber, which resulted in filmwise condensation along the hydrophilic stripes and dropwise condensation within the hydrophobic regions. Once supercooled condensation completely wetted the hydrophilic stripes, the temperature

was brought down to $-30\,^{\circ}\mathrm{C}$ to quickly freeze the water stripes before they could grow too coarse (Figure B.1). Now primed with the ice stripes, the surface was brought to $T_{\mathrm{w}} = -8\,^{\circ}\mathrm{C}$ with an ambient supersaturation of $S = 1.2$.

The ice stripes caused all dropwise condensate growing on the hydrophobic regions to completely evaporate (Figure 3.1C), which is remarkable when considering the supersaturated conditions of $S = 1.2$ (well beneath the dew point of $S \approx 1$). Within 5 min of generating the ice stripes, the condensate growing in the intermediate surface areas had completely evaporated. Furthermore, no fresh condensation was able to grow appreciably in these dry zones, such that over 90% of the overall surface was dry despite the supersaturated conditions. This lack of repopulating condensate in the intermediate regions is important, as it prevents in-plane ice bridging that would occur between the ice stripes and condensate [102, 103].

However, there are two significant limitations to this initial proof-of-concept utilizing the smooth chemical micropatterns. First, it is well-known that chemical patterns are generally not practical for real-life application in outdoor environments. The hydrophobic surface coating can degrade or become contaminated [126], while the hydrophilic regions can become more hydrophobic over time due to hydrocarbon adsorption [127]. Second, while the ice stripes predominantly grow out-of-plane over time toward the supersaturated ambient, they still exhibited some in-plane growth that trespassed into the dry zones over time. In particular, dendritic arms extended into the dry zones at in-plane growth rates of $v \sim 0.1\,\mu$m/s. The growth rate of the dendritic arms is consistent with those previously observed for the 3D growth of ice dendrites [103]; we expect that the large variance in the in-plane component of ice growth is due to localized curvature effects driving the diffusive growth.

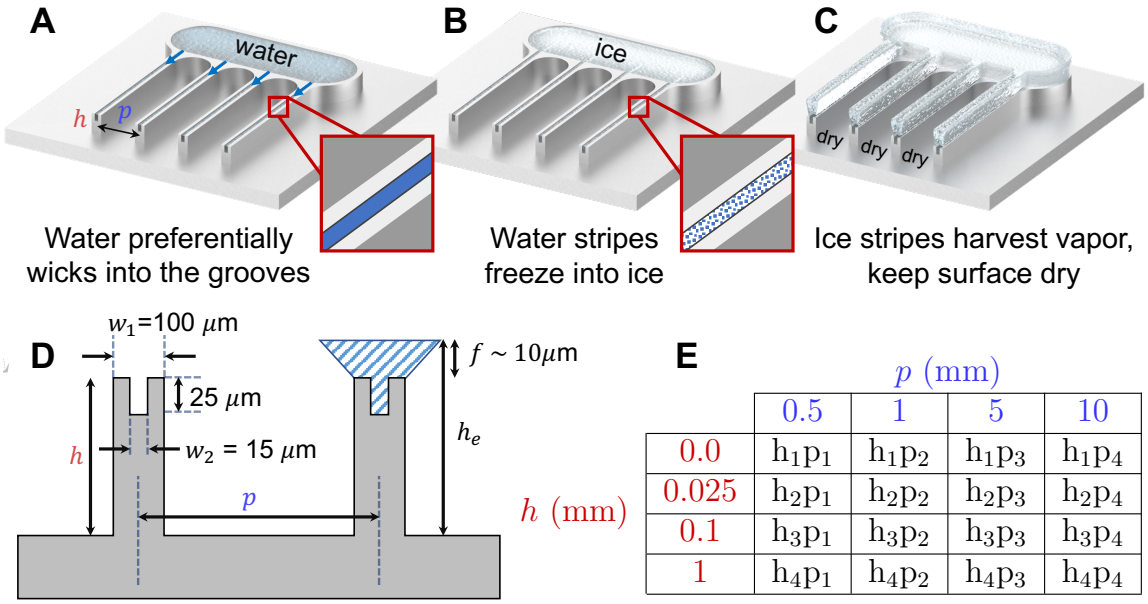

	0.5	1	5	10
0.0	h_1p_1	h_1p_2	h_1p_3	h_1p_4
0.025	h_2p_1	h_2p_2	h_2p_3	h_2p_4
0.1	h_3p_1	h_3p_2	h_3p_3	h_3p_4
1	h_4p_1	h_4p_2	h_4p_3	h_4p_4

FIGURE 3.2: Specifications of the passive anti-frosting aluminum surface. A) By machining micro-grooves along the top of each fin, water preferentially wicks along the tops of the fins. B,C) Upon freezing into ice in chilled conditions, these hygroscopic ice stripes siphon all nearby water vapor, keeping the rest of the finned surface completely dry from condensation and frost. D) The surface characteristics of the micro-grooved surface. Fins of width w_1, height h, and pitch p feature laser-cut micro-grooves of width $w_2 = 15\,\mu$m and a depth of $25\,\mu$m. The effective height of the ice stripes with respect to the floor of the substrate is estimated as $h_e = h + f$, where $f \sim 10\,\mu$m is the estimated frost thickness atop the fins. E) Dimensions of the 16 different micro-grooved aluminum samples.

3.2.3 Anti-frosting with physical patterns

Can both of these limitations be overcome by trying an alternative approach? It is becoming increasingly clear that physically patterning the surface roughness of a substrate can also result in the spatial control of deposited or condensed liquid [124, 128–130]. We therefore designed a second proof-of-concept for our passive anti-frosting surface technology, this time using purely physical patterns on a practical aluminum surface devoid of any fragile chemical coatings (Figure 3.2). Arrays of micro-grooves, $15\,\mu$m in width and $25\,\mu$m in depth, were laser-cut onto the top face of aluminum surfaces (Figures 3.2D). To fill these grooves with "ice stripes," water

was deposited in a connected reservoir that wicked along the stripes (Figure 3.2A) and subsequently froze when the surface was chilled (Figure 3.2B). For some surfaces the micro-grooves were cut along the tops of 100 μm-wide micro-fins, in an attempt to suppress the in-plane growth of the ice stripes by elevating them above the dry zones (Figure 3.2C). Sixteen total surfaces were fabricated to systematically vary two parameters: the height of the top of the micro-fins relative to the "floor" of the intermediate surface ($h = 0$, 0.025, 0.1, or 1 mm) and the pitch between grooves ($p = 0.5$, 1, 5, or 10 mm). These surfaces will be referred to by the magnitude of their height and pitch for brevity (see Figure 3.2E). For example, surface h_4p_2 refers to the largest of the four fin heights ($h = 1$ mm) and the second smallest pitch ($p = 1$ mm).

The textured aluminum surfaces were tested on a Peltier stage within a humidity chamber, analogous to the experiments with the chemically patterned surface. Water pipetted into the reservoir quickly wicked down the micro-grooves, and was frozen by cooling the surface to $T_w = -20\,^{\circ}\mathrm{C}$. After generating the ice stripes, the surface temperature was held at $T_w = -10\,^{\circ}\mathrm{C}$ with a considerable ambient supersaturation of $S = 1.5$. Top-down and side-view microscopes were utilized in tandem with digital cameras to capture the resulting in-plane and out-of-plane frost growth over 3 hr (Figure B.1). To quantify the benefits of the anti-frosting surfaces, control surfaces comprised of smooth untreated aluminum or superhydrophobic aluminum were also tested under identical conditions. Time zero corresponds to when the steady-state surface temperature and supersaturation were first obtained shortly after generating the ice stripes. For the plain or superhydrophobic aluminum surfaces, the majority of the surfaces were covered with ice after 3 hr due to condensation frosting [4] (Figures 3.3 A,B). In contrast, for the micro-finned surface primed with ice stripes, frost growth occurred solely atop the fins while the side walls and floor stayed dry from both supercooled condensation and frost (Figure 3.3C). Frost did grow on the side walls at the terminal end of the micro-fin arrays, but by angling the side-view

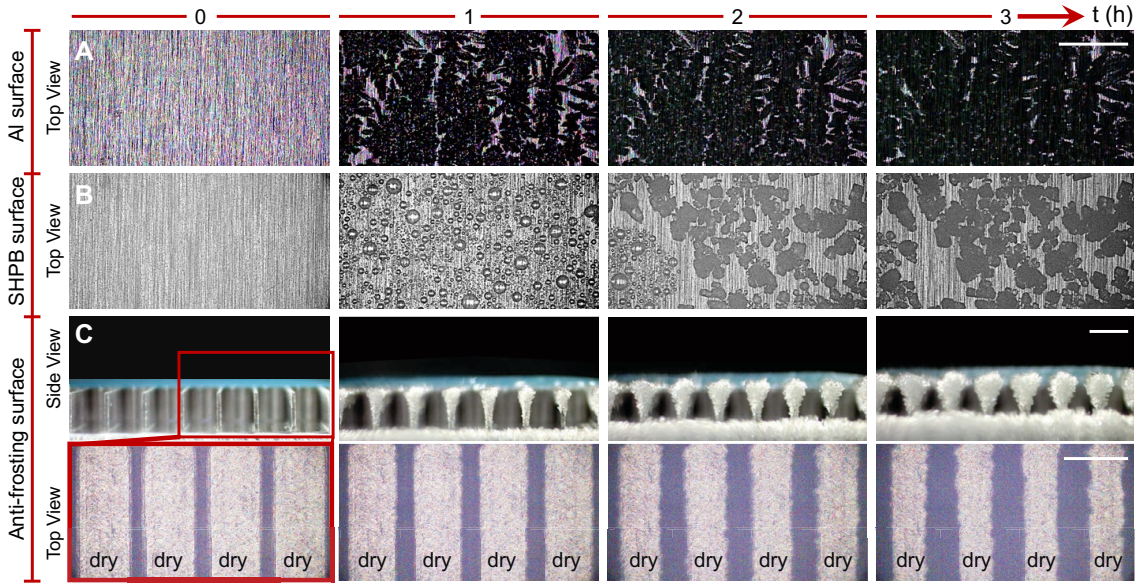

FIGURE 3.3: Experimental results of the passive anti-frosting aluminum surface. A) Smooth, untreated aluminum is completely frosted over in under 1 hr when chilled to $T_w = -10\,^{\circ}\mathrm{C}$ under supersaturated conditions of $S = 1.5$. B) Aluminum treated with a superhydrophobic nanostructure delays frost growth due to promoting jumping-droplet condensation, but still ends up frosting over. C) For one of our anti-frosting aluminum surfaces (h_4p_2), the fin tops are intentionally frozen with sacrificial "ice stripes" leaving the intermediate areas completely dry from condensation and frost even after 3 hr exposed to the same conditions. Note that frost growing along the floor and vertical walls of the surface in the side-view images is only happening at the terminal end of the fin array and does not occur within the fin array itself. Scale bars represent 1 mm.

camera slightly with respect to the axis of the fins, it was confirmed that the side walls within the fin arrays themselves remained dry.

The visual data corresponding Figure 3.3 was converted into measurements of the evolving surface coverage of frost over time. Figure 3.4 graphs the evolving frost-free surface coverage for three of the micro-finned aluminum surfaces compared against the control cases of plain or superhydrophobic aluminum. To directly compare the finned surfaces with the planar surfaces, only the horizontal surface areas were considered when calculating the frost coverage, i.e. the side walls of the fins were not included. Note that this exclusion of the side walls is actually a conservative compar-

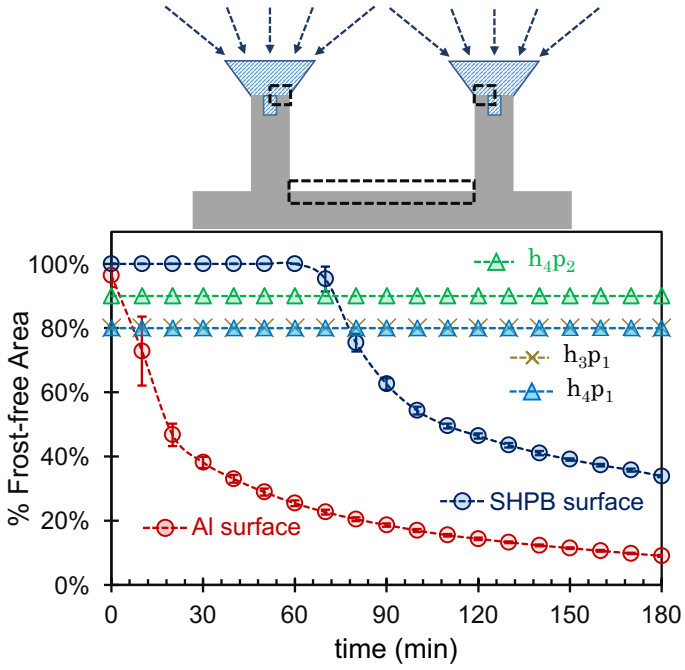

FIGURE 3.4: Surface coverage of frost over time. Measurements of the surface coverage of frost over time. Mean frost-free area over time for regular aluminum (red circles), superhydrophobic aluminum (blue circles) and the finned aluminum surfaces patterned with ice stripes (h_3p_1, h_4p_1, and h_4p_2) for conditions $T_w = -10\,^\circ\mathrm{C}$ and $S = 1.5$. The schematic above the graph illustrates the surface area considered for a unit cell of the finned aluminum surfaces. While condensation frosting occurred across the regular and superhydrophobic surfaces, the patterned aluminum surfaces remained free of condensation and frost for the entire 3 hr experiment in the areas between the sacrificial ice stripes. Results correspond to average of three separate trials and error bars represent a standard deviation.

ison, as the finned surfaces were capable of keeping these side walls dry as discussed above. We quantified the ice coverage in two different ways. In the first, only direct solid-ice contact was considered, such that ice coarsening beyond the fin tops was not counted due to its suspended state above the dry floor. In a second definition of coverage, the projected area of ice was measured to now include the coarsened ice suspended over the surface. Figure 3.4 utilizes the first definition of ice coverage, while the second definition is graphed in Figure B.2.

Shortly after freezing the water in the micro-grooves, a thin layer of ice coats the

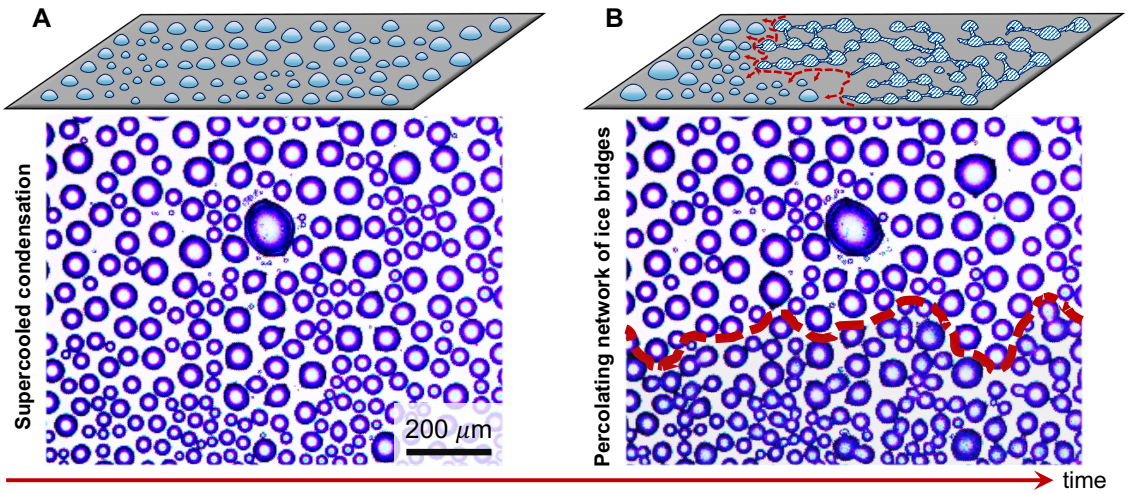

FIGURE 3.5: Frost growth via inter-droplet ice bridging. A) Supercooled condensation formed on a hydrophobic substrate held at $T_w = -10°C$ in a supersaturated environment ($S = 2.7$). B) As time goes by, one of the supercooled droplets will freeze (typically at defect or edge), which instigates a chain reaction of inter-droplet ice bridges that freeze the population of supercooled condensate. Image B is taken 34 s after the water droplet is frozen at the bottom part of the surface. These images illustrate why even non-wetting (i.e. hydrophobic or superhydrophobic) surfaces cannot prevent frost growth.

entire 100 μm widths of the fin tops. This rapid icing of the fin tops is most likely due to freezing water overflowing from the micro-grooves as it expands. This is why the surface coverage of frost (as defined in Figure 3.4) is not changing over time for the anti-frosting surfaces: the sacrificial fin tops are always completely frosted, while the bottom floors are always completely dry. The sharp edges of each fin's top corners seemed to prevent the frost from propagating down the side walls toward the bottom surface, demonstrating the importance of confining the ice stripes from the dry zones. This resulted in 80–90% of the anti-frosting surface area remaining dry, depending upon the pitch of the grooves/fins. In contrast, only about 10% of the plain aluminum sheet was dry after 3 hr. Even for the superhydrophobic surface, less than 40% of the surface remained dry after 3 hr. The enhancement of the superhydrophobic surface relative to the plain aluminum is due to the jumping-droplet mode of condensation [14], which reduces the surface coverage of supercooled con-

densate to diminish the effectiveness of the resulting inter-droplet ice bridging [102]. While more dilute than the untreated aluminum, the frost still extended across the entire superhydrophobic surface, making it clear that non-wetting surfaces cannot enable passive anti-frosting (Figure 3.5). Even prior to the formation of frost, our anti-frosting surfaces were distinguished by a complete lack of supercooled condensation between the sacrificial ice stripes, in contrast to the control surfaces where condensation is unavoidable. How long before the ice coarsening atop the fins begins to overlap with ice from neighboring fins? To more fully probe this question, a 24 hr experiment was conducted using the h_4p_2 surface for a surface temperature of $T_w = -10\,^{\circ}\mathrm{C}$ and supersaturation of $S = 1.1$ (Figure 3.6). Even after the full 24 hr had elapsed, the side walls and floor between the fins remained dry, showcasing the stable hygroscopicity of the sacrificial ice atop the fins. Keeping with the first definition of surface coverage, this resulted in a stable frost-free area of 90% for the entire 24 hr experiment. Even when using the more conservative second definition of surface coverage, about 40% of the projected area remained dry after 24 hr, indicating that it is extremely difficult for adjacent ice stripes to overlap during frost growth.

The diffusive in-plane coarsening of the ice stripes was faster for the smooth chemically patterned surface (Figure 3.7A) compared to the finned aluminum surface (Figure 3.7B) by about an order of magnitude. For the latter case of elevated ice stripes coarsening into the air, the in-plane growth rate scales as:

$$v \sim \frac{D(c_\infty - c_i)}{\rho_i(\zeta - h_e)}, \tag{3.3}$$

where $\zeta - h_e$ is the effective thickness of the concentration boundary layer with respect to the tops of the elevated ice stripes. In other words, $\zeta - h_e$ corresponds to the length scale of the out-of-plane concentration gradient that is responsible for the diffusive coarsening of the ice. Note that $h_e = h + f$ is the effective height of the ice stripes

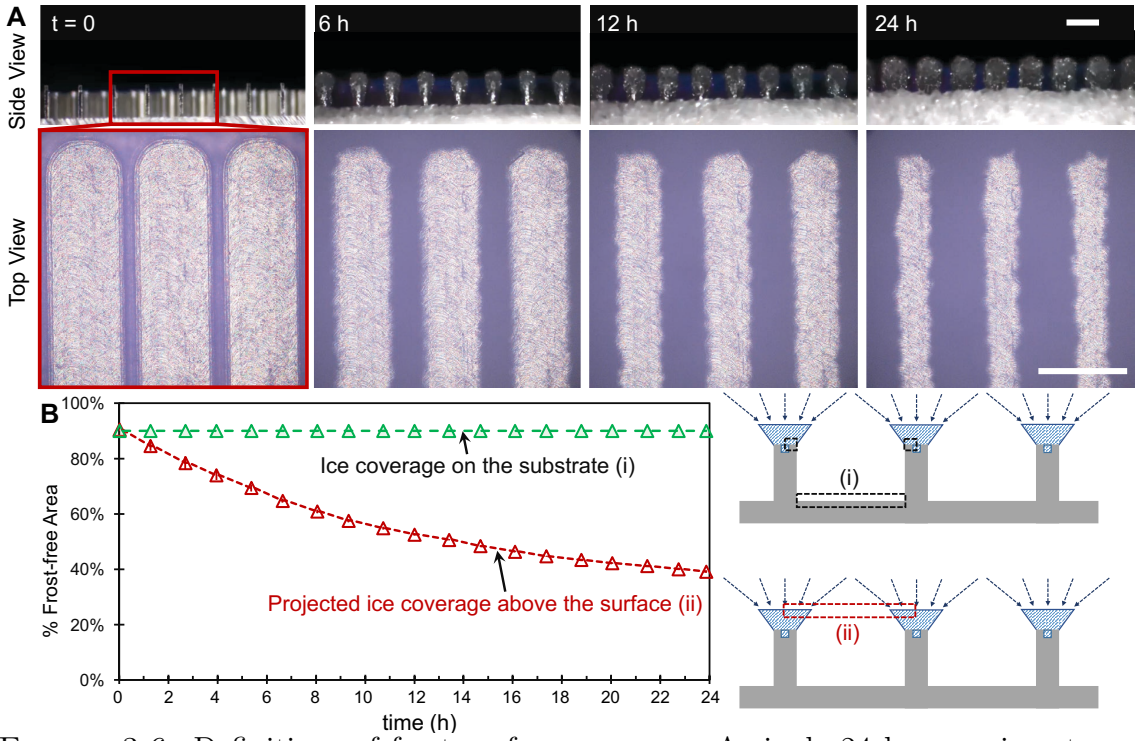

FIGURE 3.6: Definitions of frost surface coverage. A single 24 hr experiment was performed for an anti-frosting aluminum surface (h_4p_2). A) The floor and side walls between the elevated ice stripes remained free from condensation and frost for all 24 hr under conditions $T_w = -10\,^{\circ}\mathrm{C}$ and $S = 1.1$. Although the ice stripes on top of the fins coarsen into the air over time, adjacent ice stripes do not overlap with each other even after 24 hr. The scale bars represent 1 mm. B) The solid surface itself remained 90% dry throughout when using the first definition of ice coverage, see (i) in the schematic. Even when using the second definition of ice coverage to include the projected area of air-suspended ice (see (ii) in schematic), nearly half of the surface remained dry after 24 hr.

with respect to the floor of the surface, where $f \sim 10\,\mu$m is the estimated thickness of the ice atop the fins (cf. Figure 3.2D). For typical values of $D \sim 10^{-5}\,\mathrm{m}^2/\mathrm{s}$, $\rho_i \sim 1000\,\mathrm{kg/m}^3$, $(c_\infty - c_\mathrm{i}) \sim 10^{-3}\,\mathrm{kg/m}^3$, and $(\zeta - h_e) \sim 10\,\mathrm{mm}$, the diffusive growth scales as $v \sim 10\,\mathrm{nm/s}$, which is in good agreement with the experimentally measured values of ice growing radially from the fin tops (Figure 3.7B). This indicates two benefits of elevating the ice stripes: the diffusive coarsening of the ice occurs in a suspended state that is not physically touching the solid substrate, and the coarsening

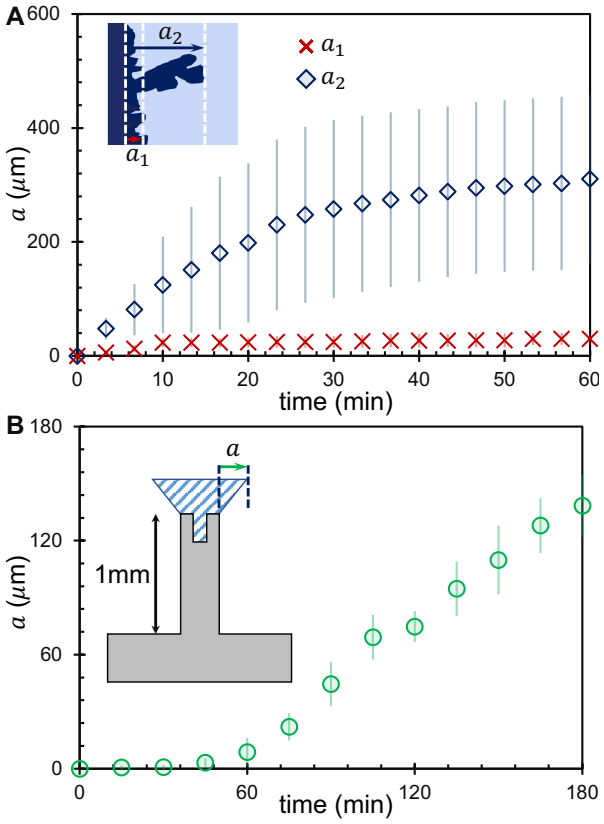

FIGURE 3.7: Experimental measurements of dendritic growth. A) Velocity of the overall in-plane coarsening of ice stripes (a_1, red crosses) as well as the in-plane growth rate of a localized dendritic arm (a_2, blue diamonds) on the chemically patterned surface for conditions of $T_w = -8\,^{\circ}\mathrm{C}$, $T_\infty = 16.6\,^{\circ}\mathrm{C}$, and $RH = 21\%$. Error bars represent the standard deviation between three different locations: top, middle, and bottom of the ice stripes. Time zero corresponds to the time when the ice strips form. B) Mean in-plane velocity of the ice as measured from the corner of the fin (a), for conditions of $T_w = -10\,^{\circ}\mathrm{C}$, $T_\infty = 14.2\,^{\circ}\mathrm{C}$, and $RH = 27.3\%$ on sample $\mathrm{h_4p_2}$. Error bars represent the standard deviation between twelve points (two points on top and two points on bottom of three stripes). From (A) and (B) it is clear that the diffusively-drive growth velocity of the elevated ice stripe is very slow, $v \sim 10\,\mathrm{nm/s}$, compared to the coarsening of ice stripes along a solid substrate, where $v \sim 100\,\mathrm{nm/s}$.

rate itself is slowed dramatically compared to when the dendrites are in physical contact with the surface.

While Figure 3.4 highlights only three of the anti-frosting prototypes for $S = 1.5$, a systematic characterization of the various surfaces is presented in Figure B.2. Regardless of the height of the ice stripes, overlapping dry zones were successful for

both $S = 1.1$ and 1.5 when $p = 0.5\,\text{mm}$ or 1 mm, but condensation frosting occurred in the areas between the ice stripes for large pitches of $p = 5\,\text{mm}$ or 10 mm. This confirms that, for a given supersaturation, having a sufficiently small gap between the ice stripes is the critical parameter for promoting overlapping dry zones. However, even though dry zones were successful for all fin heights, the ice stripes were able to grow across the solid surface when $h = 0\,\text{mm}$ or 0.1 mm, illustrating the importance of sufficiently elevating and/or confining the sacrificial ice from the rest of the surface to avoid the subsequent collapse of dry zones.

3.2.4 Modeling the overlapping dry zones

For a given fin height and pitch, the dry zones between ice stripes will no longer overlap beyond a critical supersaturation. A phase map is constructed in Figure 3.8A by systematically varying the supersaturation for all 16 micro-grooved aluminum surfaces. Experimentally, after the ice stripes were formed the surface was kept at $T_w = -10\,^\circ\text{C}$ under dry conditions, and the humidity was incrementally raised to tune the supersaturation. For each combination of h, p, and S, it was observed whether the intermediate areas between the ice stripes stayed dry or exhibited condensation frosting. For a given surface, the critical supersaturation was defined as the minimal value of S where the dry zone was disrupted by condensation/frost for the first time (Figure B.3).

For a non-isothermal system such as ours, the diffusion model must be in terms of vapor concentrations, as opposed to vapor pressures, to capture the change in temperature between the surface and the air. Therefore, our model will introduce a non-dimensional representation of the supersaturation that compares the ambient concentration to the mismatch in concentration between water and ice:

$$S^* = \frac{c_\infty}{(c_\text{w} - c_\text{i})}. \tag{3.4}$$

The critical supersaturation bisecting the two regimes of the phase map can be modeled by adapting Equation 3.2 to the textured surface:

$$S^*_{\mathrm{Cr}} \sim \frac{4(\zeta - h_e)}{p}. \tag{3.5}$$

Given the three-dimensionality of the surface, it may be tempting to modify the flux balance governing Equation 3.5 by positing $J_e \sim 2D(c_{\mathrm{w}} - c_{\mathrm{i}})/\sqrt{(p/2)^2 + h_e^2}$ as the new evaporative flux between a droplet on the floor and both ice stripe elevated on fins. However, given the excellent fit of Equation 3.5 in Figure 3.8A, we suggest that the flux balance can now be considered as occurring in midair at the level of the ice stripes, where for $p < p_{\mathrm{Cr}}$ the downward flow of vapor toward the floor is redirected toward the ice stripes. The experimental values of S^*_{Cr} are in excellent agreement with Equation 3.5 when using $\zeta - h_e \approx 6.5\,\mathrm{mm}$. Initially it seems odd that a single value of $\zeta - h_e$ could be used in Equation 3.5, given that the fin heights were ranged from $h = 0$–$1\,\mathrm{mm}$. However, this can be rationalized by observing that $h_e \ll \zeta$ across this entire parameter space, such that the small influence of h_e may be neglected for a scaling model. Of course, it would also be of interest to obtain more exact solutions to S^*_{Cr} that would capture its secondary dependence on h_e, which will now be performed in the following section.

3.2.5 Computational results

Explicit numerical solutions of the dry zones were generated using COMSOL Multiphysics software as visualized in Figure 3.8B. The steady-state concentration field was governed by the Laplace equation, $\nabla^2 c = 0$, where c is the water vapor concentration. Dirichlet conditions were given by $c = c_\infty$ at $z = \zeta$, where $z = 0$ corresponds to the floor of the surface and ζ is the height of the computational domain representing the boundary layer, and $c = c_{\mathrm{i}}$ at the interface of the ice stripes, where the value of c_{i} corresponded to $T_w = -10\,^\circ\mathrm{C}$ used for the experiments. The cross-section

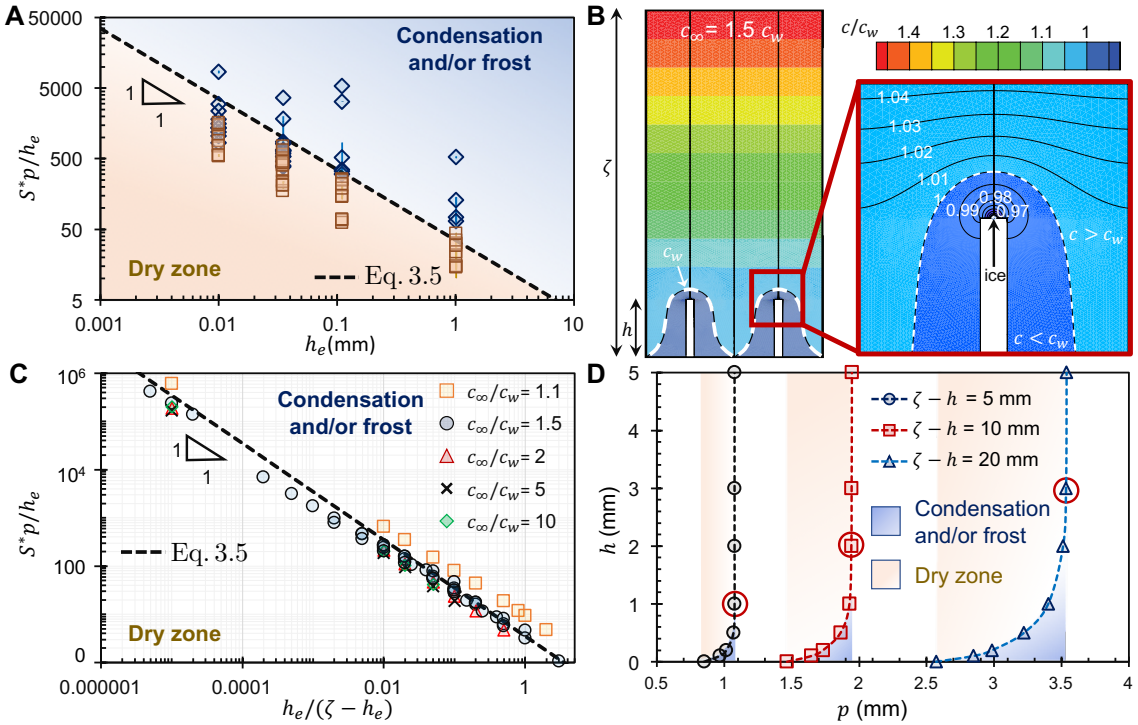

FIGURE 3.8: Experimental, theoretical and computational phase map. A) Experimental phase map shows the success (square data points) versus failure (diamonds) of overlapping dry zones for all 16 micro-grooved surfaces, as a function of the non-dimensional supersaturation $S^* = c_\infty/(c_\mathrm{w} - c_\mathrm{i})$ and the pitch p between ice stripes. The dotted line represents the prediction of S^*_Cr from Equation 3.5, which successfully demarcates the experimental regimes. The x-axis serves to differentiate between the four different fin heights (h) used experimentally, but note that Equation 3.5 does not actually depend on h_e as evidenced by the $1/h_e$ simultaneously located in the y-axis. B) Concentration field in the $x-z$ plane around two adjacent ice stripes elevated atop fins for conditions of $c_\infty/c_\mathrm{w} = 1.5$, $T_w = -10\,^\circ\mathrm{C}$, $w_1 = 100\,\mu\mathrm{m}$, $h = 1\,\mathrm{mm}$, and a cross-sectional ice radius of $r = 10\,\mu\mathrm{m}$. The magnified inset depicts the iso-concentration lines, where everything within the $c = c_\mathrm{w}$ contour represents the subsaturated dry zone where no condensation or frost can form (dark blue). C) Phase map where the computational values (data points) and theoretical values (dashed line, Equation 3.5) of the phase line are plotted as a function of S^*, p, and $\zeta - h_e$ and collapse onto a universal curve. D) Phase map capturing the secondary dependence of fin height on the dry zones. The critical pitch required for overlapping dry zones increases with h until plateauing at at $h_\mathrm{Cr} \sim p_\mathrm{Cr} \sim 1\,\mathrm{mm}$ for $\zeta - h = 5\,\mathrm{mm}$ (black circles), $h_\mathrm{Cr} \sim p_\mathrm{Cr} \sim 2\,\mathrm{mm}$ for $\zeta - h = 10\,\mathrm{mm}$ (red squares), and $h_\mathrm{Cr} \sim p_\mathrm{Cr} \sim 3.5\,\mathrm{mm}$ for $\zeta - h = 20\,\mathrm{mm}$ (blue triangles).

of the ice stripe on top of a fin is approximated as a semi-circle of radius $r = 10\,\mu$m. Dry zones were defined as the regions bound by the iso-concentration line $c = c_{\mathrm{w}}$ and were accurate to within $\pm$ 1 μm. All of the numerical results employ the following methodology. First, the fin height h, boundary layer ζ, and/or supersaturation S^* were set to their desired values to generate the concentration field. Second, the pitch p between two adjacent fins was tuned until the $c = c_{\mathrm{w}}$ iso-concentration lines about each fin overlapped for the first time to keep the intermediate surface completely dry. In this way, phase maps can be generated that capture the critical values of each parameter required to obtain overlapping dry zones.

Figure 3.8C is analogous to the phase map from Figure 3.8A, except now the data points are from numerical simulations rather than experiments. Another difference is that the experimental data points from Figure 3.8A extended far beyond either side of the critical phase line, whereas the numerical data points in Figure 3.8C represent the phase line itself. When non-dimensionalizing, it can be seen that all of the numerical data collapses onto a universal curve corresponding to the scaling model of the phase line (Equation 3.5). An advantage of this numerical approach is that $\zeta - h_e$ is explicitly known, revealing a pre-factor that was hidden in Equation 3.5: $S^*_{\mathrm{Cr}} \approx 4\beta(\zeta - h_e)/p$ where $\beta = 0.65$. This means that the value of $\zeta - h_e \approx 6.5\,$mm used to fit the scaling model to the experimental data in Figure 3.8A actually has a value of $\zeta - h_e \approx 1.0\,$cm when considering the numerical pre-factor.

Now that the numerical methods have validated the phase map, it is of interest to use this model to explicitly characterize the secondary dependence of the dry zones on the fin height. In Figure 3.8D the height of the fins was varied for a fixed S^* to reveal that the critical pitch is larger for taller fins. However, the benefit of increased fin height was found to saturate around $h_{\mathrm{Cr}} \sim p_{\mathrm{Cr}}$, at which point it is no longer beneficial to increase the fin height further. This is because the $c = c_{\mathrm{w}}$ iso-concentration line bounding the dry zones asymptotically approaches an infinite

slope for tall fins, such that more height does not result in more extension over the floor. As expected, the chosen value of $\zeta - h$ was more important than h, with the value of $h_{\mathrm{Cr}} \sim p_{\mathrm{Cr}}$ ranging widely from 1–3.5 mm as $\zeta - h$ ranged from 5–20 mm. In other words, the dry zones become much larger with increasing ζ (Figure B.4), which has real-life implications as the height of the boundary layer can be changed by tuning parameters such as the surface area [124].

The effects of the size and shape of the ice stripes themselves are modeled numerically in Figure 3.9. When the cross-sections of the ice stripes exhibit a semi-circular shape, the dry zones are about 20% larger compared to flat ice stripes (Figure 3.9A). When the boundary layer thickness is increased to $\zeta - h = 10$ mm, the dry zone increased by 70% (green circles) indicating that the geometry of the ice is secondary to the geometry of the vapor profile. In general, the dry zones increased with larger sizes of ice. For instance, the critical pitch almost doubled when ice grew from an initial radius of $r = 10\,\mu$m to instead cover the whole width of the fin ($2r = 100\,\mu$m). Finally, Figure 3.9B reveals that for a fixed width for the micro-groove containing the ice stripe ($w_2 = 20\,\mu$m), the dry zone length increases by 40% as the fin width (w_1) decreases to approach the width of its interior micro-groove. This indicates that the experimental trend of the freezing water stripe to expand over the top of the entire fin is a positive occurrence, as the dry zones are maximal when the fin top is entirely iced over.

3.3 Discussion and conclusion

While the experiments here were all performed for a fixed surface temperature of $T_w = -10\,^{\circ}$C, a recent report showed that Equation 3.1 accurately predicts the magnitude of dry zones for any possible surface temperature and ambient humidity [125]. Therefore, the design conditions where dry zones overlap can be rationally determined for any possible condition. When dry zones do overlap, the fraction of

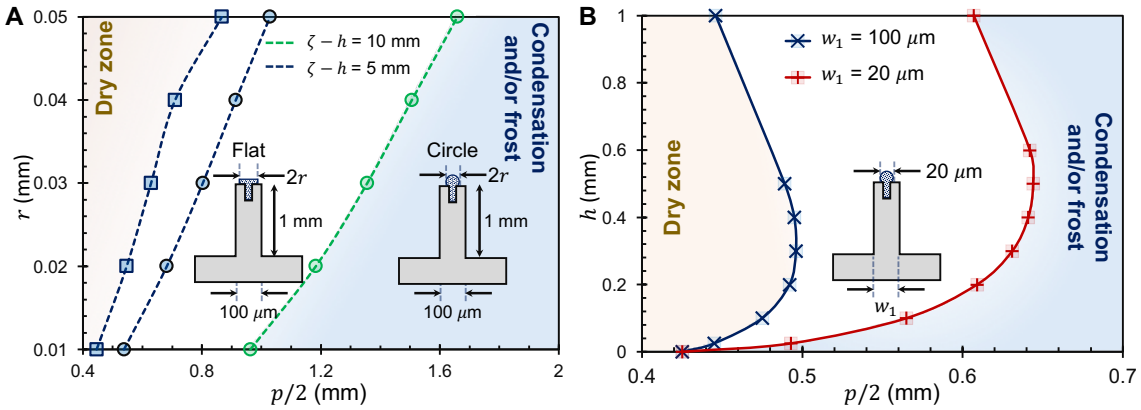

FIGURE 3.9: Computational results. Simulations of how dry zones are affected by the system geometry. A) Phase lines as a function of the size (r) and shape of the elevated ice stripes for $c_\infty/c_w = 1.5$, $\zeta - h = 5\,\text{mm}$, $h = 1\,\text{mm}$, and $w_1 = 100\,\mu\text{m}$. Circles represent ice stripes exhibiting a semi-circular shape, while squares represent a flat film of ice. B) The critical pitch as a function of the fin height h and width w_1. All other parameters are held constant, including a micro-groove width $w_2 = 20\,\mu\text{m}$, domain size $\zeta = 5\,\text{mm}$, ambient $c_\infty/c_w = 1.5$, and an ice stripe extending above the micro-groove with a hemi-spherical radius of $r = 10\,\mu\text{m}$.

the solid surface that remains dry (neglecting the vertical walls) remains fixed at $(p - w)/p$. This indicates that the dry zones could be significantly increased from our current maximum of 90% of the overall surface by further increasing the ratio of p/w using refined micro-fabrication methods. Any surface facilitating the controlled patterning of water/ice can in principal promote the overlapping dry zones, which broadens this technology to a wide variety of material choices.

The use of deposited water to create the ice stripes was useful for repeatable laboratory experiments but is obviously not always practical for real-life applications. An alternate approach would be to exploit the reduced nucleation energy barrier of properly designed features, such that the water/ice patterns can spontaneously condense from the humid air [130, 131]. The patterned aluminum surfaces used here were uniformly hydrophilic to facilitate micro-groove wicking and avoid the need for fragile hydrophobic coatings. However, as inspired by a recent report [132], it would be interesting to see if tailoring the surface wettability could favorably tune the

in-plane versus out-of-plane coarsening of the sacrificial ice stripes. Finally, future studies should probe how the aerodynamics of airfoils used on turbines or airplanes would be modified by the icy micro-patterns, or how the dry zones would be modified by convective flow and/or isothermal conditions. Actually, we expect that our anti-frosting surfaces would perform even better in natural winter environments, as the cold air would dramatically decrease c_∞ which would increase δ_{Cr} (Equation 3.1) and slow the diffusive coarsening of the ice stripes (Equation 3.3).

In conclusion, we have demonstrated both experimentally and computationally that passive anti-frosting surfaces can be achieved by micro-patterning periodic arrays of hygroscopic ice stripes to create an array of overlapping dry zones. By using physical patterns such as wicking micro-grooves to create the ice stripes, we demonstrated that practical materials such as aluminum can be converted into passive anti-frosting surfaces without requiring any fragile surface chemistry. Provided that the sacrificial ice stripes are sufficiently confined from the dry zones, for example by pinning the ice on top of elevated micro-fins, the rest of the surface remains dry indefinitely from both condensation and frost without requiring any chemicals, heat, or mechanical forces. Here, we obtained surfaces that remained up to 90% dry under chilled and supersaturated conditions, but expect that further enhancement is possible by reducing the width of the ice stripes relative to their pitch. This passive anti-frosting system seems ideal for HVAC systems in particular, which often contain elevated arrays of millimetric tubes/fins that could facilitate the sacrificial ice stripes to prevent any moisture from entering into the system.

Over time, the sacrificial ice stripes do coarsen as they diffusively attract all nearby moisture. However, two important points must be made here. First, the in-plane coarsening of the sacrificial ice stripes was one order of magnitude slower than the in-plane frost growth that occurs on conventional surfaces. This slow growth was evidenced by our observation that adjacent ice stripes did not overlap with each

other even after 24 hr of coarsening under chilled, supersaturated conditions. Second, the coarsening ice grows beyond the edge of the micro-fins in an air-suspended state. This means that even after very long time scales where the ice stripes completely overlap, the resulting frost sheet would be analogous to the "Cassie" state of ice on superhydrophobic surfaces which exhibits remarkably low ice adhesion strength [119]. The ability to use large micro-scale features and ice patterns to attain Cassie frost is a significant advance, as the superhydrophobic nanostructures previously required to obtain Cassie frost are not durable in outdoor applications. To adapt the common expression to "fight fire with fire," perhaps it is time to "fight ice with ice."

3.4 Creating ice stripes using ice nucleating proteins

When the partial pressure of ambient water vapor exceeds a critical supersaturation, heterogeneous nucleation will occur on any adjacent surface. [133] The supersaturation degree represents the ratio of the critical vapor pressure required for embryo formation, P_{n}, to the saturation pressure corresponding to the surface temperature, P_{s},

$$SSD = (P_{\mathrm{n}} - P_{\mathrm{s}})/P_{\mathrm{s}}. \tag{3.6}$$

The magnitude of SSD increases strongly with decreasing wettability and increases weakly for colder surface temperatures [134–137]. On a subfreezing surface, two different modes of heterogeneous nucleation are possible: condensation, where vapor nucleates into a supercooled liquid embryo, and desublimation, where the vapor nucleates directly into an ice embryo [138] .

The thermodynamically favorable mode of nucleation corresponds to whichever has a lower value of P_{n}, which is usually condensation but can be desublimation for sufficiently hydrophilic and/or cold surfaces [137]. It is also important to consider transient effects: for example, a hydrophilic surface that theoretically favors

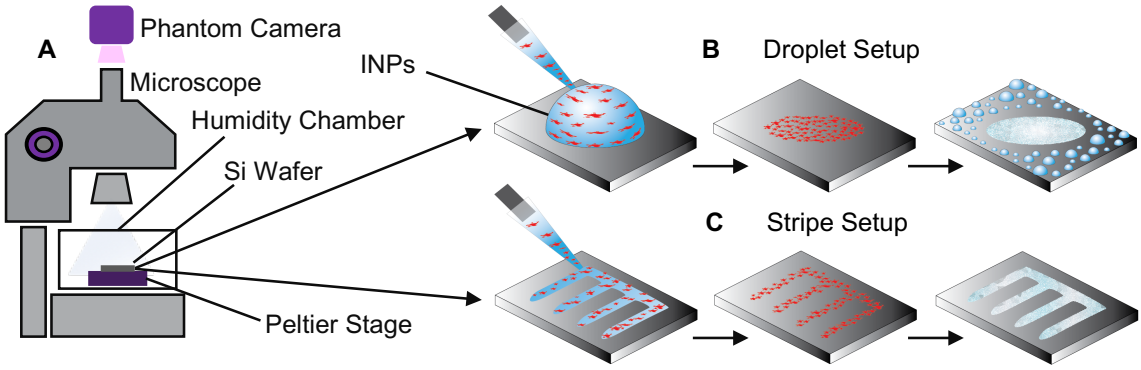

FIGURE 3.10: Setup used to visualize the modes of nucleation. A) Schematic of the experimental setup used to visualize the modes of nucleation occurring on a substrate. B) In the first set of experiments, INPs (red) were deposited onto the surface by evaporating a droplet on a hydrophobic substrate. C) For a second set of experiments, stripes of INPs were obtained by depositing water onto a hydrophobic surface containing hydrophilic stripes.

desublimation beneath a critical temperature will already exhibit condensation as it is being cooled down beneath the dew point. Therefore, supercooled condensation is virtually always the observed mode of nucleation on chilled substrates [10, 102, 103, 118, 139–141], with the impractical exception of inorganic crystals such as silver iodide [142, 143], kaolinite [144], or feldspar [145]. Many studies have utilized chemical or physical patterns to spatially control the nucleation and growth of condensate [124, 128, 131, 143, 146–152], but to date, desublimation remains elusive.

As we discussed in this chapter, ice itself exhibits a depressed vapor pressure compared to supercooled water [123], so there is interest in patterning sacrificial ice features on a surface to keep it otherwise dry from condensation and frost. However, it is tedious to have to form these ice patterns by actively depositing or condensing water and waiting for freezing to occur. If desublimation could be enabled to spontaneously create patterns of ice on an otherwise dry substrate, it could open up new possibilities for making practical anti-frosting surfaces.

Ice nucleating proteins (INPs) are renowned for their ability to rapidly freeze water with minimal supercooling [153]. This ability stems in part from hydrophilic

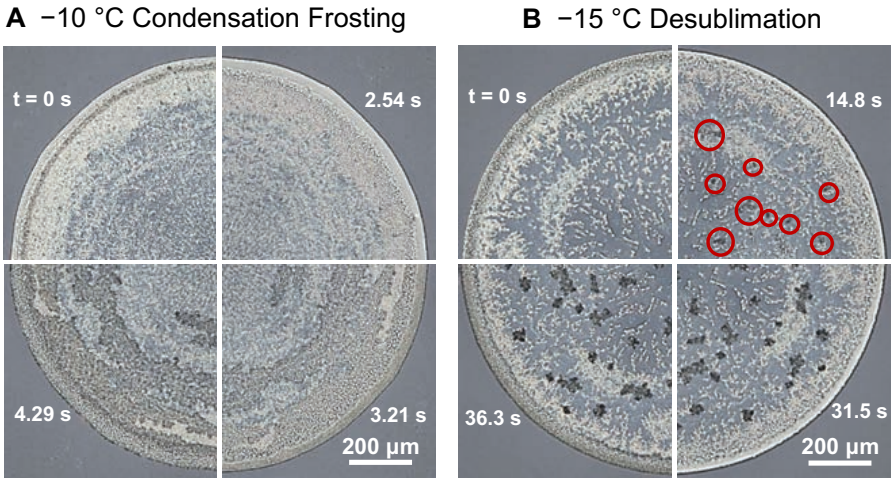

FIGURE 3.11: Characterizing condensation and desublimation. A) At $T_w = -10\,°C$ condensation forms even on the INP-laden portion of the surface, as indicated by a rainbow film that forms at 2.54 s. This supercooled film later freezes at 3.21 s (i.e. condensation frosting). B) At $T_w = -15\,°C$, discrete ice crystals (circled in red) form on the INPs, indicating desublimation. Time zero corresponds to the moment before any phase change occurs, where the particles are agglomerates of INPs left by the evaporated droplet.

and hydrophobic patterns on the INPs which lower the energy barrier for ice nucleation [154]. Further, the surface of the protein may provide a template that orients water into a lattice structure favorable for nucleating ice crystals [155, 156]. While INPs have been used extensively to freeze existing water, there are no reports of using INPs to control the mode of heterogeneous nucleation.

Here in this section, we deposit INPs on a substrate to switch the mode of heterogeneous nucleation from condensation to desublimation. Beneath a critical surface temperature, desublimation occurred exclusively on the portions of the surface laden with INPs, while supercooled condensate nucleated everywhere else. Further, by patterning the surface wettability to create stripes of INPs, we can spatially control the mode of nucleation and spontaneously create ice stripes. These stripes, acting as humidity sinks due to their lower vapor pressure, create overlapping dry zones free of condensation and frost.

Smooth hydrophobic samples were obtained by the vapor-phase deposition trichloro (1H,1H,2H,2H-perfluorooctyl)silane (Sigma-Aldrich) onto silicon wafers. The commericial product Snomax (Snomax International), produced from the bacterium *Pseudomonas syringae*, was used as the source of the INP. To control both the surface temperature and the ambient partial pressure of water vapor, the wafer was thermally bonded to a Peltier stage inside a custom-made humidity chamber (ramé-hart) as shown in Figure 3.10A.

Figure 3.10B shows one method of depositing the INPs, where a $1\,\mu$L droplet of distilled water containing 10 mg/mL of Snomax was placed onto a hydrophobic sample. The water droplet was evaporated by heating the surface to 40 °C, leaving a circular footprint of INPs on the substrate. The relative humidity of the chamber was set to correspond to a supersaturation of $S = = 1.1$. Once the appropriate humidity was obtained, the Peltier stage was then rapidly plunged down to either $T_{\mathrm{w}} = -5\,^{\circ}\mathrm{C}$, $-10\,^{\circ}\mathrm{C}$, $-15\,^{\circ}\mathrm{C}$, $-20\,^{\circ}\mathrm{C}$, or $-25\,^{\circ}\mathrm{C}$ to observe the initial mode of nucleation occurring on the surface. The supersaturation value of $S = 1.1$ was chosen to ensure that the substrate remained dry from nucleation until it reached the steady-state set-point temperature, as the silanized wafer exhibited a supersaturation degree of $SSD \approx 0.1$. The onset of nucleation was observed using a top-down optical microscope (Nikon Eclipse LV150) set at 10X magnification placed above a quartz viewing window embedded in the roof of the humidity chamber.

At $T_{\mathrm{w}} = -10\,^{\circ}\mathrm{C}$, a film of condensation formed on the portion of the substrate containing the INPs (Figure 3.11A). The liquid phase of this initial nucleation was evident from rainbow-colored fringe patterns observed within the condensing film. After several seconds, this supercooled liquid froze over into ice, which is known as condensation frosting [4]. However, when the surface was brought down to $T_{\mathrm{w}} = -15\,^{\circ}\mathrm{C}$, discrete ice crystals formed on the particle-laden surface rather than supercooled condensation as evidenced by their irregular shape and sharp contrast (Figure 3.11B).

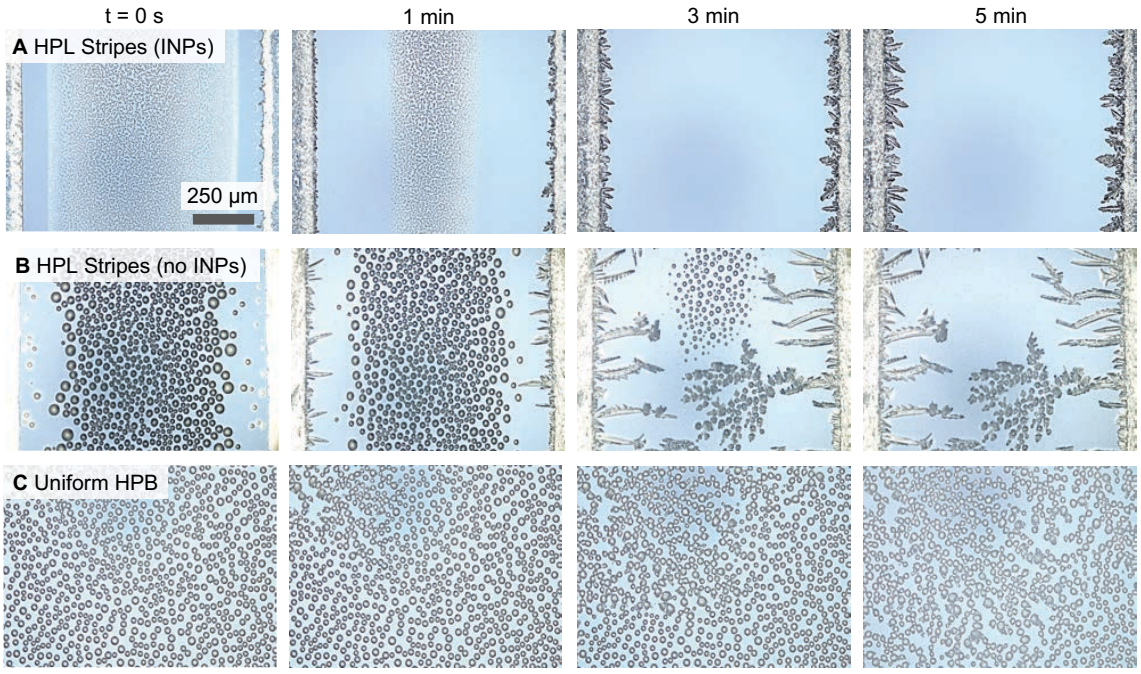

FIGURE 3.12: Using INPs to quickly freeze striped films. Experiments utilizing hydrophilic stripes (far left and right of each image) patterned across a hydrophobic backdrop (center of each image). A) When INPs were deposited along the hydrophilic stripes and the surface was cooled to $T_w = -10\,°C$, filmwise condensation initially formed along the stripes while dropwise condensation grew on the hydrophobic region. The INPs quickly froze the striped films into ice (time zero), which proceeded to evaporate the dropwise condensate by virtue of the low vapor pressure of the ice stripes. B) When the hydrophilic stripes did not contain INPs, the filmwise condensation took much longer to freeze. As a result, the dropwise condensation within the hydrophobic region cannot evaporate prior to frosting over due to inter-droplet ice bridges. C) For a uniformly hydrophobic surface without INPs, condensation frosting via inter-droplet ice bridging occurred everywhere.

This indicates that desublimation is occurring rather than condensation frosting.

This desublimation mode of nucleation was observed for all temperatures $T_w = -15\,°C$ and lower. In other words, by the time an embryo grew to $\sim 1\,\mu m$ for identification under the microscope, it was already in the ice phase. However, the initial nucleation event cannot be directly observed, as the $\sim$1–10 nm critical size of an embryo is smaller than the optical resolution of the microscope [133]. Even if a nanoscale embryo did initially exhibit the supercooled liquid phase, the INPs promote freezing

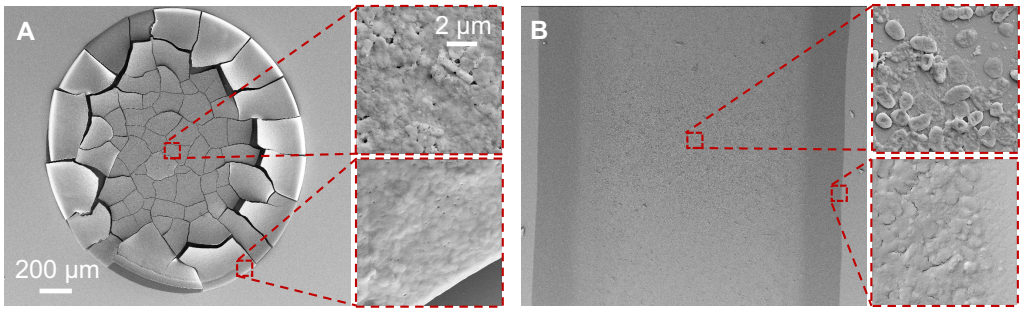

FIGURE 3.13: Scanning electron images for INPs. Scanning electron images for INPs deposited onto (A) a uniformly hydrophobic surface and (B) along a hydrophilic stripe. Top insets show INPs within the center region, while bottom insets depict the denser distribution of INPs along the edge.

at time scales and length scales so small as to be practically indistinguishable from desublimation. Throughout the manuscript, when we refer to nucleation being in the desublimation mode, we are therefore referring to desublimation in this practical (i.e. micro-scale) sense of the word.

In a second set of experiments, hydrophilic stripes were patterned along hydrophobic silicon samples as illustrated in Figure 3.10C. Stripe-shaped holes 1 mm in width were cut into an aluminum mask. This mask was placed atop a hydrophobic sample in an oxygen plasma cleaner to selectively restore the hydrophilicity of the silicon. When depositing the aqueous Snomax solution onto the surface, it preferentially spread along the hydrophilic stripes while leaving the hydrophobic background dry. The water was then evaporated and the surface cooled to a subfreezing temperature in the same manner as previously described.

Snomax deposited into the hydrophilic stripe arrays exhibited the same general behavior as that deposited onto the uniformly hydrophobic surface. In other words, condensation frosting occurred on the stripes for $T_w \geq -10\,^\circ\mathrm{C}$ while desublimation occurred for $T_w \leq -15\,^\circ\mathrm{C}$. Interestingly, the desublimated stripes of ice were able to keep the hydrophobic regions of the wafer completely dry of condensation and frost even under supersaturated conditions ($S = 1.1$). This is due to the depressed vapor

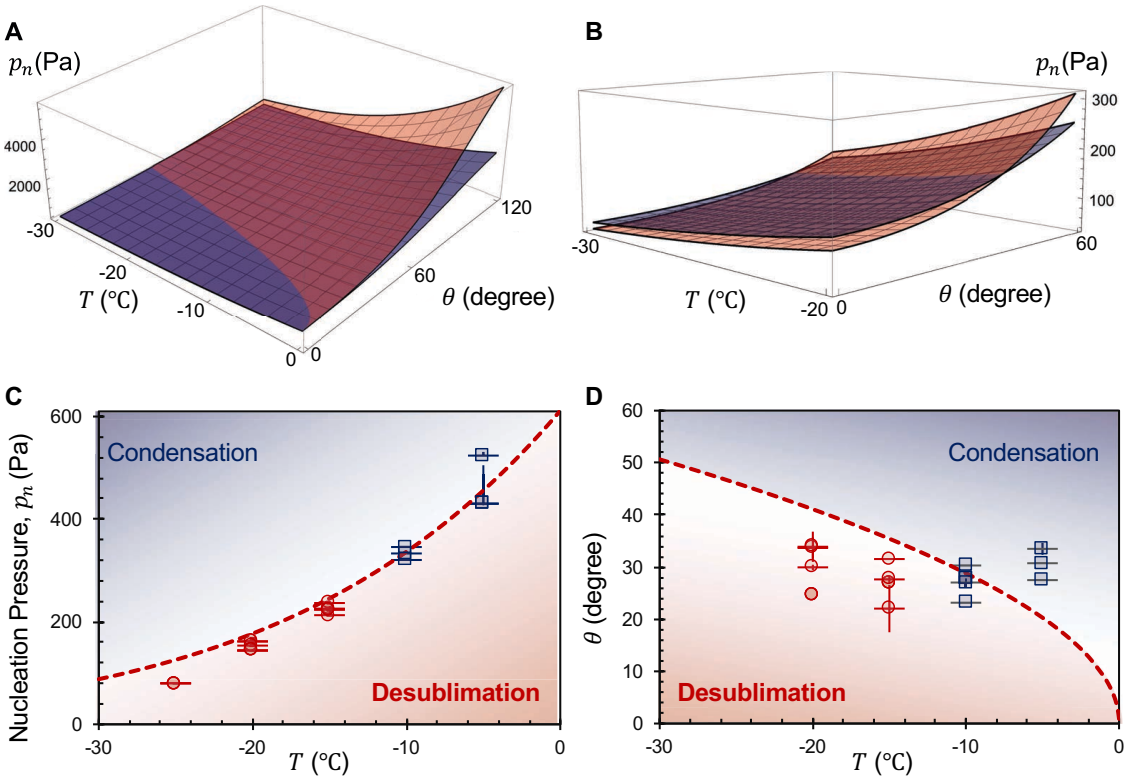

FIGURE 3.14: Critical vapor pressure required to nucleate an embryo on a surface. A) The critical vapor pressure required to nucleate an embryo on a surface (p_{n}, Equation 3.7) for condensation (blue curve) and desublimation (red curve) as a function of contact angle and surface temperature. For a given θ and T_{w}, the favorable mode of nucleation is the one corresponding to a lower value of p_{n}. B) A zoomed-in version of (A) that focuses on the intersection of the two curves. C) The intersecting values of p_n where condensation and desublimation are equally favorable, plotted against surface temperature (red dashed line). Values of p_n falling above this curve would favor condensation, while desublimation is favored beneath the curve. This phase map was validated by experimental measurements of the critical vapor pressure required to nucleate condensate (blue squares) or ice (red circles). The error bars in the x and y directions represent a standard deviation of variance in the surface temperature and air temperature, respectively, due to minor fluctuations in the chamber. D) The critical surface wettability where condensation and desublimation are equally favorable, as a function of surface temperature (red dashed line). Using Equation 3.7 to obtain an effective value of θ for each data point from (C), it can again be seen that the experimental data validates the theoretical phase map.

pressure of ice compared to liquid water at the same temperature [123], such that the ice stripes siphon all nearby moisture from the air [86]. Even for the case of con-

densation frosting at $T_w = -10\,°C$, the films of supercooled water on the hydrophilic stripes froze quickly ($\sim 10\,s$) into ice stripes. This allowed for the droplets in the hydrophobic region to be evaporated before they could freeze, drying the surface after about 1 min (Figure 3.12A). The design parameters for ensuring overlapping dry zones between ice stripes have already been characterized before [86]; here, we instead focused on the spontaneous nucleation of the ice stripes themselves.

As a control, for hydrophilic stripes not containing INPs, the time required for the filmwise condensate to freeze was longer by at least two orders of magnitude ($\sim 10\,min$). By the time of freezing onset, the droplets growing in the hydrophobic regions were too large to evaporate, resulting instead in inter-droplet ice bridging [102, 103, 157] that spread frost across the surface (Figure 3.12B). A second control surface was uniformly hydrophobic without any hydrophilic regions or deposited INPs. This surface promoted dropwise condensation everywhere, which subsequently frosted over due to inter-droplet ice bridging (Figure 3.12C). Ironically, these findings therefore show that surfaces with both hydrophilic regions and INPs are able to suppress in-plane frost growth relative to more hydrophobic surfaces.

The edges of the circles or stripes feature a more dense assemblage of INPs compared to the middle region, as evident in Figure 3.11 or Figure 3.12A. This is due to the well-known coffee-stain effect, which is ubiquitous to evaporation-induced colloidal deposition [158]. However, scanning electron microscopy revealed that the degree of inhomogeneity is less extreme than appears with optical microscopy (Figure 3.13). Regardless of the extent of inhomogeneity of the deposited INPs, they promoted the same behavior for both the circles and stripes with regards to the mode of nucleation.

The critical nucleation pressure for embryo formation, p_n, can be calculated using

the equation [133]:

$$p_{\mathrm{n}} = p_{\mathrm{s}}\left(\frac{\nu}{\overline{R}T_{\mathrm{w}}}\sqrt{\frac{4\pi}{3}\frac{\sigma^3}{kT_{\mathrm{w}}\,\ln(I^*)}f}\right), \tag{3.7}$$

where ν is the molar volume of water ($\nu \approx 18.016\,\mathrm{mL}$) or ice ($\nu \approx 19.65\,\mathrm{mL}$), $\overline{R} = 8.314$ J/mol·K is the universal gas constant, σ is the surface tension of water (for condensation) or ice (for desublimation), $k = 1.38\times10^{-23}$ J/K is the Boltzmann constant, $I^* = I_c/I_0 \sim 10^{24}$ is the ratio of the critical embryo formation rate and the kinetic constant, and $f = (2+\cos\theta)\big(1-\cos\theta\big)^2$ captures the effects of surface wettability. Note that the saturation vapor pressures of water ($p_{\mathrm{s}} = p_{\mathrm{s,w}}$) and ice ($p_{\mathrm{s}} = p_{\mathrm{s,i}}$) have already been estimated over a wide range of subfreezing temperatures [123].

Figure 3.14A shows the critical nucleation pressure for condensation ($p_{\mathrm{n}} = p_{\mathrm{n,w}}$, blue curve) and desublimation ($p_n = p_{\mathrm{n,i}}$, red curve) as a function of surface temperature and wettability. It can be seen that $p_{\mathrm{n,w}}$ and $p_{\mathrm{n,i}}$ intersect each other along a critical curve, with $p_{\mathrm{n,w}}$ being favorable (i.e. lower) on one side and $p_{\mathrm{n,i}}$ being favorable on the other. By zooming in to focus on the intersection in Figure 3.14B, it can be seen that desublimation is only favored for colder temperatures and lower contact angles.

These three-dimensional plots can be simplified into 2D plots by exclusively graphing the intersecting curve. In Figure 3.14C, the critical nucleation pressure where $p_{\mathrm{n,w}} = p_{\mathrm{n,i}}$ is plotted as a function of surface temperature (red dashed line). Above this dashed line, condensation is predicted to be favorable, whereas desublimation is favorable beneath. This graph also contains experimental measurements, where each data point represents the vapor pressure required for phase-change to first occur on the INP-laden surface for a given temperature. As expected, the observed mode of nucleation was condensation (blue squares) when the experimental p_n fell above the critical curve, whereas desublimation (red circles) was observed for

p_n values beneath the curve. Using Equation 3.7, the effective value of θ for embryos was extracted for each experimental value of p_n and T_w. This revealed that the surface areas laden with INPs exhibited an effective wettability of $\theta \approx 30°$, such that desublimation becomes favorable for $T_w < -10\,°C$ Figure 3.14D. It is also possible that the INPs are modifying the value of I^* in Equation 3.7, rather than just θ, but we presume that a change in the effective wettability is more likely due to the much weaker dependence of p_n on I^*.

In summary, substrates laden with INPs exhibited the desublimation mode of nucleation for temperatures of $T_w \leq -15\,°C$, in contrast to surface regions free of INPs which always exhibited supercooled condensation even at $T_w = -25\,°C$. Even for moderate subfreezing temperatures, such as $T_w = -10\,°C$, the INPs served to quickly freeze supercooled condensate at least two orders of magnitude faster than a conventional hydrophilic surface. By using wettability patterns to selectively deposit INPs onto a substrate, we gained spatial control over which regions of a surface promoted condensation versus desublimation. The ability of a surface to passively attain micro-patterned ice features in humid and subfreezing environments is useful for suppressing condensation frosting, as the templated ice features are hygroscopic which keeps the intermediate surface dry. Future works should examine the durability of surfaces laden with various types of ice nucleating particles, or alternately explore whether patterns of superhydrophilic features could serve the same role of promoting desublimation.

3.5 Materials and methods

3.5.1 Fabrication of the chemically patterned anti-frosting surface

Microscopic chemical patterns comprised of hydrophilic SiO_2 and a hydrophobic fluorosilane monolayer were fabricated in the same manner as Ref [131]. The only difference now is that one end of the hydrophilic stripes were connected to a large

hydrophilic pad near the edge of each sample, which facilitates the manual depositing (or freezing) of water on demand if desired. The surfaces were fabricated in a cleanroom at the Oak Ridge National Laboratory. During storage, the patterned silane monolayer was protected by a parylene coating. Shortly before testing a given sample, it was briefly exposed to an oxygen plasma to restore the hydrophilicity of the SiO_2, followed by the dry peel-off of the parylene to expose the patterned hydrophobic monolayer. When chilled beneath the dew point, supercooled condensation preferentially nucleated on the hydrophilic stripes and froze to create the pattern of ice stripes that enabled the overlapping dry zones.

3.5.2 Fabrication of the physically patterned anti-frosting surfaces

Arrays of parallel micro-grooves were laser cut into the top face of a 3.175 mm thick sheet of 6061 aluminum by Potomac Photonics, Inc. The cross section of each micro-groove was 15 μm in width and 25 μm in depth. The side walls of the micro-fins and connecting reservoir were created by micro-milling. The width of each reservoir was 2 mm, while its length was either 10 mm, 15 mm, to 30 mm depending upon the total size of the connecting micro-groove array. The depth of each reservoir was chosen so that the volume of the reservoir and the connected micro-grooves would equal 10 μL, see Figure 3.2D. This way, a 10 μL water droplet could be deposited into the reservoir to completely fill up both the reservoir and the micro-grooves via capillary action. For arrays where the micro-grooves were elevated with respect to the dry zones, the surface was first micro-milled to produce array of fins 100 μm in width, followed by laser cutting along the center of the tops of the fins. The choice of 100 μm was a balance between wanting to minimize the thickness of the fins, while also wanting to prevent bending. A total of 16 different micro-groove arrays were fabricated, where the center-to-center pitch between grooves was varied from 0.5 mm, 1.0 mm, 5.0 mm, and 10.0 mm, while the height of the fins was varied

from 0.0 mm (bottoms of grooves are beneath floor level), 0.025 mm (i.e bottoms of grooves are flush with floor level), 0.1 mm, and 1.0 mm (Figure 3.2E). The length of the micro-grooves was always 6.5 mm, such that the grooves could easily fill the entire field-of-view of the top-down microscope. Before running an experiment, the desired surface was degreased in acetone for 10 min, immersed in ethanol for 10 min, rinsed extensively with distilled water, dried with nitrogen, and left on a hotplate with temperature of 200 °C for 30 min. Finally, the surfaces were plasma cleaned for 4-5 min prior to operation (Plasma Etch Inc., PE-25). The plasma cleaning served two purposes: it maximized the capillary action of water filling the micro-grooves, while also demonstrating hat even a highly hydrophilic surface could exhibit passive anti-frosting by virtue of the ice stripes.

3.5.3 Regular aluminum surfaces

To serve as a control surface, a 50.8 μm thick sheet of aluminum alloy 1100 (McMaster Carr, 9057K124) was cut into 50.8 cm $\times$ 50.8 cm wafers. The aluminum wafers were then degreased in acetone, rinsed, and dried similar to the aforementioned patterned aluminum. Before testing an aluminum wafer, it was exposed to an oxygen plasma for 4–5 min to give it the same hydrophilic properties as the physically patterned aluminum surfaces. A new wafer was used for each experimental trial.

3.5.4 Superhydrophobic aluminum surface

Aluminum wafers were cut from a sheet of aluminum in the same way as with the regular aluminum wafers. After cleaning the samples they were submerged for 10 min in distilled water heated to 70 °C to impart an aluminum hydroxide nanostructure (see [92] more information). Surfaces were then dried on a hot plate held at 200 °C for 1 hr and plasma cleaned for 10 min prior to the vapor-phase deposition of trichloro(1H, 1H, 2H, 2H–perfluorooctyl)silane (Sigma Aldrich). The vapor-phase

deposition was performed by enclosing the aluminum surface and an open container of 25 μL of silane in a Pyrex pan placed on a hot plate at 70 °C for 24 hr. The combination of the aluminum hydroxide nanostructure and the conformal silane coating resulted in a highly superhydrophobic surface, with advancing and receding apparent contact angles of $\theta_A/\theta_R = 170°/169°$ [92].

3.5.5 Experimental setup

The desired surface was thermally bonded to a Peltier stage (ráme-hart, 100-30) using a thin film of thermal grease that is rated down to −40 °C (Thermalcote, 251G). The Peltier stage was fixed within a custom-built humidity chamber (ráme-hart), which utilizes controlled flows of humid air and/or dry air to hold the humidity at any desired set point. This humidity chamber was bolted to a stage beneath a top-down optical microscope (Nikon 150LV). A quartz window embedded into the roof of the humidity chamber allowed for top-down imaging using long working-distance lenses (Mitutuyo, M Plan APO) ranging in magnification from 5× to 20×. The top-down microscope was interfaced with a digital camera (Vision Research, Phantom v711). Simultaneously, a side-view imaging rig was built using another camera (Canon, EOS 5D Mark IV) connected to a long-distance microscope (Infinity, InfiniProbe TS-160). A quartz window was also embedded into one of the side walls of the humidity chamber, to facilitate the side-view imaging. See Figure B.1 for a visual schematic of this experimental setup.

3.5.6 Experimental methods

To test the physically patterned anti-frosting surfaces, first the air inside of the chamber ($T_\infty \approx 16°C$) was set to a relative humidity of $RH = 4\%$ to prevent any initial condensation on the surface. Then, 10 μL of distilled, food-colored water was deposited into the reservoir. The water subsequently wicked inside of the connected

micro-grooves, which was confirmed via top-down optical microscopy. After the water had filled the grooves, the surface temperature was brought down to $T_w = -20\,^\circ\mathrm{C}$ to quickly freeze the water. Now that the micro-grooves were primed with ice, the Peltier was quickly increased to $T_w = -10\,^\circ\mathrm{C}$ and the relative humidity was set to the proper value that resulted in the desired supersaturation ($S = 1.1$ or 1.5). Time zero for the top-down and side-view videos corresponded to the moment the ice stripes were first created. For the control cases of the regular or superhydrophobic aluminum, no surface priming was necessary. Instead, the Peltier was simply set to $T_w = -10\,^\circ\mathrm{C}$ and the humidity was controlled to the desired supersaturation. The ambient air temperature ranged from $T_\infty = 14.3 - 15.6\,^\circ\mathrm{C}$; for each experiment, the chamber's relative humidity was dynamically tuned over time to maintain the desired supersaturation (S) despite the slow fluctuations in T_∞ . Three trials were performed for each test surface, where each trial ran for 3 hr fixed at $T_w = -10\,^\circ\mathrm{C}$ and the desired supersaturation.

3.5.7 Image processing

Movies captured from the digital cameras were uploaded as image stacks into Mathematica. Images were divided into multiple unit cells, where each unit cell was defined as the center-to-center distance between adjacent micro-grooves. Using a custom-written code, the projected surface coverage of the frost was found by virtue of the fact that the ice had a much higher contrast than the dry surface areas. All of the binary images created from the Mathematica code were checked with the original images to qualitatively ensure that the ice was being captured with high fidelity.

4

Freezing of Soap Bubbles

"Enthusiasm just creates bubbles; it doesn't keep them from popping."

−Adora Svitak

The content of this chapter was previously published as journal manuscripts in [159], and reproduced here with minor modifications. In this chapter we are trying to elucidate the underlying physics of freezing of soap bubbles in different environmental conditions.

4.1 Introduction

Soap bubbles and films have been a source of intrigue for millennia. Their influence can be traced in a historical arc that includes Babylonian divination rituals (lecanomancy) to Impressionist paintings to the works of physicists such as Newton, Plateau, and de Gennes [160–163]. Building on this foundation, in modern times the behavior of bubbles from their birth [164, 165], wetting [166], drainage and evaporation [167, 168], to their fatal bursting [169, 170] have been comprehensively studied.

This has culminated in the practical use of bubbles for a myriad of applications such as energy harvesting [171], drug delivery [172], and cleaning devices [173–175].

Despite this prolonged attention lavished on bubbles, there exists only a brief scientific report of freezing. In 1949, Shaefer observed bubbles freezing atop Mt. Washington and commented on the number and shape of ice crystals contained therein [176]. More casually, there is an emerging trend of photographers capturing beautiful videos of the complex freezing dynamics of bubbles deposited on snow (for example, see `https://www.youtube.com/watch?v=H7pqoCJQp2I`). These dynamics are non-trivial owing to the unique geometry of a bubble: unlike droplets, puddles, or surface-bound liquid films, bubbles do not have a thermally conductive bulk volume. Therefore the extensive studies of how droplets [8–10, 104, 105, 177–179] or films [180–182] freeze cannot capture the physics of bubble freezing.

Inspired by these informal observations of freezing bubbles, here we characterize the heat transfer phenomena governing the dynamics of freezing bubbles over a wide range of conditions. Two different types of freezing dynamics were observed, depending on the experimental conditions. For bubbles freezing in an isothermal environment, the bottom-up freeze front produces a Marangoni flow that detaches ice crystals, resulting in accelerated freezing from multiple fronts growing in tandem. When bubbles are deposited on a chilled icy substrate in room temperature conditions, on the other hand, the bottom-up freeze front comes to a halt midway up the bubble due to poor conduction.

4.2 Experimental setup

Two separate sets of experiments were performed: *Isothermal Experiments*, where a walk-in freezer set both the ambient (T_∞) and substrate temperature (T_w) far beneath the melting point (T_m): $T_\infty \approx T_\mathrm{w} = -18 \pm 2\,^\circ\mathrm{C} < T_\mathrm{m}$ (Figure 4.1A), and Room Temperature Experiments, where the ambient was warmer than the melting

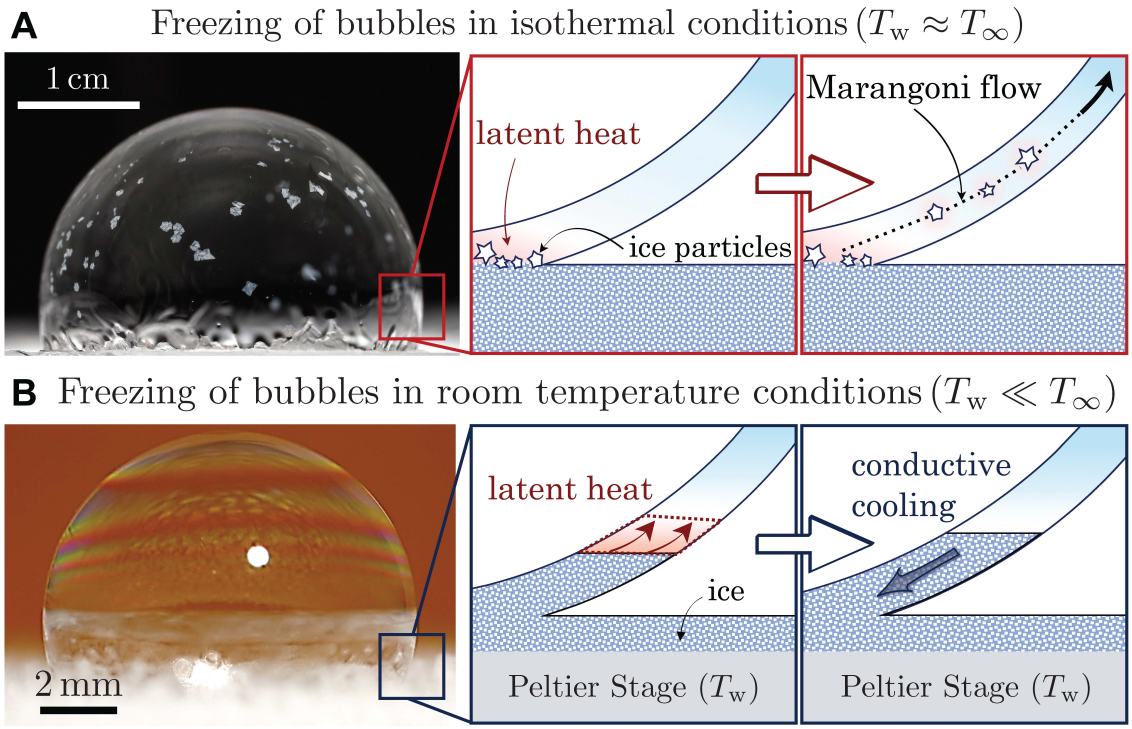

FIGURE 4.1: The dynamics of freezing bubbles under various ambient conditions. A) For bubbles deposited on an icy substrate contained within an isothermal freezer, the freeze front induced local heating at the bottom of the bubble. This resulted in a Marangoni flow strong enough to detach and entrain growing ice crystals, such that the bubble froze from multiple fronts. B) For bubbles deposited on a chilled, icy substrate in a room temperature environment, the freeze front grew bottom-up in a uniform fashion before stopping entirely at a critical height. Latent heat generated at the growing freeze front had to be continually dumped into the substrate via inefficient conduction across the frozen portion of the bubble.

point and freezing was accomplished with a chilled substrate: $T_\infty \approx 25\,^\circ\mathrm{C} > T_m > T_w$ (Figure 4.1B). In both scenarios, the bubble was deposited on an icy substrate, such that the freezing process could begin immediately. For isothermal experiments, soap bubbles enclosing air volumes of $\Omega = 500\,\mu\mathrm{L}$ or $10\,m\mathrm{L}$ were deposited onto an ice disk. For the room temperature experiments, $\Omega = 5\,\mu\mathrm{L}$ or $500\,\mu\mathrm{L}$ and the substrate was cooled anywhere from $T_w = -10\,^\circ\mathrm{C}$ to $-40\,^\circ\mathrm{C}$ and allowed to frost over. These two different conditions for the ambient produced two distinct modes of bubble freezing.

For bubbles in both sets of experiments, we used a glycerol-water soap solution

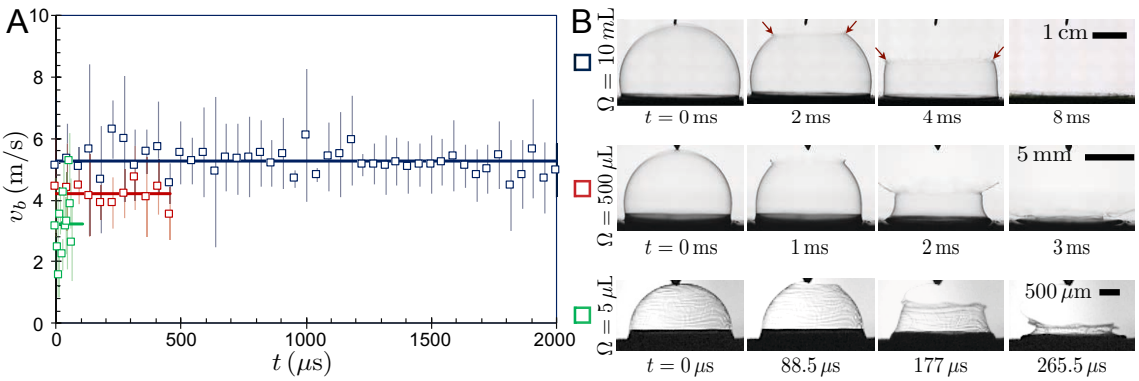

FIGURE 4.2: Determining the soap film thickness by bursting bubbles. A) Velocity of the hole's rim moving along the arc of the bubble, measured intermittently up until the rim exhibited splashing. Data series correspond to interior volumes of: $\Omega = 5\,\mu$L (green squares), $\Omega = 500\,\mu$L (red), and $\Omega = 10\,m$L (blue). Error bars correspond to one standard deviation between three trials. The air and aluminum substrate were both at room temperature, $T_\infty \approx 22 \pm 1\,^\circ$C; the air had a relative humidity of $RH = 26\%$. Constant bursting velocities (solid lines) were found from the average of all the data points for a given bubble size. B) High-speed image sequences of bursting bubbles used to measure the receding velocities of the liquid rims shown in (A). Bubbles were initially punctured with a sharp dry needle at their top. Red arrows in the first row of images show the evolving location of the rim.

exhibiting a freezing point of $T_\mathrm{m} \approx -6.5\,^\circ$C (see "Methods" section) [183]. When a calm bubble is punctured, a hole opens and grows due to the unstable surface tension forces at its rim. Using the Dupré-Taylor-Culick law, the initial film thickness of a liquid bubble (e_0) can be determined from the hole-opening velocity by balancing surface tension and inertia [184, 185]:

$$v_\mathrm{b} = \sqrt{\frac{2\gamma}{\rho e_0}}, \tag{4.1}$$

where $\gamma = 24.2$ mN/m is the solution's surface tensio=n measured by using the pendant drop method and waiting until the surfactant had reached a steady-state packing density at the free interface (Figure C.1). Using high-speed imaging, bursting velocities of $v_\mathrm{b} \approx 3.2$ m/s, $v_\mathrm{b} \approx 4.1$ m/s, and $v_\mathrm{b} \approx 5.3$ m/s were observed for $\Omega = 5\,\mu$L, $\Omega = 500\,\mu$L, and $\Omega = 10\,m$L bubbles, respectively (Figure 4.2). Given that the soap

solution is 80% water, we approximate the density (and all other thermophysical properties besides T_{m}) as that of pure water: $\rho \approx 1000\,\mathrm{kg/m^3}$. From Equation 4.1, we obtain $e_0 \approx 4.7\,\mu\mathrm{m}$ for $\Omega = 5\,\mu\mathrm{L}$, $e_0 \approx 2.7\,\mu\mathrm{m}$ for $\Omega = 500\,\mu\mathrm{L}$ and $e_0 \approx 1.7\,\mu\mathrm{m}$ for $\Omega = 10\,m\mathrm{L}$.

4.3 Bubble freezing under isothermal conditions

Figure 4.3 shows the remarkable multi-step freezing process that occurs under isothermal conditions, over a time scale of $\mathcal{O}(10\,\mathrm{s})$ for centimetric bubbles. The initial mode of freezing was a bottom-up freeze front, analogous to the bottom-up freezing of sessile droplets but more dendritic in appearance. Immediately upon contact with the icy substrate, the bubble exhibited an upward flow of velocity $v \approx 10\,\mathrm{mm/s}$ emanating from the early freeze front (Figures 4.3A,B, C.2, and C.3). Within milliseconds, this flow destabilized into plumes with a radius $R_{\mathrm{p}} \sim 1\,\mathrm{mm}$. After a typical time of $\mathcal{O}(1\,\mathrm{s})$, ice crystals about $100\,\mu\mathrm{m}$ in diameter suddenly became visible and were entrained in the upward fluid flow. Hundreds of these entrained ice crystals swirled around the bubble in a dramatic fashion, which we term the "Snow-Globe Effect." After a few seconds, the plumes dissipated and died out as the ice crystals grew larger in size. Finally, the bubble completely froze over within $\mathcal{O}(10\,\mathrm{s})$, not only from the bottom-up freeze front, but especially from the floating ice crystals as they grew and inter-locked together.

4.3.1 Possible mechanisms

The mechanism for the vertical plumes that emerge when the bubble contacts the icy surface is far from obvious. At least four types of flows can be envisaged: Marangoni flow due to non-uniform surfactant concentrations, flow due to non-uniform surface curvature (marginal regeneration), buoyant flow due to thermal effects, or a thermal

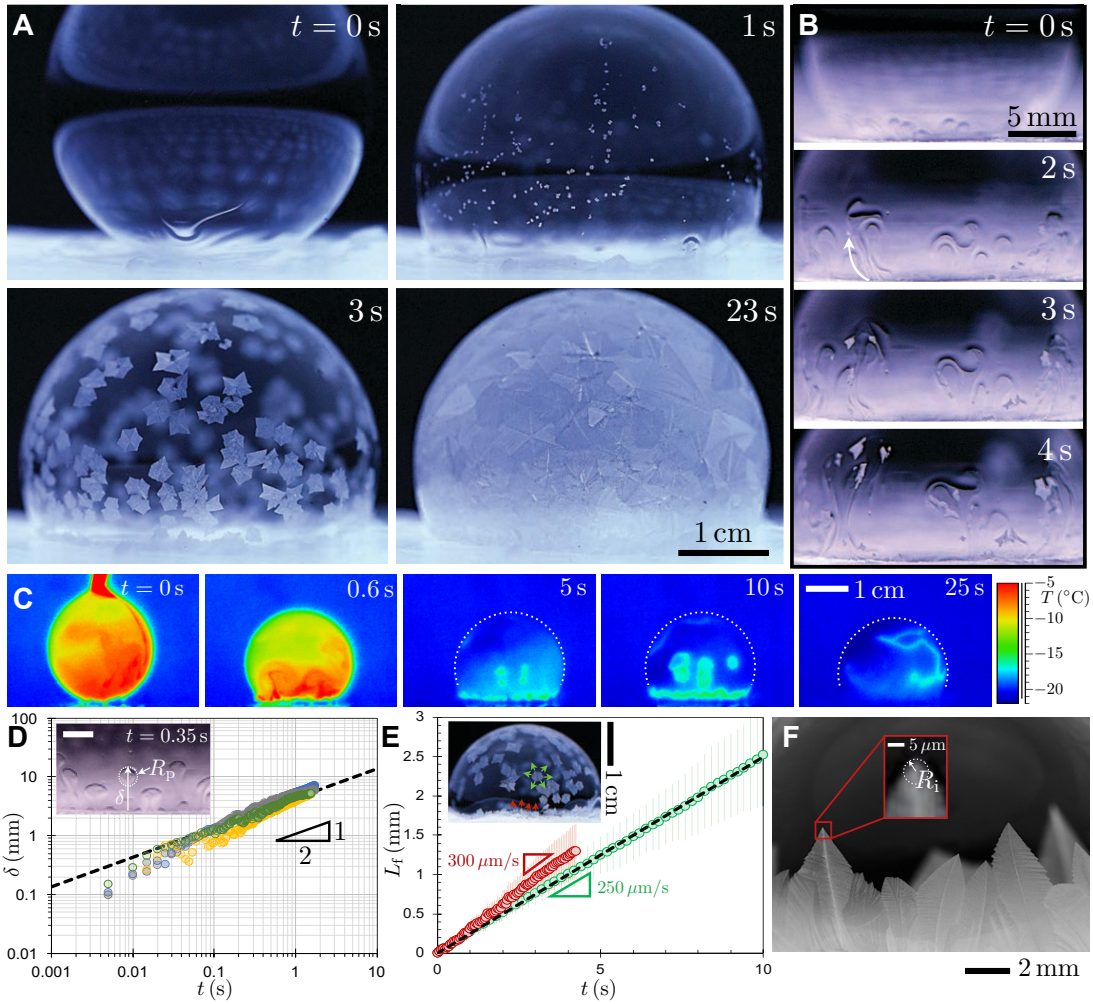

FIGURE 4.3: Freezing soap bubbles under chilled and isothermal conditions. A) Freezing of a 10 mL bubble deposited on an ice disk (Figure C.2) in a walk-in freezer chilled to $T_\infty = -18.5 \pm 0.5\,^\circ$C with $RH = 60 \pm 5\%$. B) The freeze front induced a Marangoni flow, which detached and entrained some of the growing ice particles. C) Time-lapse thermographic images, where arrows clarify the bubble-air interface. The liquid portions of the bubble assumed the freezer's temperature shortly after deposition, while the freeze fronts were warmer (i.e. near the melting temperature) due to the release of latent heat. The emissivity coefficient of ice was calibrated at $\epsilon = 0.98$. Time zero corresponds to the bubble's first contact with the icy substrate, where the top of the bubble is still adhered to the pipette (first frames of A-C). D) Displacement (δ) of four thermal plumes (different colors) were measured over time when $T_w \approx T_\infty = -19.6\,^\circ$C. Inset shows the radius of plumes was of order $R_p \sim 1$ mm. The scale bar represents 2 mm. E) Growth rate of freeze fronts coming from the substrate (red data points, $v_i \approx 300\,\mu$m/s) or from ice crystals suspended in the liquid film (green, $v_i \approx 250\,\mu$m/s) when $T_\infty = -18.4 \pm 1.7\,^\circ$C. Error bars represent a standard deviation from an average of three trials. F) The ice radius, R_i, was estimated from the tip of ice crystals growing from the substrate.

Marangoni flow induced by the latent heat of fusion. The first two flow mechanisms do not require a temperature gradient and can therefore be evaluated using bubbles deposited on a dry substrate at room temperature conditions (Figure 4.4A). The distribution of surfactant along the interface can be isolated by considering a bulk pendant drop suspended in air, where about 40 min was required to achieve a steady-state surface tension (Figure C.1). However, recall that our soap bubbles are only about 1 μm in thickness. For such thin films, having a large surface-area-to-volume ratio, the diffusion of surfactant to the free surface should be much faster [186]. For example, the ratio of diffusive time scales between the pendant drop and bubble is $R_{\text{drop}}^2/e_0^2 \sim 10^6$, such that a steady-state surface tension should be achieved within about 1 ms for the bubble. In contrast, we observed that room-temperature bubbles on dry substrates generated plumes over a very long time scale of $\mathcal{O}(10\,\text{min})$ (Figure C.4), ruling out asymmetric surfactant concentrations as a likely mechanism. Besides, the surface tension measured with the pendant drop was only changing temporally, not spatially, as the measured curvature indicated a single value of surface tension for any given time (Figure C.1).

The second mechanism of marginal regeneration, as first proposed by Mysels, Shinoda and Frankel [187], is purely geometric and owes its origin to the liquid meniscus at the foot of the bubble. The Laplace pressure difference between the bubble and the meniscus generates plumes that are long-lived [169, 188]. This agrees with our control case of room temperature bubbles, where the plumes were maintained for most of the lifetime of the bubble (Figures 4.4A and C.4A). While we can therefore attribute plumes in the room temperature bubbles to marginal regeneration, this does not necessarily explain the plumes in the freezing bubbles. For the case of freezing, the liquid meniscus will be solidified by the bottom-up freeze front within about 0.1 s (Figure C.3), which would halt the marginal regeneration. Considering that the plumes were observed to persist for several seconds for the freezing bubbles,

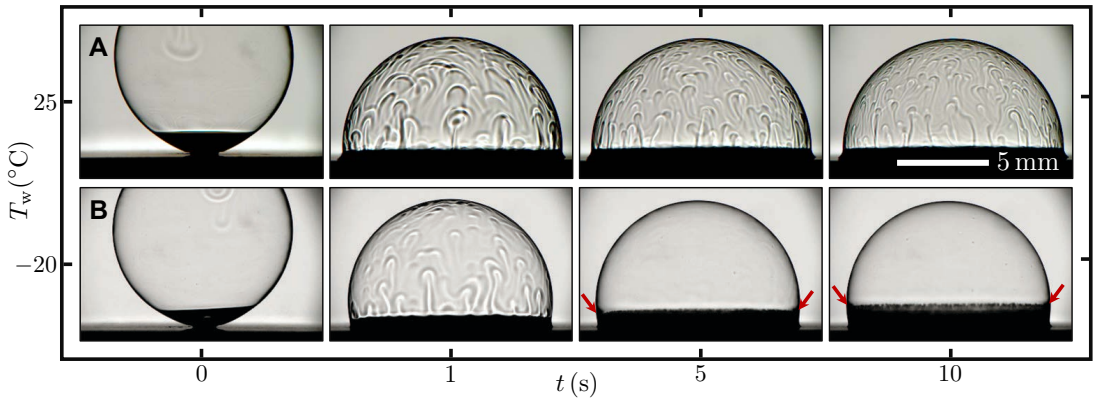

FIGURE 4.4: Contrasting mechanisms for plumes in nonfreezing vs. freezing bubbles. A) For a bubble deposited on a dry, room temperature substrate, plumes were continually generated through the ~ 10 min lifetime of the bubble due to marginal regeneration. B) For a bubble deposited on an icy cold stage ($T_w = -20\,^\circ$C), the bottom-up freeze front (red arrows) suppressed marginal regeneration but enabled a brief (~ 1 s) flow due to Marangoni freezing. In either case here, the ambient conditions were $T_\infty \approx 25\,^\circ$C with a relative humidity of $RH \approx 19\%$.

we should instead consider the thermal mechanisms of buoyancy or Marangoni flow due to the latent heat released from the freeze front.

A previous work has shown that buoyant thermal plumes can be generated in vertical soap films, where the plumes were primarily inertial [189]. Inertia is negligible in our system, as the Reynolds number is $\mathrm{Re} = \rho V^2/(\eta V/e_0) = \rho V e_0/\eta$, where $\eta \approx 2 \times 10^{-3}$ Pa s is the viscosity of water [190] at $-6.5\,^\circ$C. For typical values of $V \sim 10$ mm/s, as measured by observing the initial speed of a rising plume (Figure 4.3D), we get $\mathrm{Re} \sim 0.01$. A buoyant flow in our soap bubbles would therefore have to balance a gradient in pressure, $\Delta\rho g$, with the gradient in viscous stress, $\eta V/e_0^2$. For a typical value of $\Delta\rho \sim 1$ kg/m^3, this leads to buoyant flows of speed $V_B \sim \Delta\rho g e_0^2/\eta \sim 10$ nm/s. This is in contrast to Figure 4.3D, where the speed is not constant over time and is about 6 orders of magnitude faster ($V \sim 10$ mm/s).

This leaves us with the final possibility of a Marangoni flow induced by the latent heat released from freezing. We will refer to this process as "Marangoni freezing." The freezing-induced heating engenders a gradient in surface tension, $\Delta\gamma/\delta$, where

δ is the length scale of the temperature gradient driving the flow. This must be balanced by viscous stress, $\eta V_{\mathrm{M}}/(b + e_0/2)$, where V_{M} is the Marangoni velocity, b is the slip length of the Poiseuille flow along the bubble's film (Supplementary Figure 6), and the velocity profile was approximated as constant-slope. For our system, $b = \sqrt{\eta R/(\rho g t_{\mathrm{d}})} \sim 1\,\mu$m [167], where $t_{\mathrm{d}} \sim 10^3$ s is the drainage time scale of a centimetric bubble which was experimentally observed (Figure C.4A). Therefore $(b + e_0/2) \sim e_0$, resulting in a simplified viscous stress of $\eta\dot{\delta}/e_0$, where $\dot{\delta} = d\delta/dt = V_{\mathrm{M}}$ represents the speed a plume. Relating the surface tension stress and viscous stress and solving for δ:

$$\delta \sim \sqrt{\frac{2\Delta\gamma e_0}{\eta}}\, t^{1/2}. \tag{4.2}$$

Note that $\Delta\gamma \approx 2\,\mathrm{mN\,m^{-1}}$ for $\Delta T = T_{\mathrm{m}} - T_{\mathrm{l}} \approx 13.5\,^{\circ}\mathrm{C}$ corresponding to our degree of supercooling (Figure 4.3C) [191]. When comparing Equation 4.2 to experiments, the trajectories of thermal plumes were tracked for $\Omega = 10\,m$L bubbles (Figure 4.3D). The measurements of δ are in good agreement with 1/2-law with a numerical prefactor of 1.6, confirming the Marangoni freezing mechanism for flow in the freezing bubbles. Finally, the underlying physics for the resulting wavelength and plume radius ($R_{\mathrm{p}} \sim 1\,$mm) are non-trivial and beyond the scope of this present research, as has been noted before in the phenomenon of Marangoni bursting [192].

4.3.2 Marangoni freezing and the "Snow-Globe Effect"

Marangoni freezing occurs when Marangoni flows can be generated by freezing-induced heating at the contact line, and these flows dominate over any other possible flow. The two temperature requirements for Marangoni freezing include the condition for freezing: $T_{\mathrm{w}} < T_{\mathrm{m}}$, and the condition for vertically upward Marangoni flow: $dT/dz < 0$, such that $d\gamma/dz > 0$ [191]. For the Marangoni flow to dominate, it must be at least as fast as the rate of thermal diffusion, $V_{\mathrm{T}} \sim \alpha_{\mathrm{l}}/\delta$, where $\alpha_{\mathrm{l}} = 0.13 \times 10^{-6}\,\mathrm{m^2/s}$

is the thermal diffusivity of the liquid solution. This first flow criterion is stated in terms of the ratio of the Marangoni velocity, $V_{\mathrm{M}} \sim \Delta\gamma e_0/\eta\delta$ (from Equation 4.2), and V_{T}. This ratio is called the Marangoni number, $\mathrm{Ma} = \Delta\gamma e_0/\eta\alpha_{\mathrm{l}}$, which should be greater than or equal to 1. The second flow criterion is that the velocity due to thermal buoyancy, $V_{\mathrm{B}} \sim \Delta\rho g e_0^2/\eta$, must be negligible compared to V_{T}, resulting in a small Rayleigh number: $\mathrm{Ra} \sim \rho g e_0^2 \delta/\alpha_{\mathrm{l}}\eta \ll 1$. The above arguments can be succinctly summarized as $T_{\mathrm{t}} \lesssim T_{\mathrm{w}} < T_{\mathrm{m}}$, $\mathrm{Ma} \gtrsim 1$, and $\mathrm{Ra} \ll 1$, where T_{t} is the temperature of the top of the bubble. For the bubbles freezing in the walk-in freezer, all of the conditions were satisfied as $T_{\mathrm{t}} \approx T_{\mathrm{w}} \approx -20\,^{\circ}\mathrm{C} < T_{\mathrm{m}} = -6.5\,^{\circ}\mathrm{C}$, $\mathrm{Ma} \approx 13$, and $\mathrm{Ra} \sim 10^{-5}$. Besides generating the thermal plumes, Marangoni freezing can also be responsible for what we call the "Snow-Globe Effect," as will now be discussed.

Owing to the high Ma number, we propose that Marangoni flows shear off and entrain ice dendrities forming at the bottom-up freeze front. While we do not have any direct evidence of a flow shearing off an ice dendrite, as they are too small to be visible at the point of detachment, there are two strong justifications for this claim. First, it is highly unlikely that hundreds of homogeneous nucleation events would suddenly occur within the liquid film away from the freeze front, especially considering that the freezer temperature is too warm to promote homogeneous nucleation. This was confirmed by depositing a bubble on a dry silicon wafer (still in the walk-in freezer), where no freezing/nucleation events were observed even after 30 min (Figure C.2C). Second, whenever the suspended ice crystals first appeared (i.e. grew to a micrometric size), it was always during the Marangoni flow. Indeed, the growth of the entrained ice crystals was often highly asymmetric due to the flow, as seen in Figure 4.3B. The Marangoni flow must therefore be detaching invisibly small (i.e. nano-scale) ice particles from the bottom-up freeze front and advecting them upwards. After about 1 s of Marangoni freezing, hundreds of microscopic ice particles were suspended and growing within the film, working in tandem to heat the

surrounding liquid. At this point, the gradient in temperature and surface tension is happening in a myriad of locations and directions, as opposed to the original case of a fully out-of-plane gradient extending from the bottom freeze front. Thus the "Snow-Globe Effect" annihilates the very Marangoni flow that created it in the first place.

This ice detachment can be tentatively modeled by balancing the inertia of the thermal plume (F_{i}) with the pull-off force required to crack an ice dendrite free of its icy substrate (F_{crack}). For a dendritic contact area of πl^2, the pull-off force can be determined using the Griffith condition for crack initiation [193]:

$$F_{\mathrm{crack}} = \pi l^2 \sqrt{\frac{8E^* w_{\mathrm{ad}}}{\pi l}}, \tag{4.3}$$

where w_{ad} is the work of adhesion and $E^* = E_{\mathrm{i}}/(1-\nu_{\mathrm{i}}^2)$. Here, $E_{\mathrm{i}} = 8.7 \times 10^9$ Pa and $\nu_{\mathrm{i}} = 0.31$, are the Young's modulus and Poisson's ratio corresponding to ice, respectively [194]. The work of adhesion can be quantified as $w_{\mathrm{ad}} \approx \gamma_{\mathrm{i,l}}$ where $\gamma_{\mathrm{i,l}}$ is the interfacial energy of ice with respect to water determined from Young's relation, $\gamma_{\mathrm{i,l}} = \gamma_{\mathrm{i,v}} - \gamma\cos\theta$. Here, $\gamma_{\mathrm{i,v}} \approx 0.1$ J/m^2 is the interfacial energy of ice with respect to vapor [136], $\gamma \approx 0.02$ J/m^2 (Figure C.1), and $\theta \approx 0°$ is the intrinsic contact angle of the liquid solution on ice. Therefore, the work of adhesion between an ice dendrite and the icy substrate is $w_{\mathrm{ad}} \approx 0.08$ J/m^2. The inertia of a thermal plume is $F_{\mathrm{i}} \sim (\rho\pi R_{\mathrm{p}}^2) v_{\mathrm{M},0}^2$, where $v_{\mathrm{M},0}$ is the Marangoni velocity at the very early time limit. Experimentally, we find $v_{\mathrm{M},0} \sim 10$ mm/s by taking the derivative from the $\delta - t$ plot (Figure 4.3D) at $t < 10$ ms. Balancing the pull-off force and inertia, $F_{\mathrm{i}} \sim F_{\mathrm{crack}}$, predicts that a dendrite must be smaller than $l \lesssim 10$ nm for detachment. As shown in Figure 4.3A,B, entrained ice particles grow to $\sim 100\,\mu$m in size after ≈ 1 s of bubble deposition on the icy substrate. This is consistent with the measured growth rate of ice of $v_{\mathrm{i}} \sim 100\,\mu$m/s (Figure 4.3E), indicating that ice particles do indeed detach

from the freeze front at a nano-scale size.

The growth rate of the ice front can be modeled by using the well-known two-phase Stefan problem where a semi-infinite ($0 < y < \infty$) supercooled liquid with temperature $T_\mathrm{l} < T_\mathrm{m}$ is exposed to a temperature T_c at its boundary ($y = 0$) at time zero. The tip velocity is then given by:

$$v_\mathrm{i} = 2\lambda^2 \alpha_\mathrm{i} / R_\mathrm{i}, \tag{4.4}$$

where $\lambda \approx 0.03$ was obtained from the root of a transcendental equation (Equation 4.5), $\alpha_\mathrm{i} = 1.15 \times 10^{-6}\,\mathrm{m^2/s}$ is the thermal diffusivity of ice, and R_i is the tip radius of the ice layer [181]. For our case of $T_\mathrm{c} = T_\mathrm{m}$, the transcendental equation can be expressed as:

$$\frac{\mathrm{St_l}}{\nu\lambda\,\mathrm{erfc}(\lambda\nu)\exp((\lambda\nu)^2)} = \sqrt{\pi}, \tag{4.5}$$

where ν is the ratio of the thermal diffusivity of ice to the water defined as $\nu = \sqrt{\alpha_\mathrm{i}/\alpha_\mathrm{l}}$, $\mathrm{St_l} = (c_\mathrm{w}(T_\mathrm{m} - T_\mathrm{l}))/L$, and $L = 334 \times 10^3\,\mathrm{J/kg}$ is the latent heat of fusion. The tip diameter was crudely measured as $2R_\mathrm{i} \approx 1.28\,\mu\mathrm{m}$ (Figure 4.3F), consistent with a previous report [181] and the need to be contained within the film ($e_0 \approx 1.7\,\mu\mathrm{m}$, Figure 4.2). Plugging this value of R_i into Equation 4.4 gives a theoretical tip velocity of $v_\mathrm{i} \approx 250\,\mu\mathrm{m/s}$, in agreement with experimental growth measurements of $v_\mathrm{i} \approx 300\,\mu\mathrm{m/s}$ for the bottom-up freeze front and $v_\mathrm{i} \approx 250\,\mu\mathrm{m/s}$ for the crystals suspended within the bubble film (Figure 4.3F).

4.4 Bubble freezing under room temperature conditions

In a second set of experiments, bubbles were deposited on a cold stage set to temperature T_w within a room temperature ambient environment (Figure 4.5A). Under these conditions, freezing progressed in four stages: Marangoni freezing, partially frozen equilibrium, marginal regeneration, and collapse.

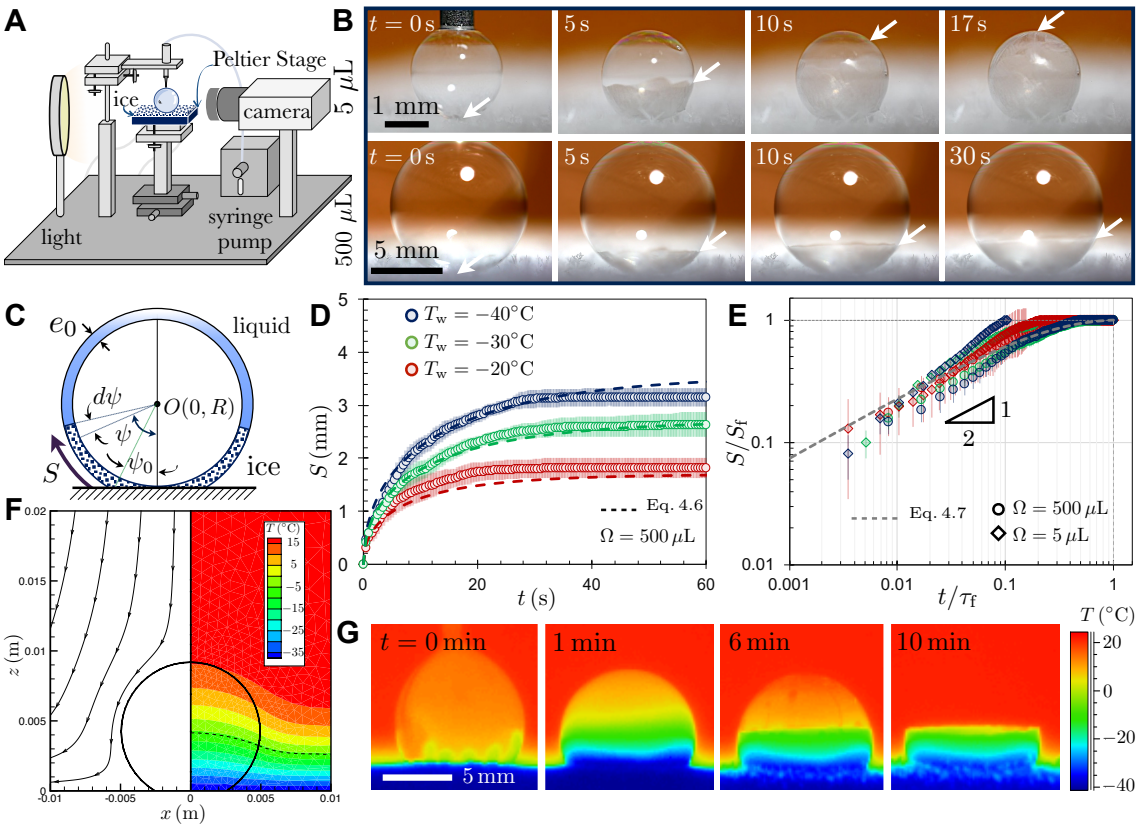

FIGURE 4.5: Freezing bubbles on a cold stage in a room-temperature environment. A) Schematic of the experimental setup, where a bubble of controlled volume is deposited on a frosted Peltier substrate using a syringe pump. B) Side-view imaging of freezing bubbles, of volume $\Omega = 5\,\mu$L and $\Omega = 500\,\mu$L on a surface chilled at $T_w = -40 \pm 1\,°$C. Arrows indicate the evolving location of the freeze front and time zero is when the bubble is first deposited. C) Schematic showing the terms used in Equation 4.6. (D) The frozen arc length of $\Omega = 500\,\mu$L bubbles over time. Data points (circles) represent experimental data, with error bars of one deviation across three trials, while dashed lines represent Equation 4.6. E) For both $\Omega = 5\,\mu$L (diamonds) and $\Omega = 500\,\mu$L (circles), plotting the frozen arc length normalized by the final arc length (S/S_f) against a non-dimensional time-scale (t/τ_f) collapsed all of the data and theory onto a universal curve. The average ambient conditions across all experiments were $T_\infty = 23.4 \pm 1.2\,°$C and a relative humidity of $RH = 42 \pm 14\%$. F) Simulation of the air temperature profile shows that near the center of the Peltier, the bubble somewhat disrupted the natural convection, resulting in greater slopes for the iso-temperature lines (see Figure C.7). The dashed line corresponds to $T = -6$ °C. G) Thermographic images of a $\Omega = 500$ μL bubble was deposited on a frosted substrate of temperature $T_w = -40 \pm 1$ °C at a room temperature with $T_\infty = 23.3 \pm 1$ °C and $RH = 23 \pm 1.5\%$.

4.4.1 Marangoni freezing

Analogous to the walk-in freezer experiments, even in room temperature experiments, we see that mere milliseconds after deposition of bubbles on a chilled icy substrate, there is a burst of Marangoni plumes moving upward from the contact line. The difference between the two experiments is the initial imposed positive temperature gradient across the bubble in room temperature experiments ($T_\mathrm{t} > T_\mathrm{w}$). This, however, has no effect on the initial stages of freezing, as the latent heat released in these experiments to creates a local region of $dT/dz < 0$. However, the negative temperature gradient is only a transient effect, such that the plumes would die out within about 5 s. Perhaps due to the transient nature of Marangoni freezing for the case of a room temperature ambient, the "Snow-Globe Effect" was not observed. For the larger $\Omega = 500\,\mu$L bubble, it is also possible that nano-scale ice particles could be entrained in the Marangoni flow, but quickly melted by the warm top of the bubble ($T_\mathrm{t} > T_\mathrm{m}$) before growing to a micro-scale size.

4.4.2 Partially frozen equilibrium

A bottom-up freeze front progressed up a bubble at an initial speed of $v \sim 0.1$ mm/s (Figure 4.5B-E); this is similar to equivalent velocity of solidification fronts in water droplets [195]. However, unlike droplets, the freeze front of a bubble came to a complete stop after $\tau_\mathrm{f} \sim \mathcal{O}(10\text{ s})$, at a location depending on the bubble size and substrate temperature. Beyond this critical time scale, bubbles exhibited a state of partially frozen equilibria where the top portion of the bubble remained liquid (see second row in Figure 4.5B). The one exception to this trend of partial freezing was for $\Omega = 5\,\mu$L and $T_\mathrm{w} = -40$ °C, in which case bubbles were able to completely freeze (see first row in Figure 4.5B). In contrast to the bottom-up freezing of droplets [8], completely frozen bubbles did not exhibit a pointy tip, as instead the water can

expand within the hollow interior.

The observed trend of incomplete freeze fronts can be rationalized by the poor thermal conductance of the long and slender soap film. Conservation of energy within the bubble's film can be expressed as $dT/dt = \alpha \nabla^2 T$, where α is the thermal diffusivity corresponding to water or ice. The thermal diffusion time scale for a bubble of radius R scales as $\tau_\mathrm{D} \sim R^2/\alpha_\mathrm{i}$. In contrast, the time scale of the freeze front motion [8], $\tau_\mathrm{f} \sim R/v$, scales as $\tau_\mathrm{f} \sim \tau_\mathrm{D} L/(c_\mathrm{i} \Delta T_\mathrm{i})$, where $c_\mathrm{i} = 2.027 \times 10^3\,\mathrm{J/kg\,K}$ is the specific heat capacity of ice and $\Delta T_\mathrm{i} \sim 10\,\mathrm{K}$ is a typical temperature difference. The diffusion time scale is about an order of magnitude smaller than the freezing time scale, $\tau_\mathrm{f} \sim 10\,\tau_\mathrm{D}$, which allows us to assume a quasi-steady temperature profile: $\nabla^2 T = 0$. This remains true for water, as its heat capacity is about two times higher than that of ice.

Given the thin film thickness of the bubbles, it is assumed that a deposited bubble is predominantly cooled by the surrounding air rather than by conduction into the substrate. The temperature field can therefore be obtained by numerically modeling the natural convection occurring in the air above the chilled substrate (see C.6). A thermal boundary layer thickness of $\zeta \approx 3\,\mathrm{cm}$ was obtained, in agreement with experimental measurements using a thermocouple and translation stage (Figure C.6). The air temperature profile was slightly modified by the presence of a bubble, which was also captured in the simulation (Figures 4.5F, C.7, and C.8).

The velocity of freeze fronts is limited by the latent heat of fusion being released. Our model assumes that this latent heat, $\dot{Q}_\mathrm{LH}$, is mostly dumped into the substrate via conduction across the frozen portion of the bubble, $\dot{Q}_\mathrm{i}$, as both the thermal conductivity and temperature gradient of the ice are much larger than the surrounding air. The liquid upper portion of the bubble is also conducting heat, $\dot{Q}_\mathrm{l}$, either toward or away from the freeze front depending on the direction of the temperature gradient. We neglect convection in the liquid portion of the bubble, as the Marangoni flow has

typically dissipated by the time the freeze front has grown appreciably. This balance of heat in versus heat out at the freeze front can be summarized as $\dot{Q}_{\mathrm{LH}} + \dot{Q}_{\mathrm{l}} = \dot{Q}_{\mathrm{i}}$, where $\dot{Q}_{\mathrm{l}}$ can be negative in some cases. For a bubble of fixed radius of curvature R, these terms can be fully expressed as:

$$\Big[\rho L R \frac{d\psi}{dt} + k_{\mathrm{l}} \frac{\Delta T_{\mathrm{l}}}{R(\pi - \psi)}\Big](2\pi R e_0 \sin\psi) \sim k_{\mathrm{i}} \frac{\Delta T_{\mathrm{i}}}{R(\psi - \psi_0)}(2\pi R e_0 \sin\psi), \tag{4.6}$$

where k_{i} and k_{l} are the thermal conductivities of ice and liquid, ΔT_{i} and ΔT_{l} are the temperature differences across the frozen and unfrozen portions of the bubble, ψ_0 is the fixed angular coordinate of the bubble's contact line (see Figure 4.5C), and ψ is the angular coordinate of the evolving freeze front. The slight difference in density between water and ice was neglected here, such that $\rho = \rho_{\mathrm{l}} \approx \rho_{\mathrm{i}}$. The freeze front is always at the melting temperature, T_{m}, while the contact line is always at the substrate temperature, T_{w}, resulting in a temperature difference of $\Delta T_{\mathrm{i}} = T_{\mathrm{m}} - T_{\mathrm{w}}$ across the frozen portion of the bubble. The temperature at the top of the bubble, T_{t}, was found from the numerical simulations of the temperature field, such that $\Delta T_{\mathrm{l}} = T_{\mathrm{t}} - T_{\mathrm{m}}$ across the liquid portion of the bubble. For the 5 μL bubbles, the liquid film tended to conduct heat away from the freeze front ($T_{\mathrm{t}} < T_{\mathrm{m}}$), while heat was conducted into the freeze front for the 500 μL bubbles ($T_{\mathrm{t}} > T_{\mathrm{m}}$, see Figure C.8A).

Canceling like terms and using a dimensionless time $t^* = t/\tau_f$, Equation 4.6 can be non-dimensionalized:

$$\frac{d\psi}{dt^*} \approx \frac{\beta_1}{\psi - \psi_0} - \frac{k_{\mathrm{l}}}{k_{\mathrm{i}}} \frac{\Delta T_{\mathrm{l}}}{\Delta T_{\mathrm{i}}} \Big(\frac{\beta_2}{\pi - \psi}\Big), \tag{4.7}$$

where β_1 and β_2 are geometrical pre-factors. As seen in Figures 4.5D and Figure C.9A, the arc length of the growing freeze front, $S(t) = R\psi(t)$, is captured by Equation 4.7 for fixed values of $\beta_1 = 1.8$ and $\beta_2 = 30$. Therefore all of the data collapses onto a universal non-dimensional curve, as shown in Figure 4.5E.

The freeze front stops propagating as $d\psi/dt^* \to 0$ at a critical angular coordinate $\psi \to \psi_\mathrm{f}$ ($S \to S_\mathrm{f}$). The energy equation is then simplified to $\dot{Q}_l = \dot{Q}_i$, such that ψ_f can be found as:

$$\psi_f = \pi - \left(\pi - \psi_0\right)\left(\frac{\beta_1 k_\mathrm{i}}{\beta_2 k_\mathrm{l}}\left(\frac{\Delta T_\mathrm{i}}{\Delta T_\mathrm{l}}\right) + 1\right)^{-1}. \tag{4.8}$$

This can also be expressed as a critical height, $h_\mathrm{f} = 2R\sin((\psi_\mathrm{f} - \psi_0)/2)$ (see Figure C.9B). Equation 4.8 is plotted in Figure 4.6, where the slope corresponds to $\beta_1 k_\mathrm{i}/\beta_2 k_\mathrm{l} = 0.35$. This results in $k_\mathrm{i}/k_\mathrm{l}$ =5.83 (for the same β_1 and β_2 as before), which is close to $k_\mathrm{i}/k_\mathrm{l} = 3.93$ corresponding to of pure water. This discrepancy is due the existence of glycerol, soap solution, and low temperatures. Three distinct regimes of freezing are possible: the non-frozen regime, where $T_\mathrm{w} \geq T_\mathrm{m}$ and $\psi_f \to \psi_0$, the completely frozen regime, where $T_\mathrm{t} \leq T_\mathrm{m}$ such that $\psi_\mathrm{f} \to \pi$, and the partially frozen regime, where $T_\mathrm{t} > T_\mathrm{m} > T_\mathrm{w}$ and $\psi_0 < \psi_\mathrm{f} < \pi$ (where ψ_f is found by Equation 4.8). Across all bubble volumes and surface temperatures, the experimental values of ψ_f collapse perfectly onto this curve, validating the model. The experimental measurements of ψ_f were complicated by the continued growth of frost on the substrate at a velocity of order 1 μm/s (Figure 4.5G and Supplementary Figures C.10 and C.11). This rate of frost growth is about two orders of magnitude slower than that of the freezing front, and can therefore be neglected aside from noting that the location of h_f slowly translates upward with the growing frost.

4.4.3 Marginal regeneration

Once a bubble reached its partially frozen equilibrium, initially there was no appreciable flow in the upper liquid portion of the bubble. After about 100 s, there was a sudden reappearance of plumes within the liquid dome (see Supplementary Figure C.4B). In contrast to the Marangoni freezing-induced plumes that were observed on initial deposition, these new plumes were because of marginal regeneration.

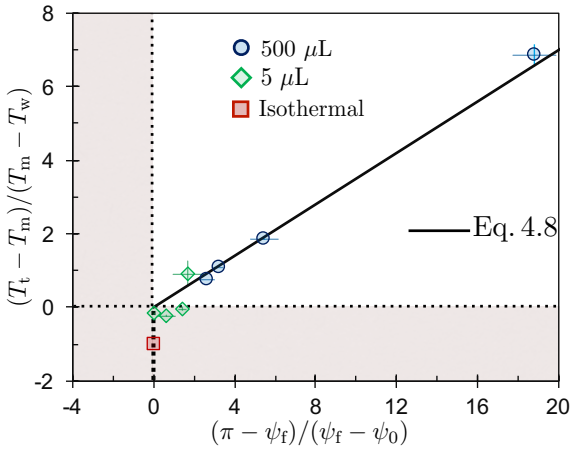

FIGURE 4.6: Partial freezing of bubbles. The critical angle at which the freeze front completely stops was found by balancing the conduction of heat across the icy and liquid portions of the bubble (Equation 4.8). The isothermal condition corresponds to the vertical dashed line, where complete freezing occurs ($\psi_f = \pi$, square data point).

Specifically, the ice-liquid boundary continually thickened at the expense of the top of the liquid dome due to drainage. This was visually evident from the appearance of interference fringes on the thinning liquid dome. The time scale of the formation of these plumes is consistent with the drainage time scale: $t_d \sim (\eta R)/(\rho g b^2) \sim 10^2 - 10^3$ s for $R \sim 1$–10 mm [167].

4.4.4 Collapse

After $\mathcal{O}(10\,\text{min})$ of partially frozen equilibrium, the liquid dome suddenly deflated and collapsed (Figure 4.7A,B). The time scale from beginning to end of the collapse ranged from $\sim 0.1 - 10$ s, depending on the trial. This gradual deflation of the liquid dome over a span of several seconds is in sharp contrast to the dynamics of drainage-induced failure, where a hole opens and rapidly spreads (Figure C.12). One possibility for the collapse is that the gradual cooling of the air within the bubble leads to a reduced internal pressure, as per Gay-Lussac's law [167]. However, for the typical value of thermal diffusivity of water/vapor with respect to air, $\alpha_v \sim 10^{-5}$ m^2/s, the

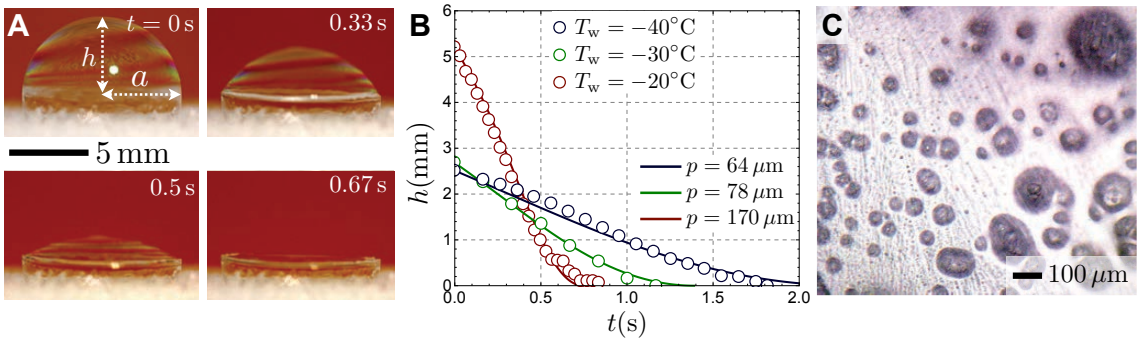

FIGURE 4.7: Collapse of the liquid dome of partially frozen bubbles. A) The sudden collapse of the liquid roof of a partially frozen $\Omega = 500$ μL bubble. Time zero corresponds to the beginning of dome collapse, which was completed in under 1 s. Conditions were $T_w = -20\,°C$, $T_\infty = 24.56\,°C$, and $RH = 58.8\%$. B) The height of the liquid dome (h) against time for different substrate temperatures, for $\Omega = 500$ μL bubbles. Solid lines correspond to the theoretical drainage model provided by Equation 4.10, for the best-fit values of p shown in the legend. C) Microscopy revealed discontinuities on the frozen portion of the bubble ($\sim 10 - 100\,\mu$m), responsible for gradually draining out the pressurized air from within the bubble.

thermal diffusion time scale of $\tau_D \sim R^2/\alpha_v \sim 0.1$ s is too fast given that the liquid remains dome-shaped for about 10 min.

Instead, consider the positive Laplace pressure of the air within the bubble, due to the convex curvature of the liquid dome. This pressure difference is given by $\Delta P = 4\gamma/r$, where $r = (a^2 + h^2)/2h$ is the liquid's radius of curvature, a is the fixed contact radius of the liquid/ice interface, and h is the height of the liquid dome (see Figure 4.7A). If the frozen portion of the bubble included small pores, this Laplace pressure would cause air to flow out of the pores with a dynamic pressure of $\frac{1}{2}\rho_{air} v_{air}^2$. Following Bernoulli's law, we can equate the dynamic pressure with the Laplace pressure to obtain:

$$v_{air} \approx \sqrt{\frac{16\gamma h}{\rho_{air}(a^2 + h^2)}}. \tag{4.9}$$

By mass conservation, $-dV/dt \sim \pi p^2 v_{air}$, where $V = (\pi h/6)(3a^2 + h^2)$ is the volume of the liquid spherical cap and p is the pore radius. Taking the derivative of

the volume with respect to h, the change in height of the liquid dome with respect to time is:

$$dh/dt \approx -8p^2\sqrt{\frac{\gamma h}{\rho_{\text{air}}(a^2+h^2)^3}}. \tag{4.10}$$

The density of the air inside a bubble was found by using the ideal gas law, $\rho_{\text{air}} = P/(R_s T_{\text{air}})$, where P is the absolute pressure, $R_s = 287.058$ J/kg K is the specific gas constant, and T_{air} is the average temperature inside the bubble which was calculated from the computational results (Figure C.8). These values of T_{air} were used to obtain $\rho_{\text{air}} \approx 1.27$ kg/m^3, 1.28 kg/m^3, and 1.29 kg/m^3 for different substrate temperature of $T_{\text{w}} = -20\,^{\circ}$C, $-30\,^{\circ}$C, and $-40\,^{\circ}$C, respectively. Choosing values for p that obtained a best fit to the experimental data results in $p \sim 10 - 100$ μm (Figure 4.7B), consistent with the size of porous features observed within the ice (see Figure 4.7C).

As evidenced by Figure 4.7C, it is possible that multiple pores exist, in which case $p^2 = N{p_{\text{avg}}}^2$ where N is the number of pores and p_{avg} is the average pore diameter. For a minority of the room temperature experiments, the liquid dome of the partially frozen bubble ruptured before the Laplace-induced collapse could occur (see Figure C.12). The time scale of bubble rupture ($\sim$1 ms) is much faster that the collapse event discussed here, further demonstrating that the collapse mechanism is fundamentally different from film rupture.

Figure 4.8 summarizes every mode of freezing in a comprehensive phase map for any possible ambient condition. The unfrozen region corresponds to the case where the substrate temperature is warmer than the melting temperature of the soap solution, preventing the heterogenous nucleation of a bottom-up freeze front. Partially frozen bubbles occur when the top of the bubble is warmer than the melting temperature, while the substrate temperature is below. Completely frozen bubbles are observed when both the surface temperature and the temperature at the top of the bubble are subfreezing ($T_{\text{t}} < T_{\text{m}}$ and $T_{\text{w}} < T_{\text{m}}$). In this region the "Snow-Globe

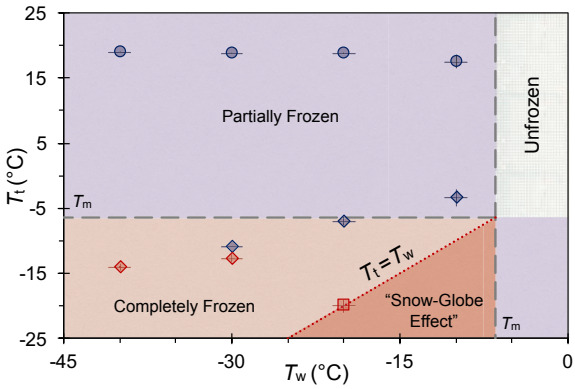

FIGURE 4.8: Regime map of different kinds of freezing behavior in soap bubbles. Bubbles completely freeze in the red regions ($T_t < T_m$ & $T_w < T_m$), while a partially frozen equilibrium occurs for bubbles in the purple area ($T_t > T_m$). The dark red region is a subset of the 'Completely Frozen' regime, where the Marangoni freezing is able to produce the "Snow-Globe Effect" due to the added criterion of $T_t \leq T_w$. Blue and red data points correspond to experimentally observed partially frozen or completely frozen bubbles, respectively, where the enclosed air volumes were either 5 μL (diamonds), 500 μL (circles), or 10 mL (square). Long dashed lines correspond to $T_t = T_m$ and $T_w = T_m$, while the dotted line corresponds to using an isothermal freezer.

Effect" is observed when $dT/dz \leq 0$, or in other words, $T_t \leq T_w$ (see diagonal line and the dark red region). This condition is satisfied inside the walk-in freezer, where the substrate temperature was equal to the temperature at the top of the bubble. Note that all types of freezing tended to produce some degree of flow due to Marangoni freezing, even though the "Snow-Globe Effect" only occurred for the isothermal case.

Finally, control tests were performed with a 1% concentration of a pure surfactant, solium dodecyl sulfate (SDS), rather than 1% dish soap. Bubbles with SDS bursted within $\mathcal{O}(10\,\text{s})$ upon deposition on an icy substrate in room temperature conditions (Figure C.13), most likely due to drainage. This drainage time scale is consistent with a previous report [167]. During the short time where the bubble was intact, the bottom-up freezing dynamics were equivalent to that with the dish soap. For the isothermal conditions, $\Omega = 500\,\mu$L bubbles containing SDS burst within $\mathcal{O}(1\,\text{s})$.

In conclusion, the freezing dynamics of soap bubbles are multifaceted and fun-

damentally distinct from the classically studied scenario of freezing bulk volumes of liquid. Under chilled and isothermal conditions, hundreds of ice particles are detached from the freeze front and swirl around the bubble in a "Snow-Globe Effect." This beautiful dance was caused by the local input of latent heat at the freeze front, causing a strong Marangoni flow capable of breaking off small ice crystals. Isothermal bubbles therefore freeze very efficiently due to hundreds of fronts growing in tandem and interlocking together. When a bubble is frozen on a cold stage in a room temperature environment, the freeze front slowly propagates upward and comes to a complete stop at a critical height. The freeze-front dynamics were found to be captured by a Stefan problem governed by a balance between latent heat and conduction across the frozen and unfrozen portions of the bubble. After the halting of the freeze front, the partially frozen bubble remains in equilibrium for many minutes, followed by the deflation and collapse of the liquid dome due to its Laplace pressure forcing air through small pores in the ice. These findings show that the dynamics of freezing liquid is highly dependent on its geometric conditions, and that a rich variety of multiphase phenomena occur when a liquid volume is neither continuous nor surface-bound.

4.5 Materials and methods

4.5.1 Materials

The soap bubbles were generated using a solution consisting of 79% (by volume) distilled water, 20% glycerol (Sigma-Aldrich, 56-81-5), and ≈1% dish soap (Palmolive®, Ultra AntiBacterial Dish Liquid). The dish soap consists of 98% inert ingredients (water, sodium laureth sulfate, lauramidopropyl betaine, sodium dodecylbenzene sulfonate, SD 3A alcohol, sodium xylene sulfonate, fragrance, tetrasodium EDTA,

and dyes), and 2% active ingredient (L-Lactic acid). For the control experiments, instead of dish soap, sodium dodecyl sulfate (Sigma-Aldrich, 75746) was used. After stirring the mixture together, it was allowed to sit overnight before running any experiments. Neglecting the effects of the soap, the freezing temperature of an 80-20% water/glycerol mixture was previously reported [183] to be $T_{\mathrm{m}} \approx -6.5\,^{\circ}\mathrm{C}$.

For the room temperature experiments, bubbles were deposited on a frosted Peltier stage (ramé-hart, Model 100-30) using a syringe pump (ramé-hart, Model 100-22). A needle with inner and outer diameters of 0.7 mm and 2.1 mm, respectively, was used. Experiments were recorded using a DSLR camera (Canon®, EOS 5D Mark III) with a macro lens (Canon MP-E 65mm f/2.8 1-5X). After freezing, the pores and/or bubble trapped within the ice were characterized using a top-down optical microscope (Nikon 150LV) with a long working-distance lenses (Mitutuyo, MPlan APO).

For the isothermal experiments, a polystyrene petri dish (VWR, 25384-326) was filled with distilled water and left in a freezer (Frigidaire, Model FRT21IL6JB2) with a temperature of $-20\,^{\circ}\mathrm{C}$ overnight. Ice disks were kept within a cooler (Igloo®) when transporting to the walk-in freezer (Conviron, Model C1008). An ice disk was allowed to sit within the walk-in freezer for at least an hour before beginning experiments, to ensure that its temperature was that of the air. For some control experiments, the bubbles were deposited on a dry silicon substrate rather than an ice disk. Experiments were recorded using a high-speed camera (Vision Research, Phantom v711). The relative humidity and air temperature of the walk-in freezer were measured by a hygrometer (E+E Elektronik, Model EE210). Thermal imaging experiments were conducted using an IR camera (FLIR SC655).

4.5.2 Lighting

For the room temperature experiments, a spotlight was used for front lighting (Advanced Illumination, Model SL164) while a square LED was used for a backlight (Advanced Illumination, Model BX0808). When imaging a frozen bubble with the top-down microscope, LED lighting was used to minimize heating effects (Nikon, LV-UEPI Universal Epi Illuminator 2). For the isothermal experiments, a round LED light (Genaray, Model SP-AD75) was placed underneath the ice disk with a horizontal orientation to illuminate the bubble (see Figure C.2A). Plumes (Figures 4.4 and C.4) were visualized using a LOWEL DP light which was kept about 5 m away from the experimental set up to minimize heating effects.

4.5.3 Image processing

Videos were imported to an open-source software (Tracker) to track three points (left most, right most, and center) of the freezing bubbles. The coordinate system was placed such that the y-axis crossed the center of the bubble while the x-axis was placed at the contact line of the bubble/substrate interface. The final angle at which the freeze front stopped propagating was found by importing the corresponding image to ImageJ.

5

Ice Wicking

"When a thing is wick, it has a life about it."

– The Secret Garden - Wick

The content of this chapter was previously published as a journal manuscript in [196], and reproduced here with minor modifications. In this chapter the capillary action of a liquid wicking across the surface of ice will be discussed.

5.1 Introduction

How liquids interact with ice is relevant to a wide variety of natural and engineered systems. Hydraulic fracturing is increasingly occurring in arctic regions; understanding how pressurized liquids and oil flows interact with ice-rich permafrost is therefore important from both environmental and economic standpoints [197, 198]. Oil spills in arctic regions interact with glaciers and ice sheets (Figure 5.1A) [199–201]. In winter months, rain drops often impact ice or snow, which affects their spreading

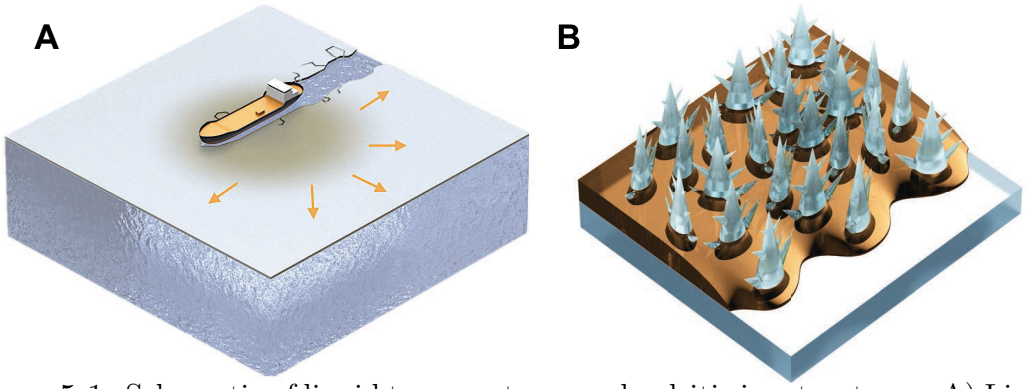

FIGURE 5.1: Schematic of liquid transport across dendritic ice structures. A) Liquid-ice interactions are relevant to a myriad of systems such as oil spills (pictured above), arctic drilling, rain impacting icy ground, or liquid-impregnated surfaces. B) An unexplored mechanism driving liquid transport across dendritic ice structures is capillary action.

behavior prior to freezing [202, 203]. Liquid-ice interactions are also important for the emerging science of using liquid-impregnated surfaces [204, 205] for anti-icing and anti-frosting applications [94, 115, 116, 206], where liquid drainage from the surface due to wicking onto ice is a pressing issue [108, 118].

Despite the increasing importance of these liquid-ice interactions, a fundamental understanding of how liquids spread across ice remains lacking. Many papers and reports posit methods for recovering oil from water and/or ice [207, 208], but are not concerned with the physics of the oil spreading in the first place. Some reports simply measure the spreading rates and/or encapsulation volumes of oil on ice, without controlling any parameters or providing any physical models [200, 201]. Various mechanisms for oil spreading on ice have been posited and modeled, including gravitational spreading, spreading by wetting until reaching an equilibrium contact angle, buoyant encapsulations into ice fissures, and drifting of the ice sheets themselves [209–211]. But capillary action across the dendritic surface of ice/frost, curiously, has never been studied to our knowledge.

For virtually all forms of ice and frost, their outermost structure is comprised

of dendritic ice crystals [212, 213]. The shape, size, and density of these dendrites will govern how a liquid wicks across an icy surface (Figure 5.1B). Previous research has shown that the morphology of frost varies widely depending upon the underlying surface wettability [102, 141]. This is because frost grows by a process known as condensation frosting, where supercooled condensate nucleates on the surface in a manner highly dependent upon surface wettability, which later freezes into the foundational frost structure [4].

In this paper, we characterize the capillary action of silicone oils wicking across the dendritic surface of ice. To vary the morphology of the dendrites, frost sheets of differing thicknesses were grown on aluminum surfaces that were either superhydrophilic (SHPL), hydrophilic (HPL), hydrophobic (HPB), or superhydrophobic (SHPB). To determine whether liquids can wick inside of bulk ice, a second set of experiments was performed using a column of frozen water.

5.2 Experimental methods

5.2.1 Surface fabrication

The dendritic structure of frost sheets was varied by tuning the wettability of the underlying aluminum surface. The nanostructure required to promote the SHPL surface was generated by dipping the aluminum in hot water (70 °C) for 10 min, which imparts an aluminum hydroxide nanostructure [214]. The HPL surface was simply the untreated aluminum plate. To render aluminum HPB, a monolayer of trichloro(1H,1H,2H,2H-perfluorooctyl)silane (Sigma Aldrich) was coated by vapor-phase deposition. Finally, SHPB aluminum combined the aluminum hydroxide nanostructure of the SHPL surface with the same silane coating as the HPB recipe [215]. Silane coatings are not durable under long-term tests [126], but are adequate

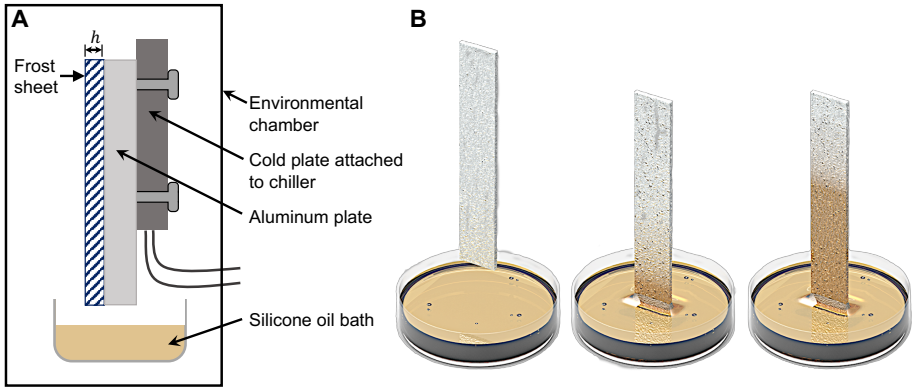

FIGURE 5.2: Experimental setup of the ice wicking. A) Side view of the experimental setup in an environmental chamber. B) Depiction of dipping a vertically oriented sheet of frost into an oil bath to observe ice wicking.

for the fundamental laboratory characterizations performed here. Regardless of wettability, the dimensions of each aluminum plate were 20.3 cm × 7.6 cm × 1.3 cm.

5.2.2 Dendritic ice setup

Experiments were conducted in an environmental chamber (Electro-Tech Systems, Model 5503) where the humidity could be adjusted and the temperature could be monitored (Figure 5.2A). The backside of a vertically-oriented aluminum plate was bolted to a cold plate held to $T_w = -5\,°C$ by a circulating chiller (Thermo Scientific, Accel 500 LT). A thin layer of thermal paste was spread between the cold plate and aluminum plate to minimize thermal losses.

To grow frost, the supersaturation in the chamber was set to $S = 3$. The temperature in the environmental chamber was $T_\infty = 12\,°C$, so the humidity was set to $RH = 90\%$ to achieve $S = 3$. The frost growth was monitored from the side using a digital camera (Nikon D5300) to measure the evolving thickness of the frost sheet over time. Once the frost sheet was grown to the desired thickness ($h = 1$ mm or 3 mm), the humidity was lowered to $RH = 30\%$ to attain $S = 1$. This ensured that the frost layer was neither growing nor shrinking for the subsequent wicking

experiment.

Silicone oil of viscosity 10 cSt or 100 cSt (Sigma Aldrich) was mixed with 0.1 % by volume of fluorescent dye (Risk Reactor, DFSB-175). A plastic container holding 40 mL of dyed silicone oil was positioned underneath the bottom of the frosted aluminum plate. After allowing the oil bath to submerge the bottom edge of the aluminum plate, oil continuously traversed up the frost by capillary action (Figure 5.2B). A UV lamp was directed at the front face of the plate to fluoresce the oil. The Nikon camera was positioned on a tripod to capture the oil wicking up the front face of the frosted aluminum. A picture was captured every 30 s for the 10 cSt oil and every 60 s for the 100 cSt oil for a total time of 3 hr.

To obtain displacement versus time curves, the oil front was measured using the open-source Tracker software along three vertical lines distributed evenly across the front face of the plate. Wicking along the vertical edges of the front face were ignored due to edge effects that affected the condensation [124] and subsequent frost growth. Two clamps were blocking the view of the wicking front near the bottom of the plate along the edges, further motivating the avoidance of tracking the edges. The displacement was averaged across the three reference lines to provide an effective value for each time stamp. One trial was performed for all 16 combinations of surface wettability, frost thickness, and oil viscosity. To confirm that using a single trial for each combination is sufficient, three completely separate trials were conducted for the case of 10 cSt oil wicking up 1 mm thick frost on the HPB plate, with no appreciable difference in performance between trials.

5.2.3 Bulk ice setup

A second set of experiments was performed using a column of frozen water to determine if oil can wick inside of bulk ice. A 14 cm × 14 cm × 5 cm watertight aluminum chamber was machined which included detachable panels on the front and bottom

faces of the chamber. By closing the front panel but removing the bottom panel to expose a hole 1.3 cm in diameter, the chamber was turned upside down and filled with distilled water. The chamber was then sealed, turned right side up, and its back face was bolted to a cold plate held to $T_w = -5\,^{\circ}\mathrm{C}$ using the circulating chiller. After the water was completely frozen, both panels were removed. Removing the side panel exposed a hole of dimensions $11.4\,\mathrm{cm} \times 1.0\,\mathrm{cm}$ running vertically along the center of the chamber's front face. The bottom of the chamber was suspended over the same fluorescent oil bath used in the first set of experiments. The oil bath was raised until submerging the hole in the bottom of the chamber. The digital camera and UV lamp were directed at the opened front face of the chamber, to visualize whether any oil was able to wick up the column of ice via the hole in the bottom of the chamber. To complement the time-lapse images from the camera, the oil bath was placed on a digital mass balance to track its change in mass over time.

5.3 Results and discussion

5.3.1 Dendritic ice

Figure 5.3 visualizes the morphology of frost growing on aluminum plates that were either HPL, HPB, or SHPB. By employing side-view imaging during the earliest stages of frost growth, the geometry of individual dendritic structures can be clearly visualized (Figure 5.3A). Regardless of the surface wettability, the dendrites contained side branches which typically were angled upward with respect to the horizontal.

Although individual dendrites looked similar across all surfaces, when zooming out to a larger field-of-view, the effects of wettability became apparent (Figure 5.3B). Namely, the continuity of the frost features decreased considerably with decreasing surface wettability. The HPL surface promoted supercooled filmwise condensation that froze into continuous ice sheets [141]. During frost growth, dendritic structures

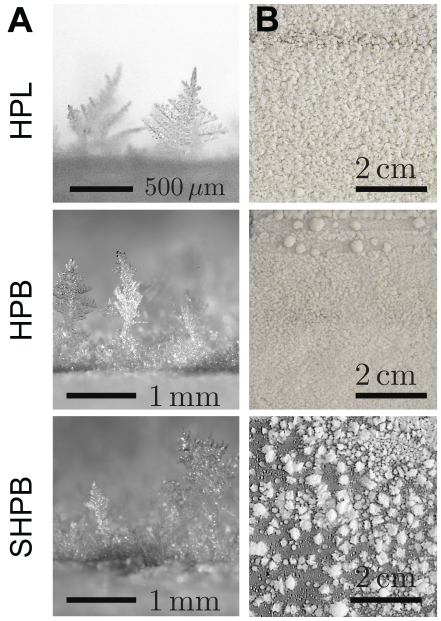

FIGURE 5.3: Morphology of ice dendrites. A) Side-view imaging of individual ice dendrites after $t \sim 10\,\mathrm{s}$ of frost growth. The surface temperature was $T_\mathrm{w} = -30\,^\circ\mathrm{C}$ with ambient conditions of $T_\infty \approx 23\,^\circ\mathrm{C}$ and $RH \approx 54\%$. B) For 3 mm thick frost sheets, top-down imaging reveals that the overall frost morphology varies dramatically for HPL, HPB, and SHPB surfaces.

grew uniformly atop the ice sheet. In contrast, the non-wetting HPB surface promoted dropwise condensation which froze into ice droplets connected by inter-droplet ice bridges [102,103]. Given that ice is hygroscopic [123], the subsequent out-of-plane frost growth was concentrated atop the frozen droplets (and ice bridges), leaving dry zones about the surrounding areas [86, 125]. The chilled SHPB surface promoted jumping-droplet condensation [14], which minimized both its droplet size distribution and the success rate of inter-droplet ice bridges [102]. As a result, many frozen droplets were both small and isolated from each other, resulting in maximal dry zones between sparse features that attracted most of the dendritic growth.

Figure 5.4A depicts the capillary action of 10 cSt silicone oil wicking up 3 mm thick frost sheets grown on all four different aluminum substrates: SHPL, HPL, HPB, and SHPB. The wicking rate was similar for the SHPL and HPL surfaces, which makes

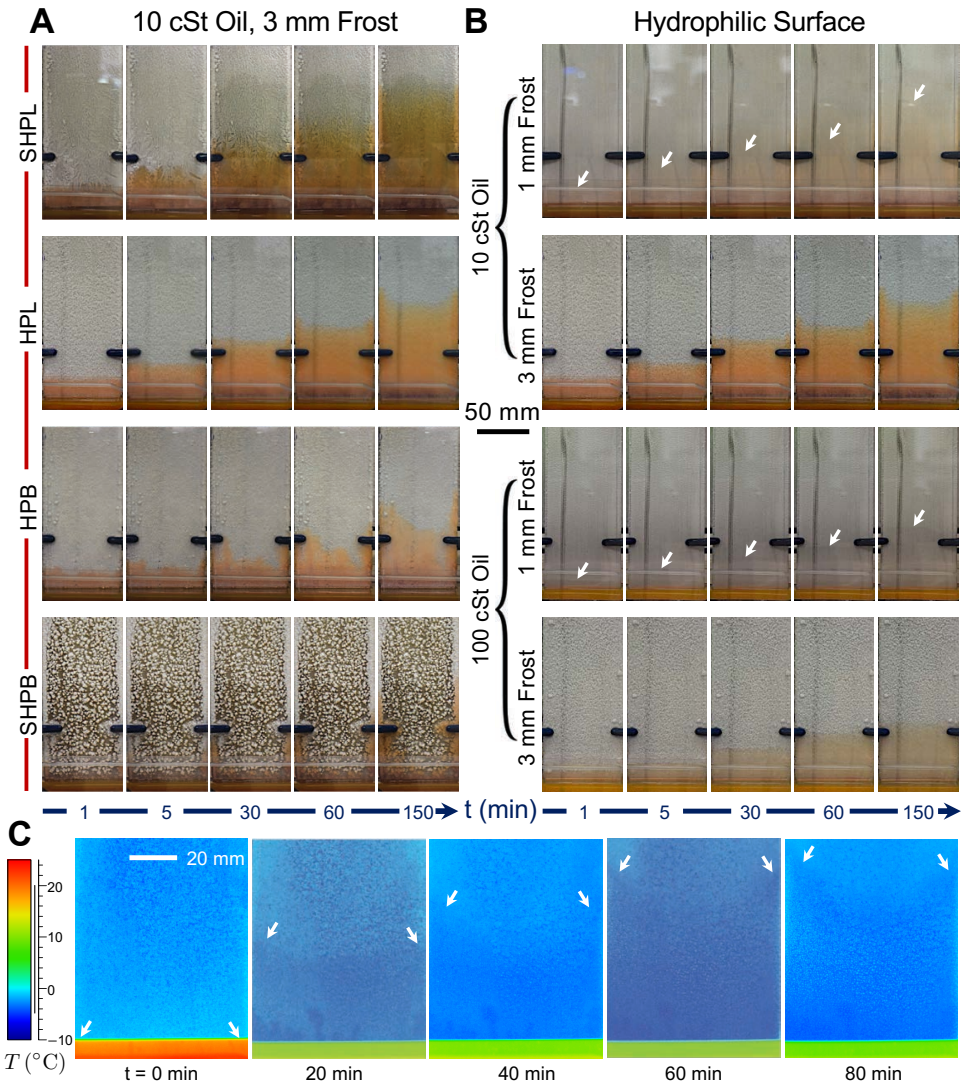

FIGURE 5.4: Wicking rates of silicone oils up frosted aluminum plates. Wicking rates of silicone oils up frost sheets grown on vertically oriented aluminum plates held to $T_w = -5\,°C$. A) 10 cSt silicone oil wicking up 3 mm thick frost sheets, for wettabilities ranging from SHPL to SHPB. B) Silicone oil wicking across frost grown on a HPL aluminum plate, where the oil viscosity and frost thickness were varied. See supplemental movies 1 and 2 for the wicking dynamics corresponding to (A) and (B). C) Time-lapse thermographic images of 10 cSt silicone oil wicking up a HPL surface covered with 3 mm of frost. The substrate was chilled to $T_w = -10\,°C$ while the ambient conditions were $T_\infty \approx 23\,°C$ and $RH \approx 65.6\%$. The emissivity coefficient of ice was calibrated to $\epsilon = 0.98$. White arrows were added digitally to b) and c) to help visualize the location of the wicking front.

sense given that both of these surfaces grew dendrites from a uniform film of frozen condensate. For the HPB and especially the SHPB surfaces, the aforementioned discontinuities in dendritic growth resulted in a more tortuous pathway for the liquid during ice wicking. As a result, the wicking rate was slower for the HPB and ground down to a near-halt on the SHPB surface.

In Figure 5.4B, the surface wettability was always HPL while the oil viscosity and frost thickness were now varied. As expected, 10 cSt silicone oil wicked considerably faster than the 100 cSt oil. The frost thickness had a more subtle effect, with 1 mm thick frost wicking slightly faster than the 3 mm frost. Dendritic structures become more sparse with increasing height, particularly in our case when the air was much warmer than the substrate. Therefore the faster wickability of the thinner frost sheet can be rationalized by the fact that its dendritic structure is more dense than the top portion of a taller frost sheet.

It is prudent to check whether the oil is warming or even melting the frost during wicking. An IR camera (FLIR SC655) was used to measure the temperature profile during the wicking of 10 cSt oil up 3 mm thick frost on a HPL substrate. The IR camera could not fit within the environmental chamber, so an open environment was used. The ambient conditions corresponded to a supersaturation of $S \approx 6$ with respect to a substrate temperature of $T_{\mathrm{w}} = -10\,^{\circ}\mathrm{C}$, such that the frost was still growing during wicking. Given that the difference in wicking between the 1 mm and 3 mm frost sheets was minor, we do not anticipate that the slight growth of the 3 mm frost during the IR experiment will have any appreciable effect. The IR imaging revealed that the oil reservoir cooled down by about 10 ° due to its contact with the bottom of the chilled aluminum plate; however, the temperature of the frost itself was always subfreezing and actually cooled by a few degrees when exposed to the oil (Figure 5.4C). This is because the thermal conductivity of silicone oil is an order of magnitude larger than air, such that submerging dendrites in oil reduces

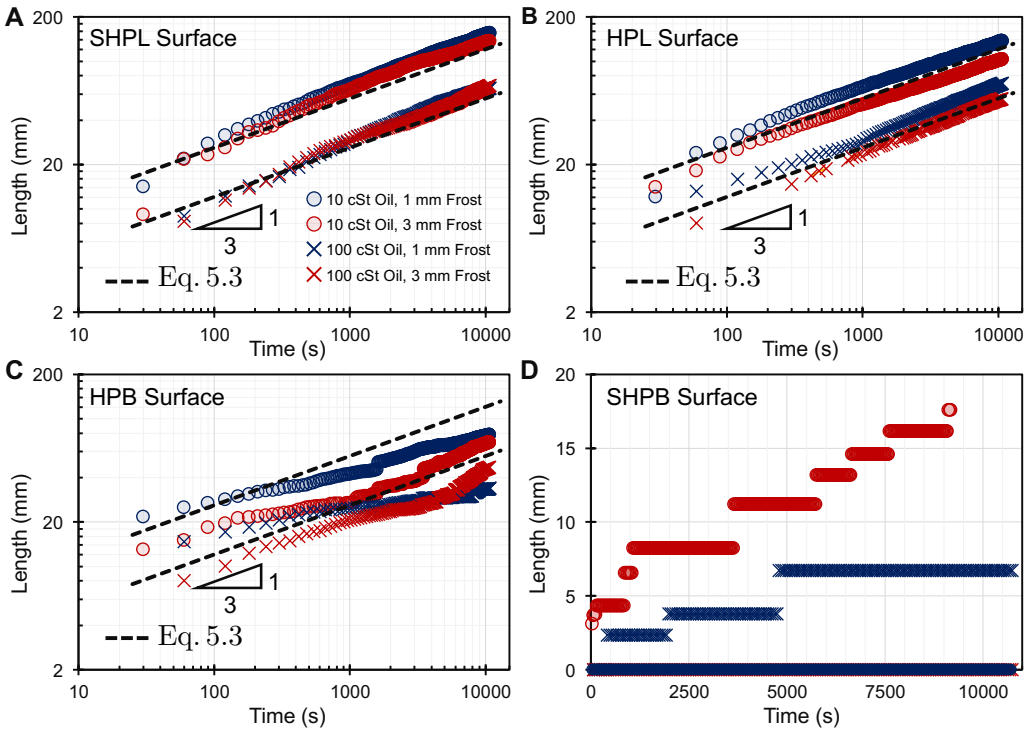

FIGURE 5.5: Displacement vs. time for silicone oils wicking up frosted surfaces. Displacement vs. time for silicone oils wicking up vertically oriented frost sheets. A,B) The oil displacement for frost grown on SHPL and HPL surfaces follows a 1/3 power law slope, in agreement with Equation 5.3 which models wicking up vertical arrays of corners. C) The oil displacement for frost grown on HPB aluminum decays beneath this 1/3 power law, due to the non-uniform coverage of the frozen dropwise condensation. D) For frost grown on SHPB surfaces, the oil either did not wick at all or only in slow increments due to the dilute coverage of jumping-droplet condensation. Dashed lines in (a–c) all correspond to Equation 5.3 for $\beta = 0.4$.

their thermal resistance. The temperature of the silicone oil within the frost was approximately constant (i.e. within a couple of degrees of $T_w = -5\,^{\circ}\mathrm{C}$), indicating that its viscosity was not changing appreciably with height.

For conventional porous structures, the capillary action of a liquid can be understood as a competition between surface tension and viscous dissipation. The classical Lucas-Washburn equation represents this balance as:

$$L(t) = \sqrt{\frac{\gamma R_{\mathrm{eff}} \cos\theta}{2\eta}} t^{1/2}, \tag{5.1}$$

where L is the displacement of the liquid front over time, γ and η are the surface tension and viscosity of the liquid, R_{eff} is the effective pore radius, and θ is the liquid's intrinsic contact angle with the surface. For many wicking materials, including ice [216], the wettability approaches $\cos\theta \approx 1$ which simplifies the equation. We deposited a $10\,\mu$L droplet of silicone oil on a smooth icy substrate and observed that it completely flattened into a thin film, confirming that $\theta \approx 0°$.

In Figure 5.5, we graph the displacement curves for all 16 combinations of surface wettability (SHPL, HPL, HPB, or SHPB), oil viscosity (10 cSt or 100 cSt), and frost thickness (1 or 3 mm). For each data series, a best-fit was obtained for a power law slope α, where $L \propto t^{\alpha}$. Surprisingly, none of the 16 trials promoted wicking that obeyed Washburn's law of $\alpha = 1/2$. Instead, the power law slopes averaged for each surface wettability were $\alpha = 0.34 \pm 0.05$ for the SHPL surface, $\alpha = 0.34 \pm 0.06$ for the HPL surface, and $\alpha = 0.3 \pm 0.2$ for the HPB surface.

The slightly smaller value of α for the HPB surface, and its much larger variability across trials, is readily explained by the discontinuous profile of dendrites growing atop a frozen population of dropwise condensation. Indeed, for the case of the SHPB surface where the density of frozen droplets and inter-connected ice bridges was even more dilute, the power law slope was effectively $\alpha = 0$ for the majority of the time. There were only occasional jumps in displacement in cases where the oil could reach the next row of droplets via inter-droplet ice bridges.

Focusing then on the SHPL and HPL surfaces, the primary mystery is why wicking across uniform frost sheets resulted in $\alpha \approx 1/3$ rather than the $\alpha \approx 1/2$ prescribed by Washburn's Law. Recall that Washburn's law assumes that the porous media is able to support the weight of the imbibed liquid, such that only capillarity and viscous dissipation are at play. However, not all geometries can support a liquid's weight, with vertically-oriented capillary tubes [217] or corners [218, 219] being two well-known examples. In such cases, the capillary rise is restrained by gravity in

addition to viscosity, which modifies the governing equation. Looking carefully at the slopes in Figure 5.5A,B during the first 100 s of wicking, they appear to be larger than the average value of $\alpha \approx 1/3$, indicating that gravity is indeed playing a role after a moderate height rise.

Looking carefully at Figure 5.3A, the side branches extending from each mother branch resemble a close-packed array of corners. Therefore, we will briefly summarize the findings of Ponomarenko, Quéré, and Clanet on capillary rise up corners [219] to see if this can rationalize our results. Accounting for the effects of gravity, they developed the following governing equation:

$$\frac{\gamma}{r h_r} \sim \rho g + \eta \frac{\dot{h}_r}{r^2}, \tag{5.2}$$

where ρ is the liquid density and $h_r(r,t)$ is the location of the liquid front where r is the radius of an imaginary vertical tube that fits within the corner. Integrating and solving for the maximal height h of the meniscus, they found a universal scaling law independent of the corner geometry:

$$h(t) \approx \beta \left(\frac{\gamma^2 t}{\eta \rho g} \right)^{1/3}, \tag{5.3}$$

where β is a numerical pre-factor. We also note that Equation 5.3 was independently observed for wicking up an array of parallel micro v-grooves [220], which is more directly analogous to dendritic structures than the former case of a single continuous corner. Even if the complex structure of dendritic ice is an amalgam of both corners and closed channels, the $t^{1/3}$ law in the corners will dominate the $t^{1/2}$ law in the channels due to gravity stopping the Lucas-Washburn front before it can overtake the front in the corners [219].

This scaling law of $t^{1/3}$ is a perfect match to the $\alpha \approx 1/3$ observed here for the continuous frost sheets, confirming that the geometry of ice dendrites can be

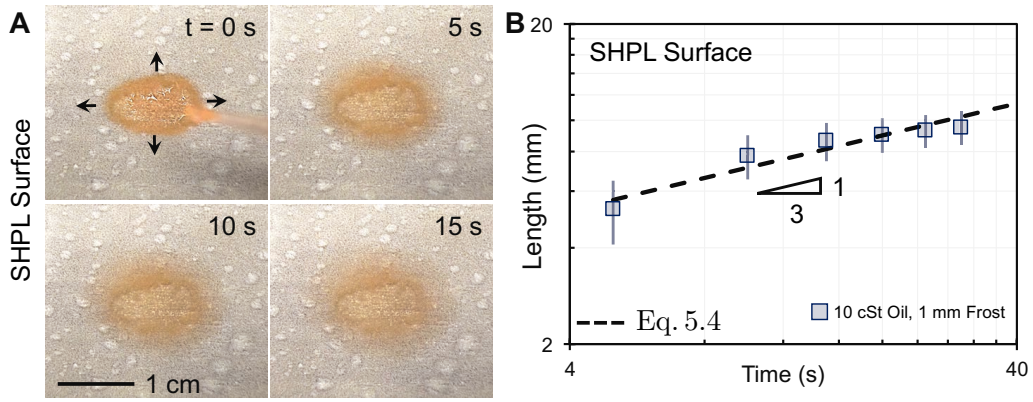

FIGURE 5.6: Radial spreading of silicone oil on a frosted horizontally-oriented surface. A) Radial spreading of a 50 μL droplet of 10 cSt silicone oil on a horizontally-oriented SHPL substrate covered with a 1 mm tall frost sheet. B) The radial spreading of the droplet was measured every 5 s for 30 s by averaging the radial displacement on all four sides of the droplets. Error bars are one standard deviation of the average of the four measurements. The data obeys the $t^{1/3}$ power law predicted by Equation 5.4.

considered analogous to a series of corners. Indeed, when graphing Equation 5.3 for each oil viscosity in Figure 5.5, an excellent fit is obtained to the SHPL and HPL data when using a constant value of $\beta = 0.4$. For the 10 cSt silicone oil, the physical parameters were $\gamma \approx 20\,\text{mN/m}$, $\rho \approx 930\,\text{kg/m}^3$, and $\eta \approx 17.2\,\text{mPa·s}$. For the 100 cSt silicone oil, $\gamma \approx 20\,\text{mN/m}$, $\rho \approx 960\,\text{kg/m}^3$, and $\eta \approx 187\,\text{mPa·s}$. The near-constant value of γ is based off our previous measurements for silicone oils using the pendant drop method [221], while the values of ρ and η are from the manufacturer. The γ and ρ values correspond to room temperature values, which is a reasonable approximation given their weak dependence on temperature. The viscosity values, which do depend strongly on temperature, were given by the manufacturer corresponding to 0 °C to better approximate the conditions during the ice wicking.

Alas, the universality of capillary rise up corners does prevent us from extracting the effective pore size for the frost. However, a study by Warren [222] revealed that the radial spreading of a droplet along a horizontal surface of wedge-shaped

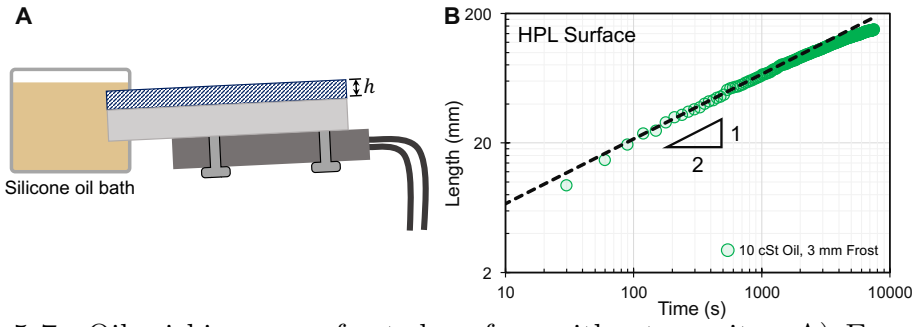

FIGURE 5.7: Oil wicking on a frosted surface without gravity. A) Experimental setup for connecting the bottom of a slightly-inclined frosted substrate to an oil reservoir. B) The displacement of 10 cSt silicone oil was measured every 30 s for over 2 hr by averaging three points (left, right, and center) of the oil/frost interface. The data obeys the $t^{1/2}$ power law predicted by Equation 5.1 (dashed line).

micro-grooves can reveal the characteristic groove spacing (l):

$$R(t) \sim \left(\frac{\gamma (l\Omega)^{1/2}}{\eta} \right)^{1/3} t^{1/3}, \tag{5.4}$$

where Ω is the finite droplet volume. In order to find l for our uniform frost sheets, a $\Omega = 50\,\mu$L droplet of 10 cSt silicon oil was deposited on a horizontally-oriented SHPL aluminum substrate covered with a 1 mm frost sheet (Figure 5.6A). As depicted in Figure 5.6B, the experimentally measured rate of radial droplet spreading was in good agreement with Equation 5.4 when $l \approx 138\,\mu$m. This is in excellent agreement with our experimental imaging (Figure 5.3A), which indicated that the side branches of dendrites formed wedges of a characteristic length scale $l \sim 100\,\mu$m.

If the surface is both horizontally oriented and connected to an infinite reservoir, Washburn's law should at last be reclaimed. A final experiment was therefore performed where the frosted substrate was only tilted by about 10° with respect to the horizontal, such that gravity is negligible for moderate oil displacements. The bottom end of the tilted aluminum plate was inserted into a snug hole cut into the side of the oil reservoir (Figure 5.7A). The HPL surface was used to ensure that the frost was as continuous as possible. The resulting displacement of 10 cSt silicone oil

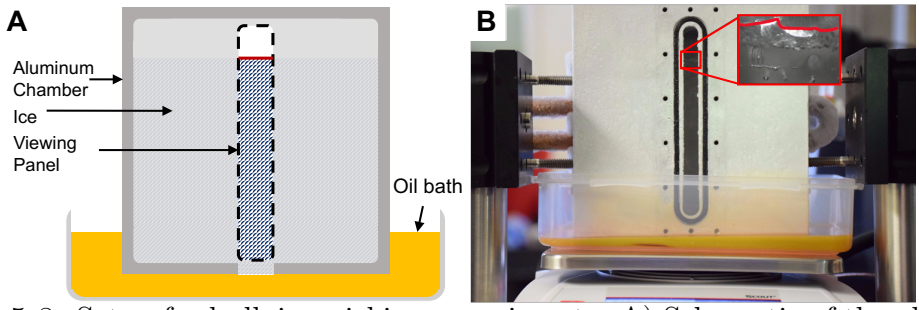

FIGURE 5.8: Setup for bulk ice wicking experiments. A) Schematic of the aluminum chamber containing frozen water. After freezing is complete, bottom and side panels are removed to expose the bottom of the ice column to an oil bath and a side wall of the ice column for imaging any resulting wicking. B) Photograph of the chamber full of ice and submerged in oil. The top of the ice column visible in the viewing window is outlined in the red inset.

across a 3 mm frost sheet was in perfect agreement with the Lucas-Washburn equation (Figure 5.7B) for an effective pore size of $R_{\text{eff}} \approx 8\,\mu$m. It makes sense that R_{eff} is smaller than l, as the former represents an amalgam of length scales formed by the hierarchical dendrites while the latter represents the extent of wedges formed by the primary branches.

5.3.2 Bulk ice

Having characterized ice wicking for the dendritic surfaces of ice, we now turn to bulk ice. As summarized in Experimental Methods, the bottom of a column of frozen water was submerged into an oil bath to observe whether oil could wick up the column. The side walls of the ice column were sealed off from its exposed bottom using an aluminum chamber, such that oil could only progress up the column by penetrating through the bulk ice itself. One side wall of the ice column was partially exposed for imaging via a removable panel (Figure 5.8A).

An issue that emerged was frost growing on the outside of the chamber walls, allowing oil to wick up the chamber from the outside. This can be seen in Figure 5.8B as an orange glow on the lower portion of the chamber's walls. To minimize this

issue, a thin sheet of UV transparent borosilicate glass with an O-ring glued around its perimeter was clamped to the front face of the chamber. The O-ring thermally insulated the glass sheet from the chilled aluminum chamber to prevent condensation or frost from growing on the glass. Frost growth was still unavoidable on other portions of the aluminum chamber, resulting in a total loss of about 2 g of oil from the bath due to wicking. However, the glass window prevented any frost near the exposed portion of the ice column, to ensure that any fluorescent oil in this region must correspond to bulk wicking through the column itself.

After suppressing the outer frost growth around the exposed ice column, imaging did not detect a rising oil front. The mass balance similarly did not register any loss in oil mass, apart from the aforementioned 2 g loss to frost on some outer portions of the chamber. To ensure that this 2 g did not correspond to any bulk wicking, a control experiment was performed where the bottom of the ice column was sealed from the oil bath during submersion. The mass balance still detected a final loss of 2 g of oil, indicating that this entire mass corresponds to wicking up the chamber's frost.

Atmospheric ice forms with a hexagonal lattice structure, which exhibits an effective pore radius of less than 1 nm [138]. In contrast, the molecular size of the silicone oil (estimated from the molar mass and density) was approximately 3 nm^3 for the 10 cSt sample and 19 nm^3 for 100 cSt. This explains why no oil was able to wick through the bulk ice column: the liquid molecules simply couldn't fit through the ice lattice. We therefore expect that for most liquids, wicking is not possible through bulk volumes of ice in the absence of appreciable fissures or grain boundaries.

5.4 Conclusion

By growing frost on an inclined substrate and submerging its bottom edge in oil, we captured the capillary action of liquids wicking across the dendritic ice. For continu-

ous frost sheets grown on superhydrophilic or hydrophilic surfaces, the displacement of oil obeyed a $t^{1/3}$ scaling law when the surface was vertically oriented. This was rationalized by considering that dendritic ice includes arrays of vertically oriented micro-grooves, which are well known to produce a universal $t^{1/3}$ law regardless of the specific geometry and shape of the structure. When the surface was tilted only slightly with respect to the horizontal, the displacement reverted to the classical $t^{1/2}$ Lucas-Washburn law. For frost sheets grown on hydrophobic or superhydrophobic surfaces, the dropwise or jumping-droplet modes of condensation frosting resulted in more dilute frost features capable of slowing or even halting the wicking rate.

In short, the capillary-driven transport of liquids across ice can be tuned by changing the surface orientation or the wettability of the underlying substrate. Capillary action is maximal for frost grown on a hydrophilic and horizontally-oriented substrate and minimal for a non-wetting and vertically-oriented substrate. The thickness of the frost sheets also played a secondary effect, with slightly faster wicking observed for shorter frost layers. Finally, we found that liquids are completely unable to penetrate (i.e. wick) into bulk volumes of frozen water due to the small pore size of ice's lattice structure. These findings should result in a better understanding of how liquids interact with icy surfaces for arctic drilling, hydraulic fracturing, or anti-icing liquid-impregnated surfaces.

6

Effect of Nano-Roughness on Jumping Droplet Condensation

"If you've got the feeling, jump up, touch the ceiling."

−House of Pain, excerpt from song 'Jump Around'

The content of this chapter was previously published as a journal manuscript in [121], and reproduced here with minor modifications. This chapter both experimentally and analytically studies the effect of height, diameter, and pitch of the nanopillars on the critical jumping diameter.

6.1 Introduction

For nearly a century, it has been known that dropwise condensation on a hydrophobic surface exhibits a heat transfer coefficient that is 5–7 times larger than filmwise condensation on a hydrophilic surface [223, 224]. This disparity can be understood by considering the liquid condensate as a thermal barrier between the steam and the substrate; filmwise condensation exhibits a continuous layer of water over the surface,

while dropwise condensation features discrete droplets and exposed portions of the wall [225]. Conventionally, sustained dropwise condensation has been accomplished by implementing a vertical surface orientation to enable gravitational removal [224]. The critical size of droplet departure, D_c, therefore scales to the capillary length: $D_c \sim (\gamma/\rho g)^{1/2}$, where γ is the liquid-vapor surface tension, ρ is the liquid density, and g is the gravitational acceleration [226, 227]. For the dropwise condensation of water, $D_c \sim 1\,\text{mm}$, which in the absence of non-condensable gas results in a maximal heat transfer coefficient of $k \approx 10-100\,\text{kW/m}^2\text{K}$ for steam pressures ranging from $P_\infty \approx 10-100\,\text{kPa}$ [126, 224, 228]. It has been demonstrated both experimentally and theoretically that the heat transfer coefficient of dropwise condensation increases linearly with decreasing droplet departure size, [229–231] but the practical necessity of gravitational forcing precludes any reduction in D_c beneath the capillary length scale.

In 2009, Boreyko and Chen discovered an entirely new mode of dropwise condensation that reduces the departing droplet size by several orders of magnitude compared to gravitational removal without requiring any external forces [14]. When dropwise condensate grows to $D_c \sim 10\,\mu\text{m}$ on a nanostructured or hierarchical superhydrophobic surface, the droplets are able to jump out-of-plane upon coalescence due to surface energy being converted to kinetic energy [14, 232]. It has already been experimentally confirmed that the reduced departure size of jumping-droplet condensation results in at least 30 % larger heat transfer coefficients than with dropwise condensation [233], and can even exhibit 60 % enhancement when adding hydrophilic patterns to accelerate droplet nucleation [234]. Jumping-droplet condensation is also useful for self-cleaning particulate matter [235–238], delaying frost growth [102, 157, 239], designing planar thermal diodes [240, 241], and hotspot cooling of electronics [242, 243]. Furthermore, many follow-up studies on jumping droplets have shed light into their incipient droplet growth [12, 13, 15, 16, 244–250],

hydrodynamics [215,251–267], directional jumping on microstructures, [268,269] heat transfer [101, 270–278], and electrostatic charge [279–282].

There is an emerging consensus that a superhydrophobic surface can only promote a suspended Cassie state for condensate (required for jumping) when the length scale of its surface features is of order 100 nm or smaller [12,13,247,283,284]. To understand why, first consider that nucleating embryos are generally around 1–10 nm in size, [133] such that they tend to nucleate within a unit cell of surface roughness and must be able to inflate over the surface to achieve the large apparent contact angles necessary for jumping [247]. Two conditions were attributed to a growing embryo being able to successfully inflate into a large contact-angle droplet: (1) The suspended Cassie state must be energetically favorable compared to the impaled Wenzel state, and (2) The nucleation density of the condensate must be smaller than the density of the surface features (to prevent flooding) [13]. While the first condition can sometimes be satisfied by microscale roughness in addition to nanoscale, the second condition only holds true for nanoscale features under typical thermodynamic conditions.

Despite this progress in understanding which surfaces tend to promote jumping droplets, to date it remains completely unknown how to predict the minimum jumping-droplet size (D_c) for a given substrate or to what extent its value could be tuned with changes in the surface structure. Previous reports which explicitly measured D_c utilized only one or two different surfaces that were highly disordered, [13, 16, 247, 248, 264] making it impossible to correlate D_c with the underlying nanostructure. The consistency of $D_c \approx 10\,\mu$m reported over a variety of surfaces makes it tempting to posit a viscous limit that is surface-independent, but this seems unlikely given that the Ohnesorge number $Oh \sim \mu/\sqrt{\rho\gamma D}$ predicts a viscous limit of $D_c \sim 10$ nm (for $Oh_c \sim 1$), which is three full orders of magnitude smaller. We therefore hypothesize that D_c is surface-dependent and jumping-droplet condensation can be further enhanced by tuning the underlying superhydrophobic nanostructure.

Here, we experimentally measure the critical jumping diameter of droplets on six different types of superhydrophobic nanopillars, and develop a theoretical model that successfully predicts D_c solely from the surface topography with no floating parameters. On our engineered surfaces, the minimum jumping diameter was observed to range widely from $D_c \approx 2\,\mu$m up to $D_c \approx 25\,\mu$m as the diameter, pitch, and height of the pillars were varied. By correlating a theoretical model with the experimental results and extrapolating to a wider variety of surface geometries, it is revealed that nanoscale jumping-droplet condensation should be possible when the pillars are sufficiently tall and slender. These findings reveal that, unlike dropwise condensation where $D_c \sim 1\,$mm is rigidly mandated by the capillary length, the minimum departure diameter of jumping-droplet condensation is a complex function of the surface topology and can be further reduced with continued advancements in nanofabrication.

6.2 Results and discussion

Superhydrophobic nanopillar arrays were fabricated by thermally dewetting platinum films on silicon wafers coated with SiO_2, which creates a non-lithographic etch mask [221, 285]. To generate six different nanopillar topographies, the thickness of the platinum film was varied to tune the average pillar diameter (d) and center-to-center pitch (l), while the height (h) of the nanopillars was tuned using different etch times in a reactive ion etcher. These nanopillar arrays were all rendered superhydrophobic by the vapor-phase deposition of a fluorinated silane. To controllably grow condensation, a given surface was horizontally oriented on a Peltier stage set to $T_s = 1\,^\circ$C inside of a custom-made humidity chamber (ramé-hart) with fixed relative humidity $RH = 50\%$ and air temperature $T_\infty = 16.5\,^\circ$C. The resulting condensation dynamics were captured using a high-speed camera attached to a top-down microscope with a 20X lens that looked through a quartz window outfitted at the top of

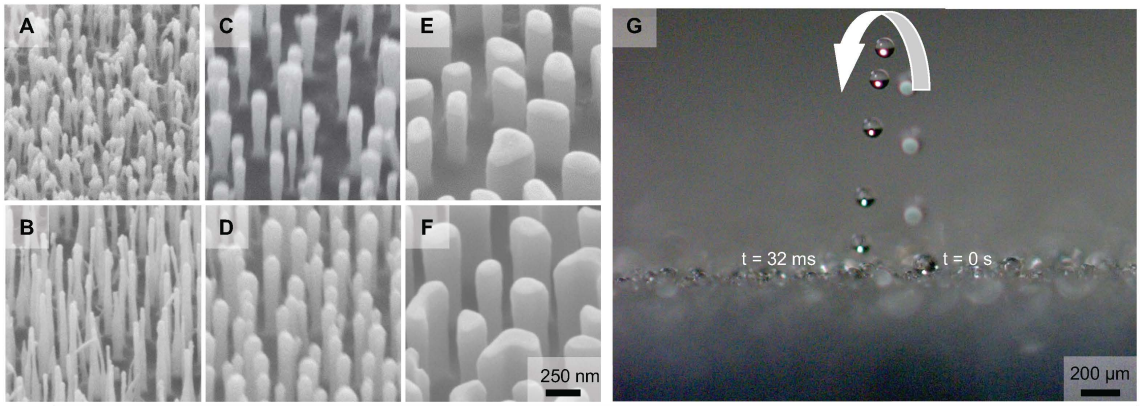

H

	Height, h (nm)	Average Pillar Diameter, d (nm)	Solid Fraction, φ	Pitch, l (nm)	Surface Roughness, r	Advancing Contact Angle, θ_A^*	Receding Contact Angle, θ_R^*	Critical Contact Angle, θ_c	Nucleation Density, (drops/mm^2)
S1	400	34 ± 23	0.14	81 ± 35	7.53	164 ± 3	159.7 ± 1.7	97	8,448
S2	750				13.2	162.3 ± 0.5	159.9 ± 0.6	94	11,175
S3	400	101 ± 35	0.16	181 ± 88	3.47	162.0 ± 1.8	147 ± 3.0	105	5,744
S4	750				5.64	164.6 ± 1.8	154 ± 2	99	9,589
S5	400	344.2 ± 187	0.21	537 ± 269	2.49	158.4 ± 1.3	113 ± 8.0	110	3,080
S6	750				3.81	160.7 ± 1.4	118 ± 8	103	5,120

FIGURE 6.1: Specifications of superhydrophobic surfaces. A–F) Scanning electron micrographs of surfaces S1–S6, respectively. The topography of the superhydrophobic nanopillars was systematically varied using three different values of pillar diameters and pitches (increasing from left to right) and two different pillar heights (shorter on top and taller on bottom). G) Side-view high-speed microscopy confirmed that surfaces S1–S4 promoted jumping-droplet condensation, whereas no jumping occurred on surfaces S5 and S6. H) Table summarizing the physical parameters of each surface. The nucleation densities correspond to the number of droplets visible on each surface prior to coalescence events, with environmental conditions of $T_s = 1\,^{\circ}\mathrm{C}$, $T_\infty = 16.5\,^{\circ}\mathrm{C}$, and $RH = 50\%$ ($S = 1.4$).

the chamber. See the Methods section and Figure D.1 in the Supporting Information for more details on the fabrication and experimental setup.

6.2.1 Experimental results

The topography (h, d, and l) of surfaces S1–S6 are detailed in Figure 6.1H and were used to calculate the roughness ratio r, while the solid fraction ϕ was calculated from scanning electron micrographs. It was subsequently confirmed that the suspended Cassie state is thermodynamically favorable compared to the impaled Wenzel state,

which is true when: [28]

$$\theta_a > \theta_c, \qquad \text{with} \qquad \cos\theta_c = -\frac{1-\phi}{r-\phi}, \tag{6.1}$$

where $\theta_a = 113.5 \pm 0.5°$ is the intrinsic (advancing) contact angle on a smooth silanized surface. As seen in Figure 6.1H, Equation 6.1 is satisfied for all six surfaces used here. Finally, the receding and advancing apparent contact angles of sessile droplets were measured using a goniometer. Every surface exhibited an advancing apparent contact angle of approximately $\theta_A \gtrapprox 160°$ and a contact angle hysteresis that was small ($\theta_A - \theta_R < 15°$, S1–S4) or moderate ($\theta_A - \theta_R < 50°$, S5 and S6), which is indicative of a superhydrophobic Cassie state. When condensation formed on surfaces S1–S4, micrometric droplets spontaneously mobilized upon coalescence; this dynamic behavior was confirmed to be out-of-plane jumping by utilizing a side-view microscope (Figure 6.1G). On surfaces S5 and S6, no jumping events were observed at all regardless of the diameter of the droplets.

To find the critical diameter of jumping droplets on surfaces S1–S4, top-down high-speed videos of the condensing surfaces were recorded at 5,000 fps. The minimum droplet diameter that enables jumping upon coalscence (D_c) can be deduced by playing back high-speed videos of droplets coalescing over a wide range of droplet diameters. Specifically, the critical diameter is revealed by measuring the largest droplet diameters that do *not* jump upon coalescence (D^-) and the smallest droplet diameters that *do* jump upon coalescence (D^+). When measuring a large enough sample size of coalescing droplets, such that $D^- \approx D^+$ is true, it follows that $D_c \approx D^+$. Note that all diameter measurements are referring to the averaged diameters of the individual droplets just *prior* to merging together into a single droplet. For simplicity, the diameters of coalescing pairs of droplets must be within 20 % of each other to be included in the analysis.

Figure 6.2 shows high-speed imaging of the smallest possible droplets that jump

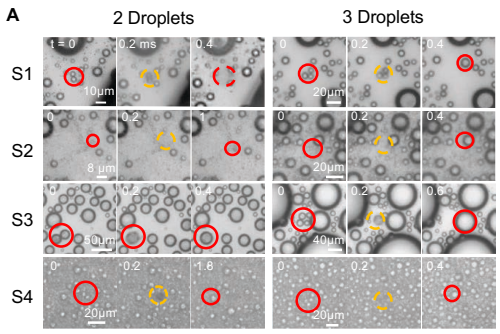

B

	2 droplets		3 droplets		4 droplets		5 droplets	
	D- (μm)	D+ (μm)	D- (μm)	D+ (μm)	D- (μm)	D+ (μm)	D- (μm)	D+ (μm)
S1	5.0 ± 0.5	5.8 ± 0.6	7.4 ± 0.5	7.6 ± 0.9	8.1 ± 0.7	9.3 ± 0.6	16 ± 3	16 ± 4
S2	—	2.5 ± 0.5	—	3.9 ± 1.5	—	12.4 ± 0.7	—	12 ± 1.4
S3	26.8 ± 1.4	—	21 ± 4	22.4 ± 1.6	16.6 ± 1.0	17.2 ± 1.0	16 ± 3	16.1 ± 1.3
S4	6.8 ± 1.0	5.7 ± 0.6	7.2 ± 0.4	7.4 ± 0.5	8.6 ± 1.8	8.3 ± 0.7	13 ± 7	9.9 ± 1.2

FIGURE 6.2: Critical diameter of jumping droplets on the SHPB substrates. Measurements of the critical diameter of jumping droplets on six different superhydrophobic nanopillared substrates. A) The smallest jumping event is shown for each surface for 2-droplet or 3-droplet coalescence events. Time zero corresponds to the time immediately before coalescence/jumping occur; the droplet(s) are circled in red when on the substrate and in yellow when air-borne. B) Table showing the average diameter of the largest non-jumping droplets, D^-, and the smallest jumping droplets, D^+. The critical size for jumping, D_c, lies somewhere in between and can be conservatively defined as $D_c \approx D^+$.

off surfaces S1–S4 upon 2-droplet or 3-droplet coalescence events (Figure 6.2A). See Figure D.2 in the Supporting Information for images of 4-droplet and 5-droplet jumping at the critical size. The topology of the nanopillars has a clear effect on the critical diameter of jumping (Figure 6.2B). The smallest jumping droplets were observed on the tall and slender nanopillars (surface S2), where $D_c \approx 2\,\mu$m for 2-droplet coalescence events which is an order of magnitude smaller than previously reported values [13, 16, 247, 248, 264]. Indeed, this may not even be the true lower limit for S2: no values of D^- could be measured as every single observable coalescence event resulted in successful jumping. Surfaces S1 and S3 both exhibit slightly larger $D_c \approx 5\,\mu$m, which makes sense given that each of these surfaces exhibit only 1 of the 2 qualities of S2: nanopillars on surface S1 are slender but not tall, while nanopillars on S3 are tall but not as slender. Surface S4 exhibits a markedly larger $D_c \approx 25\,\mu$m as it is neither tall nor slender. Surfaces S5 and S6, which did not exhibit jumping, exhibit values of d and l that are even larger than with S3 and S4. Still, the lack of jumping

is somewhat surprising given that the Cassie state is favorable (at least globally) and the nucleation density is still much smaller than the pillar density (Figure 6.1H). In particular, surfaces S1, S2, and S4 all confirm that the typical value of $D_c \sim 10\,\mu$m reported in the literature is not the lower limit and that jumping-droplet condensation can be further optimized by tuning the underlying nanostructure.

The rate of jumping events was also observed to be affected by the nanostructure. Histograms of the number of jumping droplets that occur in a 10 min period of time for surfaces S1–S4 are shown in Figure 6.3, where both transient (i.e. initial 10 min of growth) and steady-state (recorded after 30 min of growth) periods were considered. As with the measurements of D_c, the results are segregated by the number of droplets present in a given coalescence event. These histograms were created by recording at 1 fps for 10 min and manually counting each jumping event that occurs. While such a slow frame rate can no longer explicitly capture the jumping trajectory, it can be easily inferred from the sudden disappearance of 2 or more neighboring droplets from one frame to the next. Static coalescence events, where droplets merged but remained in place, were not counted in the histogram counts.

For both transient and steady-state growth, there were more jumping droplets on surface S2 than any of the other surfaces by at least an order of magnitude. For example, over 300 droplet pairs jumped off S2 during the first 10 min of growth, compared to less than 10 over the same time span on any other surface. Clearly there is a correlation between reducing D_c and maximizing the frequency of droplet jumping, which is intuitive given that low values of D_c increase the number of coalescence events that can promote jumping. In general, it can be seen from Figure 6.3 that as D_c increases, it also tends to increase the probability of multi-droplet (3 or more) jumping events relative to pairwise jumping. Surfaces S1, S3, and S4 feature more jumping events during steady-state growth compared to initial growth, as the average droplet diameter is maximal at steady-state such that $D > D_c$ is true

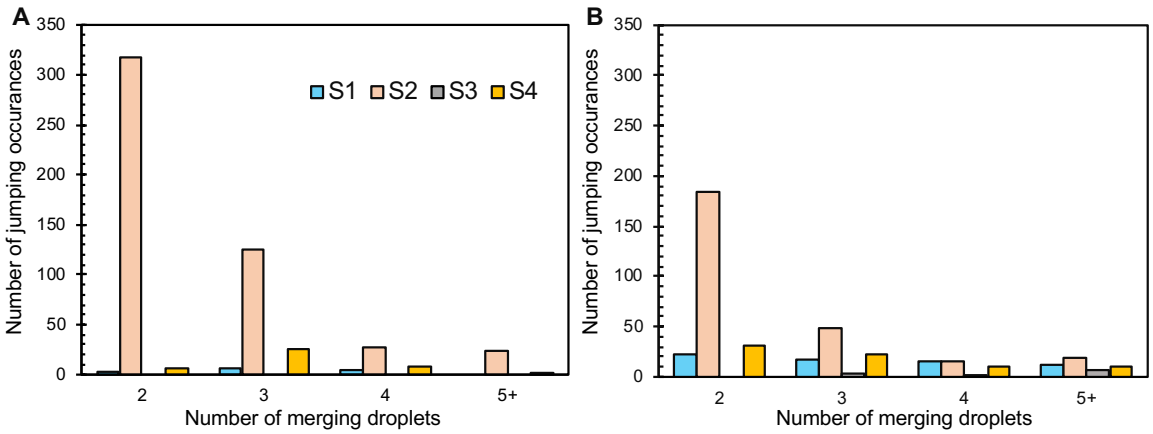

FIGURE 6.3: Histograms of jumping-droplet condensate. Histograms of jumping-droplet condensate during: A) Transient (initial) growth and B) Steady-state growth for each surface. Videos are taken over a 1.28 mm × 0.8 mm field-of-view for A) 10 min after the first clearly developed droplet or B) 30 min wait time after the first clearly developed droplet followed by another 10 min of recording.

more often upon coalescence. Conversely, since surface S2 promoted jumping for all coalescence events, twice as much jumping was observed on S2 during transient growth compared to steady-state, as there are a greater number of droplets and more coalescence events in the first moments of condensation.

During the preparation of this manuscript, new works were published by Cha *et al.* and Mouterde *et al.* that similarly observed unprecedentedly small ($D_c \approx 1\,\mu$m) jumping droplets on ultra-fine superhydrophobic nanostructures [286, 287]. It is therefore important to contextualize the contributions of the present work that are distinct from these prior observations of $D_c \approx 1\,\mu$m. The report by Cha *et al.* focused on demonstrating that the hydrodynamics of coalescence-induced jumping are still governed by capillary-inertial effects even for $\sim 1\,\mu$m droplets [286]. Mouterde *et al.* discovered that measuring the adhesion of a deposited droplet atop a condensing surface can reveal information about the size distribution and wetting-state of the condensate [287]. Here, we instead focus on systematically varying the topology (h, d, and l) of superhydrophobic nanotextures to determine how D_c varies when tun-

ing the surface morphology. In addition to our experiments, we will now develop a rational model that can explicitly predict D_c as a function of the surface structure.

6.2.2 Theoretical growth model

Using classical nucleation theory [133, 137], the critical radius of a stable liquid embryo when it first nucleates on a surface was calculated to be $r^* \approx 1\,\text{nm}$ for our surfaces (see full calculation in Methods). This indicates that embryos will tend to nucleate within the roughness of our superhydrophobic nanostructures, as $r^* \ll (l-d)$ for all six surfaces. Furthermore, the nucleation density of condensate forming on each surface under our experimental conditions (cf. Figure 6.1H) was observed to be smaller than the packing densities of the nanopillars (1 pillar/l^2) by 4 orders of magnitude for surfaces S1 and S2, 3 orders of magnitude for surfaces S3–S5, and 2 orders of magnitude for surface S6. It follows that each liquid embryo nucleates within a single unit cell of nanoroughness and tends to grow in isolation (without any coalescence events) until reaching a microscopic size.

Based on the above calculations, we hypothesize that the relationship between the nanostructure topology and the resulting critical jumping size can be rationalized with a 3-step energetic model considering the incipient growth of an isolated embryo nucleating within a unit cell of nanoroughness (Figure 6.4). Initially, a nucleated droplet will exhibit a spherical-cap shape governed by the (advancing) intrinsic contact angle of the surface. This spherical-cap shape will be lost once the droplet becomes large enough to fill the footprint of the unit cell and become constrained by the side-walls of the nanopillars. For hydrophobic surfaces where $\theta_A \approx 90^\circ$ for both the floor and the side-walls, the shape of a droplet constrained within a unit cell can be approximated as a rectangular cuboid bounded by the rounded nanopillars at the corners (see Figure D.3).

Our model first considers a droplet that is constrained inside of a unit cell but

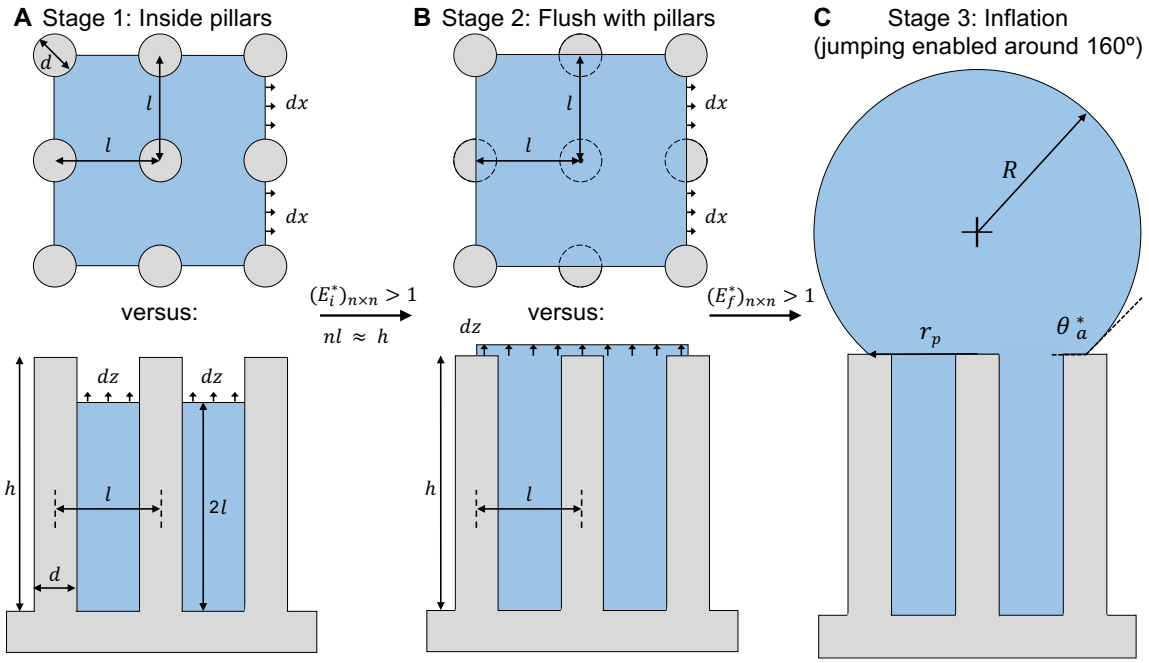

FIGURE 6.4: Schematic of the three-stage energetic model. Schematic of the three-stage model that correlates the critical jumping diameter (D_c) to the underlying nanostructure topology (h, d, l). A) The first stage of the model determines how many unit cells (n×n) a droplet constrained inside of the nanopillars must fill before it can reach the pillar tops ($n = 2$ in the schematic); B) The second stage begins with the critical value of n_c attained from stage one and predicts whether additional unit cells must be filled before upward inflation into the air becomes energetically preferable to lateral growth; C) In the third and final stage, the droplet's pinned radius prescribed by stages one and two is used to find the critical droplet diameter where the apparent contact angle inflates to 160° to promote jumping upon coalescence.

whose top face has not yet reached the pillar tops. It can be calculated whether it is energetically favorable for such a droplet to expand laterally into an adjacent unit cell *versus* preferentially upward toward the top of the present unit cell. This comparison is necessary for any surface structure where the height of the features is greater than the pitch, which is true for all of our surfaces except S5. The change in surface energy for a droplet to grow sideways into a second unit cell by an incremental distance dx can be expressed as:

$$(\Delta E_{\mathrm{i,s}})_{1\times 1} = \gamma[(l-d) - 2l\cos\theta_A - (l-d)\cos\theta_A]dx, \tag{6.2}$$

where the terms on the right-hand side represent the energetic cost of expanding the top liquid-vapor interface, wetting the side-walls of the nanopillars, and wetting the floor, respectively (see Figure D.3). Note the subscript i refers to the droplet being completely "inside" of the unit cell, the subscript s is for "sideways" growth, and 1×1 is referring to the number of unit cells that this droplet is currently occupying. Conversely, the energetic cost inherent to upward growth by an equivalent dz is:

$$(\Delta E_{\mathrm{i,u}})_{1\times 1} = \gamma[4(l-d) - \pi d\cos\theta_A]dz, \tag{6.3}$$

where the first term on the right-hand side accounts for the expanding free interfaces of the droplet's sides while the second term is for the wetting of the nanopillars' side-walls. The preferential direction of droplet growth can be predicted by setting $dx = dz$ and taking the ratio of the incremental surface energies:

$$(E_{\mathrm{i}}^*)_{1\times 1} = \frac{(\Delta E_{\mathrm{i,s}})_{1\times 1}}{(\Delta E_{\mathrm{i,u}})_{1\times 1}} = \frac{(l-d)(1-\cos\theta_A) - 2l\cos\theta_A}{4(l-d) - \pi d\cos\theta_A}, \tag{6.4}$$

where lateral growth into an adjacent unit cell is favorable when $(E_{\mathrm{i}}^*)_{1\times 1} < 1$ while upward growth toward the top of the unit cell occurs for $(E_{\mathrm{i}}^*)_{1\times 1} > 1$.

For surface geometries where $(E_{\mathrm{i}}^*)_{1\times 1} < 1$ is true, it is assumed that a droplet will proceed to grow within the surface roughness until evenly constrained within 2×2 unit cells, such that the width and height of the droplet are now $2l$ instead of l (Figure 6.4A). Subsequently $(E_{\mathrm{i}}^*)_{2\times 2}$ is checked, and this process is repeated until either $(E_{\mathrm{i}}^*)_{n\times n} > 1$ or the height of the droplet reaches the tops of the nanopillars ($nl \approx h$). For a droplet constrained by $n \times n$ unit cells, the modified surface energies are:

$$(\Delta E_{\mathrm{i,s}})_{n\times n} = n\gamma[(l-d) - 2nl\cos\theta_A - (l-d)\cos\theta_A]dx, \tag{6.5}$$

$$(\Delta E_{\mathrm{i,u}})_{n\times n} = n\gamma[4(l-d) - n\pi d\cos\theta_A]dz, \tag{6.6}$$

which are compared to determine the direction of growth for any size droplet:

$$(E_{\mathrm{i}}^{*})_{n\times n} = \frac{(\Delta E_{\mathrm{i,s}})_{n\times n}}{(\Delta E_{\mathrm{i,u}})_{n\times n}} = \frac{(l-d)(1-\cos\theta_A) - 2nl\cos\theta_A}{4(l-d) - n\pi d\cos\theta_A}. \tag{6.7}$$

Figure 6.5A is a graphical representation of stage one growth for the six surfaces used here. Surface S2 is able to exhibit $(E_{\mathrm{i}}^{*})_{n\times n} > 1$ at $n = 6$, well before $nl/h > 1$ is true at $n = 10$, indicating that the droplet is now able to grow preferentially up the side walls of the nanopillars instead of continuing to expand outward. All of the other surfaces were instead first satisfied by $nl/h > 1$, in other words, the constrained droplets grew uniformly within the roughness and reached the top remaining in the shape of a constrained cube.

The second stage of the model now considers what happens to a growing condensate droplet once its top interface is level (i.e. wetting) the tops of the nanopillars and pinned at its four corners (Figure 6.4B). To reiterate, the switch to this second stage of the model occurs as soon as $(E_{\mathrm{i}}^{*})_{n\times n} > 1$ or $nl \approx h$ is true, with this critical value of $n \times n$ from the first stage being used as the initial footprint of the water droplet for the second phase. At this point, a droplet can either grow laterally while remaining flush with the pillar tops, or inflate upwards into the ambient.

As before, we first consider the case of a single unit cell and then extrapolate to any cell size. If a droplet is able to completely fill a single unit cell (ex: S5), the comparison of the surface energies required for sideways growth *versus* upward inflation are:

$$(E_{\mathrm{f}}^{*})_{1\times 1} = \frac{(\Delta E_{\mathrm{f,s}})_{1\times 1}}{(\Delta E_{\mathrm{f,u}})_{1\times 1}} = \frac{(l-d)(1-\cos\theta_A) - 2h\cos\theta_A}{\pi l}, \tag{6.8}$$

where the numerator is equivalent to Equation 6.4 except that l is now swapped with h for the final term and the denominator approximates the upward bulge as a cylindrical disk of diameter l. Expanding to consider any $n \times n$ unit cells, the

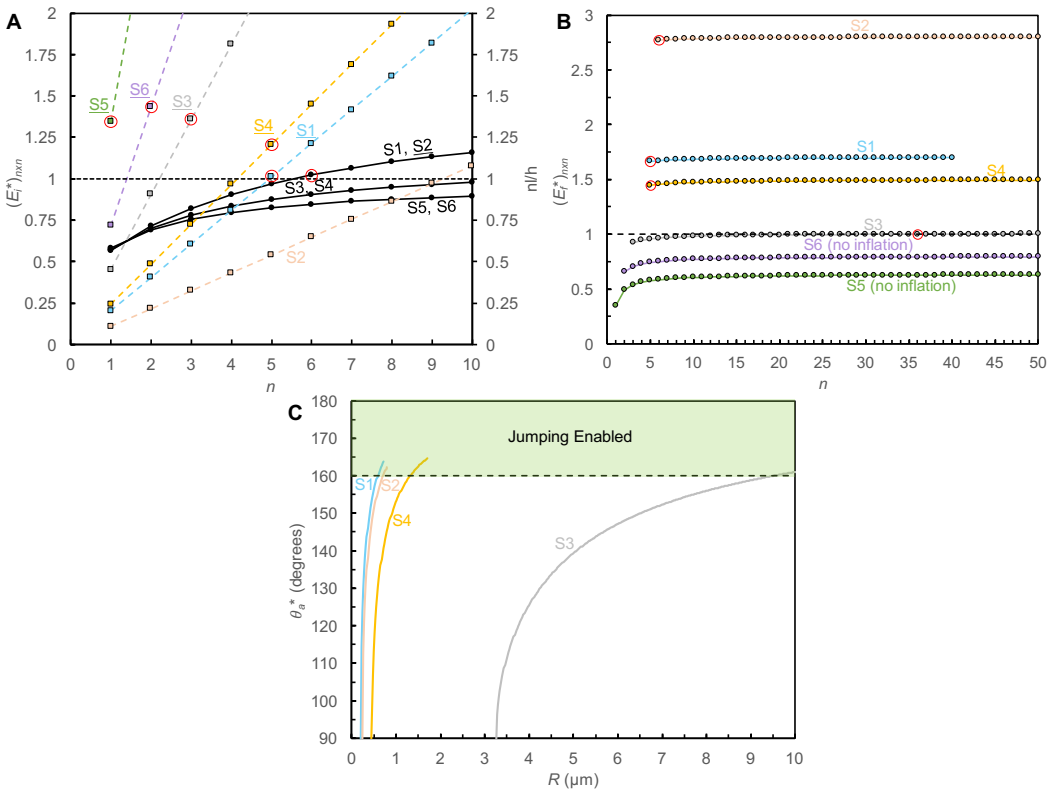

FIGURE 6.5: Graphical depiction of the three-stage growth model. Graphical depiction of the three-stage growth model for the geometries of the six surfaces used here. A) Prediction of how many unit cells ($n \times n$) a droplet must fill before it first reaches the pillar tops, which is satisfied when $(E_{\mathrm{i}}^*)_{n\times n} > 1$ (left y-axis and solid lines) or $nl/h > 1$ (right y-axis and dotted lines). A red circle is drawn around the critical value of n_c where either of these conditions is first satisfied. B) Calculating the critical value of n_c where $(E_{\mathrm{f}}^*)_{n\times n} > 1$ and upward inflation can first occur, which never occurs for surfaces S5 or S6. C) Inflation of a droplet starting from a pinned radius of $R_p = 0.5nl$ and apparent contact angle of 90°, to determine the value of R_c where $\theta_a^* \approx 160°$ and jumping is enabled.

energetic cost of sideways growth compared to upward inflation is now:

$$(E_{\mathrm{f}}^*)_{n\times n} = \frac{(\Delta E_{\mathrm{f,s}})_{n\times n}}{(\Delta E_{\mathrm{f,u}})_{n\times n}} = \frac{[(nl-d)(1-\cos\theta_A) - 2nh\cos\theta_a]}{n\pi l}, \tag{6.9}$$

where the modified terms in the numerator reflect the fact that the pillar-top faces are additionally being wetted by the water during the dx growth. If $(E_{\mathrm{f}}^*)_{n\times n} < 1$, the droplet's footprint is iteratively increased to $(n+1) \times (n+1)$ until $(E_{\mathrm{f}}^*)_{n\times n} > 1$. Note that this second stage of the model is somewhat analogous to a growth model

developed by Enright *et al.* [13], except that our model additionally accounts for the wetting of the side walls and top faces of the nanopillars which were neglected in their model. Another key distinction is that their growth model assumed that a droplet was already flush with the pillar tops even inside of just one unit cell, whereas we determined a critical number of unit cells that had to first be filled as defined by the first stage above.

In Figure 6.5B, the second stage of this model is represented graphically for all six surfaces. The initial value of n was obtained from stage one, and it can be seen that the value of $(E_f^*)_{n\times n}$ increases weakly with increasing n. For surfaces S1, S2, and S4, the condition of $(E_f^*)_{n\times n} > 1$ is immediately satisfied at the starting value of n obtained from stage one. Thus, for tall and/or slender nanopillars, it is clear that stage-one growth is the primary bottleneck regarding the value of D_c. For shorter and/or larger nanopillars, on the other hand, the dominant constraint switches to this second stage. For example, surfaces S5 and S6 never exhibit $(E_f^*)_{n\times n} > 1$ for any value of n, suggesting that the droplets never inflate upward which is in agreement with the complete lack of jumping-droplet behavior on these surfaces experimentally. This solves the mystery of why jumping did not occur despite the two conditions specified by Enright *et al.* being satisfied [13]. An interesting case is surface S3, which is finally able to satisfy $(E_f^*)_{n\times n} > 1$ once $n_c = 36$; this footprint is an order of magnitude larger than with the more tall and/or slender nanopillars (S1, S2, and S4), where $n_c \approx 5$. Three-dimensional plots that help illustrate the parameter space where stage-one *versus* stage-two growth is the bottleneck for D_c are depicted in Figure D.4 in the Supporting Information.

Once $(E_f^*)_{n\times n} > 1$ becomes true for a critical value of n_c, the droplet proceeds to inflate into the air with a pinned contact radius of $r_p \approx (1/2)n_c l$. At this point we now switch to the third and final stage of the model, which correlates r_p with the critical droplet diameter D_c required for jumping to successfully occur upon

coalescence events. As previously established by Miljkovic *et al.* [271, 272, 286], as a droplet inflates on a superhydrophobic surface with a pinned contact radius r_p, its apparent contact angle varies as:

$$\theta_a^* = \cos^{-1}\left(\frac{r_p}{R}\right) + \frac{\pi}{2}, \tag{6.10}$$

where R is the radius of curvature of the droplet and the apparent contact angles being considered are $\theta_a^* > 90^\circ$ (Figure 6.4C). Reviewing the literature on jumping-droplet condensation, it seems generally true that jumping will occur if the droplets' contact lines exhibit the Cassie wetting state as they inflate beyond the pinned contact radius and if $\theta_a^* > 160^\circ$ prior to the coalescence event [232, 286]. Provided that the Cassie state is energetically favorable for a given superhydrophobic surface (true for all six of our surfaces), we can therefore predict the critical droplet diameter for jumping to occur by rearranging Equation 6.10 and solving for $\theta_a^* \approx 160^\circ$:

$$D_c = \frac{2r_p}{\cos 70^\circ}. \tag{6.11}$$

This simple geometrical relation is illustrated in Figure 6.5C, to finally arrive at the predicted value of D_c for each surface. Our theoretical model predicts a critical jumping diameter of $D_c = 1.2$, 1.4, 19, and 2.6 μm, respectively, for surfaces S1–S4, and no jumping for surfaces S5 and S6. These values all agree with their experimental counterparts to within a factor of two (Figure 6.6), which is impressive given the complete lack of any floating or empirical parameters in the theoretical model. The only exception is surface S1, which is off by a larger (but still respectable) factor of 4. We attribute this minor discrepancy to the bundling together of slender nanopillars by capillarity [285,288], which tended to occur on surface S1 (Figure 6.1A) and changed its geometry somewhat compared to its theoretical approximation where the pillars were assumed to be vertically oriented.[1] Regardless, the model can not

[1] This capillary bundling of slender pillars surprisingly did not occur with surface S2, despite its increased pillar height, perhaps due to some minor variation in conditions during its fabrication.

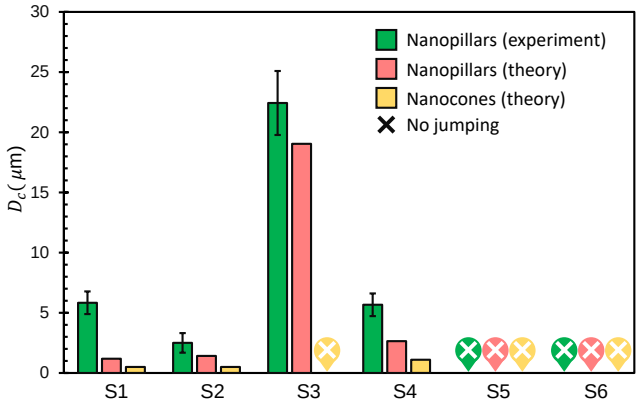

FIGURE 6.6: Comparison of the experimental and theoretical critical diameters of jumping-droplet condensate. Comparison of the experimental (green) and theoretical (pink) critical diameters of jumping-droplet condensate for surfaces S1 – S6. Experimental values of D_c correspond to the smallest pair of droplets able to jump on a given surface (D^+ in Figure 6.2), except for surface S3 where it corresponds to the smallest 3-droplet jumping event as no pairwise jumps occurred. The theoretical performance of equivalent nanocone surfaces is also provided (yellow, see full derivation of nanocone theory in Section D.5).

only predict whether jumping can occur on a given surface, but to a surprising accuracy can even extract the critical (minimum) size of jumping droplets. Our model therefore provides a rational understanding of how the nanostructure architecture tunes the critical departure diameter of jumping-droplet condensation.

Finally, a computer code was developed in Mathematica to automate this three-stage model and predict D_c over a wide parameter space. Specifically, the pitch was varied by $15\,\text{nm} \leq l \leq 1{,}225\,\text{nm}$ and the pillar diameter was varied from $10\,\text{nm} \leq d \leq 250\,\text{nm}$, with the condition that $l > d$ must always be true. The value of D_c was then calculated for all possible combinations of d and l for a given pillar height; here, three values of $h = 500\,\text{nm}$, $1{,}000\,\text{nm}$, and $3{,}000\,\text{nm}$ were used. The program iteratively increased the value of n for stages 1 and 2 until the critical n_c was found for each stage, and finally plugged the second-stage n_c into the third-stage inflation model to find D_c. If the program reached a maximum value of $n_{max} = 200$ for either of the first two stages, it was concluded that no jumping would occur for this surface

and a boolean 'false' was returned in lieu of a critical diameter.

The results of this program are shown in Figure 6.7A–C as three-dimensional graphs plotting D_c vs. d and l for a given h. For a given pitch and pillar diameter, the critical diameter of the jumping droplets is typically larger with increasing pillar height, which indicates that stage-one growth is the most common bottleneck. However, this is not always the case, as explained above for surfaces S3 and S4 where stage-two growth was the bottleneck that now favors larger values of h to minimize D_c. Increasing the pillar height tended to increase the range of values of pitch where jumping was possible. Interestingly, these plots reveal that nano-droplet jumping is possible for properly designed nanostructures, as also indicated by a recent experimental report [286]. A phase map was also created (Figure 6.7D) which shows every possible combination of non-dimensionlized values of d/l, h/l, and n in which jumping droplets can occur. For instance, when $n \leq 100$ and $h/l \leq 200$, jumping will only occur on the substrate if $d/l \leq 0.6$.

6.2.3 Discussion

Our model successfully captures the inflation of nucleating embryos into large contact angle droplets, which is only the first criteria required for jumping-droplet condensation to occur [247]. The second criteria is that coalescence must occur amongst two or more of these inflated droplets, which partially converts the droplets' surface energy to kinetic energy [14]. It is important to note that our model here is solely focused on the first step (inflation) required for droplet jumping, as the hydrodynamics of the coalescence-induced jumping itself has already been comprehensively studied by numerous experimental [14, 264, 266], theoretical [252, 253, 286], and computational [255, 257, 258] works. Even for small ($D_c \sim 1\,\mu$m) jumping droplets, it has already been established experimentally [286] and computationally [257] that the coalescence process remains in the capillary-inertial regime (i.e. D_c is not con-

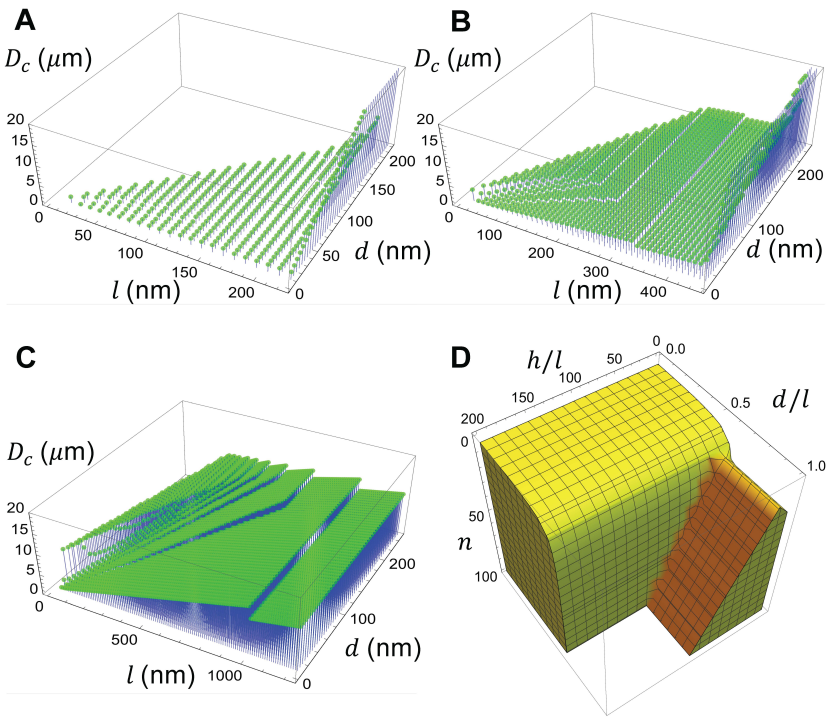

FIGURE 6.7: Theoretical value of the critical diameter of jumping droplets. Theoretical value of the critical diameter of jumping droplets which can occur on a substrate with pitch l and pillar diameter d for different pillar heights of: A) $h = 500\,\text{nm}$, B) $h = 1{,}000\,\text{nm}$, and C) $h = 2{,}000\,\text{nm}$. D) A three-dimensional phase map shows the possible combinations of n, d/l, and h/d in which jumping droplets can occur. The shaded volume represents where jumping occurs, whereas no jumping is possible in the white exterior.

strained by viscous effects). Therefore, inflation is the primary factor governing D_c even for $1\,\mu$m droplets. However, it is interesting to note that once jumping is enabled for droplets of order $\sim 1\,\mu$m or smaller, the critical size of jumping may now be limited by the nucleation density, rather than by inflation, as droplets are unable to coalesce until they grow large enough to reach their nearest neighbor. Thus, to improve jumping droplets even further will be highly sensitive to the ability to maximize the nucleation density, for example by overlaying dense arrays of hydrophilic features [234, 276].

The model developed here is for pillars of constant diameter (nanopillars). However, recent works have shown that tapered pillars (nanocones) can enhance the

robustness of rebounding droplets and jumping-droplet condensation on superhydrophobic surfaces [287, 289, 290]. Very recently, Mouterde *et al.* observed that nanocones serve to decrease the critical jumping diameter to $D_c \sim 1\,\mu$m, rather than the $D_c \sim 10\,\mu$m typically observed on conventional nanopillars [287]. In light of these findings, we re-derived our 3-stage droplet growth model for the case of nanocones of height h, basal diameter d, and pitch l (see derivation and corresponding Figures D.5–D.7 in the Supporting Information). By directly comparing our models for nanopillars (Figure 6.5) and nanocones (Figure D.7), two different aspects of the critical jumping size become apparent. Firstly, our work reveals that nanopillars are not inextricably limited to $D_c \sim 10\,\mu$m, as we were able to achieve the same enhancement of $D_c \sim 1\,\mu$m on nanopillars that Mouterde *et al.* could only observe with nanocones. In other words, in addition to the shape of the pillars mattering, our model explicitly reveals how the value of D_c for a given pillar shape can vary by orders of magnitude by tuning the pillar diameter, pitch, and height. Secondly, our model validates the observation of Mouterde *et al.* that, all other things being equal (i.e. equivalent h, d, l, and θ_A), nanocones are typically superior to nanopillars. In Figure 6.6, we compare the theoretical values of D_c for nanopillars *versus* equivalent nanocones, and find that D_c is decreased by a factor of 2–3 for the nanocones. Our model attributes this to the nanocones decreasing the energy barrier for upward growth relative to lateral growth for droplets still inside of the roughness, such that $(E_{\mathrm{i}}^*)_{n\times n} > 1$ is true for smaller values of n (Figure D.7a). However, we also found that nanocones are actually inferior in the context of stage two growth, as the value of $(E_{\mathrm{f}}^*)_{n\times n}$ does not increase with n like with nanopillars (Figure D.7B). This is why surface S3, which was our only surface limited by stage two growth instead of stage one, is predicted to actually fare worse (no jumping) if equivalent nanocones were used.

Our growth model assumes that most liquid embryos nucleate within the surface roughness, as opposed to on top of the nanopillars. Direct experimental evidence

that embryos tend to nucleate within the surface roughness of superhydrophobic surfaces has been previously demonstrated in a wide variety of reports on jumping-droplet condensers [13,14,247,284,286,287,291], which is most likely due to a reduced nucleation energy barrier along the edges where the pillars meet the floor [268]. However, some recent works have shown that certain types of surface structures can alternately promote nucleation on top of the roughness, in effect bypassing the first two stages of our growth model. Wen *et al.* demonstrated that sufficiently tall and dense nanowires serve to reduce the permeation of vapor molecules into the roughness, such that droplets tend to form atop the structure [292]. Park *et al.* included macroscopic bumps on their nanostuctured surface, finding that the millimetric features served to focus vapor diffusion onto their tops [128]. Another tactic is to design surfaces with ultra-small nanocavities, such that the critical size of a nucleating embryo exceeds the size of the cavity [293]. When hydrophilic features are patterned atop a superhydrophobic surface, embryos tend to nucleate on the elevated hydrophilic regions due to the decreased energy barrier for nucleation [234, 276]. Finally, Aili *et al.* recently discovered that coalescence is not the only possible mechanism to promote jumping: isolated droplets growing within a nanostructured micromesh were able to jump by an asymmetric Laplace pressure [267].

6.3 Conclusion

The critical diameter where condensing droplets can jump off the surface upon coalescence is highly dependent upon the underlying nanostructure of the surface. Experimentally, we show that the critical jumping diameter can be reduced by an order of magnitude compared to previous reports (down to $D_c \approx 2\,\mu$m) by designing nanostructures that are slender and densely packed. A theoretical model is developed that successfully predicts the critical jumping size as a function of the surface topology, with excellent agreement to the experimental results. By expanding

this model into phase space that was unexplored experimentally, it is revealed that nano-droplet jumping should be possible, indicating that the performance ceiling for jumping-droplet condensation still has not been reached. It is our hope that these findings encourage the advanced nanofabrication of slender nanostructures that can serve to further enhance condensation heat transfer while also promoting anti-dew, anti-frosting, and self-cleaning surface technology.

6.4 Materials and methods

6.4.1 Surface fabrication and characterization

All surfaces were fabricated in the Oak Ridge National Laboratory's cleanroom at the Center for Nanophase Materials Sciences. An electron beam evaporator was used to deposit a 3 nm, 5 nm, or 10 nm thick platinum film on 100 nm thermally grown SiO_2 on a <100> Si substrate. The sample was heated in a Rapid Thermal Processor (Easy Tube 3000, First Nano, Ronkonkoma, NY) at full power for 8 s in a hydrogen and argon ambient to dewet the platinum film. The measured maximum temperature within the process chamber was approximately 850 °C. The thickness of the platinum film determines the diameter and the pitch of the dewetted metal droplets (cf. Figure 6.1H) which were used as an etch mask. Two etching processes: SiO_2 etch followed by Si etch, were carried out in an inductively coupled plasma ion etching system (Oxford Plasmalab 100, Oxford Instruments, UK). The etching process of the 100 nm SiO2 was carried out in a mixture of O_2 and C_4F_8 at flow rates of 2 sccm and 45 sccm, respectively, at 15 °C, 7 mTorr, and 200 W RF for 65 s. The etching conditions for the Si layer were 5 sccm Ar, 25 sccm SF_6, and 60 sccm C_4F_8 flow rates at 20 °C, 10 mTorr, and 30 W RF. The nanopillars were etched to heights of 400 nm or 750 nm as controlled by the known silicon etching rate.

The surfaces were modified to become superhydrophobic *via* the vapor-phase deposition of trichloro(1H, 1H, 2H, 2H–perfluorooctyl)silane (Sigma-Aldrich) at 70 °C

overnight. The intrinsic wettability of water on the silane coating was found by additionally performing vapor-phase deposition on a clean SiO_2 wafer and measuring its receding ($\theta_r = 89° \pm 1°$ and advancing ($\theta_a = 113.5° \pm 0.5°$) contact angles using a goniometer (ramé-hart model 590) and five trials for each measurement. A similar protocol was following to measure the advancing and receding apparent contact angles on the superhydrophobic surface (Figure 6.1H). Whenever the surfaces began to exhibit minor surface contamination during experimental condensation studies, they were cleaned by submerging them into a bath of isopropyl alcohol for 20 min followed by a distilled water bath for 10 min. Scanning electron micrographs were taken FESEM at the Nanoscale Characterization Fabrication Laboratory at Virginia Tech (Zeiss LEO 1550). The surfaces were first stripped of silane using a plasma cleaner, and then deposited with a 4 nm film of iridium to enhance the surface's conductive properties and enhance the image quality.

6.4.2 Experimental setup

The samples were thermally bonded to a Peltier stage (ramé-hart) using a thin film of water. All experiments were performed within a customized humidity chamber (ramé-hart) where the Peltier stage was set to $T_s = 1.0 \pm 1.0\,°\mathrm{C}$ with environmental conditions of $RH = 50 \pm 2\%$ and air temperature $T_\infty = 16.5 \pm 0.5°\mathrm{C}$. This corresponds to a partial pressure of water vapor of $P_\infty = 939\,\mathrm{Pa}$ in the ambient, compared to a saturation pressure of $P_{\mathrm{sat}} = 657\,\mathrm{Pa}$ at the substrate, resulting in a supersaturation of $S = 1.4$. The entire humidity chamber was bolted to the x–y stage of a top-down optical microscope (Nikon LV150). To avoid perturbing the millimetric diffusive boundary layer about the condensing surface, the chamber was designed to exhibit a 2 cm gap between its quartz roof and the substrate, which required an extra long working-distance 20X lens (Mitutoyo Plan Apo SL, WD = 30.5 mm). The microscope was connected to a high-speed camera (Phantom v711) that filmed the

coalescence and jumping-droplet dynamics at 5,000 fps. To count the number of jumping events over a 10 min time span, the frame rate was reduced to 1 fps.

6.4.3 Data analysis details

The uncertainty in measuring the diameters of the coalescing droplets is approximately $\pm 0.5\,\mu$m, which corresponds to the $1\,\mu$m pixel length of the magnified camera. The uncertainties of D^- and D^+ in Figure 2B were obtained by averaging the values over 5 trials and either taking the standard deviation or $\pm 0.5\,\mu$m, whichever was larger. Two-droplet coalescence events were only considered if the pre-merged droplets were within 20 % of each other in size. Multi-droplet (3 or more) coalescence events generally exhibit wide ranges in droplet sizes, so the diameters of all drops prior to coalescence were simply averaged to obtain the diameters seen in Figure 2B. Videos recording the rates of jumping over 10 min. time spans were analyzed manually by going frame-by-frame through the image stack in ImageJ and identifying all cases where droplets suddenly disappeared from one frame to the next.

6.4.4 Calculation of critical nucleation size

The specific Gibbs free energy change associated with nucleation can be related to the nucleation pressure in the following manner:

$$\Delta\tilde{g} = -\frac{RT_w}{v}\ln\frac{p_{n,w}}{p_{s,w}} = -\frac{2\gamma}{r^*}, \tag{6.12}$$

where r^* is the critical radius required for a nucleating embryo to be able to grow. By combining Equations 3.7 and 6.12, we obtain $r^* \approx 1$ nm for our conditions of $T = 1\,^\circ$C and $\theta_R = 89^\circ$ over the full range of possible values for the kinetic constant: $r^* = 1.17$ nm for $I_0 \sim 10^{28}$ and $r^* = 1.24$ nm for $I_0 \sim 10^{31}\,\mathrm{m^{-2}s^{-1}}$.

7

'Sneezing' Plants

Pathogen Transport via Jumping-Droplet Condensation

"The answer is blowin' in the wind."

−Bob Dylan, from song "Blowin' in The Wind"

The content of this chapter was previously published as journal manuscripts in [294], and reproduced here with minor modifications. This chapter reveals a new mechanism for the transmission of diseases from one plant to the other.

7.1 Introduction

The spread of plant pathogens through the atmosphere involves processes of liberation (takeoff and ascent), drift (passive horizontal transport), and deposition (descent and landing) [17,21]. Liberation is influenced by various ecological and environmental factors that dictate the timing and mechanism of release, drift is associated with the passive, directed movement away from the ground surface in turbulent air currents,

and deposition involves descent and landing at a new destination [17]. Knowledge of these processes may assist growers and producers in making rational and informed management decisions, for example the application of a fungicide to control a specific plant pathogen [18–20].

Wheat represents about one quarter of the world's food supply [295], and plant pathogens threaten the global productivity of this staple food crop [24]. Wheat losses to plant diseases are extremely costly to food security because these crop losses are realized after most input costs and management decisions have been made. One of the most devastating diseases of wheat is leaf rust caused by the fungus *Puccinia triticina*. The liberation and dispersal of urediniospores of *P. triticina* (among others) have been attributed to wind [296] and rainsplash [297, 298].

Wheat leaves are known to exhibit a superhydrophobic surface wettability [299]. Previous studies have demonstrated that properly engineered superhydrophobic surfaces can enable jumping-droplet condensation via a two-step process. First, nanoscale embryos nucleate within the surface roughness but inflate into large-angle micro-droplets whose outer contact line exhibits the suspended Cassie state [13, 121, 247]. Second, these low-adhesion micro-droplets coalesce during natural growth, which converts surface energy into kinetic energy by virtue of the expanding liquid bridge breaking symmetry as it impacts the substrate [257, 258, 300]. Jumping-droplet condensation has been observed on engineered superhydrophobic surfaces [13,14,121,247, 300], cicada wings [235], lotus leaves [236], geckos [237], and water strider legs [260].

Previous studies of jumping-droplet condensation were confined to exotic organisms such as lotus leaves; here, we show that jumping-droplet condensation occurs on the leaves of the common wheat plant. For diseased leaves, we demonstrate that jumping-droplet condensation is an important liberation mechanism for pathogenic spores. The jumping dynamics are sufficient to propel the spores beyond the laminar boundary layer, enabling subsequent dispersal by gentle winds. While recent

reports have demonstrated that jumping droplets can remove dust or pollen from a superhydrophobic surface [235–237], the scope was limited to the self-cleaning of the individual organism. Here, we instead reveal the ironic twist of liberating particles in the new context of pathogenic material: jumping droplets can free spores from a given leaf, but subsequent dispersal can spread the disease across the crop. Spores are conventionally sorted into two different types: those actively ejected and those released by strong winds [301]. Our findings show that both types are simultaneously possible in a complementary fashion, with jumping-droplet ejection dominating in gentle conditions while wind-induced vibration/shear can remove spores in gusty conditions.

7.2 Results

The jumping-droplet mechanism of spore liberation requires a natural dew cycle on a superhydrophobic surface, as conceptualized in Figure 7.1A for the case study of wheat leaves. Wheat plants grown in a Conviron growth chamber were innoculated by spraying mineral oil mixed with urediniospores (*P. triticina*). The plants were then incubated in a dew chamber for 24 hr to promote infection and subsequently returned to the growth chamber. Within 7–12 days, the leaves developed lesions and urediniospores indicative of leaf rust (Figure 7.1B), see 'Materials and Methods'.

The contact angles of 10 μL droplets deposited on wheat leaves were measured on a goniometer (ramé-hart, Model 590) using the shrink-swell method. On healthy wheat leaves, the advancing and receding apparent contact angles were $\theta_A = 127 \pm 5^\circ$ and $\theta_R = 117 \pm 3^\circ$, respectively, while droplets on the central region of diseased leaves exhibited a more hydrophobic $\theta_A = 144 \pm 6^\circ$ and $\theta_R = 138 \pm 9^\circ$ (Figure E.1A). These contact angles are at the very low end of the superhydrophobicity spectrum, as most superhydrophobic surfaces exhibit $\theta_A > 150^\circ$ [227]. However, these contact angles are highly dependent upon the size of the droplets, as micrometric condensate can

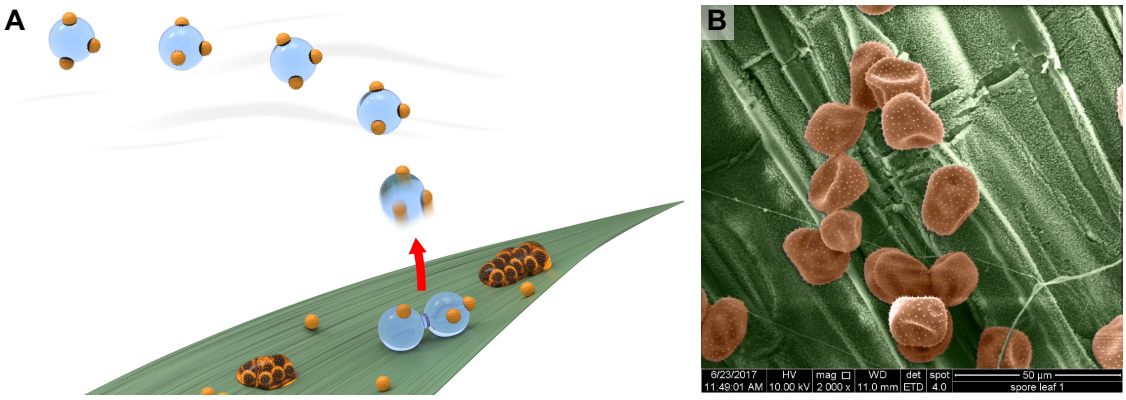

FIGURE 7.1: Jumping-droplet mechanism of spore liberation. A) Schematic of the liberation of rust spores via the coalecence-induced self-propulsion of dew droplets growing on diseased wheat leaves. The self-propulsion is predominantly out-of-plane, resulting in the spore-laden droplets clearing the boundary layer for dispersal in the wind. B) False-colored ESEM micrograph of a sporulated wheat leaf. The radius of a typical *P. triticina* spore is $r_s = 8.0 \pm 1.9\,\mu$m.

exhibit larger angles. Regardless, the low contact angle hysteresis of $\theta_A - \theta_R \leq 10^\circ$ indicates that air pockets are trapped beneath the deposited droplets to promote the low-adhesion Cassie state, which satisfies the second (and more important) criteria for superhydrophobicity [227]. For the diseased wheat leaves in particular, the wettability was found to be heterogeneous, with either end of the leaf being less hydrophobic: $\theta_A = 120 \pm 20^\circ$ and $\theta_R = 100 \pm 30^\circ$.

Interestingly, the urediniospores themselves were found to be hydrophobic. While droplets could not be directly deposited on the microscopic urediniospores, their wettability could instead be inferred from condensation experiments. Urediniospores were observed to aggregate at the free interface of a condensing liquid droplet (Figure E.1B), indicating that the spores are not strongly hydrophilic. In other words, hydrophobic spores will more strongly deform the local interface in order to meet their contact angle requirements, leading to curvature-induced forces that aggregate the particles. Secondly, condensate was sometimes observed to nucleate and grow as satellite droplets atop the spore-laden interface of a mother droplet, rather than

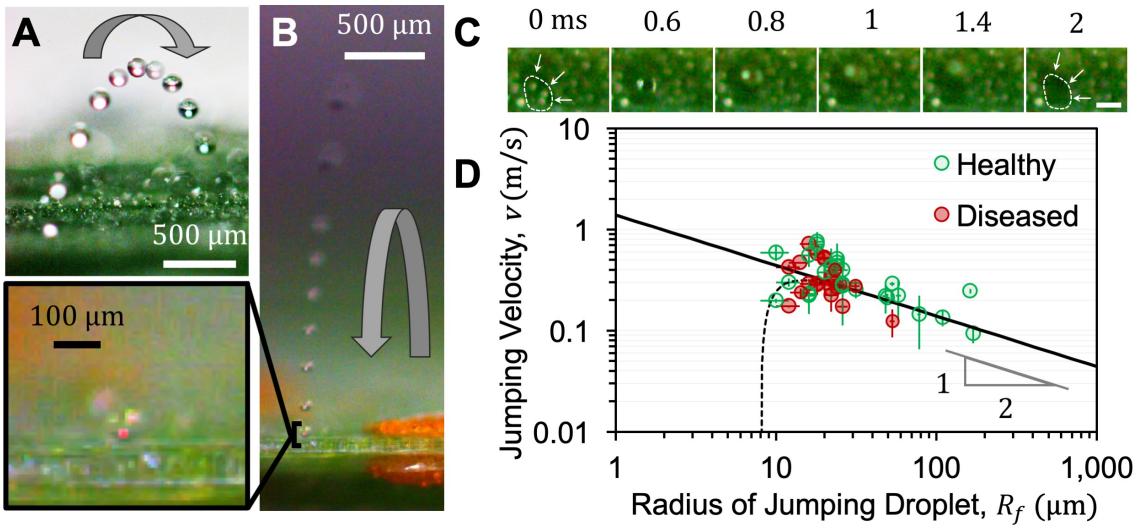

FIGURE 7.2: Dynamics of jumping-droplet condensation on healthy and diseased wheat leaves. A) High-speed time-lapse photography of a coalesced dew droplet (final radius $R \approx 78\,\mu$m) jumping from a healthy leaf. The total time of the time-lapse arc is $t \approx 26.7$ ms. B) First confirmation that jumping droplets can liberate spores from a pustule of the rust *P. triticina* on a wheat leaf. Time-lapse images show a droplet ($R \approx 36\,\mu$m) jumping several millimeters off the surface and falling back down over a time $t \approx 40$ ms. Inset shows an orange urediniospore, roughly 10 μm in diameter, that is carried by the jumping droplet. C) Top-down microscopy of three spores being liberated by jumping droplets. From the second to the fourth frames, a dew droplet vertically jumps off the leaf surface due to coalescence. A comparison between the first and last frames shows that the jumping droplet removed the spores from the leaf's surface within 2 ms. Scale bar represents 100 μm. D) Jumping velocity plotted against the final radius of the jumping droplet. The solid and dotted lines in Figure 7.2D correspond to Equation 7.2 for no spore ($n=0$) and one spore ($n=1$) respectively.

immediately coalescing (Figure E.1C). This is suggestive of the spores promoting two separate liquid interfaces on either side, which is only possible for hydrophobic contact angles. We note that this observation of satellite droplets has also been observed when condensing on a bed of hydrophobic particles (i.e. liquid marbles) [302].

In Figure 7.2A, we show that jumping-droplet condensation occurs on the leaves of the common wheat plant. The condensation was formed by thermally bonding a healthy leaf section (2 cm × 2 cm) on a Peltier stage set to $T_w = 0\,^\circ$C for ambient conditions of $T_\infty = 21 \pm 6\,^\circ$C and $RH = 55 \pm 17\%$. Side-view microscopy was obtained

using a high-speed camera (Phantom v711) attached to a 5× magnification lens (Canon MP-E). Microscopic dew droplets were observed to exhibit quasi-spherical apparent contact angles, larger than that of the macroscopic deposited droplets, to facilitate the jumping upon coalescence. We attribute the enhanced superhydrophobicity of the condensed droplets to the non-homogeneity of the leaf's surface, such that smaller droplets can avoid local hydrophilic features that are inescapable to larger droplets.

Repeating the side-view imaging with a rusted wheat leaf, we were able to directly observe spores adhering to jumping droplets as they ejected from the surface (Figure 7.2B). Rather than being encapsulated within a jumping droplet, the hydrophobic *P. triticina* spores tended to remain at the droplet's free surface even during jumping. The limited magnification and side-view perspective does leave some room for doubt that the orange pixels could be a lighting effect, rather than liberated spores. More conclusive evidence was therefore obtained by switching to a top-down optical microscope, where the spores could be directly observed on the leaf's surface prior to their jumping-induced transport (Figure 7.2C).

The initial velocity of jumping droplets was captured using side-view high-speed microscopy for both healthy and diseased wheat leaves (Figure 7.2D). When two droplets of radii R merge together, a perfect conversion of excess surface energy to kinetic energy predicts a jumping velocity of $v = \sqrt{3(2-2^{2/3})}(\gamma/\rho R)^{1/2}$, where $\gamma \approx 75.7\,\mathrm{mN/m}$ and $\rho \approx 1000\,\mathrm{kg/m^3}$ are the surface tension and density of water at 0 °C. However, this predicted value exceeds the experimentally observed jumping rates by a factor of 5 [14]. Mouterde et al. has recently shown that this apparent discrepancy can be resolved by invoking a conservation of momentum argument [303, 304]:

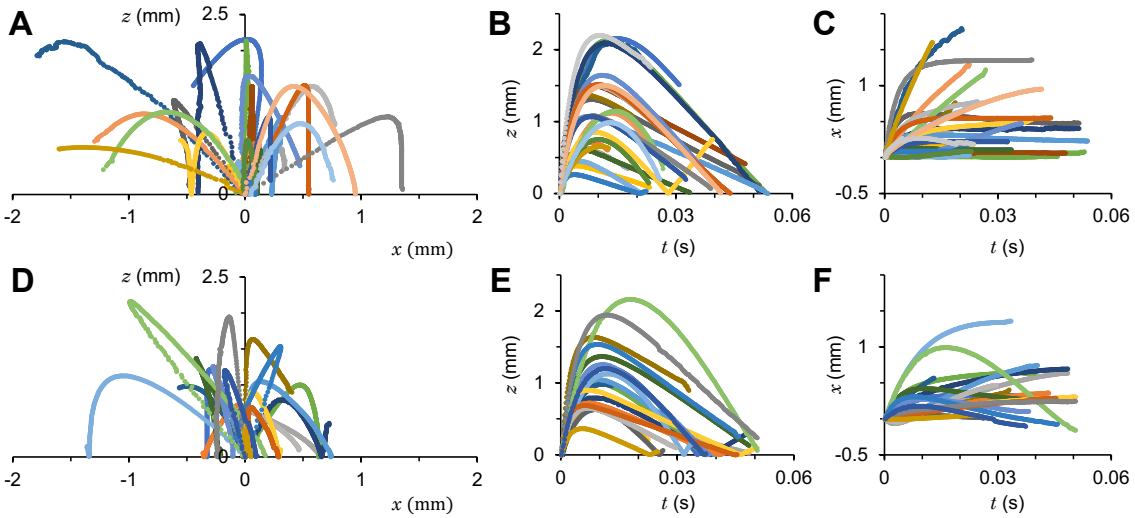

FIGURE 7.3: Trajectories of jumping droplets. A–C) Trajectories of the center of mass of jumping droplets on a healthy leaf. D–F) Analogous trajectories for droplets jumping from diseased leaves. The field-of-view of the microscopes were limited to about 2.5 mm and we restricted ourselves to cases where the peak and subsequent falling of a jumping droplet was visible. Bends in the trajectories of droplets are associated with the rotation of the droplets as well as drag forces.

$$v = \frac{\epsilon^{5/2}}{2\left(1+\epsilon^3\right)^{5/6}} \left(\frac{\gamma}{\rho R_{\mathrm{f}}}\right)^{1/2}, \tag{7.1}$$

where R_{f} is the post-merged radius and $\epsilon = r/R$ is the degree of asymmetry between merging two droplets of radius R and r $(R > r)$. Using this new approach yields the proper pre-factor of about 0.2 even for a perfectly symmetric merging $(\epsilon = 1)$. The rest of the energy is primarily dissipated as droplet oscillations inherent to the hydrodynamics of jumping [257, 258]. The measured initial jumping velocities obeyed Equation 7.1 across an order of magnitude of values for the droplet size with an average asymmetry of $\epsilon = 0.7$. The moderate scatter in experimental values of v about Equation 7.1 may also be attributed to the possibility of coalescence events involving more than two droplets [264] and losses due to adhesion of the liquid with the solid, which might be non-negligible on the wheat surface.

Droplets jumping from sporulating leaves did not exhibit any noticeable changes

in velocity compared to healthy leaves, indicating that the spores do not appreciably impact the hydrodynamics of droplet self-propulsion (Figure 7.3). Using side-view high-speed imaging, trajectories of jumping droplets in the z-x plane were obtained (Figures 7.3A,D). It was observed that these lateral trajectories can exceed 2 mm in the absence of any appreciable wind. A typical wheat leaf is only about 5 mm in width (Figure E.3), suggesting that most droplets are capable of vaulting beyond the leaf's edge regardless of the wind conditions.

The z-coordinate (Figures 7.3B,E) and x-coordinate (Figures 7.3C,F) of jumping droplets were plotted as a function of time. Combining this information yields the values of $v_x = dx/dt$ and $v_z = dz/dt$ for all times. These velocities were then used to obtain $v = (v_z^2 + v_x^2)^{1/2}$ as a function of time for every jump. The initial value of v for each jump is used as the jumping velocity in Figure 7.2D. Droplets that moved out of focus early in a jump, due to appreciable movement in the y-direction, were not considered in our analysis.

To understand why the addition of a spore does not affect the ballistics of jumping microdroplets, we re-derive Equation 7.1 with the larger droplet containing n spores of size r_s (see Figure E.2 and Section E.1 for a complete derivation). Defining R_f to be the post-merged radius of the jumping droplet *including* any spores, $R_\mathrm{f}^3 \approx R^3 + r^3 + nr_\mathrm{s}^3$. Assuming the spore density is comparable to water and that the effects of the spores on the interfacial area cancels out before and after merging, we obtain a modified version of Equation 7.1:

$$v_s = \left(1 - \frac{nr_\mathrm{s}^3}{R_\mathrm{f}^3}\right)^{5/6} v. \tag{7.2}$$

Note that in the absence of any spores ($n = 0$), Equation 7.2 becomes Equation 7.1. In Figure 7.2D, the dotted line corresponds to Equation 7.2 for one spore. It will be later shown that most of the spore-laden jumping droplets carried one urediniospore

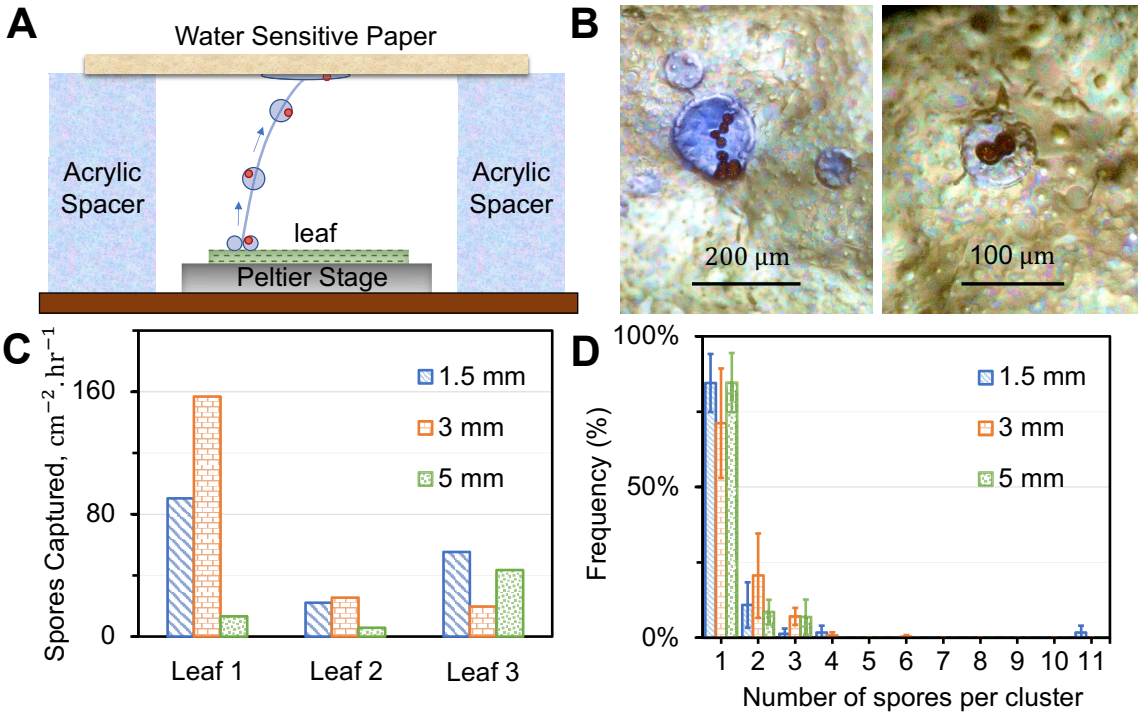

FIGURE 7.4: Quantifying liberated spores. A) Schematic of experimental set-up to capture the spores carried off the wheat leaf by jumping dew droplets. Water sensitive paper is placed a fixed height above a condensing wheat leaf. B) Experimental micrograph of droplets and spores caught by the water sensitive paper during jumping-droplet condensation. The blue regions represent the splatter pattern of the impacting jumping droplets, while spores carried by droplets are brownish red in color. C) Spores liberated per unit unit area of the wheat leaf per hour as captured by the water sensitive paper placed at heights of $h = 1.5, 3$ and 5 mm. D) Frequency distribution of spores carried off by individual jumping droplets. We see that at any given height, more than 80% of the droplets jumping with spores have only one spore adhering to them.

(Figure 7.4D). Equation 7.2 shows that jumping with spores is equivalent to jumping on healthy leaves, unless the droplet is beneath a critical size of about $R_{\mathrm{f}} \approx 10\mu$m where the cubic term $r_{\mathrm{s}}^3/R_{\mathrm{f}}^3$ causes a sharp decrease in v_s as R approaches the spore size. This crossover in regimes was not observed experimentally due to the fact that on a moderately superhydrophobic surface, condensate does not inflate to a sufficiently large contact angle required for jumping until growing to at least 10 μm in size [121].

To quantify the rate of spore liberation from a diseased leaf surface, a small piece of water-sensitive paper was placed above a condensing leaf surface with the out-of-plane separation fixed by acrylic spacers of height h =1.5, 3 or 5 mm (Figure 7.4A). Wheat leaf samples, 1 cm × 3 cm, were inoculated with *P. triticina* in the same manner as the previous experiments and were held at $T_w = 0\,^\circ$C to induce jumping-droplet condensation. The ambient conditions ranged from $T_\infty = 20-30\,^\circ$C and $RH = 50-60\%$ depending on the day. After exactly 1 hr of condensation, the opposing paper was removed and analyzed under a microscope to quantify jumping-droplet impact events (blue splatter) and transported spores (red), as shown in Figures 7.4B and E.4. It was confirmed via side-view microscopy that the condensation never came close to large enough to "bridge" across the millimetric gap, such that all water and spores on the paper correspond to jumping droplets crossing the gap. To ensure repeatability of the results, three different sporulating leaves were used. Three sections were cut from each leaf, such that all three spacer heights were tested for each leaf.

The mean rates of spore liberation were $56 \pm 28\,\text{cm}^{-2}\text{hr}^{-1}$ across the 1.5 mm gap, 67 ± 63 $\text{cm}^{-2}\text{hr}^{-1}$ for the 3 mm gap, and $21 \pm 16\,\text{cm}^{-2}\text{hr}^{-1}$ for the 5 mm gap (Figure 7.4C, see section E.2). As expected, fewer spores were able to traverse the 5 mm gap compared to the 1.5 mm or 3 mm gaps, although it is impressive that an appreciable amount of spores were still able to travel this far given the large viscous drag exerted on jumping droplets [305]. Despite the large degree of heterogeneity in the results, it was consistently found across multiple wheat plants that condensation was able to liberate spores at rates of $\mathcal{O}(10)\,\text{cm}^{-2}\text{hr}^{-1}$ and propel them at least 1.5–5 mm from the surface. Assuming a total wheat leaf area of $10\,\text{cm}^2$ and a natural dew cycle of 1 hr/day, about 100 urediniospores could be liberated by jumping-droplet condensation each day per diseased leaf. About 75% of jumping droplets contained just a single urediniospore, with the remainder carrying up to 11 (Figure 7.4D).

For spores located on the underside of a leaf, or for vertically oriented leaves, the

jumping-droplet effect is only needed to detach the spores from the leaf surface. After this initial liberation, gravity and/or wind can facilitate the subsequent dispersal of the spores. However, for spores on the top face of a leaf, jumping droplets must propel spores beyond the laminar boundary layer for wind-induced pathogen transport to be possible. Otherwise, the jumping-droplets (and spores) would simply fall back to the same leaf in a slightly different location. The thickness of a laminar boundary layer at a distance x downwind from the leading edge of a horizontal leaf can be estimated as

$$\delta \sim (\nu x/U)^{1/2}, \tag{7.3}$$

where $\nu = 1.5 \times 10^{-5}\,\mathrm{m}^2/\mathrm{s}$ is the air's kinematic viscosity and U is the wind speed. Typical wind speeds are $U \approx 0.01$–$10\,\mathrm{m/s}$. Taking the width of the leaf, which is typically 5 mm, as the characteristic length scale, we obtain a boundary layer of thickness of $\delta \approx 0.086 - 2.7\,\mathrm{mm}$. Given our findings that jumping droplets can launch spores up to 5 mm from the surface, it seems that they can liberate spores beyond the boundary layer for virtually any wind speed. Once clear of the boundary layer, jumping droplets of typical radius $R_\mathrm{f} \approx 30\,\mu\mathrm{m}$ should be able to suspend in winds as slow as $U \sim 0.1\,\mathrm{m/s}$ for subsequent long-range dispersal.

Finally, control experiments were performed to compare how spore liberation by jumping-droplet condensation compares to the already-known mechanisms of vibration and wind shear. Sporulated leaves were fixed to a mechanical vibration stage and the speed of oscillation was gradually increased until spores were able to catapult from the surface (Figure 7.5A,B). A critical vibrational speed of about $v_v \approx 0.6\,\mathrm{m/s}$ was found, where $v_v = 2\pi f A$, f is the imposed frequency, and A is the peak amplitude measured by the side-view high-speed camera (Figure E.5). Even with the best-case scenario of a leaf being perfectly perpendicular to a wind flow, this would require a

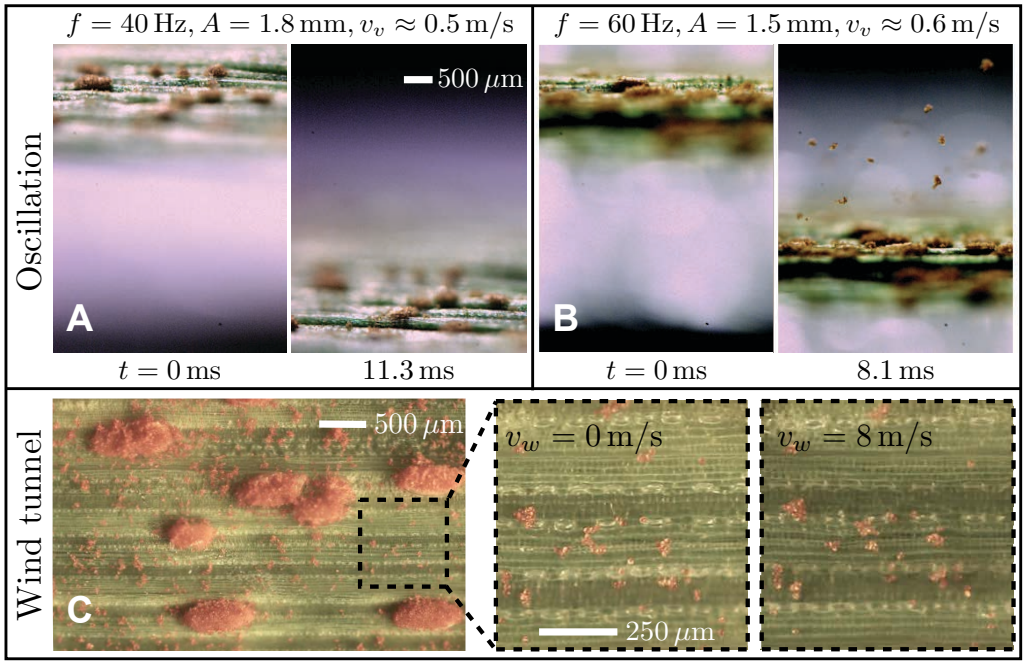

FIGURE 7.5: Spore liberation via vibration or wind shear. A) Vibration of a sporulated leaf at $f = 40\,\mathrm{Hz}$ and a peak-to-peak amplitude of $2A = 3.6\,\mathrm{mm}$ was not strong enough the detach any spores. B) At a critical frequency of $f = 60\,\mathrm{Hz}$, some of the spores were catapulted from the leaf. C) Top-down microscopy of a spore-laden leaf before (left) and after (right) subjecting to an 8 m/s wind. Nearly all of the spores remained adhered to the leaf.

wind speed of at least $U \sim 1\,\mathrm{m/s}$ (see Section E.3). A leaf was also placed within a wind tunnel, where liberation was characterized by comparing spore counts before and after subjecting the leaf to wind. For a typical wind speed of 8 m/s [306], a subset of spore agglomerates were able to initially shear off the leaf's surface, but the other agglomerates and nearly all of the isolated spores remained adhered (Figures 7.5C and E.6). This is in agreement with a previous report [307].

In addition to dry dispersal, wind could also shear a spore-laden droplet from a wheat leaf (Figure 7.6A). The wind shear must overcome the droplet's lateral adhesion force, which can be approximated as [308]:

$$F_{\mathrm{adh}} \approx \pi a \gamma (\cos\theta_{\mathrm{R}} - \cos\theta_{\mathrm{A}}), \tag{7.4}$$

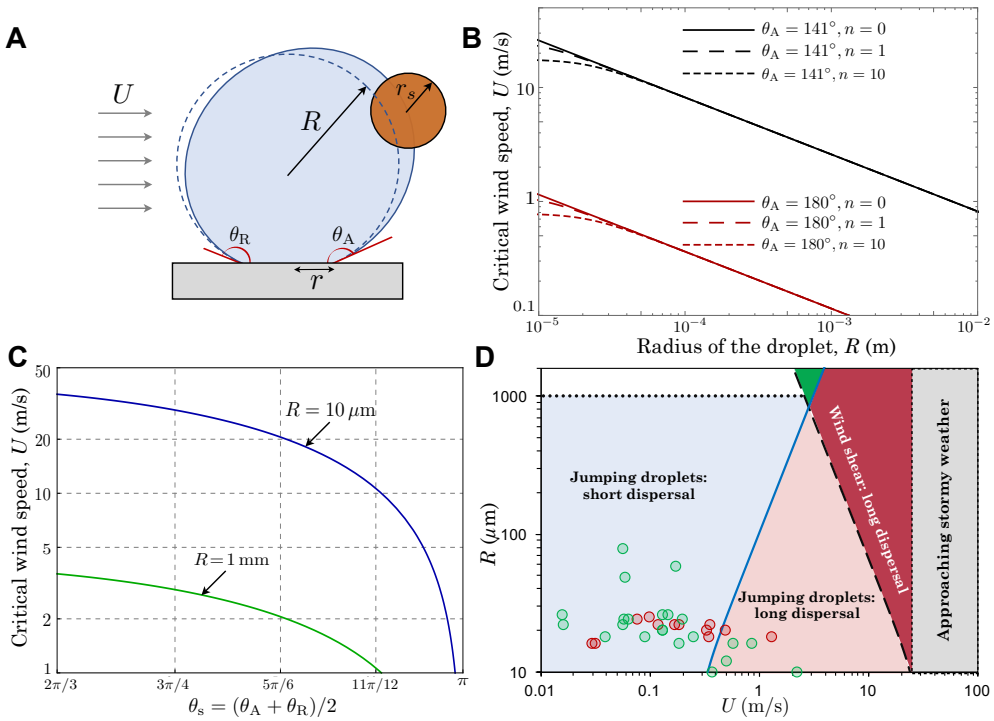

FIGURE 7.6: Phase map for the different modes of liberation and dispersal for spore-laden droplets. A) Schematic of wind shearing a spore-laden droplet. B) Critical wind speed required to shear spore-laden droplets from the leaf surface (Equation 7.6). The black lines correspond to $\theta_s \approx 141°$ and hysteresis $\Delta\theta = 6.4°$, as was found for our diseased wheat leaves. Red lines correspond to an idealized surface with $\theta_A = 180°$ and $\Delta\theta = 6.4°$. C) Variation of the critical wind speed with the average contact angle of the sliding droplet. D) Phase map for the different modes of liberation and dispersal for spore-laden droplets. The black dashed line corresponds to Equation 7.6, which is the minimum wind speed required to shear off a droplet from a wheat leaf ($n = 1$). The blue line corresponds to the minimum wind speed required to fully suspend liberated droplets, to enable long-range dispersal (Equation 7.7). The dotted black line scales to the capillary length (~ 1 mm), beyond which droplets are too big to jump. Data points correspond to droplets jumping from healthy leaves (green circles) or diseased leaves (red), where Equation 7.3 was used to solve for the wind speed U required for the experimental jumping height to correspond to the boundary layer (δ) for a leaf of $x = 5$ mm width.

where a is the droplet's contact radius with the surface. The contact radius can be expressed in terms of the spore-laden droplet's radius of curvature: $a = R_s \sin\theta_s$, where $R_s^3 \approx R^3 + nr_s^3$ accounts for both the volume of the pure liquid (of radius R) and adhered spores of quantity n and radius r_s, while $\theta_s \approx (\theta_A + \theta_R)/2$ is the

average apparent contact angle of the sliding droplet. Making these substitutions into Equation 7.4 and using trigonometric relations:

$$F_{\mathrm{adh}} \approx 2\pi\gamma(R_{\mathrm{s}} \sin\theta_{\mathrm{s}}) \sin\frac{\theta_{\mathrm{A}} + \theta_{\mathrm{R}}}{2} \sin\frac{\theta_{\mathrm{A}} - \theta_{\mathrm{R}}}{2} \approx \pi\gamma(R_{\mathrm{s}} \sin^2\theta_{\mathrm{s}})\Delta\theta, \tag{7.5}$$

where $\Delta\theta = (\theta_{\mathrm{A}} - \theta_{\mathrm{R}})$. For large-angle droplets on non-wetting surfaces, the force exerted by the wind is approximately: $F_{\mathrm{wind}} \approx 1/2\rho_a U^2(\pi R_{\mathrm{s}}^2)$. Solving for the critical wind speed, the spore-laden droplet will be removed when $F_{\mathrm{wind}} \approx F_{\mathrm{adh}}$:

$$U_{\mathrm{c}} \approx \sqrt{\frac{2\gamma}{\rho_a R_{\mathrm{s}}}} \sin\theta_{\mathrm{s}} \sqrt{\Delta\theta}. \tag{7.6}$$

As expected, Equation 7.6 shows that it is more difficult to dislodge a smaller droplet. From our goniometric measurements of droplets on sporulated leaves, $\theta_{\mathrm{s}} \approx 141^\circ$ and $\Delta\theta \approx 6.4^\circ$. Figure 7.6B plots U_{c} against the liquid-only radius of curvature, $R \approx (R_{\mathrm{s}} - nr_{\mathrm{s}})^{1/3}$, for the cases of $n = 0, 1$, or 10 (black curves). For large millimetric droplets, the critical wind velocity scales as $U_{\mathrm{c}} \sim 1\,\mathrm{m/s}$ regardless of how many spores are in the droplet. This is comparable to the critical wind speed for dry dispersal. For micrometric droplets, adding spores now serves to weakly decrease U_{c}, but the critical wind speed now scales as $U_{\mathrm{c}} \sim 10\,\mathrm{m/s}$. This means that, for all but the largest droplets, the wind velocities required to shed spore-laden droplets are high enough to transport dry spores anyway, with no droplets required. The red curves correspond to a hypothetical superhydrophobic surface that would have a perfect $\theta_{\mathrm{A}} = 180^\circ$, but retains the same modest hysteresis as our leaves. Even for this idealized case, $U_{\mathrm{c}} \sim 1\,\mathrm{m/s}$ is required for wind to shed micrometric droplets, comparable to wind-induced dry dispersal. In Figure 7.6C we show across a wide range of non-wetting contact angles that $U_{\mathrm{c}} \sim 1\,\mathrm{m/s}$ for $R_{\mathrm{s}} = 1\,\mathrm{mm}$ droplets and $U_{\mathrm{c}} \sim 10\,\mathrm{m/s}$ for $R_{\mathrm{s}} = 10\,\mu\mathrm{m}$ droplets.

While large ($R_s \approx 5\,\text{mm}$) spore-laden droplets can be sheared off by moderate $U \sim 1\,\text{m/s}$ winds (or by gravity at vertical orientations), the subsequent dispersal of such droplets would be impossible. This can be seen from a simple scaling relation. For a droplet to be carried a sufficient distance by the wind, the inertia of the wind, $\rho_a U^2 R_s^2$, has to be greater than the weight of the droplet, $\rho g R_s^3$. This yields:

$$U > \sqrt{\frac{\rho g R_s}{\rho_a}}, \tag{7.7}$$

which for $R_s \approx 5\,\text{mm}$ requires $U_c \approx 10\,\text{m/s}$ for dispersal anyway. Additionally, for the specific context of spore-laden dew droplets, it can be difficult to grow droplets this large in the first place. In contrast, for the $R \approx 30\,\mu\text{m}$ size typical of jumping droplets, $U_c \approx 0.5\,\text{m/s}$ to be suspended in the wind.

Figure 7.6D summarizes the four primary regimes of liberating spore-laden droplets. For low wind speeds (blue region), jumping droplets can clear the boundary layer but their dispersal is only short-range, as the wind cannot fully support the weight of the droplets. For moderate wind speeds (pink), jumping droplets can fully suspend in the wind for long-range dispersal. For high wind speeds and large droplets, wind shear can shed droplets for short-range dispersal (green). Finally, for very high wind speeds, the wind can both shear the droplets from the surface and fully support their weight for long-range dispersal (red). In short, spore liberation and dispersal via some combination of vibration, wind, and/or gravity requires conditions of $U \sim 1$–$10\,\text{m/s}$ and only tends to be effective for removing some of the larger spore agglomerates. Microscopic jumping droplets, on the other hand, enable even isolated spores to clear the boundary layer, can be suspended in winds as slow as $U \sim 0.1\,\text{m/s}$ for long-range dispersal, and even in the near absence of wind can vault spores beyond the leaf's edges.

7.3 Discussion

This coalescence-induced catapulting of spores from a surface is reminiscent of ballistospores being launched from thousands of fungal species [309]. However, there are two important mechanistic differences. First, a ballistospore must be delicately hinged to an outgrowth known as a sterigma, such that the shift in center-of-mass induced by coalescence can detach the spore from this weak attachment [310]. Second, this elevation of the spore above the actual surface of the fungi requires creative surface chemistry to trigger coalescence: hygroscopic substances are secreted from the proximal end of the spore to generate a Buller's drop, which coalesces with a hydrophilic film located on the spore itself [311]. For these reasons, ballistospore ejection is exclusively tailored to liberate native fungal spores from their outgrowths and is incapable of removing foreign pathogens. Indeed, this combination of three-dimensional architecture and localized surface chemistry is so complex that even a primitive effort at ejecting a synthetic ballistospore was only recently achieved [312]. In contrast, jumping-droplet condensation should be able to liberate a wide variety of non-native pathogens from any location on a non-wetting surface and does not require sterigma or chemicals.

In conclusion, naturally forming dew is sufficient to liberate pathogenic material from non-wetting organisms. The mechanism is the jumping-droplet mode of condensation that occurs on superhydrophobic surfaces. Specifically, we found that jumping-droplet condensation on diseased wheat leaves was capable of liberating leaf rust spores at rates of $\mathcal{O}(10)\,\mathrm{cm}^{-2}\mathrm{hr}^{-1}$, which corresponds to about 100 spores per leaf for an hour-long dew cycle. The 2–5 mm jumping heights of the spore-containing droplets is sufficient to clear the boundary layer even in calm conditions (~ 0.01 m/s), enabling subsequent dispersal to nearby plants via wind and/or gravity regardless of leaf orientation. In contrast, we showed that the wind-induced libera-

tion of dry spores required much stronger winds ($\sim$1–10 m/s) and only tends to be effective for large spore agglomerates. For non-wetting plants, we therefore propose that jumping-droplet condensation can be considered as a new key mechanism for plant pathogen dispersal, in addition to strong winds and rainsplash. This explosive ejection of pathogenic material from the condensing surface could be a positive attribute for the organism in question, but could also be responsible for spreading the disease to its neighbors. Thus it turns out that plants, like tetrapods, are capable of 'sneezing.'

7.4 Materials and methods

7.4.1 Cultivating wheat leaves

A seed mix of susceptible winter wheat lines (Massey, and testing line VA-135) were provided by the Griffey lab at Virginia Tech. This was used to grow wheat plants in a Conviron growth chamber with the following settings: long day 12/12 hr, light intensity 120 μmol $m^{-2}s^{-1}$, temperature 24 °C, and a relative humidity of 50%. Urediniospores of *P. triticina* (= *P. triticina* Roberge ex Desmaz. f. sp. *tritici*) race TCRKG were maintained at −80 °C and conditioned in a 1.5 mL Eppendorf tube at 45 °C in a hot water bath for 5 min. The tube was agitated twice during the incubation. The 1.5 mL tube was then placed, lid open, in an upright 50 mL Falcon tube with a moistened paper towel for 3 hr. Following this humidity treatment, spores were suspended in a 50 mL conical tube in 30 mL of sterile water with 0.1% Tween 20 as a surfactant (Fisher Scientific) and aerosolized with a Prevail atomizer unit (Chicago Aerosol) onto 6 week old wheat plants. Inoculated plants were incubated in the dark at 100% humidity (136 DL dew chamber, Percival Scientific) for 24 hr at 18 °C to encourage infection, and then removed back to controlled growth conditions

for disease development. Symptoms of leaf rust (the development of brown/orange lesions) and signs of the fungus (uredinia bearing urediniospores on the leaf surface) appeared within 7 to 12 days.

7.4.2 Experimental setup

For condensation experiments on the wheat leaves, a Peltier stage was used (Linkam, Model T95-PE). A section of a wheat leaf was thermally bonded to the Peltier element with a thin coating of thermal grease (Thermalcote, Part No. 251 G, $k = 0.765\,\mathrm{W/m{\cdot}K}$). For spore counting experiments, acrylic spacers were placed on two sides of the Peltier element such that another (longer) piece of acrylic could bridge the gap. Water sensitive paper (Syngenta, Part No. 347456, original size 76×26 mm) was adhered to the underside of the bridging acrylic by taping its outer edges, such that the gap between the wheat leaf and paper was either 1.5 mm, 3 mm or 5 mm. The experiment was run for 1 hr by chilling the Peltier stage down to 0 °C, during which condensation readily grew on the surface of the leaf. The paper was then removed from the setup and placed under a microscope to quantify the adhered spores.

7.4.3 Imaging

We made use of the Vision Research Phantom v711 high-speed color camera, which is capable of recording up to 7,500 frames per second at full $1{,}280 \times 800$ resolution. The high-speed camera was mounted on an optical microscope (Nikon, Eclipse LV150) for top-down imaging. A 20× Mitutoyo objective lens (Part No. 378-810-3) was used for counting the number of spores. The top-down perspective was useful for obtaining statistical information on the dispersal rates of fungal spores over time due to jumping droplets. For side-view imaging of the jumping droplets, the high-speed

camera was attached to either a macro lens (Canon, MP-E 65mm, 1–5× mag) or a long-distance microscope (Infinity Infiniprobe TS-160, 1–16× mag).

7.4.4 Mechanical vibration

A 5 cm long segment was cut from a typical sporulated wheat leaf and taped to a flat stage fixed to a mechanical wave driver (PASCO, SF-9324). The amplitude and frequency of the driver were controlled using a function generator (Agilent, 33210A) along with a power amplifier (KROHN-HITE 7500). The frequency of vibration was gradually increased to find the critical frequency required to detach spores from the leaf surface.

7.4.5 Air flow

Wind tunnel experiments were conducted in an Airtech X-Stream wind tunnel (Model 57889). For a given velocity of the air flow, a 5 mm segment of a sporulated wheat leaf was double-sided taped on a lab jack and left inside the wind tunnel for 5 min.

8

Multi-Layered Porous Superhydrophobic Surfaces

"There's a little white duck, sitting in the water
A little white duck, doing what he oughter."
—Burl Ives

This chapter studies the effect of layers porous superhydrophobic surfaces on the critical implement pressure.

8.1 Introduction

Traditional drag reduction techniques fall into two categories: (1) insertion of air pockets/microbubbles, polymers, or small molecular weight lubricants into the boundary layer to increase fluid velocity near the wall [313] and (2) modification of the solid surface with riblets or other surface roughness to delay the transition from laminar to turbulent boundary layers, and interrupt flow or produce a 'slip-like' finite and stable fluid velocity at the wall [314]. Fibers, polymers, and a combination of fibers

and polymers inserted into the boundary layer can result in 15%, 36%, and 60% drag reduction, respectively. There is also synergism in the use of polymers and microbubbles. The fiber type matters with synthetic fibers like nylon yielding more consistent results than natural fibers like cellulose because of less surface roughness and aspect ratio (length to diameter, L/D) variation in the synthetic fiber. These techniques are well studied and have significant drawbacks: insertion of materials into the boundary layer is wasteful and does not take advantage of natural processes that have the benefit of millions of years of evolution. Structured surfaces do take advantage of natural processes but most proposals to date are expensive and not scalable. However, optimal drag reduction is achieved through the use of boundary layer modifying agents as well as surface roughness, i.e., natural riblets and the mucous layer on the sharkskin surface or feather barbs and preen oil on Gannet's feathers [315]. Deformability of the solid surface could also play a role.

Over the past decade, it has become apparent that superhydrophobic surfaces have the potential to significantly decrease drag for water vessels [316]. The enabling mechanism is the nano/micro-structure of a superhydrophobic surface, which promotes a suspended ("Cassie") wetting state where air pockets are trapped within the surface roughness [227,317]. While the classical no-slip rule of fluid mechanics is still valid for the water resting atop the solid fraction (i.e. liquid-solid interface) of the surface, the water above the air pockets is able to flow, resulting in partial slip and reduced friction [316]. Experimental measurements of water flowing over superhydrophobic surfaces have already revealed drag reductions of up to 40% for laminar flows [318–320] and (more importantly for the context of macroscopic watercraft) up to 50% for turbulent flows [321,322]. Another benefit of the air pockets promoted by superhydrophobic surfaces is their proven ability to greatly reduce corrosion [323,324] and marine fouling [325,326]. Unfortunately, it is now well known that the suspended Cassie state of a submerged superhydrophobic surface is extremely fragile and can

undergo a wetting transition to an impaled ("Wenzel") state, due to the water pressure exceeding a critical value [28, 316, 327] or the air pockets slowly dissolving over time [328–330].

This undesirable Cassie-to-Wenzel wetting transition is generally considered to be irreversible for most superhydrophobic surfaces, even when the Cassie state is thermodynamically stable and a restoring force (vibration, stretching, etc.) is applied (see Figure 8.1A,B) [28–30]. However, it has been recently reported that two-tier superhydrophobic surfaces can facilitate partial wetting transitions, where one of the two tiers of roughness still exhibit air pockets and a dewetting transition back to the full Cassie state is now possible (see Figure 8.1C) [1, 32, 331]. Ironically, it seems that nature already learned this lesson: duck feathers not only have multiple tiers of surface roughness [332, 333], but are also multiple layers deep, which could facilitate multiple partial wetting transitions that preserve the functional air pockets and are easily reversible back to the fully suspended Cassie state state (Figure 8.1D). Indeed, we hypothesize that this is exactly why ducks shake their feathers after emerging from a dive!

In this chapter, we study the wetting of layers of duck feathers in order to fabricate synthetic feathers that exhibit the following properties: a) Maximal pressure resistance to irreversible wetting transitions and b) Exhibit air pockets with long-term durability under prolonged submersion. In nature, most macroscopic organisms moving on water possess feathers over their skin for enhanced functionality. While lots of previous research has characterized the durability of underwater air pockets [327–330, 334, 335], they have always utilized a single-layered structure. Indeed, previous theory predicts that the critical pressure for water impalement is solely a function of the in-plane topography, and is independent of the depth of the surface structure [316, 333]. Unlike previous reports, this chapter reveals that multi-layered surfaces serve to compress air pockets during partial impalement, thereby greatly

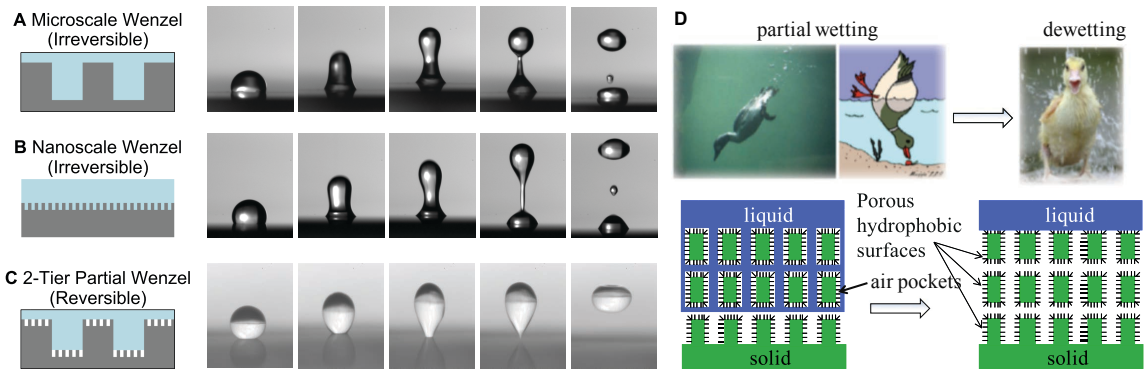

FIGURE 8.1: Dewetting transitions on SHPB surfaces. A-B) Wenzel state is only irreversible for single-tier superhydrophobic surfaces. C) A hierarchical surface facilitates partial Wenzel states that are easily reversible. Reprinted with permission from [1]. D) Here we hypothesize that the hierarchical roughness of duck feathers, combined with the additional hierarchy of multiple feather layers, similarly promotes partial and reversible wetting.

increasing the durability of the entrapped air.

8.2 Problem statement

Emissions of CO_2 due to commercial ships totaled 901 megatonnes in 2013 and are projected to double by 2050 [336], which would account for 8% of all industrial emissions of CO_2 worldwide. While the energy consumption of shipping vessels is not currently required to be reported by the industry [336], it can be estimated to be equivalent to 4 kWh per day per person for populations living in developed countries [337]. The cost of hull corrosion and fouling must also be considered; for example, it is estimated that fouling results in fuel efficiency losses and maintenance costs totaling $56M per year for the Navy's DDG-51 class of mid-sized naval surface ships [338]. These statistics motivate the need to engineer innovative coatings for ship hulls capable of reducing their skin friction and fouling, which would have a tremendous impact on both the environment and economy.

Various animals like sharks, dolphins, and birds have been studied for their drag

reducing ability during swimming [315, 339, 340]. The animals use a combination of body surface structure and swimming energetics to delay the onset of a turbulent boundary layer. "Sharkskin" riblets are well-known and the sharkskin motif has been leveraged for engineered drag reducing coatings [314]. The bird case is the least studied and the one that is relevant to this chapter. Lovvorn et al have shown that penguin feathers decrease the drag on the penguin below that which is expected from shape alone [340]. Recent work has shown that the hierarchical feather structure provides the necessary microstructure to achieve the superhydrophobic Cassie state [333,341]. Actual feathers have small barbules that intermesh at very short distances which in turn are coated with nano-hairs. The small structural features provide the texture to allow the fluid to remain suspended above entrapped air.

We suggest that a ship with a bare hull is analogous to naked skin, and desire to obtain a proof-of-concept that a "feathered" ship can uniquely impart desirable functionalities such as reduced drag, anti-corrosion, and anti-fouling. In this chapter, first we are going to characterize wetting/dewetting transitions of natural/synthetic feathers. To quantitatively characterize the critical pressure required for water to impale both natural (Figure 8.2A) and synthetic (Figure 8.2B) duck feathers, a custom-built pressure chamber was used (Figure 8.2C).

8.3 Experimental setup

The pressure chamber was custom built by the Engineering Science & Mechanics machine shop out of polycarbonate and Swagelok fittings were used to attach the pressure regulator/gauge and vent. Optical imaging of wetting/dewetting transitions were characterized using a digital camera (Canon EOS 5D Mark III).

8.3.1 *Natural feathers*

Natural duck wing feathers: Mallard, Grey Duck, and Peking Duck, were obtained from specialty companies and were gently cleaned by immersion in isopropyl alcohol and water, followed by hang drying. Environmental scanning electron micrographs of the feather structures were taken at Virginia Tech's Nanoscale Characterization and

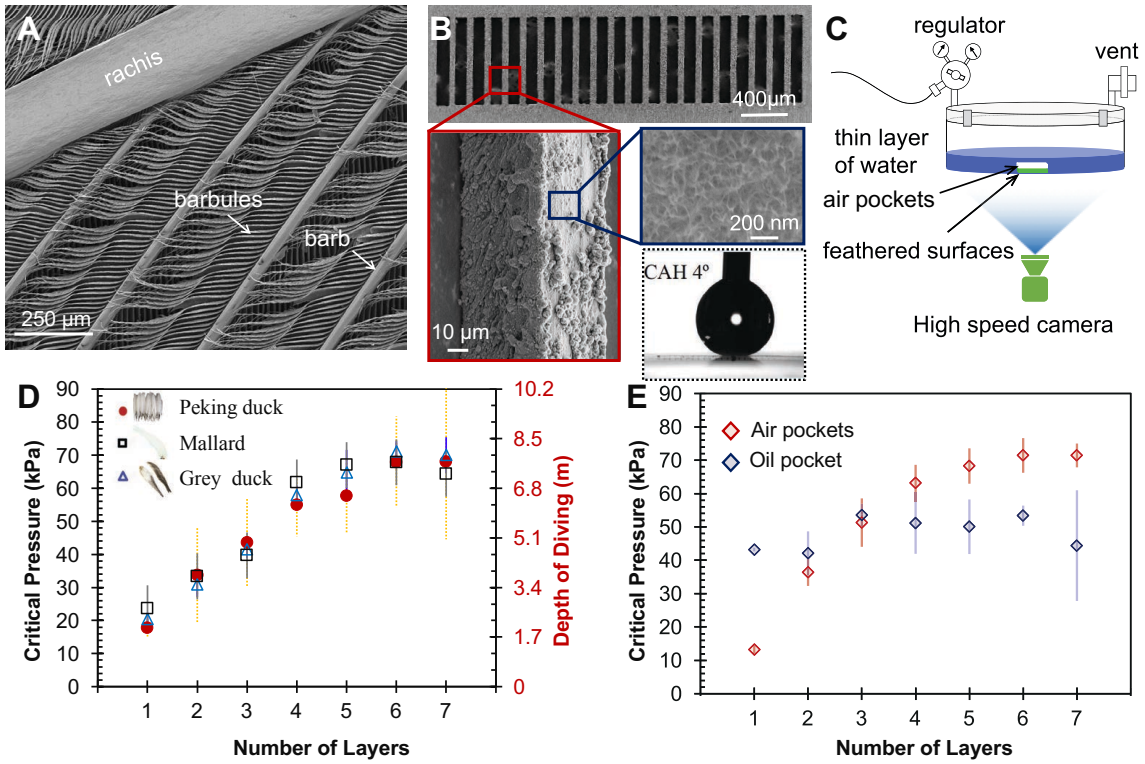

FIGURE 8.2: Morphology of duck feathers and effect of layers of feathers on wetting transition. A) ESEM of the barbs and barbules of a Mallard's wing feather. B) A synthetic feather composed of an array of microscopic aluminum "barbules" (enlarged barbule shown in red inset), which in turn were coated with an aluminum hydroxide nanostructure (blue inset). C) Experimental setup of the pressure chamber used for experiments. D) The critical pressure (left y-axis) for water impalement increases with number of layers. The corresponding depth of diving is shown on the right y-axis. Three different duck species were used. E) Results for superhydrophobic aluminum "barbules" showing similar behavior to natural duck feathers (red data series). Additionally, the aluminum feathers were impregnated with oil to show that the layering effect goes away when replacing air pockets with an incompressible fluid (blue data series).

Fabrication Laboratory (NCFL), which revealed that the feather barbs exhibited a diameter of 20 μm and were spaced about 350 μm apart. Extending transversely from the barbs was a second tier of roughness, called barbules, which had a diameter of 10 μm and spacing of 25 μm (Figure 8.2A). Note that the topography of the barbules is the most important, because wetting transitions are controlled by the smallest length-scale features.

8.3.2 Synthetic feathers

Inspired by the geometry of the barbules of natural feathers, we fabricated synthetic feathers (Figure 8.2B). Aluminum foil 50 μm in thickness was mailed to a specialty laser cutting company (Potomac Photonics, Inc.). An array of slots (100 μm wide) were cut into the foil, resulting in aluminum grooves that were 50 μm wide with a spacing of 150 μm. While slightly larger than the topography of natural barbules, the machinability of the foil had to also be considered. In nature, barbules are hairy, so a hot-water immersion recipe was used to coat the aluminum "barbules" with an aluminum hydroxide nanoroughness [268], followed by a conformal hydrophobic silane coating to render the synthetic feathers superhydrophobic (Figure 8.2B).

Feathers were stacked atop each other with the number of layers ranging from one to seven, with water-resistant tape holding the feathers together and securing them to the bottom of the chamber. After adding a shallow pool of water and sealing the chamber, the pressure of regulated nitrogen gas enclosed above the pool was gradually increased until the water has penetrated through all of the feather layers to reach the bottom of the container. This critical impalement is easily observed using a digital camera looking through the bottom wall of the transparent polycarbonate chamber.

8.4 Results and discussion

Figure 8.2D shows that the critical pressure for full impalement increases significantly with increasing layers of feathers, highlighting the unique functionality of multi-layered surfaces. The results show, for the first time, that the critical pressure for full impalement increases significantly with increasing layers of feathers, highlighting the unique functionality of multi-layered surfaces (Figure 8.2D). This dramatic finding is in contrast to the widely-accepted theory in surface science that the critical pressure for water impalement only depends on the pore size and is independent of the depth/number of layers. To see if the effect can be duplicated in a "synthetic" feather system, "barbules" were formed by laser cutting into aluminum (Al, Figure 8.2B) and the laser cut aluminum stacked in 1-7 layers. Both qualitatively and quantitavely, the critical pressure for impalement was identical to that of the natural feathers, increasing dramatically with the number of layers (Figure 3E). It should be noted that even a conservative goal of reducing ship hull drag by 10% would result in savings of approximately 1% of worldwide CO_2 emissions.

8.5 Theoretical model

Before considering multiple layers of feathers, let us begin with the baseline case of the critical water pressure required to impale a single feather. There is now a consensus in the literature that the critical impalement pressure represents the Laplace pressure required for the meniscus to achieve an advancing contact angle [329, 333]. Recall that for a meniscus of axisymmetric curvature, the Laplace pressure is represented by $\Delta P = P_w - P_g = 2\gamma/R$, where P_w is the water pressure, P_g is the pressure of the entrapped gas pockets, $\gamma \approx 0.072$ N/m is the surface tension of the water/gas free interface, and R is the radius of curvature of the meniscus. Once the contact angle of a meniscus reaches this advancing value, it will continually slide down the side walls

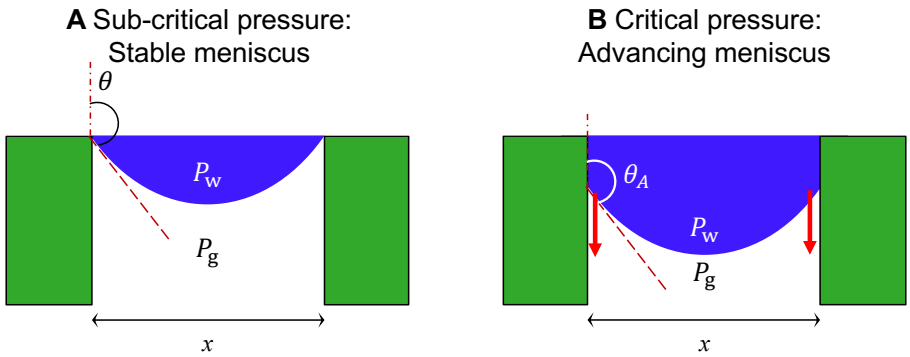

FIGURE 8.3: Critical pressure for Cassie to Wenzel state transition. A) For sub-critical Laplace pressures ($\Delta P < \Delta P_c$), the water meniscus is stable because its contact angle with the side walls is less than the advancing angle ($\theta < \theta_A$). B) At a critical Laplace pressure (ΔP_c), the meniscus continually invades the entrapped air pockets due to its advancing contact angle.

of the surface structure until reaching the bottom. This concept can be observed in Figure 8.3. For simplicity, let us assume that the synthetic barbules are rectangular in cross-section (rather than circular), which was the case for the laser-cut barbules. In this case, the critical Laplace pressure is given by:

$$\Delta P_c = P_{w,c} - P_g = \frac{2\gamma \cos\theta_A}{x}, \tag{8.1}$$

where x is the edge-to-edge width between two adjacent barbules (also can be defined as the critical length scale of the superhydrophobic surface "texture"). Using the controlled wettability (θ_A =160) and geometry ($x = 100$ μm) of our laser-cut barbules. Equation 8.1 predicts a critical pressure of $\Delta P_c = 1.35$ kPa. The apparent advancing contact angle of our laser-cut aluminum was already quite high at (θ_A =160). However, the gap between barbules, $x = 100$ μm, was relatively large in the context of non-wetting surface roughness. Therefore, one can consider the Nanoscribe to fabricate arrays of synthetic barbules where the gap size is decreased by two orders of magnitude down to $x = 1$ μm. These small-scale synthetic barbules could be coated with an equivalent superhydrophobic coating, this would result in a critical pressure of $\Delta P_c \sim 100$ kPa required to impale a single feather. This would represent

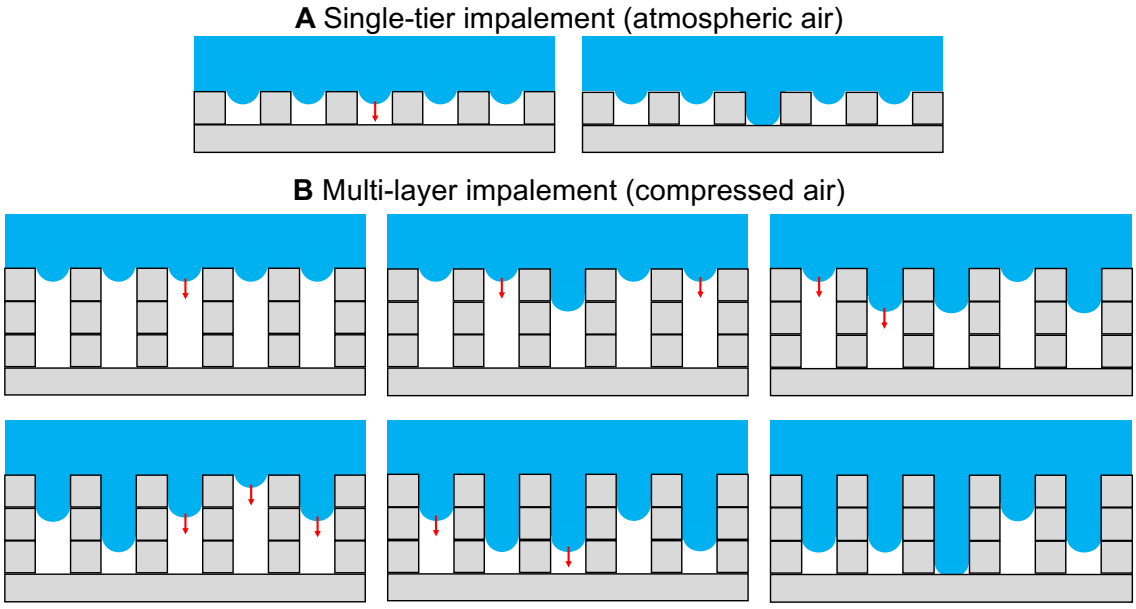

FIGURE 8.4: Model of how the number of layers affects impalement.

a dramatic enhancement compared to the current aluminum feathers, where $\Delta P_c \sim 1$ kPa.

To better understand the effects of layers on impalement pressure, we will also develop a probabilistic model guided by the concepts illustrated in Figure 8.4. First, consider a surface (i.e., "skin") that is only covered by a single feather layer (Figure 8.4A). The water will preferentially impale the feather through whichever pore is largest (or has a hydrophilic defect), while thousands if not millions of other pores will remain dry. Provided that the air can escape from between the feather and skin as the water advances through the defective pore, this means that the water can reach the skin with negligible air compression overall. Conversely, now consider the multi-layered case (Figure 8.4B). At the top layer, the water will preferentially advance at whichever pore is weakest, similar to before. However, after filling this initial pore, the water will encounter a different pore within the second feather layer. This new pore is no longer likely to represent the weakest point, as there are many other pores still to be considered for the other menisci remaining atop the first layer.

Thus, before this second layer can be impaled, the water will instead proceed to impale other pores within the first layer. Eventually, enough pores in the first layer are impaled that the weak link can be within the second layer in addition to the first. However, once again, upon impaling the first pore in the second layer, it is unlikely that the third layer could be penetrated right away at this localized point when compared to all the pores still available for penetration in the first and second layers. This logic flow continues in a probabilistic manner until, finally, the water manages to penetrate one of the pores in the bottom layer. By this point, however, the air/vapor has compressed significantly, which results in a much larger water pressure needed to obtain the critical Laplace pressure. In other words, the layers are not changing ΔP_c, but rather, increasing P_g which serves to increase $P_{w,c}$. This hypothesis has already been confirmed in Figure 8.4E, where the pores were filled with an incompressible oil rather than air, and no increase in was observed with increasing the number of layers.

In addition, to impalement due to water pressure, the gas pockets against diffusion should also be stabilized. In practical scenarios, water is not fully saturated with dissolved air, such that the air molecules located in the trapped air pockets will gradually diffuse into the suspended water [327, 329]. At first glance, this would seem to be a crushing blow to the prospect of trapping gas pockets underwater indefinitely. However, recent reports have solved this issue. While the diffusion of air away from the pockets is indeed unavoidable, it is thermodynamically possible to simply replace this air with water vapor over time. Specifically, it has been shown that the water vapor pockets will remain thermodynamically stable (i.e., avoid liquid condensation) when the following condition is met [330, 342]:

$$x < -\frac{4\gamma}{P_w - P_g}. \tag{8.2}$$

For our synthetic feathers with $x = 100\,\mu$m, for example, this would imply that vapor

pockets should be thermodynamically stable up to at least 3 kPa. This value will be increased to ≈ 300 kPa for the case of $x = 100\,\mu$m barbules gap size. If this became the limiting factor (as opposed to the impalement pressure), of course even smaller values of x could be attempted.

8.6 Conclusion

In nature, birds exhibit multiple layers of superhydrophobic feathers that repel water. Inspired by bird feathers, we compared the wetting characteristic of a single porous superhydrophobic surface to stacks of multiple surfaces. For both the natural and synthetic feathers, we found that the critical water pressure required for impalement increased by up to an order of magnitude by increasing the number of layers. We attributed this to the more tortuous path required for water to fully penetrate through the air pockets when layers are used, which serves to compress the entrapped air. To confirm this hypothesis, feathers impregnated with an incompressible oil did not exhibit any added resistance to water impalement when adding multiple layers.

9

Conclusions and Future Work

"The past cannot be changed. The future is yet in your power."

—Mary Pickford

9.1 Summary and conclusion

As outlined in Chapter 1, the motivation of this work has been to understand the dynamical phase-change phenomena which happen in our daily life. We accomplished that in chapters 2–8 for a wide variety of phenomena. Our observations can be summarized as follows:

In Chapter 2, experimentally, a drone camera captured the dynamics of a queue of cars accelerating from rest through a traffic intersection on a Smart Road. The flow efficiency through the green light remained constant even as the initial bumper-to-bumper spacing between the cars at rest was increased by over a factor of 20. While cars queued in close-packed "solid phase" configurations obviously need to drive a shorter distance to cross the intersection, this advantage was completely offset by

the lag time inherent to changing back into a loose-packed "liquid phase" for flow to safely resume (latent heat). This surprising finding challenges the longstanding convention of drivers inducing phase transitions at traffic stoppages, as we show that cars should maintain their regular spacing for increased safety with no loss in efficiency. Finally, motion-capture experiments with pedestrian traffic reveal that latent heat becomes negligible for slower-moving systems, which should indeed utilize close-packed queues.

In Chapter 3, inspired by the fact that ice itself can evaporate nearby liquid water droplets, we presented a passive anti-frosting surface in which the majority of the surface remains dry indefinitely.We fabricated an aluminum surface exhibiting an array of small metallic fins, where a wicking micro-groove was laser-cut along the top of each fin to produce elevated water "stripes" that freeze into ice. As the saturation vapor pressure of ice is less than that of supercooled liquid water, the ice stripes serve as overlapping humidity sinks that siphon all nearby moisture from the air and prevent condensation and frost from forming anywhere else on the surface. Our experimental results show that regions between stripes remain dry even after 24 hours of operation under humid and supercooled conditions.

In Chapter 4, we show for bubbles freezing under isothermal conditions that the latent heat released at the freeze front produces a dramatic Marangoni flow. This flow is strong enough to detach and entrain ice crystals growing from the freeze front, producing a beautiful swirling effect reminiscent of a snow-globe. As a result, a bubble freezes from multiple fronts growing in tandem, locking together like hexagons on a soccer ball. Under room temperature conditions, a bubble freezing on a chilled temperature stage exhibits a partially frozen equilibrium, due to the poor conduction across the thin film. The unfrozen bubble dome deflates over time, as the pressurized air escapes through micro-pores in the ice.

In Chapter 5, we characterize the physics of how liquids wick along icy structures.

We conducted an experimental and theoretical study for how fluorescent oils can wick along surface ice (i.e. dendrites) or bulk ice (frozen water). Surface ice was generated by growing frost on vertically-oriented aluminum plates of varying surface wettability. Oils wicking up hydrophilic frost sheets followed a surprising 1/3 scaling law with respect to time, in contrast to Washburn's law of 1/2. We rationalized this by considering the dendritic structure as an array of micro-corners, which have recently been found to exhibit the same 1/3 law. We also found that by using non-wetting surfaces, wicking rates approaching zero are possible due to the isolated distribution of frozen dropwise condensate from which the dendrites grow. This suggests that surface wettability can be exploited to tune and even halt the rate of ice wicking. Finally, we found that bulk wicking into a column of frozen water is not possible, due to the pore size of an ice lattice being smaller than the liquid molecules.

In Chapter 6, both experimentally and theoretically, we have show the direct correlation between the critical jumping diameter and the topology of the underlying surface structure. Experimentally, we fabricate six different nanopillar topologies and show that the critical jumping size varies widely and can be reduced by at least an order of magnitude compared to previous reports. Theoretically, we develop a three-stage incipient growth model that predicts how large a droplet must grow on a given surface before it inflates into the spherical shape required for coalescence-induced jumping. Remarkably, our model's predicted critical diameter agrees with the experimental measurements within a factor of two, without requiring any floating parameters. This chapter represents a substantial advancement in understanding how the quality of jumping-droplet condensation is dependent upon the underlying nanostructure, which should serve to optimize future condenser designs and better enable self cleaning and anti-fogging surfaces.

In Chapter 7, we report a new ecological mechanism for the liberation of pathogenic spores from non-wetting plants: naturally occurring dew cycles. While it is well-

known that severe winds or rain-splash can liberate spores from plants, this is the first demonstration of condensation ejecting spores from a plant's surface. Using side-view highspeed microscopy, we show that micrometric condensate spontaneously launches several millimeters from the leaf's surface, taking adhered pathogenic spores with it. The out-of-plane jumping motion is triggered by coalescence events that occur during condensation, which partially converts surface energy into kinetic energy. Specifically, we characterized the jumping-droplet-induced liberation of urediniospores of *P. triticina* from the leaves of the common wheat plant. By placing water-sensitive paper opposite a condensing leaf, we were able to quantify spore liberation rates of order 10 cm^{-2} hr^{-1} during a dew cycle. These liberated spores were capable of jumping up to 5 mm from the leaf's surface, more than enough to clear a typical laminar boundary layer for subsequent dispersal by the wind and/or gravity. Spores liberated by jumping-droplets are capable of long-range dispersal in winds as slow as 0.1 m/s, compared to our control experiments where even 10 m/s winds are only capable of removing larger agglomerates of spores from the leaf's surface. Leaf rust, caused by the fungus *P. triticina*, is one of the most significant diseases affecting wheat yields. Our findings in this chapter shed light on how this disease, among others, spreads amongst wheat crops. While the sudden expulsion of pathogen-laden droplets is certainly beneficial for the particular leaf in question, the subsequent dispersal is likely to spread disease to neighboring plants. In this respect, we suggest that condensation growing on diseased plants can be conceptually analogous to a 'sneeze.'

In Chapter 8, we have discussed how water fowl exhibit multiple layers of superhydrophobic feathers that repel water by trapping air pockets. The structure of feathers is typically hierarchical, with multiple barbules extending from each barb. Inspired by bird feathers, we have fabricated and utilized two-tier porous superhydrophobic surfaces and compare the wetting characteristics of a single surface to

stacks of multiple surfaces. The superhydrophobic feathers (both natural and synthetic) were submerged in water in a closed pressure chamber. Pressurized gas was regulated to measure the critical pressure for the water to fully penetrate through the surfaces as a function of the number of layers of feathers. It was found that the water pressure required for impalement increased significantly with an increasing number of layers. This is in direct contrast to conventional models positing that only the cross-sectional topography of a porous surface governs the critical wetting pressure, with the depth/layers of the surface playing no role. We attribute the importance of layering to the increased compression of the trapped gas pocket, which acts as a resistive force against the water. Our findings suggest that layered coatings could enable robust underwater superhydrophobicity to promote anti-drag and anti-fouling.

9.2 Future Directions

9.2.1 Optimizing safety and efficiency of queuing and merging on highways

Recall that our preliminary results demonstrated that maintaining liquid-phase packing during queuing did not negatively impact the departure flow rate compared to solid-phase queues. However, in the context of highway traffic, lane merging is another important aspect of traffic flow. By systematically varying the packing density of cars in motion on a two-lane highway and observing the resulting flow dynamics when the second lane has to merge into the first, we hypothesize that the overall flow rate may improve dramatically compared to the jamming inherent to merging in a solid-phase configuration. The results of such studies could also be used for autonomous vehicles which will lead the next transportation transformation, as intelligent systems can take over human manual driving and possibly reduce transportation accidents and casualties.

9.2.2 Passive anti-icing/frosting transmission lines

During cold seasons, ice accretion can increase the weight of transmission lines by 5X, causing them to become compromised or even severed. As a future plan of the presented anti-frosting technology (Chapter 3), one can identify simple physical patterns, such as extruded grooves or washers, that will control the spatial distribution of ice to reduce its weight and/or adhesion to the transmission lines.

9.2.3 Optimizing the overlapping dry zone

In this study, for the chemical micro-patterned anti-frosting surfaces, arrays of horizontal ice stripes were used. However, it is possible that a different shape for the ice stripes would get a larger dry zone.

9.2.4 Characterize the capillarity of oil spreading across snow

Instead of frosted surface which was used in this work one can study the wicking of oil across snow piles or frozen droplets.

9.2.5 Water tunnel testing of engineered 'feather-like' superhydrophobic surfaces

As mentioned in detail before, the reduction in drag for single-layer superhydrophobic surfaces is well known (approximately 50%). Completely unknown, however, is how this reduction in drag is affected by having partial impalement in a multi-layered feathered surface. One can gradually increase the dynamic pressure of the flow within the water tunnel, in order to vary how many layers of a multi-layered surface are effectively impaled with water. This should yield estimations of drag reduction as a function of the number of layers that are impaled.

Moreover, as we mention in Chapter 8, even when feather layers are able to withstand the desired water pressure, the air pockets could still slowly dissolve into the water over time. Therefore, the long-term durability of the air pockets should

be characterized using bottom-up imaging of the air layer and seeing how long it takes to collapse. Two strategies that could be attempted are: 1) Halting the air dissolution by matching the air pressure in the cavities to the partial pressure of air in the water [329], or 2) Designing the air pockets to have the dissolving air get replaced by water vapor that is stably in the gas phase [330].

Appendix A

Group Motion

A.1 Car motion through a traffic light

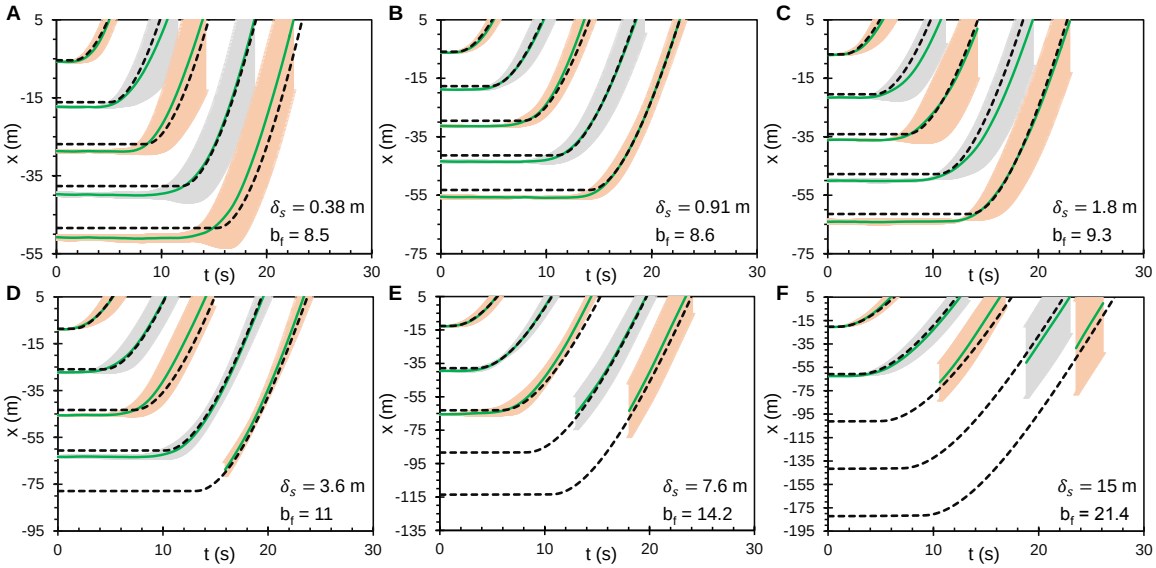

FIGURE A.1: Experimental (solid green lines) and theoretical (dashed black lines) displacements of the even numbered cars driving from rest through a traffic light. The shaded region about each experimental line represents the standard deviation of the three trials and the odd numbered cars are omitted for visual clarity. The initial location of the lead car's front bumper is defined as $x = 0$ and each vehicle effectively clears the intersection upon reaching $x = 5$ m. The initial bumper-to-bumper spacings of the cars were: (A) $\delta_s = 1.25$ ft (0.38 m), (B) $\delta_s = 3$ ft (0.91 m), (C) $\delta_s = 6$ ft (1.8 m), (D) $\delta_s = 12$ ft (3.6 m), (E) $\delta_s = 25$ ft (7.6 m), and (F) $\delta_s = 50$ ft (15 m). It can be seen that the OVM displacement curves agree with the real-life values within experimental uncertainty, with the exception of some minor disagreement in initial locations which was due to imperfections in lining up cars on the Smart Road.

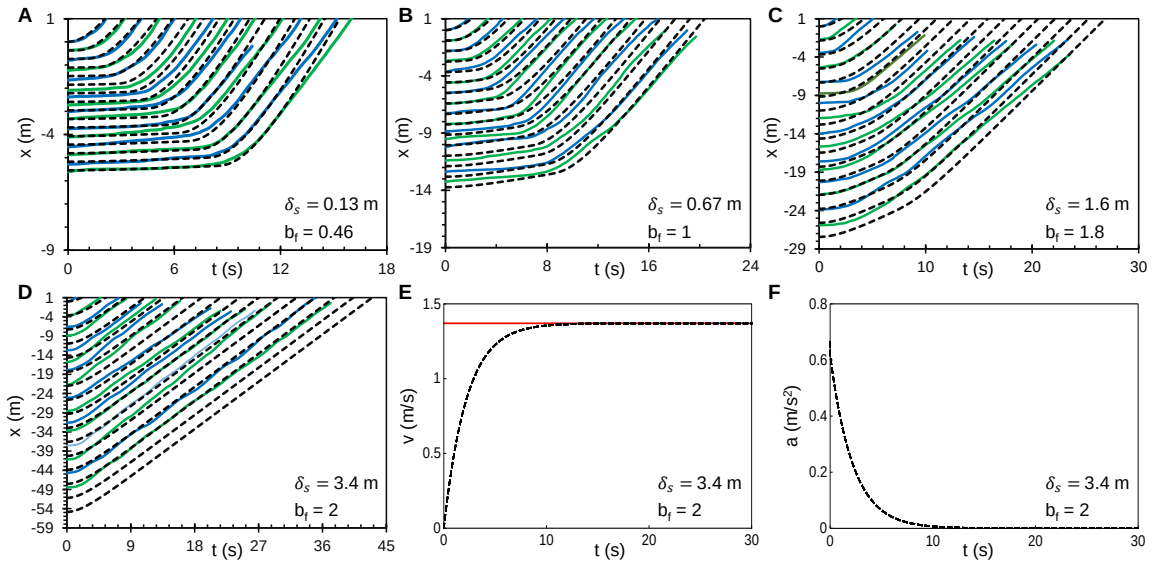

FIGURE A.2: Experimental (solid lines) and theoretical (dashed lines) displacements of 16 pedestrians motion from rest through an assigned line. The initial location of the lead person is defined as $x = 0$ and each person effectively exits the line upon reaching $x = 1\,\mathrm{m}$. The initial spacing (period) between each person was: (A) close-packed ($\delta_s = 0.13\,\mathrm{m}$), (B) $\delta_s = 0.67\,\mathrm{m}$, (C) $\delta_s = 1.6\,\mathrm{m}$, (D) $\delta_s = 3.4\,\mathrm{m}$. Experimental lines represent an average of 3 trials and the alternating blue and green colors are to help guide the eye. The theoretical velocity (E) and acceleration (F) curves of all 16 pedestrians walking from rest were identical for $\delta_s = 3.4\,\mathrm{m}$, showing the complete lack of latent heat at sufficiently large spacings. The red line in (E) shows the maximum speed achieved by pedestrians in the study ($V_{\max} = 1.37\,\mathrm{m/s}$).

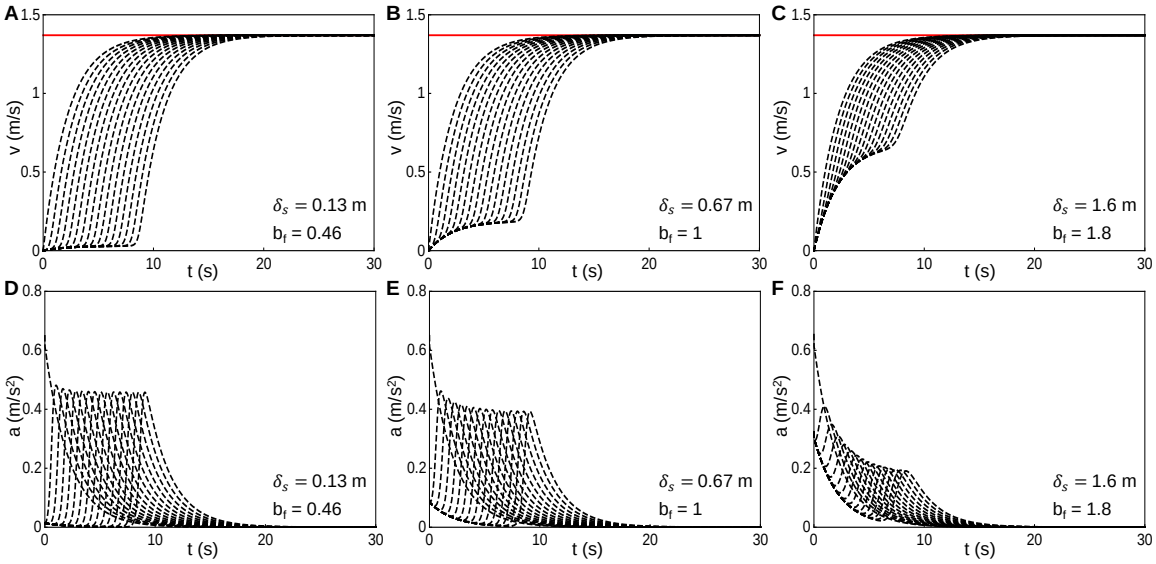

FIGURE A.3: Theoretical velocities of the 16 pedestrians in the line walking from rest for: (A) close-packed ($\delta_s = 0.13$ m), (B) $\delta_s = 0.67$ m, and (C) δ_s 1.6 m. The red line shows the maximum speed achieved by pedestrians in the study (Vmax = 1.37 m/s). Theoretical accelerations of the 16 pedestrians walking from rest for: D) close-packed ($\delta_s = 0.13$ m), (E) $\delta_s = 0.67$ m, and (F) δ_s 1.6 m.

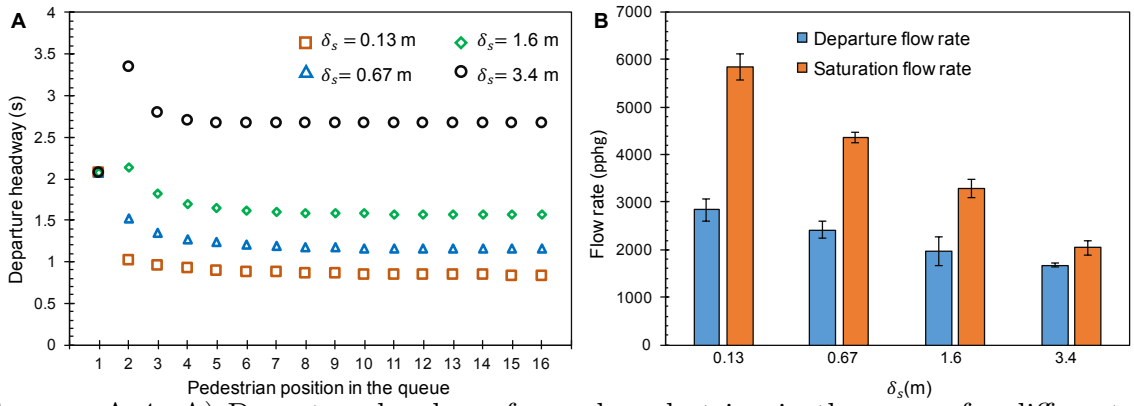

FIGURE A.4: A) Departure headway for each pedestrian in the queue for different gap spaces between pedestrians at rest (δ_s), obtained from the OVM model best-fit to the experiments. As with the vehicular traffic, the saturation headway is defined as the steady-state departure headway occurring from the fourth person in the queue onward. The saturation headway is increased by a factor of 3 as δ_s varies from 0.13 m to 3.4 m. B) Experimental departure and saturation flow rates for different spacings, in terms of the number of people who depart the line per hour of "green" (pphg). Both the transient (departure) flow rate and the saturation flow rate decrease with increasing spacing, showing that the effects of latent heat are minor for pedestrian traffic.

Appendix B

Characterizing Frost Growth

B.1 Setup and concepts

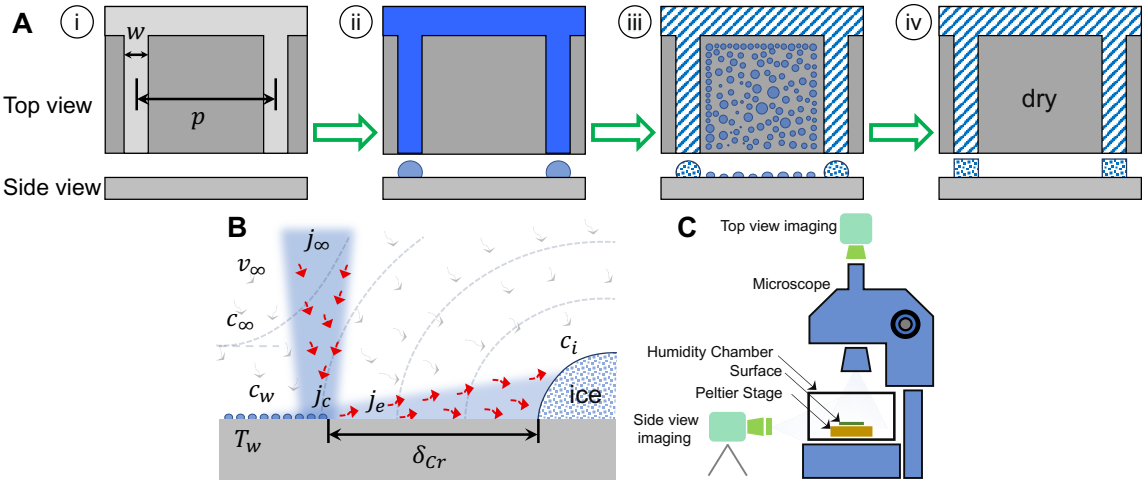

FIGURE B.1: A) Bird's-eye-view (top cartoons) and side-view (bottom cartoons) of the chemically patterned surface used to obtain the proof-of-concept of the overlapping dry zones. (i) An interconnected array of thin hydrophilic stripes (light gray) with width of w is micropatterned against a hydrophobic backdrop (dark gray). (ii) Supercooled water deposited or condensed onto the surface will preferentially fill the hydrophilic stripes. (iii) At chilled temperatures, the interconnected water stripes will freeze before the supercooled condensation on the hydrophobic regions, both due to the lower nucleation barrier and the larger volume. (iv) The array of ice stripes will now serve as overlapping humidity sinks, which will evaporate any condensate already on the hydrophobic surface and subsequently keep it dry from dew or frost. B) Schematic of the vapor flow around ice. The dry zone width (δ_{Cr}) can be found by balancing a droplet's in-plane evaporation flux, J_e, and out-of-plane condensation flux, J_c. C) Experimental setup for characterizing frost growth.

B.2 Surface coverage

Let's define three modes of failure: i) Dry zone failure, where condensation/frost can nucleate in the areas between the ice stripes ($p > 4\delta_{Cr}$); ii) Branching failure, where the ice stripes are able to grow along the solid substrate to invade the dry zones; iii) Set-up failure, where frost initially formed between the grooves prior to the freezing of the ice stripes due to the hydrophilicity of the plasma-treated aluminum.

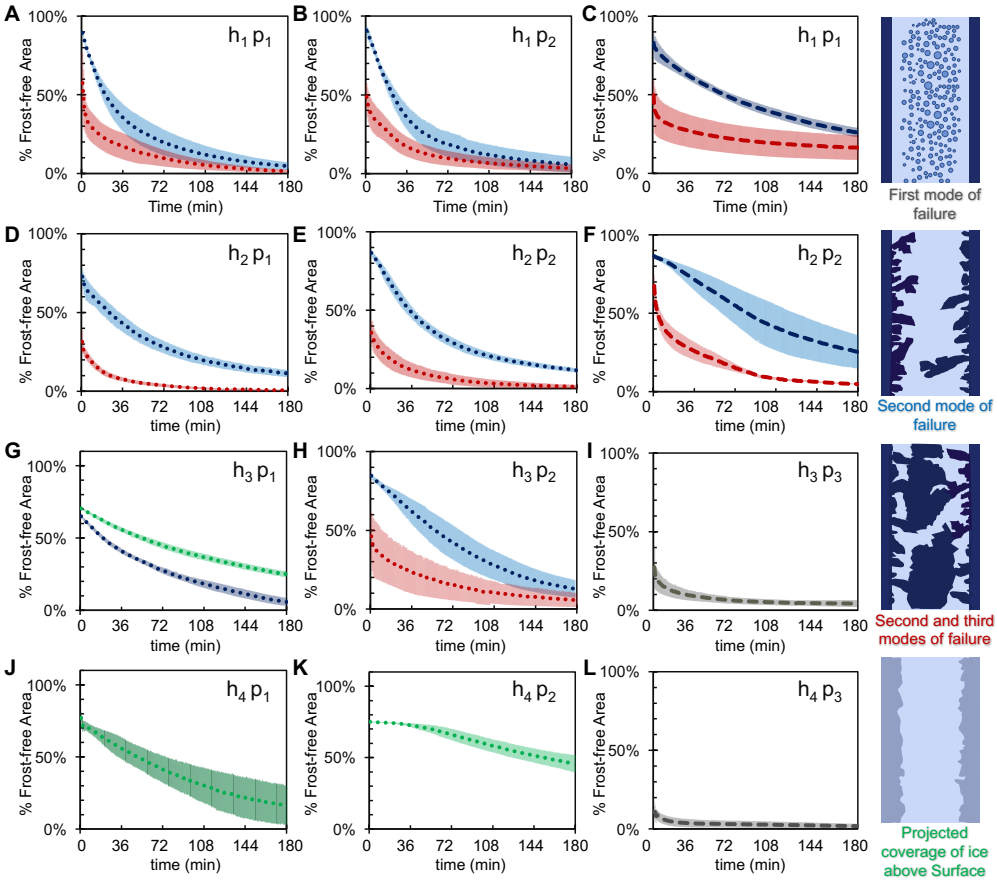

FIGURE B.2: The surface coverage of frost was defined here as the projected area of all frost visible from the top-down microscope, including the in-air coarsening of the elevated ice stripes above the floor. The three modes of failure are denoted by gray, blue, and red, respectively (see illustrations on right side of figure). For surfaces where the dry zones were maintained and the ice stripes were fully suspended in the air, the frost-free surface area is now signified by green data points. Dotted data points correspond to a supersaturation of $S = 1.5$ (A, B, D, E, G, H, J, and K), while dashed data points correspond to $S = 1.1$ (C, F, I, and L). The shaded region demonstrates one standard deviation between three trials.

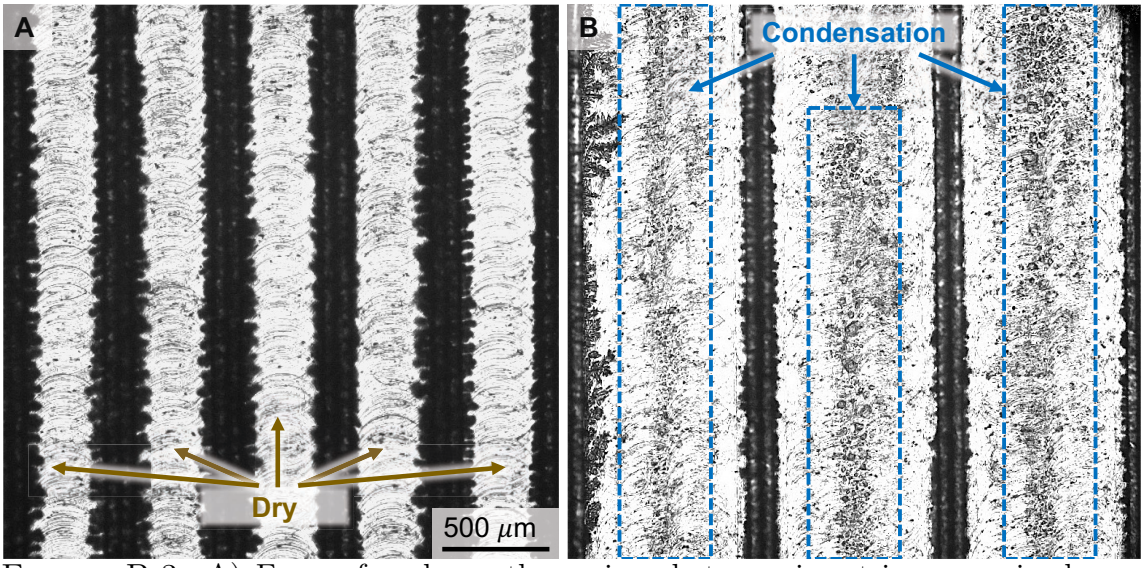

FIGURE B.3: A) For surface h_3p_1, the regions between ice stripes remain dry as indicated by the visible machine marks of the aluminum floor. B) In contrast, for a surface where the ice stripes exhibit a larger pitch, h_3p_2, the formation of supercooled condensation is easily observed which subsequently frosts over. Conditions were $T_w = -10\,^{\circ}\mathrm{C}$ and $T_\infty = 15.1\,^{\circ}\mathrm{C}$ in both cases, with $RH = 92\%$ for a and $RH = 53\%$ for B.

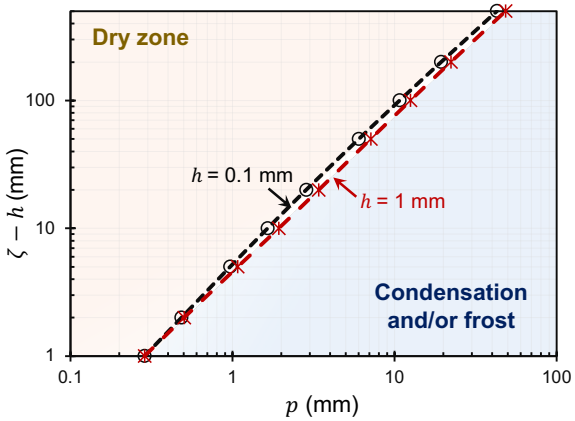

FIGURE B.4: This phase map shows that the domain size is linearly proportional to the dry zone, while the height (h) of the micro-fins elevating the ice stripes plays a secondary role.

Appendix C

Characterizing Freezing Bubbles

C.1 Surface tension measurements

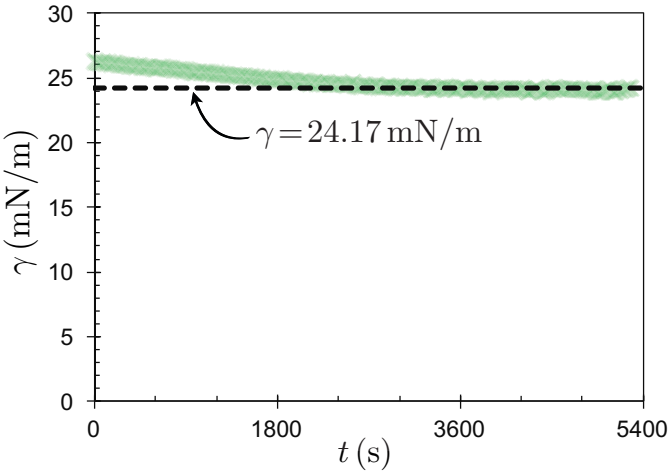

FIGURE C.1: The pendant drop method was used to measure the surface tension of the solution-air interface (ramé-hart, Model 590). The air temperature was $T_\infty = 21.3 \pm 0.7\,^\circ$C with a relative humidity of $RH = 36\%$. The slight decay in the measured surface tension over time was a result of the presence of 1% surfactant (i.e. dish soap) in the solution. After about 40 min, the surface tension value remained constant at $\gamma = 24.17$ mN/m.

C.2 Experimental setup for the isothermal environment

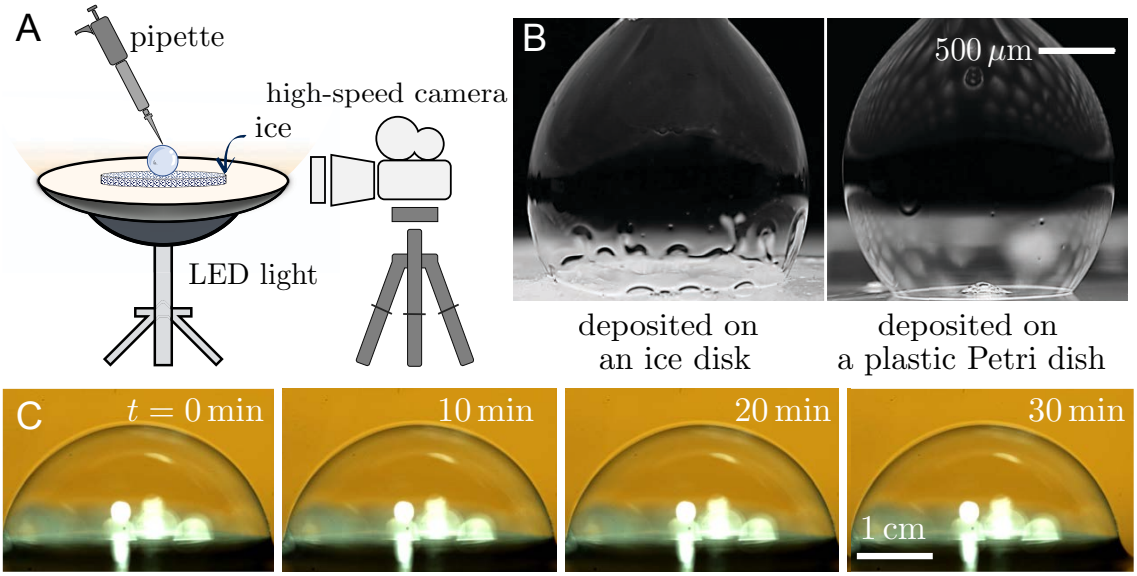

FIGURE C.2: (A) An ice disk and underlying light were placed on the floor of a walk-in freezer $T_\infty \approx -20\,^\circ\mathrm{C}$. The freezing dynamics of deposited bubbles were then captured with a high-speed camera. (B) When the bubble was deposited on an ice disk, a strong Marangoni flow was observed during freezing (left image). In contrast, During bubble freezing, a strong Marangoni flow was observed where the bubble was deposited on an ice disk (right image). This shows that the Marangoni flow is a direct result of the latent heat input by the freeze front. (C) When depositing the bubble on a dry silicon wafer in the freezer, there were no freezing events or Marangoni flow even after 30 min.

C.3 Marangoni flow for bubbles freezing in an isothermal environment

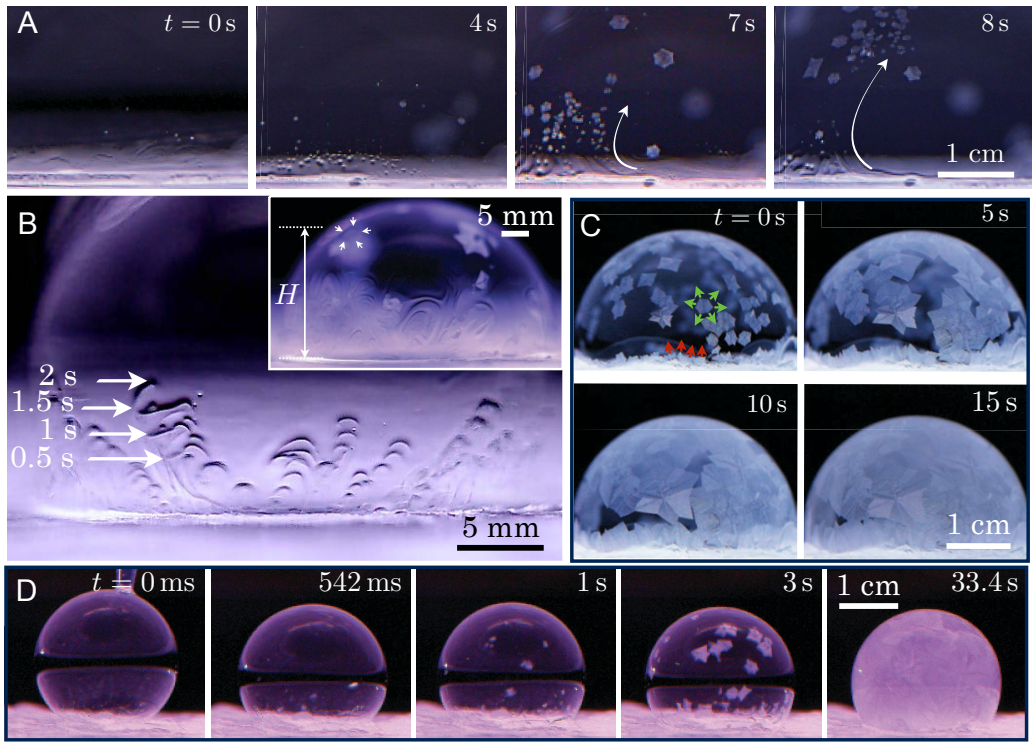

FIGURE C.3: (A) Visualization of the bottom-up Marangoni flow caused by local heating at the freeze front. This flow removed ice crystals from the freeze front and carried them up the bubble (white arrows). The bubble was deposited on an ice disk in a walk-in freezer with $T_w \approx T_\infty = -19 \pm 1\,^\circ\text{C}$. (B) Time-lapse sequence of the Marangoni flow that resulted from depositing a bubble of volume $\Omega = 10\,\text{mL}$ on an ice disk in the freezer ($T_w \approx T_\infty = -19.6\,^\circ\text{C}$). Time zero corresponds to when the bubble was first deposited onto the ice disk. Arrows show the location of the Marangoni flow. The inset shows the height (H) at which a thermal plume travels when a $\Omega = 10\,\text{mL}$ bubble was deposited on an ice disk in a walk-in freezer with $T_w \approx T_\infty = -19.1\,^\circ\text{C}$. Arrows show the periphery of the thermal plume. (C) Bubbles froze from the cooperative growth of the bottom-up freeze front (red arrows) and the suspended ice particles (green arrows). (D) The transient time scale ($\sim 100\,\text{ms}$) required for a $\Omega = 10\,\text{mL}$ bubble to achieve the equilibrium angle is quite small relative to total freezing time scale ($\sim 10\,\text{s}$). In other words, the ratio of spreading time to the freezing time is $\mathcal{O}(10^{-2})$.

C.4 Marginal regeneration

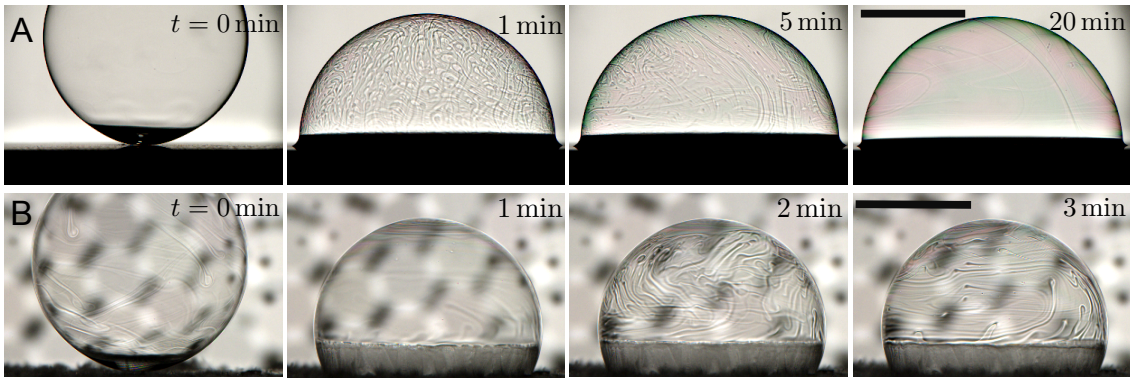

FIGURE C.4: (A) For a bubble deposited on a dry, room temperature substrate, plumes were continually generated through the ~ 10 min lifetime of the bubble due to marginal regeneration. In this case, the marginal regeneration is likely due to the mismatch in curvatures of the liquid meniscus wetting the surface versus the curvature of the bubble dome. (B) For a bubble deposited on a chilled substrate ($T_w = -20 \pm 1\,^{\circ}\text{C}$), marginal regeneration occurs only after the bubble reached to its partially frozen equilibrium (~ 100 s), most likely due to film drainage toward the frozen portion of the bubble. For both (A) and (B), experiments were conducted in a room with $T_\infty = 24.2 \pm 0.8\,^{\circ}\text{C}$ and $RH = 25 \pm 8\%$. Scale bars represent 5 mm.

C.5 Schematic of flow inside the liquid film

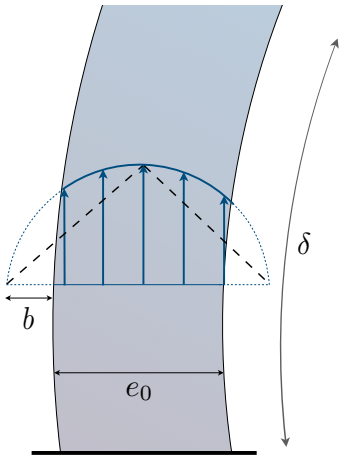

FIGURE C.5: Schematic showing the notations used in Equation 4.2 where the surface tension gradient, $\Delta\gamma/\delta$, was balanced by viscous stress, $\eta V/(b + e_0/2)$. As is shown, δ is the length scale of the temperature gradient driving the flow and b is the slip length of the Poiseuille flow along the bubble's film. Blue arrows show the parabolic velocity profile while the black dashed lines show the constant velocity profile used in this study as an approximation.

C.6 Computational method

Thanks to the axisymmetric nature of a bubble, computations were performed in 2D as shown in Figure C.7A. The 5 cm × 7.5 cm rectangular Peltier stage was approximated as a circular stage of radius $r_p = 3$ cm denoted by ob in Figure C.7A. The bubble was placed at the center of the circular stage. The top edges around the Pelter stage were treated as rounded corners (ab) of radius $r_0 = 0.5$ cm, in order to avoid recirculations that may adversely affect convergence. A weakly compressible fluid flow is considered for the air outside the bubble; the velocity inside of the bubble is set to zero at all times. The no-slip condition was applied on the bubble surface (ta), Peltier stage (ab), and the transition corner (bc). The pressure at the upper corner of the domain space farthest from the Peltier (point f) was set to an atmosphere ($P_{atm} = 1$ atm). Heat transfer was considered in the whole computational domain including the bubble. The bubble surface was defined as a sharp interface on which the temperature and heat flux are both continuous. The flow and heat transfer within the bubble film were neglected. The temperature at the Peltier stage (ob) was set to T_w while the temperature of the outer domain boundaries (de, ef, and fg) was set to T_∞. An adiabatic boundary condition was adopted on the rounded corner bc and vertical wall cd. The boundary go is the axis of axisymmetry where symmetry conditions are applied. Initially, the velocity was set to zero and the temperature was set to T_∞ inside of the whole domain. To obtain the solution at steady-state, each simulation was run for a flow time of 1,000 s. All computations were carried out using the laminar flow and heat transfer modules of COMSOL Multiphysics 5.3a.

The governing equations include the momentum equation

$$\rho\frac{\partial \mathbf{u}}{\partial t} + \rho(\mathbf{u}\cdot\nabla)\mathbf{u} = \nabla\cdot\left[-p\mathbf{I} + \mu\left(\nabla\mathbf{u} + (\nabla\mathbf{u})^T\right) - \frac{2}{3}\mu(\nabla\cdot\mathbf{u})\mathbf{I}\right] + \rho\mathbf{g}, \qquad \text{(C.1)}$$

the continuity equation

$$\frac{\partial \rho}{\partial t} + \nabla \cdot (\rho \mathbf{u}) = 0, \tag{C.2}$$

and the heat equation

$$\rho C_p \frac{\partial T}{\partial t} + \rho C_p \mathbf{u} \cdot \nabla T = \nabla \cdot (k \nabla T). \tag{C.3}$$

Here $\mathbf{u}$ is the velocity, ρ is the density, p is the pressure, T is the temperature, and $\mathbf{g}$ is the gravitational acceleration. The equation of state and material parameters of the air, including the specific heat under constant pressure C_p, thermal conductivity k, and dynamic viscosity μ, are directly obtained from the built-in material library of COMSOL. Air convection/circulation inside the bubble has not been considered as the bubble surface is assumed to be immobile. In this case, the natural convection outside the bubble does not cause air motion inside the bubble. Moreover, the film thickness ($\sim 1\,\mu$m) is too small to elicit any appreciable thermal resistance across the film. Rather, a sharp interface used and the temperature is assumed continuous across the interface.

C.6.1 Measurements of the air temperature profile above the substrate

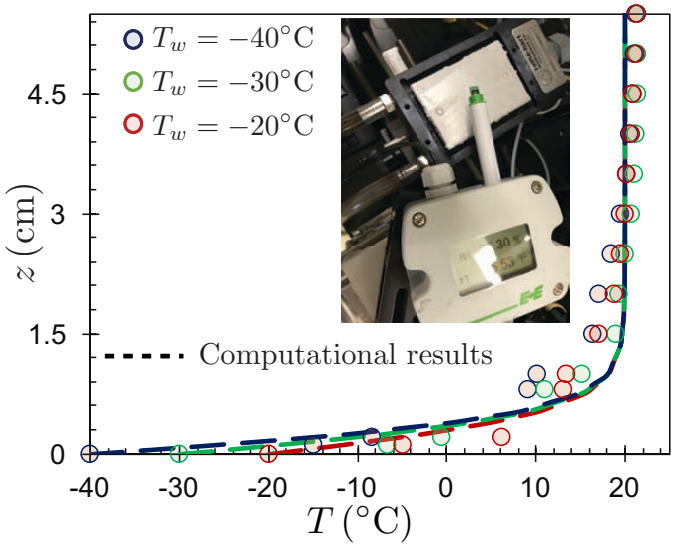

FIGURE C.6: Without any bubbles on the substrate, the air temperature profile was measured as a function of the height above the Peltier stage. The surface temperature of the Peltier was either $T_w = -40\,°\text{C}$ (blue circles), $T_w = -30\,°\text{C}$ (green), and $T_w = -20\,°\text{C}$ (red). These experimental results were validated against the corresponding computational results obtained using COMSOL Multiphysics (dashed lines).

C.6.2 Simulation of the air temperature profile above the substrate

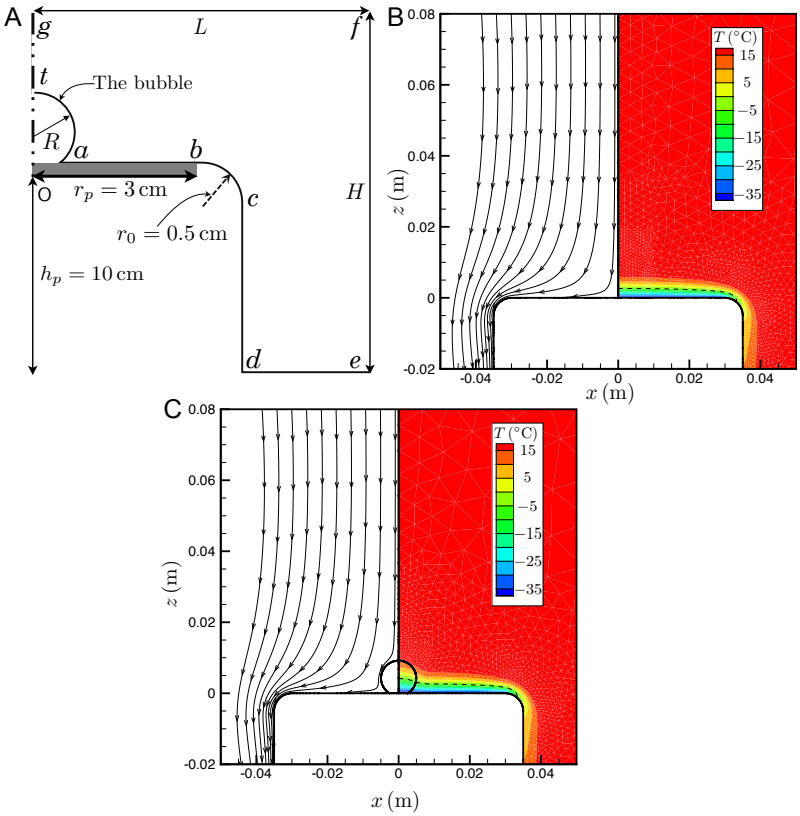

FIGURE C.7: (A) Schematic of the computational domain defined in COMSOL for the the air temperature measurements. (B) Computational solution of Equations C.1 to C.3 for a Peltier stage temperature of $T_w = -40\,^\circ\mathrm{C}$ in the absence of a deposited bubble. The left half of this image depicts the velocity field due to natural convection, while the right half shows the resulting temperature field. (C) Computational solution with a $\Omega = 500$ μL bubble placed in the center of a Peltier stage set to $T_w = -40\,^\circ\mathrm{C}$. The dashed line in (B) and (C) corresponds to $T = -6\,^\circ\mathrm{C}$.

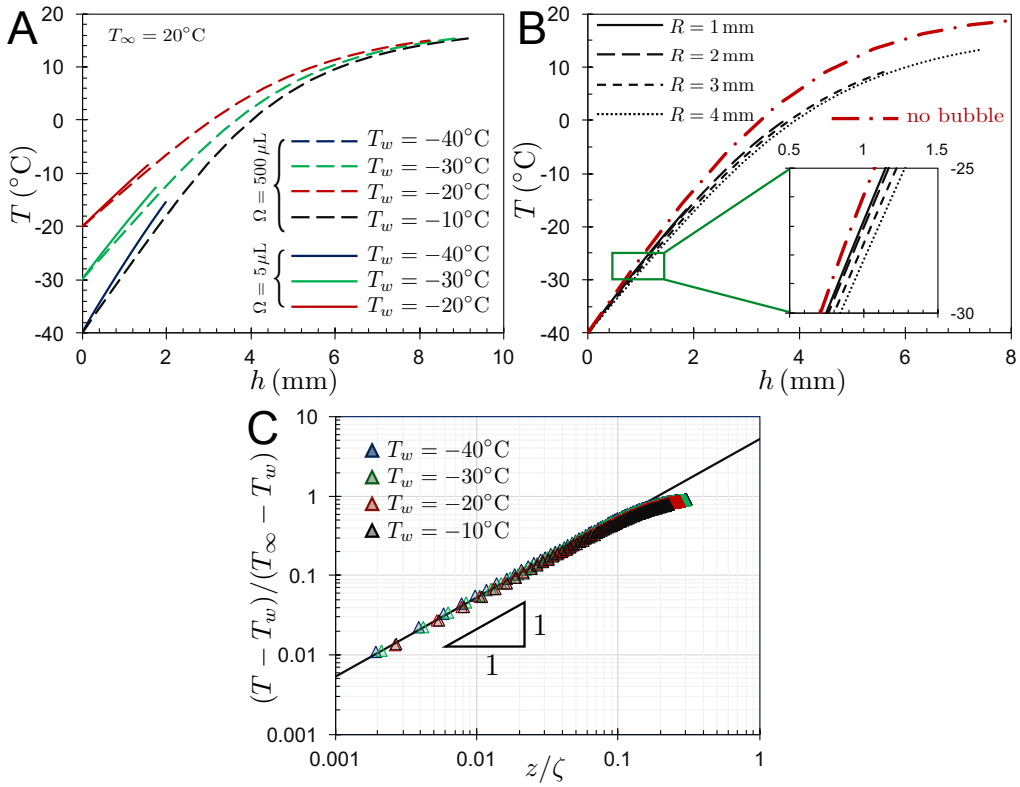

FIGURE C.8: (A) Steady-state temperature profiles of bubbles (prior to freezing) as a function of the height above the chilled Peltier stage. The two different bubble volumes correspond to those used experimentally: $\Omega = 5\ \mu$L (solid lines) and $\Omega = 500\ \mu$L (dashed lines), while the Peltier was either $T_w = -20\,°$C (red), $T_w = -30\,°$C (green), or $T_w = -40\,°$C (blue). (B) Steady-state temperature profiles of bubbles, where the Peltier is now fixed at $T_w = -40\,°$C while the bubble size is more widely varied from $R = 1\,$mm to $R = 4\,$mm (or no bubble at all). (C) When the temperature is non-dimensionalized with respect to $T_\infty - T_w$ and plotted against z/ζ, the computational data collapses onto a single curve for $z/\zeta < 0.1$. In this regime, the air is primarily cooled by conduction ($\nabla^2 T = 0$, black line). For $z/\zeta > 0.1$, natural convection becomes increasingly important. For all of these simulations, the air temperature was kept at a constant value of $T_\infty = 20\,°$C while the contact angle of the bubble was $\psi_0 = 149.0°$ similar to that seen in the experiments.

C.7 Freeze front dynamics in a room temperature environment

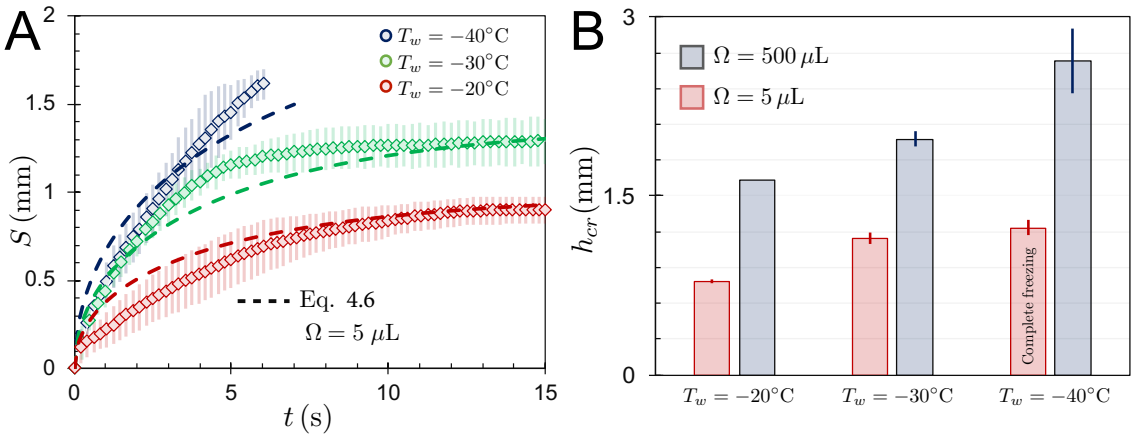

FIGURE C.9: (A) Experimental measurements (data points) and theoretical model (dashed lines) of the frozen arc length (S) against time. This graph is specifically for $\Omega = 5\,\mu$L bubbles, complementing Figure 4.5D in the main manuscript which focuses on $\Omega = 500\,\mu$L bubbles. The maximal value of S represents a complete bubble freezing for a surface temperature of $T_w = -40\,°$C and represents the halting of the freeze front for $T_w = -20\,°$C and $T_w = -30\,°$C. The theoretical results correspond to Equation 4.6, where $\beta_1 = 1$ and $\beta_2 = 30$. (B) The mean critical height from the substrate where the freeze front stopped for $\Omega = 5\,\mu$L (red) and $\Omega = 500\,\mu$L (blue) bubbles versus surface temperature. Error bars show one standard deviation between three trials. The average ambient conditions across all experiments were $T_\infty = 23.4 \pm 1.2\,°$C and a relative humidity of $RH = 42 \pm 14\%$.

C.8 Effects of frost growth on bubble freezing

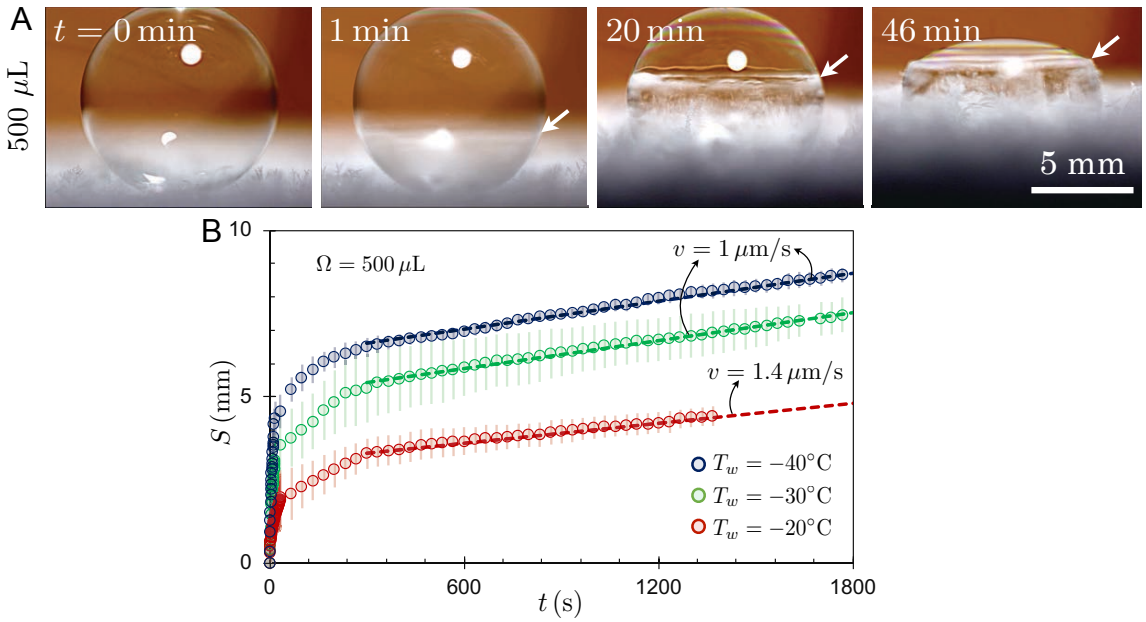

FIGURE C.10: A) For bubbles deposited on a frosted substrate in a room temperature environment, the frost thickness grew over time. This served to gradually translate the thermal boundary layer, ζ, upward with respect to the Peltier and extend the maximal height of the bubble's freeze front. However, the progression and eventual halting of the freeze front itself was completed within 1 min (2nd frame), such that it was not directly affected by the frost growth aside from subsequently being translated (3rd and 4th frames). B) The velocity of out-of-plane frost growth from the surface was modeled as $v \sim D(c_\infty - c_i)/\zeta$, where D is the diffusivity of water vapor in air, and c_∞ and c_i are the ambient vapor concentration and saturation vapor concentration over ice, respectively. For typical values of $D \sim 10^{-5}$ m^2/s, $c_\infty - c_i \sim 10^{-3}$ kg/m^3, and $\zeta \sim 10^{-2}$ m, the frost growth velocity is calculated as $v \sim 1$ μm/s which agrees with the experimental growth rate (dotted lines). Again, it is clear that the growth and halting of the freeze front is completed within tens of seconds (large initial slope), prior to being translated upward due to frost growth.

C.9 Thermographic images of freezing bubbles in a room temperature environment

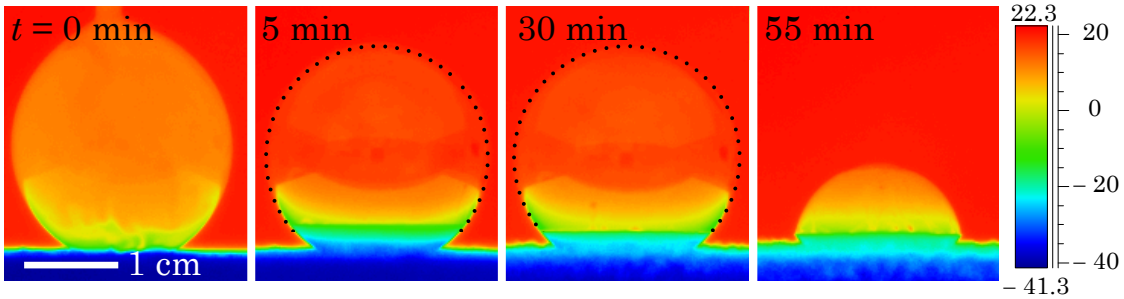

FIGURE C.11: A $\Omega = 10\,\text{mL}$ bubble was deposited on a frosted substrate of temperature $T_w = -40 \pm 1$ °C at a room temperature with $T_\infty = 23.3 \pm 1$ °C and $RH = 23 \pm 1.5\%$. The emissivity coefficient of ice was calibrated to $\epsilon = 0.98$. For better visualization of the periphery of the bubble (bubble-air interface), black dotted circles are drawn. While the latent heat did locally increase the temperature at the contact line, this did not generate strong Marangoni flows (as with the isothermal experiments) because the upper portion of the bubble was quite warm. The freeze front halted after $t_f \sim 10\,\text{s}$; the slight increase in the height of the freeze front over long time scales was simply due to frost growth on the substrate (see Figure C.10). In the final frame, the liquid dome atop the bubble collapsed.

C.10 Bursting of a partially-frozen bubble

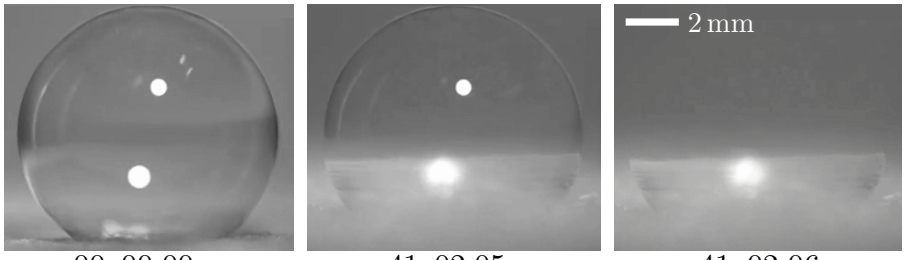

00:00.00 41:02.05 41:02.06

FIGURE C.12: A $\Omega = 500$ μL bubble was deposited on a frosted substrate of temperature $T_w = -30 \pm 1$ °C at a room temperature with $T_\infty = 23.8 \pm 1$ °C and $RH = 43.1\%$. The liquid dome atop the bubble was stable for 41 min and 2.05 sec (second frame). However, unlike the liquid collapse mechanism which is discussed in Figure 4.7, the liquid dome atop the bubble pops immediately. The time lapse between the second and third frame is 10 ms.

C.11 Control experiments using a pure surfactant

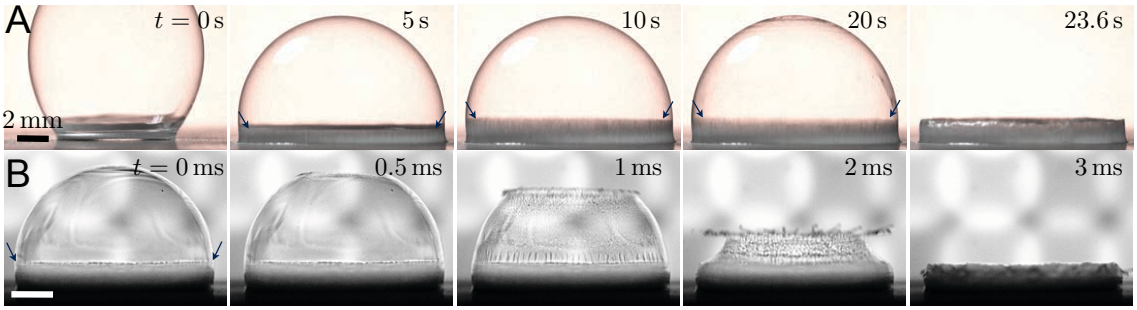

FIGURE C.13: (A) Freezing of a $\Omega = 500$ μL bubble that was made using a solution containing 1% SDS, rather than dish soap, as the surfactant. The bubble was deposited on an icy substrate with a temperature of $T_w = -20 \pm 1\,^{\circ}\mathrm{C}$ in an environment of $T_\infty = 22.1\,^{\circ}\mathrm{C}$ and $RH = 13.7\%$. Arrows show the location of the freeze front. Bubbles with 1% SDS mostly burst within $\mathcal{O}(10\,\mathrm{s})$. Drainage induced thinning of the bubble from top was responsible for the bursting of the bubble. (B) High-speed imaging showing the rapid bursting of a bubble at the end of its lifetime.

Appendix D

Characterizing Surface Topography

D.1 Fabrication method

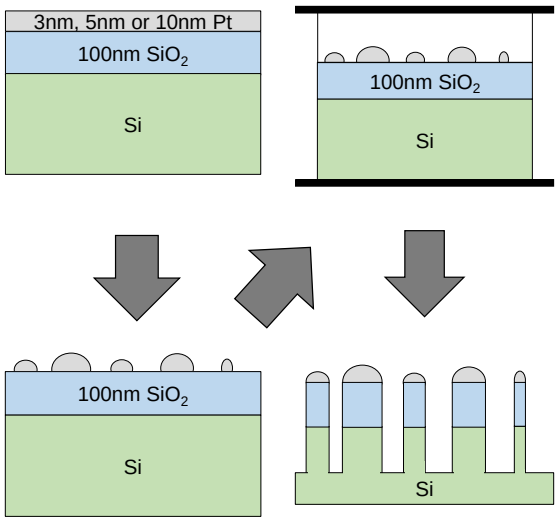

FIGURE D.1: Non-lithographic fabrication method to create six different silicon nanopillar arrays. Platinum films of thickness 3 nm, 5 nm, or 10 nm (upper-left) were thermally dewet to create an etch mask (lower-left); the thickness of the initial film determined the average diameter and pitch of the nanopillars. Subsequently, reactive ion etching (upper-right) was used to create nanopillars (lower-right) whose height was either 400 nm or 750 nm. By combining parameters, this resulting in six unique nanopillar topologies (see Methods section for more fabrication details).

D.2 Droplet coalescence events

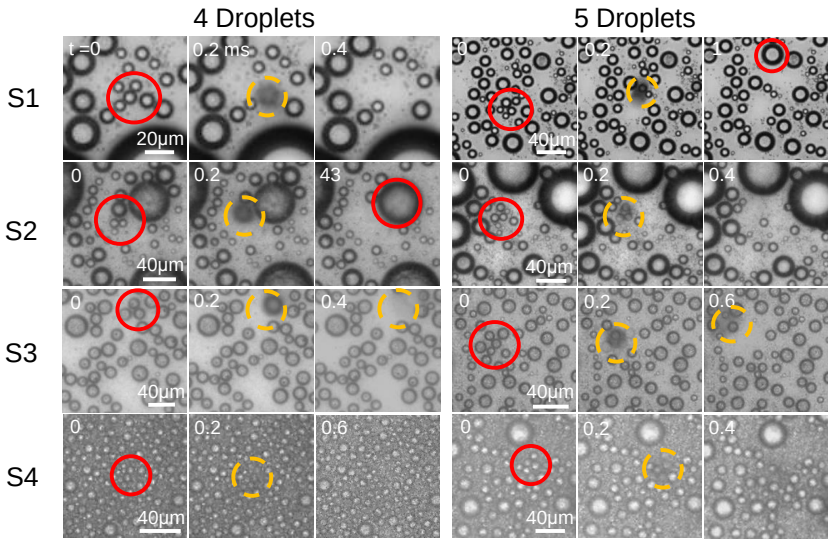

FIGURE D.2: Four-droplet and five-droplet coalescence events that capture the critical jumping size for each superhydrophobic surface. This figure serves as an extension of 2-droplet and 3-droplet jumping seen in Figure 6.2. Here, red circles indicate that the droplets are on the surface, while yellow indicates jumping.

D.3 Schematic of energetic growth model

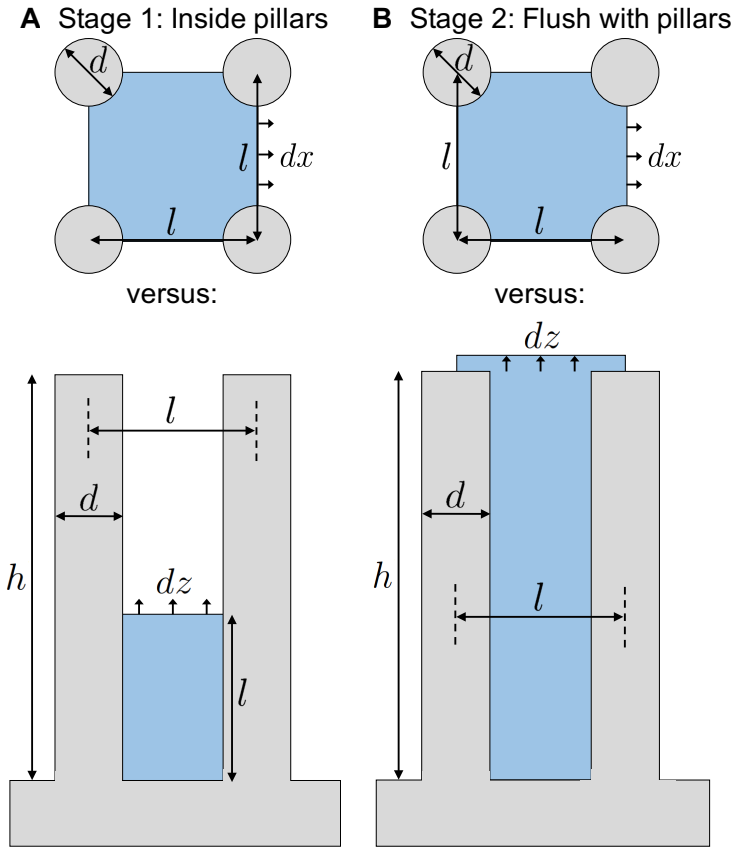

FIGURE D.3: Schematic of: A) First-stage and (B) second-stage of the energetic growth model for the initial case where $n=1$. Note that $n=1$ is only possible for the second-stage when $n_c=1$ for the first, which only occurred here for surface S5. Unlike when $n>1$, no pillar tops are being wetted for dx growth in stage two, as it was assumed that the droplet is pinned at its four corners such that only non-corner pillar tops are wetted during advancement.

D.4 Droplet coalescence events

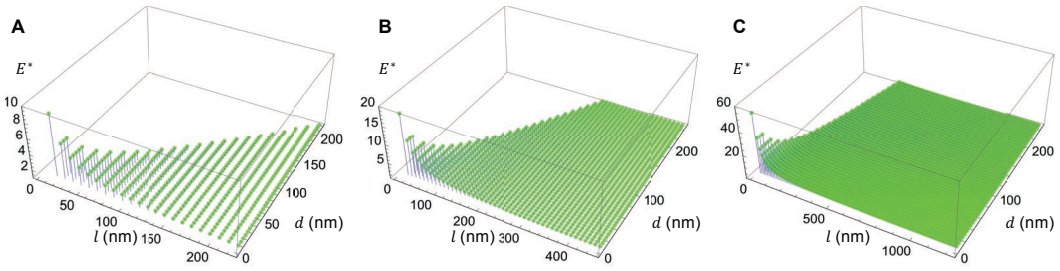

FIGURE D.4: 3D plots which show the value of E_{f}^* at the critical value of n_c as a function of pitch (l) and pillar diameter (d) for three different pillar heights of A) $h = 500\,\mathrm{nm}$, B) $h = 1000\,\mathrm{nm}$, and C) $h = 3000\,\mathrm{nm}$. When $E_{\mathrm{f}}^* \gg 1$ at n_c, this indicates that the first-stage of growth (i.e. reaching the pillar tops) was the primary bottleneck governing the value of D_c. Conversely, for $E_{\mathrm{f}}^* \approx 1$, the second stage is now the constraint (i.e. inflation into ambient), such that n must be iterated beyond the n_c value of stage one.

D.5 Full derivation of nanocone theory

Consider a surface decorated with an array of nanocones, where d is the basal diameter of each cone, h is the cone height, and l is the center-to-center pitch between adjacent cones (Figure D.5). The half-angle of the cone tip is given by β, such that $\tan\beta = d/(2h)$. We can now model the growth of a liquid embryo inflating within $n \times n$ unit cells of roughness. As with the cylindrical nanopillars, we assume that the roof of a droplet constrained within a unit cell(s) will be approximately flat, such that its height is equivalent to nl, which should be valid for hydrophobic nanocones with relatively small values of β. With this simplification, we can obtain analytical expressions for the sideways growth versus upward growth of a condensate droplet that is uniformly constrained within a unit cell(s), analogous to our model for nanopillars derived in the main manuscript.

Starting with sideways growth, it is helpful to construct the energy barrier from three subgroups. First, the energetic cost of expanding the ceiling and wetted floor of the droplet between the bases of the cones will be identical as with the nanopillars:

$$(\Delta E_{i,s1})_{1\times 1} = \gamma[(l-d) - (l-d)\cos\theta_A]dx, \tag{D.1}$$

where the first and second terms inside the brackets represent the expanded roof and wetted floor (see Figure D.5), respectively. Second, the new liquid-solid contact on the sides of the cones will extend by dx over a wetted diagonal ($l/\cos\beta$), rather than the wetted vertical (l) we saw with nanopillars:

$$(\Delta E_{\mathrm{i,\ s2}})_{1\times 1} = -2\gamma\cos\theta_A\frac{l}{\cos\beta}dx. \tag{D.2}$$

Third, there will be an extra roof term that accounts for the fact that the nanocones, unlike the nanopillars, do not exhibit vertical side walls. In other words, as a droplet grows laterally past the nanocones, even the projected fraction of the droplet that

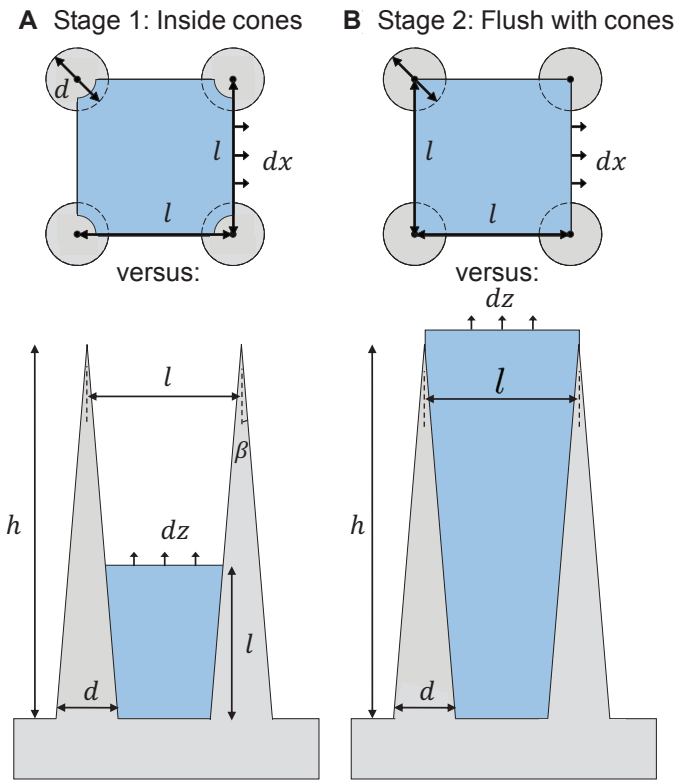

FIGURE D.5: Schematic of the: (A) First-stage and (B) second-stage of the energetic growth model adapted for nanocones, for the initial case of $n = 1$.

rests over the bases of the nanocones will exhibit an upper free interface:

$$(\Delta E_{\mathrm{i,\,s3}})_{1\times 1} = 2\gamma l \tan\beta dx. \tag{D.3}$$

Finally, Putting everything together, we obtain the total energy barrier inherent to lateral growth within a unit cell of nanocones:

$$(\Delta E_{\mathrm{i,\,s}})_{1\times 1} = \gamma[(l-d) - \frac{2l}{\cos\beta}\cos\theta_A - (l-d)\cos\theta_A + 2l\tan\beta]dx. \tag{D.4}$$

By adding the appropriate multipliers, this can be extended to any $n \times n$ unit cells (Figure D.6):

$$(\Delta E_{\mathrm{i,\,s}})_{n\times n} = n\gamma[(l-d) - \frac{2nl}{\cos\beta}\cos\theta_A - (l-d)\cos\theta_A + 2nl\tan\beta]dx. \tag{D.5}$$

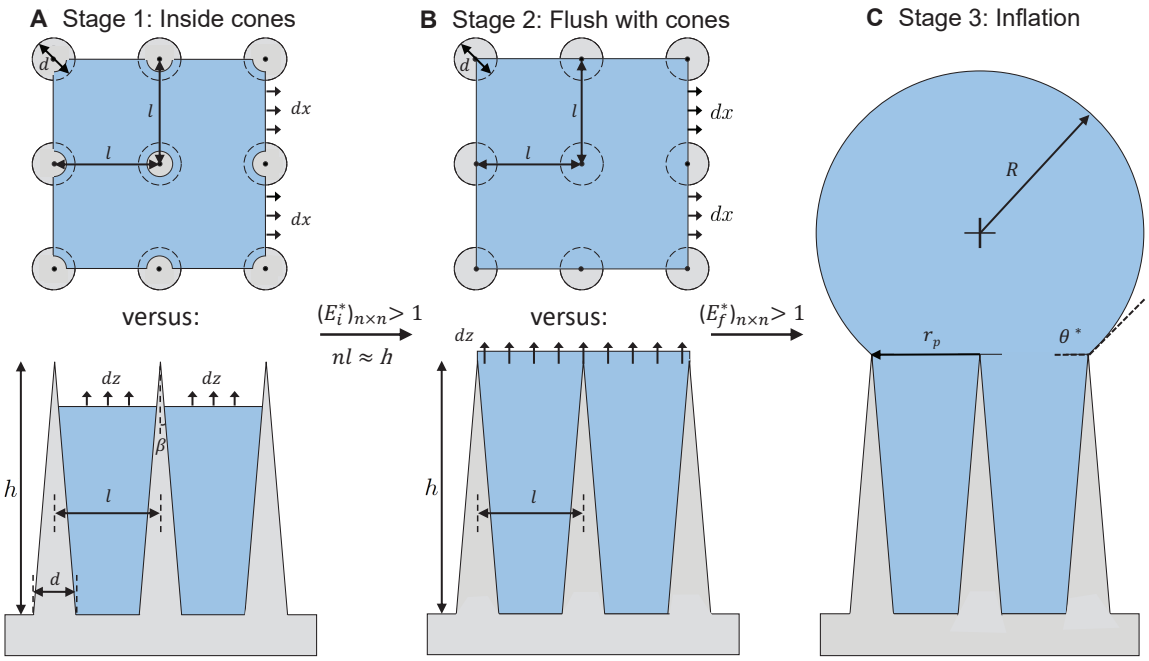

FIGURE D.6: Schematic of the three-stage model that correlates the critical jumping diameter (D_c) to the underlying conical nanotexture (h, d, and l), for a sample case of 2×2 unit cells of roughness ($n = 2$). A) The first stage of the model determines how many unit cells ($n \times n$) a droplet constrained inside of the nanocones must fill before it can reach the top; B) The second stage begins with the critical value of n attained from stage one and predicts whether additional unit cells must be filled before upward inflation into the air becomes energetically preferable to lateral growth; C) In the third and final stage, the droplet's pinned radius prescribed by stages one and two is used to find the critical droplet diameter where the apparent contact angle inflates to a large enough value (160°) to promote jumping upon coalescence.

Comparing Equations D.4 and D.5 to Equations 6.2 and 6.5 from Chapter 6, it can be seen that the energy barrier for sideways growth is increased for nanocones. Specifically, the second term now contains $l/\cos\beta$ rather than l, and there is a fourth term which is entirely new. This suggests that the energy barrier for growing sideways past nanocones will always be larger than with nanopillars.

Switching to upward growth, let's again build the energy barrier from three smaller pieces. First, the expanding free interfaces of the droplet's four sides is given as:

$$(\Delta E_{\mathrm{i,\ u1}})_{1\times 1} = 4\gamma[(l-d) + (2l+dz)\tan\beta]dz, \tag{D.6}$$

where the first term inside the bracket represents the area between the bases of the cones, while the second term is the area of the droplet's sides that is within the projected area of the cones (i.e. above the base). The second piece of the energy barrier accounts for wetting the side walls of the cones:

$$(\Delta E_{\mathrm{i,\ u2}})_{1\times 1} = \pi\gamma(2h - 2l - dz)\cos\theta_A \tan\beta \sec\beta dz, \tag{D.7}$$

which was obtained by calculating the lateral area of a truncated cone of lower radius $R_l = (h - l)\tan\beta$, upper radius $R_u = (h - l - dz)\tan\beta$, and height dz. The final piece of the upward-growth energy barrier considers the new area of the top free surface of the water:

$$(\Delta E_{\mathrm{i,\ u3}})_{1\times 1} = \pi\gamma(2h - 2l - dz)\tan^2\beta dz, \tag{D.8}$$

where the initial and final areas were given by $A_i = l^2 - \pi R_l^2$ and $A_f = l^2 - \pi R_u^2$. Adding all of these subgroups together yields the total energy barrier for upward growth within a single unit cell:

$$\begin{aligned}(\Delta E_{\mathrm{i,\ u}})_{1\times 1} = \gamma[4((l-d)+(2l+dz)\tan\beta) + \pi(2h-2l-dz)\cos\theta_A\tan\beta\sec\beta \\ + \pi\tan^2\beta(2h-2l-dz)]dz.\end{aligned} \tag{D.9}$$

When extending to $n \times n$ unit cells:

$$\begin{aligned}(\Delta E_{\mathrm{i,\ u}})_{n\times n} = n\gamma[4((l-d)+(2nl+dz)\tan\beta) + n\pi(2h-2nl-dz)\cos\theta_A\tan\beta\sec\beta \\ + n\pi\tan^2\beta(2h-2nl-dz)]dz.\end{aligned} \tag{D.10}$$

When comparing Equations D.9 and D.10 to Equations 6.3 and 6.6, again some differences emerge. The first term (free sides of droplet) is larger for the nanocones due to the tapering of the side walls. However, the tapering also serves to decrease the second term (liquid-solid area), so these differences largely cancel out. Finally, the new third term (top free surface) may increase the energy barrier somewhat, but

the extent would depend upon the value of β. By taking the ratio of the right-hand side of Equation S5 over the right-hand side of Equation S10, we obtain the energy barrier ratio $(E_{\mathrm{i}}^{*})_{n\times n}$ where upward growth is preferred for ratios exceeding one.

To gain a quantitative understanding of whether nanopillars versus nanocones better promotes upward growth during inflation, we must compare $(E_{\mathrm{i}}^{*})_{n\times n}$ for identical values of h, d, and l. Analogous to Figure 6.5A, Figure D.7A graphs the energetics of stage one growth for the six surfaces but now with equivalent nanocones. The right y-axis, which represents the constrained droplet growing uniformly until reaching the cone tops at $nl/h>1$, is unchanged from the equivalent nanopillar model. The left y-axis, which plots $((E_{\mathrm{i}}^{*})_{n\times n})$, is clearly enhanced when compared to equivalent nanopillars. Indeed, while only surface S2 achieved $(E_{\mathrm{i}}^{*})_{n\times n}>1$ prior to $nl/h>1$ for nanopillars, for nanocones this is achieved for surfaces S1–S4. In other words, the nanocones better promote the exclusive upward growth of condensate, so the droplets can reach the pillar tops with a smaller footprint compared to uniform growth.

Recall that the first stage of droplet growth is repeated for iteratively increasing values of n until either $(E_{\mathrm{i}}^{*})_{n\times n}>1$ or $nl/h>1$ is true. At this point, the droplet will grow to become flush with the tops of the nanocones, and the second stage of the model must be derived for the case of nanocones. For a droplet that is able to completely fill a single unit cell, the energy barrier for sideways versus upward growth is given by:

$$(E_{\mathrm{f}}^{*})_{1\times 1}=\frac{(\Delta E_{\mathrm{f,s}})_{1\times 1}}{(\Delta E_{\mathrm{f,u}})_{1\times 1}}=\frac{(l-d)(1-\cos\theta_A)-(2h/\cos\beta)\cos\theta_A+d}{\pi l}, \qquad \text{(D.11)}$$

which is identical to Equation 8 except for the second term in the numerator being modified from h to $2h/\cos\beta$ and the additional third term to account for the roof of the droplet over the cones. When extending to account for any number of unit cells

with the droplet pinned at the four corners:

$$(E_{\mathrm{f}}^{*})_{n\times n} = \frac{(\Delta E_{\mathrm{f,s}})_{n\times n}}{(\Delta E_{\mathrm{f,u}})_{n\times n}} = \frac{n(l-d)(1-\cos\theta_A) - n(2h/\cos\beta)\cos\theta_A + nd}{n\pi l}. \quad \text{(D.12)}$$

Interestingly, the n terms all cancel, such that the energy ratio is the same regardless of the size of the droplet. This is in stark contrast to stage two behavior for a droplet growing within nanopillars, where $(E_{\mathrm{f}}^{*})_{n\times n}$ increased with n (Equation D.9). The second stage of the nanocones theory has been plotted fir six difference surfaces in Figure D.7B. From this plot it is obvious that $(E_{\mathrm{f}}^{*})_{n\times n}$ does not depend on n. Analogues to the nanopillars, surfaces S5 and S6 never exhibit $(E_{\mathrm{f}}^{*})_{n\times n} > 1$ for any value of n. However, in contrast to the nanopillars, for surface S3, $(E_{\mathrm{f}}^{*})_{n\times n} > 1$ will not be satisfied for any value of n meaning that the droplets never inflate upward. This shows that stage two growth is actually inferior for nanocones compared to nanopillars, which was problematic for surface S3 since the critical value of n was governed by stage two rather than by just stage one.

Finally, the critical droplet diameter for jumping to occur can be predicted by using Equation 6.11 for surfaces S1, S2, and S4 (see Figure D.7C). All of the obtained critical jumping values (D_c) for the nanocones are smaller than those reported earlier in Chapter 6 for nanopillars, confirming that nanocones are generally superior to nanopillars.

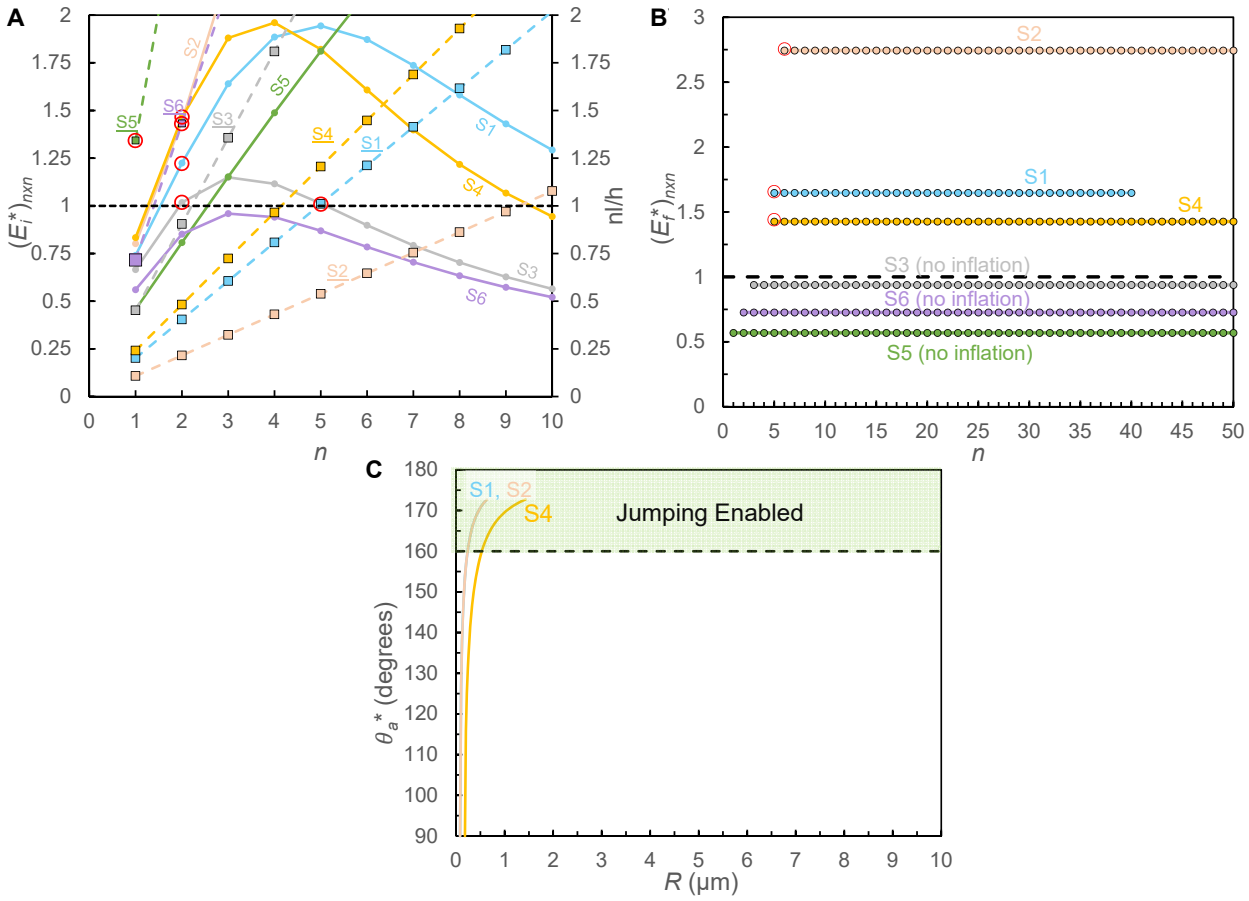

FIGURE D.7: Graphical depiction of the three-stage growth based on the nanocone model for the geometries of the six surfaces. A) Prediction of how many unit cells ($n \times n$) a droplet must fill before it grows to the top of the nanocones, which is satisfied when $(E_i^*)_{n\times n} > 1$ (left y-axis and solid lines) or $n\,l\,/h > 1$ (right y-axis and dotted lines). A red circle is drawn around the critical value of n_c where either of these conditions is first satisfied. B) Calculating the critical value of n_c where $(E_f)_{n\times n} > 1$ and upward inflation can first occur, which never occurs for surfaces S3, S5, or S6. C) Inflation of a droplet starting from a pinned radius of $R_p = 0.5\,n_c l$ and apparent contact angle of 90°, to determine the value of R_c where θ^* and jumping is enabled.

Appendix E

Wettability of Wheat Leaves

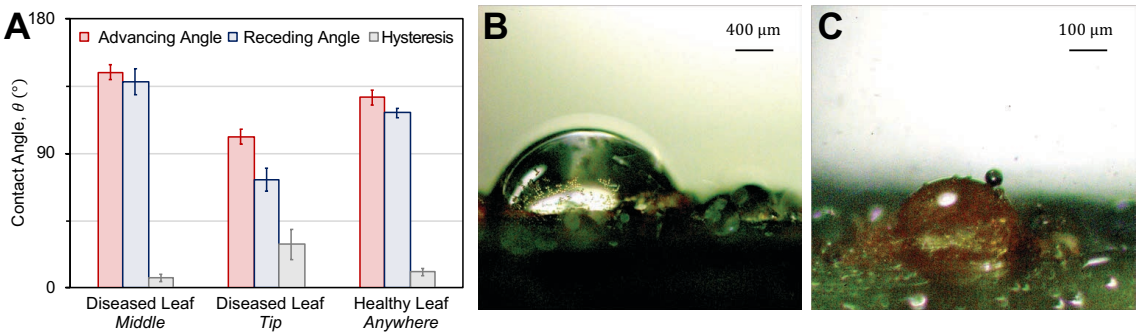

FIGURE E.1: A) Advancing and receding contact angles as measured on diseased and healthy wheat leaves. Results correspond to an average of three separate trials, and error bars represent a standard deviation. B) Self-assembly of spores on the surface of a wheat leaf. In particular, agglomerates of spores are visible near the bottom portion of the droplet where the light is reflected. C) A 50 μm diameter satellite droplet condenses atop the interface of a spore-laden 300 μm droplet, without coalescing.

E.1 Model for jumping with spores

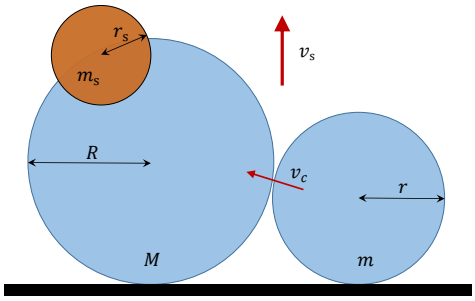

FIGURE E.2: Schematic of two dew droplets merging, where a spore is adhering to the larger droplet.

We draw from the argument of Mouterde *et al.* [303] in order to derive the velocity of coalescence-induced jumping of dew droplets with spores. Consider two droplets, the larger one having a radius R and the smaller one has a radius r. Let n spores of radius r_s adhere to the larger droplet (Figure E.2). The degree of asymmetry is given by $\epsilon = r/R$. Let R_f be the post-merged radius of the jumping droplet, including the spores.

By conservation of mass, it follows that:

$$R_f^3 = R^3 + r^3 + nr_s^3. \tag{E.1}$$

This equation can be re-written in terms of ϵ as:

$$\frac{R_f^3}{R^3} = 1 + \epsilon^3 + \frac{nr_s^3}{R^3}. \tag{E.2}$$

The capillary-inertial velocity with which the smaller droplet merges with the larger one is $v_c \sim r/\tau_c$, where τ_c is the time scale that can be obtained by equating the capillary force γr with inertia $\rho r^3 v_c^2 \sim \rho r^5/\tau_c^2$:

$$\tau_c = 2\sqrt{\frac{\rho r^3}{\gamma}}. \tag{E.3}$$

The pre-factor of 2 was found experimentally in [303]. Therefore $v_c = 1/2(\gamma/\rho r)^{1/2}$. Conservation of momentum dictates:

$$(M + m + m_s)v_s = mv_c. \tag{E.4}$$

Plugging in for the masses and v_c we get:

$$\begin{aligned}
v_s &= \frac{1}{2}\sqrt{\frac{\gamma}{\rho R}}\,\frac{\epsilon^{5/2}}{1+\epsilon^3+nr_{\mathrm{s}}^3/R^3} \\
&= \frac{1}{2}\sqrt{\frac{\gamma}{\rho R}}\,\epsilon^{5/2}\,\frac{R^3}{R_{\mathrm{f}}^3} \\
&= \frac{1}{2}\sqrt{\frac{\gamma}{\rho R_{\mathrm{f}}}}\,\epsilon^{5/2}\,\left(\frac{R}{R_{\mathrm{f}}}\right)^{5/2} \\
&= \frac{1}{2}\sqrt{\frac{\gamma}{\rho R_{\mathrm{f}}}}\,\epsilon^{5/2}\,\frac{1}{R_{\mathrm{f}}^{5/2}}\left[\frac{R_{\mathrm{f}}^3 - nr_{\mathrm{s}}^3}{1+\epsilon^3}\right]^{5/6} \\
&= \frac{1}{2}\sqrt{\frac{\gamma}{\rho R_{\mathrm{f}}}}\,\frac{\epsilon^{5/2}}{(1+\epsilon^3)^{5/6}}\left(1-\frac{nr_{\mathrm{s}}^3}{R_{\mathrm{f}}^3}\right)^{5/6} \\
&= \left(1-\frac{nr_{\mathrm{s}}^3}{R_{\mathrm{f}}^3}\right)^{5/6} v.
\end{aligned} \tag{E.5}$$

E.2 Spore-counting experiments

E.2.1 Protocol and design

Three wheat leaves were selected from three-month-old plants, inoculated eight days prior to the experiments. Each diseased leaf was divided into a top, middle, and bottom section as shown in Figure E.3A. We conducted spore-counting experiments only with the middle part, as it was visibly more sporulated than the top and the bottom. The middle section was then further divided into three sections – upper, central and lower.

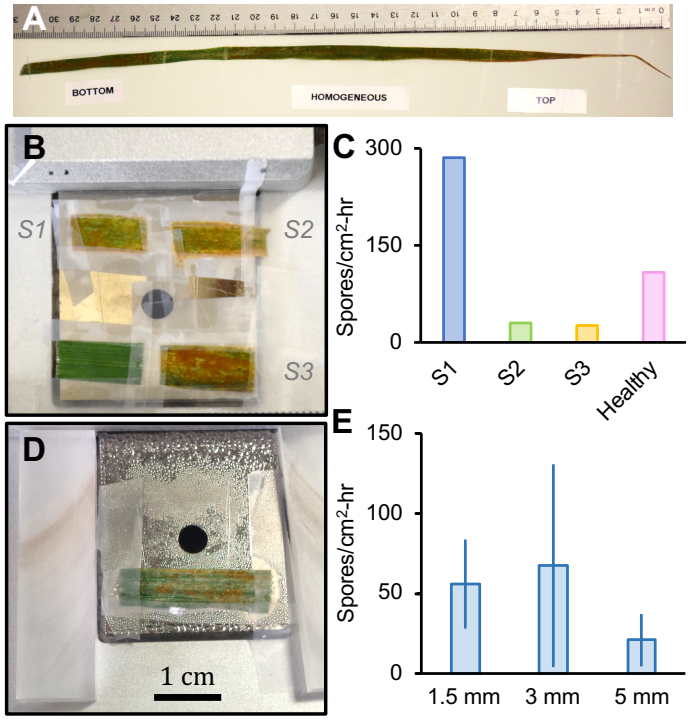

FIGURE E.3: A) A typical sporulated wheat leaf and its divisions. The middle section was usually the more homogenous and densely sporulated section. B) Preliminary setup with 4 wheat leaves: 3 diseased and 1 healthy, all put together on a Peltier Stage with a water-sensitive paper at a height of 1.5 mm above the leaf. C) Evidence of cross-talk: spores were collected even over the healthy leaf. D) Final setup comprising only one leaf. E) Number of spores liberated from the leaf surface in 1 hr as collected at a height 1.5 mm, 3 mm and 5 mm respectively.

In our preliminary experimental design, four leaf pieces were simultaneously

bonded to the Peltier stage, each piece being a 1 cm × 3 cm portion. Three of these pieces were from three different diseased leaves while one was a control from a healthy leaf. The cut pieces were thermally bonded to a Peltier stage (Figure E.3B) and the absorbent paper was held above the Peliter using the acrylic spacers as described in Materials and Methods. The motive for placing four different leaves all together on the Peltier stage was to directly compare their spore liberation rates under absolutely identical conditions. However, as seen in Figure E.3C, spores were collected even for the water-sensitive paper lying over the healthy leaf which had no spores. Even when we tried the same experiment with only one sporulated leaf and one healthy leaf, spores were still observed to collect on the paper above the healthy leaf. As a control test, a healthy leaf was placed in isolation on the Peltier stage and no spores were found on the paper as expected. This means that the spores over the healthy leaf in the other cases were due to oblique jumping trajectories from the diseased leaves.

Therefore only one leaf section should be tested at a time, otherwise it is impossible to know which spore came from which leaf section. The final set-up thus comprises only a single leaf on the Peltier stage (Figure E.3D). Experiments were done for heights of 1.5 mm, 3 mm and 5 mm respectively. Figure E.3E shows the average number of spores collected from 1 hr at different heights from the leaf surface.

E.2.2 Spore counting and clustering protocol

The water-sensitive Sygenta paper is unique in its property of changing color from yellow to blue when water touches it. However, spores collected on the paper sometimes showed a blue splash pattern, and sometimes did not. This was because micrometric droplets that carry spores were not always large enough to cause the paper to change color. Furthermore, the process of raster-scanning and counting often took hours, and in that time the paper could possibly lose moisture and consequently lose some color too. Therefore we focused more on the quantification of the spores, which were

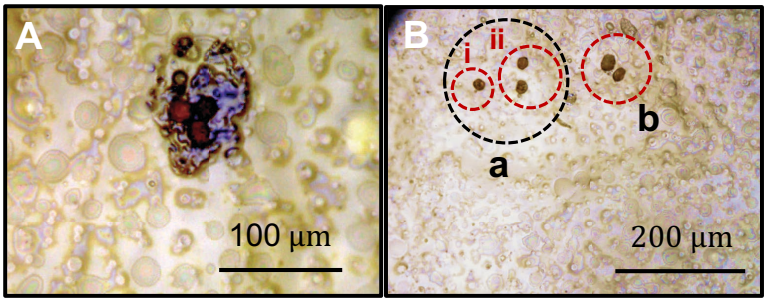

FIGURE E.4: Spore-Counting Experiments: A) Experimental micrograph of three sporse collected on the water-sensitive paper with a splash pattern. B) Spores collected on the paper without a splash pattern. Red circles indicate clusters separated by one-spore distance or less.

easy to identify, as opposed to the droplets carrying the spores.

To estimate how many spores were adhering to a single jumping droplet that reached the paper, the following protocol was followed:

1) When a blue pattern was visible (Figure E.4A), all spores within the blue region were considered to be within a single droplet. It is of course possible that a second droplet (with or without spore) had jumped onto the same spot, thus giving a false impression of more spores per jumping droplet than really existed. However, the density of droplets and spores on the paper was moderate enough that such cases can be considered rare and neglected for the purposes of estimating spore clusters per droplet.

2) For smaller jumping droplets, the blue pattern was not always visible on the paper. In this case, we assume that spores on the paper were from the same droplet if the edge-to-edge distance between any two spores is less than the size of the spore diameter ($\approx 20\,\mu$m). An illustration of this method is shown in Figure E.4B). A is not considered as a cluster, but B is. This is because unlike B, A has sub-units i and ii which are separated by more than 1 spore distance.

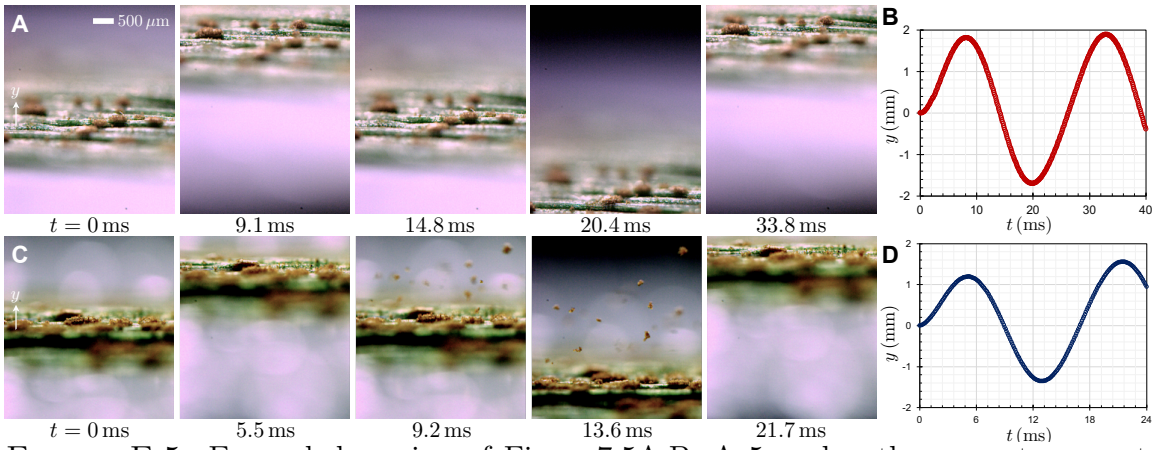

FIGURE E.5: Expanded version of Figure 7.5A,B. A 5 cm length segment was cut from a typical sporulated wheat leaf and directly taped to a mechanical wave driver (PASCO, SF-9324). The amplitude and frequency of the driver were controlled using a function generator (Agilent, 33210A) along with a power amplifier (KROHN-HITE, 7500). The resulting vibration was captured using a side-video high-speed camera. A,B) No spores were removed from the leaf when the frequency was set to 40 Hz with a peak-to-peak amplitude of 3.6 mm. C,D) In contrast, some of the spores were detached from the leaf when the frequency was set to 60 Hz with a peak-to-peak amplitude of about 3 mm, which corresponds to a maximum velocity of $v_v \approx 0.6$ m/s.

E.3 Vibration experiments: vertical dislodging of dry spores

The following scaling analysis can roughly estimate the wind velocity required to generate the critical vibration necessary for spore liberation. The acceleration imparted by the vibration stage is $4\pi^2 f^2 A$, where f is the frequency and A is the amplitude. For the best-case scenario of the wind attacking the leaf perpendicularly, the wind imparts a force $F_w \sim (1/2)\rho_a U^2 A_l$, where A_l is the leaf area. This force is equated to $\rho_l A_l t 4\pi^2 f_c^2 A_c$, where $t \sim 10^{-4}$ m is the typical thickness of the wheat leaf and the critical vibrational acceleration was achieved at $f_c = 60$ Hz and $A_c = 1.5$ mm (Figure E.5C,D). A sporulated leaf has a density close to water, $\rho_l \sim 10^3$ kg/m^3. This gives a critical wind speed of $U_c \sim (8\pi^2 f_c^2 A_c t \rho_l / \rho_a)^{1/2}$. Plugging in all values, we obtain $U_c \sim 1$ m/s.

E.4 Wind Tunnel experiments: shearing off dry spores

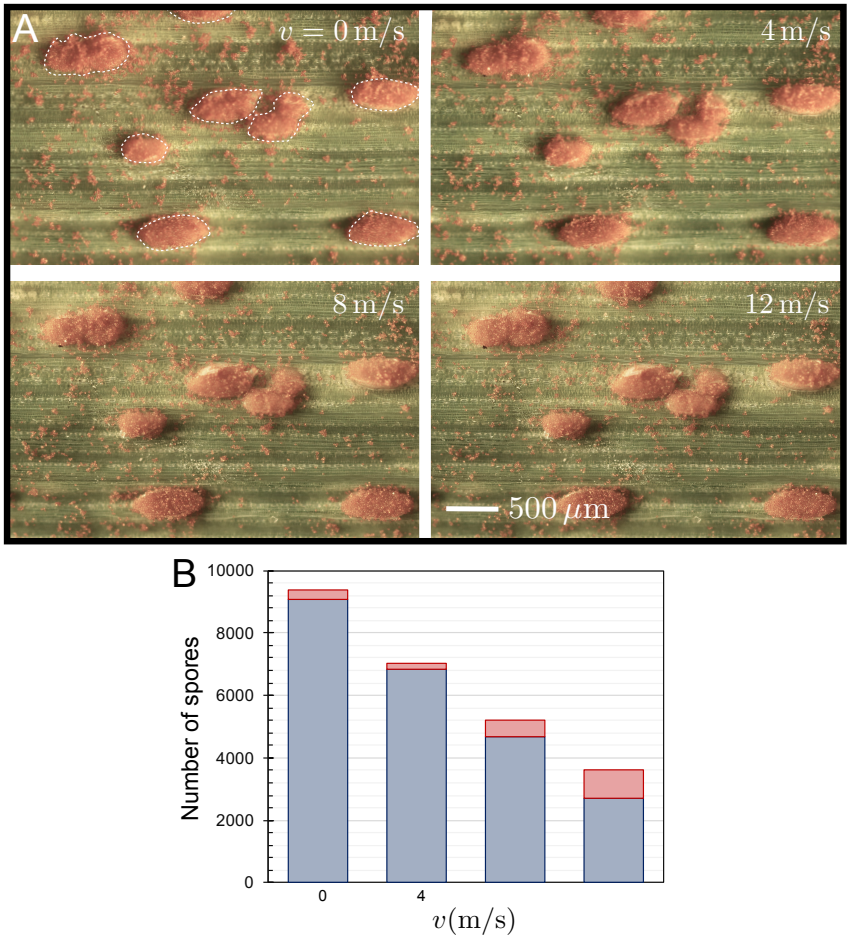

FIGURE E.6: A) Experimental results of a sporulated wheat leaf under air flow with different velocity. Top-down microscopy was used to compare the initial spore distribution (first frame) to that after being subjected to 4, 8, or 12 m/s winds (frames 2–4). B) A histogram comparing the total number of isolated spores (red) and spores contained within agglomerates (blue) before and after being subjected to the various wind speeds. The pustules were not counted, only spores residing on the actual leaf surface. The number of spores contained within agglomerates was estimated by measuring the total projected surface area of an agglomerate and dividing by the 10 μm spore diameter, assuming that most clusters only contained about one layer of spores. These measurements reveal that while gusts of wind are effective at removing the larger spore clusters, they are ineffective at removing isolated spores. Indeed, the number of isolated spores on the surface actually increases with wind speed, which is likely due to a subset of spores within a sheared cluster remaining on the surface during liberation.

Bibliography

[1] J. B. Boreyko and C. P. Collier. Dewetting transitions on superhydrophobic surfaces: when are wenzel drops reversible? *J. Phys. Chem. C*, 117:18084–18090, 2013.

[2] P. G. Michael, F. C. Leeming, and W. O. Dwyer. Headway on urban streets: observational data and an intervention to decrease tailgating. *Transp. Res. Part. F Traffic Psychol. Behav.*, 3:55–64, 2000.

[3] D.K. Sarkar and M. Farzaneh. Superhydrophobic coatings with reduced ice adhesion. *J. Adhes. Sci. Technol.*, 23:1215–1237, 2009.

[4] S. Nath, S. F. Ahmadi, and J. B. Boreyko. A review of condensation frosting. *Nanosc. Microsc. Therm.*, 21:81–101, 2017.

[5] L. Huang, Z. Liu, Y. Liu, Y. Gou, and J. Wang. Experimental study on frost release on fin-and-tube heat exchangers by use of a novel anti-frosting paint. *Exp. Therm. Fluid Sci.*, 33(7):1049–1054, 2009.

[6] M. B. Bragg, A. P. Broeren, and L. A. Blumenthal. Iced-airfoil aerodynamics. *Prog. Aero. Sci*, 41:323–362, 2005.

[7] C.W. Gurganus, J.C. Charnawskas, A.B. Kostinski, and R.A. Shaw. Nucleation at the contact line observed on nanotextured surfaces. *Phys. Rev. Lett.*, 113:235701, 2014.

[8] A. G. Marín, O. R. Enríquez, P. Brunet, P. Colinet, and J. H. Snoeijer. Universality of tip singularity formation in freezing water drops. *Phys. Rev. Lett.*, 113(5):054301, 2014.

[9] S. Jung, M. K. Tiwari, N. V. Doan, and D. Poulikakos. Mechanism of supercooled droplet freezing on surfaces. *Nat. Commun.*, 3:615, 2012.

[10] S. Jung, M. K. Tiwari, and D. Poulikakos. Frost halos from supercooled water droplets. *Proc. Natl. Acad. Sci. U.S.A.*, 109:16073–16078, 2012.

[11] P. G. de Gennes, F. Brochard-Wyart, and D. Quéré. *Capillarity and wetting phenomena: drops, bubbles, pearls, waves*. Springer Science & Business Media, 2013.

[12] K. Rykaczewski, W. A. Osborn, J. Chinn, M. L. Walker, J. H. J. Scott, W. Jones, C. Hao, S. Yao, and Z. Wang. How nanorough is rough enough to make a surface superhydrophobic during water condensation? *Soft Matter*, 8:8786–8794, 2012.

[13] R. Enright, N. Miljkovic, A. Al-Obeidi, C. V. Thompson, and E. N. Wang. Condensation on superhydrophobic surfaces: the role of local energy barriers and structure length scale. *Langmuir*, 28:14424–14432, 2012.

[14] J. B. Boreyko and C. H. Chen. Self-propelled dropwise condensate on superhydrophobic surfaces. *Phys. Rev. Lett.*, 103:184501, 2009.

[15] N. Miljkovic, R. Enright, and E. N. Wang. Effect of droplet morphology on growth dynamics and heat transfer during condensation on superhydrophobic nanostructured surfaces. *ACS Nano*, 6:1776–1785, 2012.

[16] G. Q. Li, M. H. Alhosani, S. Yuan, H. R. Liu, A. A. Ghaferi, and T. J. Zhang. Microscopic droplet formation and energy transport analysis of condensation on scalable superhydrophobic nanostructured copper oxide surfaces. *Langmuir*, 30:14498–14511, 2014.

[17] S.A. Isard and S.H. Gage. *Flow of life in the atmosphere*. PhD thesis, 2001.

[18] D.E. Aylor. Long-range transport of tobacco blue mold spores. *Agr. Meteorol.*, 27:217–232, 1982.

[19] D.E. Aylor. A framework for examining inter-regional aerial transport of fungal spores. *Agr. Forest Meteorol.*, 38:263–288, 1986.

[20] D.E. Aylor. Biophysical scaling and the passive dispersal of fungus spores: relationship to integrated pest management strategies. *Agr. Forest Meteorol.*, 97:275–292, 1999.

[21] S.A. Isard, S.H. Gage, P. Comtois, and J.M. Russo. Principles of the atmospheric pathway for invasive species applied to soybean rust. *AIBS Bulletin*, 55:851–861, 2005.

[22] D. G. Schmale III and S. D. Ross. Highways in the sky: scales of atmospheric transport of plant pathogens. *Annu. Rev. Phytopathol.*, 53:591–611, 2015.

[23] R. Trostle. Global agricultural supply and demand: Factors contributing to the recent increase. *Food Commodity Prices Outlook Report WRS-0801, ERS, USDA, Washington DC*, 2008.

[24] G. Bai and G. Shaner. Scab of wheat: Prospects for control. *Plant Dis.*, 78:760–766, 1994.

[25] G. Bai. Management and resistance in wheat and barley to fusarium head blight. *Annu. Rev. Phytopathol*, 42:135–161, 2004.

[26] C.E. Windels. Economic and social impacts of fusarium head blight: changing farms and rural communities in the northern great plains. *Phytopathology*, 90:17–21, 2000.

[27] J. J. Pestka. Deoxynivalenol: toxicity, mechanisms and animal health risks. *Anim. Feed Sci. Tech.*, 137:283–298, 2007.

[28] A. Lafuma and D. Quéré. Superhydrophobic states. *Nat. Mater.*, 2:457–460, 2003.

[29] T. N. Krupenkin, J. A. Taylor, T. M. Schneider, and S. Yang. From rolling ball to complete wetting: the dynamic tuning of liquids on nanostructured surfaces. *Langmuir*, 20:3824–3827, 2004.

[30] E. Bormashenko, R. Pogreb, G. Whyman, Y. Bormashenko, and M. Erlich. Vibration-induced cassie-wenzel wetting transition on rough surfaces. *Appl. Phys. Lett.*, 90:201917, 2007.

[31] T. N. Krupenkin, J. A. Taylor, E. N. Wang, P. Kolodner, M. Hodes, and T. R. Salamon. Reversible wetting-dewetting transitions on electrically tunable superhydrophobic nanostructured surfaces. *Langmuir*, 23:9128–9133, 2007.

[32] J. B. Boreyko, C. H. Baker, C. R. Poley, and C. H. Chen. Wetting and dewetting transitions on hierarchical superhydrophobic surfaces. *Langmuir*, 27:7502–7509, 2011.

[33] N. Kumari and S. V. Garimella. Electrowetting-induced dewetting transitions on superhydrophobic surfaces. *Langmuir*, 27:10342–10346, 2011.

[34] S.F. Ahmadi, A.S. Berrier, W.M. Doty, P.G. Greer, M. Habibi, H.A. Morgan, J.H.C. Waterman, N. Abaid, and J.B. Boreyko. Latent heat of traffic moving from rest. *New J. Phys.*, 19:113034, 2017.

[35] N. Garber and M. Zhao. Distribution and characteristics of crashes at different work zone locations in virginia. *Transport Res. Rec.*, pages 19–25, 2002.

[36] J. Daniel, K. Dixon, and D. Jared. Analysis of fatal crashes in georgia work zones. *Trans. Res. Rec.*, pages 18–23, 2000.

[37] D. Helbing. Traffic and related self-driven many-particle systems. *Rev. Mod. Phys.*, 73:1067, 2001.

[38] M. Tribus. *Thermostatics and thermodynamics*. Center for Advanced Engineering Study, Massachusetts Institute of Technology, 1961.

[39] M Tribus. *Rational Descriptions, Decisions and Designs*. Elsevier, 2016.

[40] H. Reiss, Audrey Dell Hammerich, and E. W. Montroll. Thermodynamic treatment of nonphysical systems: Formalism and an example (single-lane traffic). *J. Stat. Phys.*, 42:647–687, 1986.

[41] J.L. Ross. The impacts of molecular motor traffic jams. *Proc. Natl. Acad. Sci. U.S.A.*, 109:5911–2, 2012.

[42] C. Leduc, K. Padberg-Gehle, V. Varga, D. Helbing, S. Diez, and J. Howard. Molecular crowding creates traffic jams of kinesin motors on microtubules. *Proc. Natl. Acad. Sci. U.S.A.*, 109:6100–6105, 2012.

[43] M. Ballerini, N. Cabibbo, R. Candelier, A. Cavagna, E. Cisbani, I. Giardina, V. Lecomte, A. Orlandi, G. Parisi, A. Procaccini, and M Viale. Interaction ruling animal collective behavior depends on topological rather than metric distance: Evidence from a field study. *Proc. Natl. Acad. Sci. U.S.A.*, 105:1232–1237, 2008.

[44] Y. Katz, K. Tunstrom, C.C. Ioannou, C. Huepe, and I.D. Couzin. Inferring the structure and dynamics of interactions in schooling fish. *Proc. Natl. Acad. Sci. U.S.A.*, 108:18720–18725, 2011.

[45] P. DeLellis, G. Polverino, G. Ustuner, N. Abaid, S. Macrì, E.M Bollt, and M Porfiri. Collective behaviour across animal species. *Sci. Rep.*, 4:3723, 2014.

[46] J.P. Steimel, J.L. Aragones, H. Hu, N. Qureshi, and A. Alexander-Katz. Emergent ultra–long-range interactions between active particles in hybrid active–inactive systems. *Proc. Natl. Acad. Sci. U.S.A.*, 113:4652–4657, 2016.

[47] E. Tomer, L. Safonov, and S. Havlin. Presence of many stable nonhomogeneous states in an inertial car-following model. *Phys. Rev. Lett.*, 84:382, 2000.

[48] W. Leutzbach. *Introduction to the theory of traffic flow*, volume 47. Berlin: Springer-Verlag, 1988.

[49] M. Bando, K. Hasebe, A. Nakayama, A. Shibata, and Y. Sugiyama. Dynamical model of traffic congestion and numerical simulation. *Phys. Rev. E*, 51:1035, 1995.

[50] M. Bando, K. Hasebe, K. Nakanishi, A. Nakayama, A. Shibata, and Y. Sugiyama. Phenomenological study of dynamical model of traffic flow. *J. Phys. I*, 5:1389–1399, 1995.

[51] T. Nagatani. Jamming transition in the traffic-flow model with two-level crossings. *Phys. Rev. E*, 48:3290–3294, 1993.

[52] I. Prigogine and R. Herman. *Kinetic theory of vehicular traffic*, volume 100. Elsevier Publishing Company, 1971.

[53] M. Sasaki and T. Nagatani. Transition and saturation of traffic flow controlled by traffic lights. *Phys. A*, 353:531–546, 2002.

[54] M. Batista. Optimal velocity functions for car-following models. *J. Zhejiang Univ. Sci. A*, 11:520–529, 2010.

[55] G. K. Kamath, K. Jagannathan, and G. Raina. A computational study of a variant of the optimal velocity model with no collisions. In *2016 8th International Conference on Communication Systems and Networks (COMSNETS)*, 2016.

[56] A. Nakayama, M. Kikuchi, A. Shibata, Y. Sugiyama, S. Tadaki, and S. Yukawa. Quantitative explanation of circuit experiments and real traffic using the optimal velocity model. *New J. Phys.*, 18:043040, 2016.

[57] L. Li and X. Chen. Vehicle headway modeling and its inferences in macroscopic/microscopic traffic flow theory: A survey. *Transport Res. C-Emer.*, 76:170–188, 2017.

[58] S. Tadaki, M. Kikuchi, M. Fukui, T. Yosida, A. Nakayama, K. Nishinari, A. Shibata, Y. Sugiyama, and S. Yukawa. Phase transition in traffic jam experiment on a circuit. *New J. Phys.*, 15:e94351, 2013.

[59] S.I. Tadaki, M. Kikuchi, M. Fukui, A. Nakayama, K. Nishinari, A. Shibata, Y. Sugiyama, T. Yosida, and S. Yukawa. *In Traffic and Granular Flow'13*, chapter Critical Density of Experimental Traffic Jam, pages 505–511. Springer International Publishing, 2015.

[60] B.S. Kerner and H. Rehborn. Experimental properties of phase transitions in traffic flow. *Phys. Rev. Lett.*, 79:4030, 1997.

[61] M. Treiber, A. Hennecke, and D. Helbing. Congested traffic states in empirical observations and microscopic simulations. *Phys. Rev. E*, 62:1805, 2000.

[62] C.J. Jin, W. Wang, R. Jiang, and H. Wang. An empirical study of phase transitions from synchronized flow to jams on a single-lane highway. *J. Phys. A.*, 47:125104, 2014.

[63] C.J. Jin, W. Wang, R. Jiang, H.M. Zhang, H. Wang, and M.B. Hu. Understanding the structure of hyper-congested traffic from empirical and experimental evidences. *Transp. Res. Part C*, 60:324–338, 2015.

[64] B.S Kerner. *The physics of traffic: empirical freeway pattern features, engineering applications, and theory.* Springer, 2012.

[65] M. Bando, K. Hasebe, K. Nakanishi, and A. Nakayama. Analysis of optimal velocity model with explicit delay. *Phys. Rev. E*, 58, 1998.

[66] G.H. Peng, X. H. Cai, C. Q. Liu, B. F. Cao, and M. X. Tuo. Optimal velocity difference model for a car-following theory. *Phys. Lett. A*, 375:3973–3977, 2011.

[67] R. Mahnke, J. Kaupuzs, J. Hinkel, and H. Weber. Application of thermodynamics to driven systems. *Eur. Phys. J. B*, 57:463–471, 2007.

[68] H. Weber and R. Mahnke. In traffic and granular flow'11. pages 57–62. Springer Berlin Heidelberg, 2013.

[69] T. Nagatani. The physics of traffic jams. *Rep. Prog. Phys*, 65:1331, 2002.

[70] D. Helbing, A. Johansson, J. Mathiesen, M. H. Jensen, and A. Hansen. Analytical approach to continuous and intermittent bottleneck flows. *Phys. Rev. Lett.*, 97:168001, 2006.

[71] T. Kretz, A. Grünebohm, and M. Schreckenberg. Experimental study of pedestrian flow through a bottleneck. *J. of Stat. Mech.*, 2006:P10014, 2006.

[72] Armin Seyfried, Oliver Passon, Bernhard Steffen, Maik Boltes, Tobias Rupprecht, and Wolfram Klingsch. New insights into pedestrian flow through bottlenecks. *Transportation Science*, 3:395–406, 2009.

[73] D. Helbing, I.J. Farkas, P. Molnar, and T. Vicsek. Simulation of pedestrian crowds in normal and evacuation situations. *Pedestrian and evacuation dynamics*, 21:21–58, 2002.

[74] V. Hendrik, B. Jeroen, D. B. Liesje, R. Genserik, and W. Tony. A review of optimisation models for pedestrian evacuation and design problems. *Safety Sci.*, 87:167–178, 2016.

[75] R. Akcelik. *Traffic signals: capacity and timing analysis*. ARRB Group Limited, 1981.

[76] J. Joseph and G.L. Chang. Saturation flow rates and maximum critical lane volumes for planning applications in maryland. *J. Transp. Eng.*, 131:946–952, 2005.

[77] Y. Tong, L. Zhao, L. Li, and Y. Zhang. Stochastic programming model for oversaturated intersection signal timing. *Transp. Res. Part C*, 58:474–486, 2015.

[78] D. Branston and H.V. Zuylen. The estimation of saturation flow, effective green time and passenger car equivalents at traffic signals by multiple linear regression. *Transp. Res. Part D*, 12:47–53, 1978.

[79] J.A. Bonneson. Study of headway and lost time at single-point urban interchanges. *Trans. Res. Rec.*, 32:30–39, 1993.

[80] H. Perrin, P. Martin, and B. Hansen. Modifying signal timing during inclement weather. *Trans. Res. Rec.*, 1748:66–71, 2001.

[81] T. Limanond, S. Chookerd, and N. Roubtonglang. Effects of countdown timers on queue discharge characteristics of through movement at a signalized intersection. *Transp. Res. Part D*, 17:662–671, 2009.

[82] A. Sharma, L. Vanajakshi, and N. Rao. Effect of phase countdown timers on queue discharge characteristics under heterogeneous traffic conditions. *Trans. Res. Rec.*, 2130:93–100, 2009.

[83] E. Matsoukis and S.T. Efstathiadis. An investigation of the variability of start-up lost times and departure headways at signalized intersections in urban areas. *WIT Trans. Sci. Eng.*, 66:53–61, 2013.

[84] J.J. Lu and J.C. Pernia. The differences of driving behavior among different driver age groups at signalized intersections. *IATSS Res.*, 24:75–84, 2000.

[85] D.S. Hurwitz, K.P. Heaslip, S.D. Schrock, J. Swake, P. Marnell, H. Tuss, and E. Fitzsimmons. Implications of distracted driving on start-up lost time for dual left-turn lanes. *J. Transp. Eng.*, 139:23–930, 2013.

[86] S. F. Ahmadi, S. Nath, G. J. Iliff, B. R. Srijanto, C. P. Collier, P. Yue, and J. B. Boreyko. Passive anti-frosting surfaces using microscopic ice patterns. *ACS Appl. Mater. Interfaces*, 2018.

[87] J. L. O'Brien, S. F. Ahmadi, K. C. Failor, C. E. Bisbano, M. D. Mulroe, S. Nath, B. A. Vinatzer, and J. B. Boreyko. Spatial control of condensation and desublimation using ice nucleating proteins. *Appl. Phys. Lett.*, 113:153701, 2018.

[88] T. M. Schutzius, S. Jung, T. Maitra, P. Eberle, C. Antonini, C. Stamatopoulos, and D. Poulikakos. Physics of icing and rational design of surfaces with extraordinary icephobicity. *Langmuir*, 31(17):4807–4821, 2015.

[89] M. J. Kreder, J. Alvarenga, P. Kim, and J. Aizenberg. Design of anti-icing surfaces: smooth, textured or slippery? *Nat. Rev. Mater.*, 1:15003, 2016.

[90] D. Chen, M.D. Gelenter, M. Hong, R.E. Cohen, and G.H. McKinley. Icephobic surfaces induced by interfacial nonfrozen water. *ACS Appl. Mater. Interfaces*, 9:4202–4214, 2017.

[91] K. Golovin, S.P. Kobaku, D. H. Lee, E. T. DiLoreto, J. M. Mabry, and A. Tuteja. Designing durable icephobic surfaces. *Sci. Adv.*, 2:e1501496, 2016.

[92] K. R. Murphy, W. T. McClintic, K. C. Lester, C. P. Collier, and J. B. Boreyko. Dynamic defrosting on scalable superhydrophobic surfaces. *ACS Appl. Mater. Interfaces*, 9:24308–24317, 2017.

[93] H. Sojoudi, M. Wang N.D. Boscher, G.H. McKinley, and K.K. Gleason. Durable and scalable icephobic surfaces: similarities and distinctions from superhydrophobic surfaces. *Soft Matter*, 12:1938–1963, 2016.

[94] P. Irajizad, M. Hasnain, N. Farokhnia, S. M. Sajadi, and H. Ghasemi. Magnetic slippery extreme icephobic surfaces. *Nat. Commun.*, 7:13395, 2016.

[95] D. L. Beemer, W. Wang, and A. K. Kota. Durable gels with ultra-low adhesion to ice. *J. Mater. Chem. A*, 4:18253–18258, 2016.

[96] J. Kang, H. Kim, K. S. Kim, S. K. Lee, S. Bae, J. H. Ahn, Y. J. Kim, J. B. Choi, and B. H. Hong. High-performance graphene-based transparent flexible heaters. *Nano Lett.*, 11:5154–5158, 2011.

[97] V. Volman, Y. Zhu, A. R. O. Raji, B. Genorio, W. Lu, C. Xiang, C. Kittrell, and J. M. Tour. Radio-frequency-transparent, electrically conductive graphene nanoribbon thin films as deicing heating layers. *ACS Appl. Mater. Interfaces*, 6:298–304, 2014.

[98] L. Chen, Y. Zhang, and Q. Wu. Effect of graphene coating on the heat transfer performance of a composite anti-/deicing component. *Coatings*, 7:158, 2017.

[99] L. Cao, A. K. Jones, V. K. Sikka, J. Wu, and D. Gao. Anti-icing superhydrophobic coatings. *Langmuir*, 25:12444–12448, 2009.

[100] L. Mishchenko, B. Hatton, V. Bahadur, J. A. Taylor, T. Krupenkin, and J. Aizenberg. Design of ice-free nanostructured surfaces based on repulsion of impacting water droplets. *ACS Nano*, 4:7699–7707, 2010.

[101] T. Maitra, M. K. Tiwari, C. Antonini, P. Schoch, S. Jung, P. Eberle, and D. Poulikakos. On the nanoengineering of superhydrophobic and impalement resistant surface textures below the freezing temperature. *Nano Lett.*, 14:172–182, 2014.

[102] J. B. Boreyko and C. P. Collier. Delayed frost growth on jumping-drop superhydrophobic surfaces. *ACS Nano*, 7:1618–1627, 2013.

[103] J. Guadarrama-Cetina, A. Mongruel, W. Gonzalez-Vinas, and D. Beysens. Percolation-induced frost formation. *Europhys. Lett.*, 101:16009, 2013.

[104] T.M. Schutzius, S. Jung, T. Maitra, G. Graeber, M. Kohme, and D. Poulikakos. Spontaneous droplet trampolining on rigid superhydrophobic surfaces. *Nature*, 527:82–85, 2015.

[105] G. Graeber, T. M. Schutzius, H. Eghlidi, and D. Poulikakos. Spontaneous self-dislodging of freezing water droplets and the role of wettability. *Proc. Natl. Acad. Sci. U.S.A.*, 114:11040–11045, 2017.

[106] J. Guadarrama-Cetina, R. D. Narhe, D. A. Beysens, and W. Gonzalez-Vinas. Droplet pattern and condensation gradient around a humidity sink. *Phys. Rev. E*, 89:012402, 2014.

[107] J. Guadarrama-Cetina, A. Mongruel, W. Gonzalez-Vinas, and D. Beysens. Frost formation with salt. *Europhys. Lett.*, 110:56002, 2015.

[108] X. Sun, V. G. Damle, A. Uppal, R. Linder, S. Chandrashekar, A. R. Mohan, and K. Rykaczewski. Inhibition of condensation frosting by arrays of hygroscopic antifreeze drops. *Langmuir*, 31:13743–13752, 2015.

[109] X. Sun and K. Rykaczewski. Suppression of frost nucleation achieved using the nanoengineered integral humidity sink effect. *ACS Nano*, 11:906–917, 2016.

[110] E. V. Novotny, D. Murphy, and H. G. Stefan. Increase of urban lake salinity by road deicing salt. *Sci. Total Environ.*, 406:131–144, 2008.

[111] R. B. Jackson and E. G. Jobbagy. From icy roads to salty streams. *Proc. Natl. Acad. Sci. U.S.A.*, 102:14487–14488, 2005.

[112] J.W. Snodgrass, J. Moore, S.M. Lev, R.E. Casey, D.R. Ownby, R.F. Flora, and G. Izzo. Influence of modern stormwater management practices on transport of road salt to surface waters. *Environ. Sci. Technol*, 51:4165–4172, 2017.

[113] S.R. Corsi, S.W. Geis, J.E. Loyo-Rosales, C.P. Rice, R.J. Sheesley, G.G. Failey, and D.A. Cancilla. Characterization of aircraft deicer and anti-icer components and toxicity in airport snowbanks and snowmelt runoff. *Environ. Sci. Technol*, 40:3195–3202, 2006.

[114] K. Golovin and A. Tuteja. A predictive framework for the design and fabrication of icephobic polymers. *Sci. Adv.*, 3:e1701617, 2017.

[115] P. Kim, T. S. Wong, J. Alvarenga, M. J. Kreder, W. E. Adorno-Martinez, and J. Aizenberg. Liquid-infused nanostructured surfaces with extreme anti-ice and anti-frost performance. *ACS Nano*, 6:6569–6577, 2012.

[116] S. B. Subramanyam, K. Rykaczewski, and K. K. Varanasi. Ice adhesion on lubricant-impregnated textured surfaces. *Langmuir*, 29:13414–13418, 2013.

[117] S. Ozbay, C. Yuceel, and H. Y. Erbil. Improved icephobic properties on surfaces with a hydrophilic lubricating liquid. *ACS Appl. Mater. Interfaces*, 7:22067–22077, 2015.

[118] K. Rykaczewski, S. Anand, S. B. Subramanyam, and K. K. Varanasi. Mechanism of frost formation on lubricant-impregnated surfaces. *Langmuir*, 29:5230–5238, 2013.

[119] S. B. Subramanyam, V. Kondrashov, J. Rühe, and K. K. Varanasi. Low ice adhesion on nano-textured superhydrophobic surfaces under supersaturated conditions. *ACS Appl. Mater. Interfaces*, 8:12583–12587, 2016.

[120] Y. Zhang, M. R. Klittich, M. Gao, and A. Dhinojwala. Delaying frost formation by controlling surface chemistry of carbon nanotube-coated steel surfaces. *ACS Appl. Mater. Interfaces*, 9:6512–6519, 2017.

[121] M. D. Mulroe, B. R. Srijanto, S. F. Ahmadi, C. P. Collier, and J. B. Boreyko. Tuning superhydrophobic nanostructures to enhance jumping-droplet condensation. *ACS Nano*, 1:8499—8510, 2017.

[122] D. Torresin, M. K. Tiwari, D. D. Col, and D. Poulikakos. Flow condensation on copper-based nanotextured superhydrophobic surfaces. *Langmuir*, 29:840–848, 2013.

[123] D. M. Murphy and T. Koop. Review of the vapour pressures of ice and supercooled water for atsmopheric applications. *Q. J. R. Meteorol. Soc.*, 131:1539–1565, 2005.

[124] M. G. Medici, A. Mongruel, L. Royon, and D. Beysens. Edge effects on water droplet condensation. *Phys. Rev. E*, 90:062403, 2014.

[125] S. Nath, C. E. Bisbano, P. Yue, and J. B. Boreyko. Duelling dry zones around hygroscopic droplets. *J. Fluid Mech.*, 853:601–620, 2018.

[126] A. T. Paxson, J. L. Yague, K. K. Gleason, and K. K. Varanasi. Stable dropwise condensation for enhancing heat transfer via the initiated chemical vapor deposition (icvd) of grafted polymer films. *Adv. Mater.*, 26:418–423, 2014.

[127] D.J. Preston, N. Miljkovic, J. Sack, R. Enright, J. Queeney, and E.N. Wang. Effect of hydrocarbon adsorption on the wettability of rare earth oxide ceramics. *Appl. Phys. Lett.*, 105:011601, 2014.

[128] K. C. Park, P. Kim, A. Grinthal, N. He, D. Fox, J. C. Weaver, and J. Aizenberg. Condensation on slippery asymmetric bumps. *Nature*, 531:78–82, 2016.

[129] H. Chen, L. Zhang, P. Zhang, D. Zhang, Z. Han, and L. Jiang. A novel bioinspired continuous unidirectional liquid spreading surface structure from the peristome surface of *Nepenthes alata*. *Small*, 13:1601676, 2017.

[130] C.W. Lo, V. Sahoo, and M.C. Lu. Control of ice formation. *ACS Nano*, 11:2665–2674, 2017.

[131] J. B. Boreyko, R. R. Hansen, K. R. Murphy, S. Nath, S. T. Retterer, and C. P. Collier. Controlling condensation and frost growth with chemical micropatterns. *Sci. Rep.*, 6:19131, 2016.

[132] J. Liu, C. Zhu, K. Liu, Y. Jiang, Y. Song, J.S. Francisco, X.C. Zeng, and J. Wang. Distinct ice patterns on solid surfaces with various wettabilities. *Proc. Natl. Acad. Sci. U.S.A.*, 114:11285–11290, 2017.

[133] V. P. Carey. *Liquid–Vapor Phase-Change Phenomena, 2^{nd} ed.* CRC Press, Boca Raton, FL, 2007.

[134] N. H. Fletcher. *Physics of Rain Clouds*. Cambridge University Press, Cambridge, UK, 1962.

[135] C. T. Sanders. *The influence of frost formation and defrosting on the performance of air coolers*. PhD thesis, Delft University of Technology, 1974.

[136] B. Na and R. L. Webb. A fundamental understanding of factors affecting frost nucleation. *Int. J. Heat Mass Transfer*, 46:3797–3808, 2003.

[137] S. Nath and J. B. Boreyko. On localized vapor pressure gradients governing condensation and frost phenomena. *Langmuir*, 32:8350–8365, 2016.

[138] P. V. Hobbs. *Ice Physics*. Clarendon Press, Oxford, England, 1974.

[139] H. Wang, L. Tang, X. Wu, W. Dai, and Y. Qiu. Fabrication and anti-frosting performance of super hydrophobic coating based on modified nano-sized calcium carbonate and ordinary polyacrylate. *Appl. Surf. Sci.*, 253:8818–8824, 2007.

[140] M. He, J. Wang, H. Li, X. Jin, J. Wang, B. Liu, and Y. Song. Superhydrophobic film retards frost formation. *Soft Matter*, 6:2396–2399, 2010.

[141] Q. Zhang, M. He, X. Zeng, K. Li, D. Cui, J. Chen, J. Wang, Y. Song, and L. Jiang. Condensation mode determines the freezing of condensed water on solid surfaces. *Soft Matter*, 8:8285–8288, 2012.

[142] G. W. Bryant, J. Hallett, and B. J. Mason. The epitaxial growth of ice on single-crystalline substrates. *J. Phys. Chem. Solids*, 12:189–195, 1959.

[143] C. Walker, S. Lerch, M. Reininger, H. Eghlidi, A. Milionis, T.M. Schutzius, and D. Poulikakos. Desublimation frosting on nanoengineered surfaces. *ACS Nano*, 12:8288–8296, 2018.

[144] B. Wang, D. A. Knopf, S. China, B. W. Arey, T. H. Harder, M. K. Gilles, and A. Laskin. Direct observation of ice nucleation events on individual atmospheric particles. *Phys. Chem. Chem. Phys.*, 18:29721–29731, 2016.

[145] A. Kiselev, F. Bachmann, P. Pedevilla, S. J. Cox, A. Michaelides, D. Gerthsen, and T. Leisner. Active sites in heterogeneous ice nucleation–the example of k-rich feldspars. *Science*, 355:367–371, 2017.

[146] L. Zhai, M. C. Berg, F. C. Cebeci, Y. Kim, J. M. Milwid, M. F. Rubner, and R. E. Cohen. Patterned superhydrophobic surfaces: toward a synthetic mimic of the namib desert beetle. *Nano Lett.*, 6:1213–1217, 2006.

[147] K. K. Varanasi, M. Hsu, N. Bhate, W. Yang, and T. Deng. Spatial control in the heterogeneous nucleation of water. *Appl. Phys. Lett.*, 95:094101, 2009.

[148] S. P. R. Kobaku, A. K. Kota, D. H. Lee, J. M. Mabry, and A. Tuteja. Patterned superomniphobic–superomniphilic surfaces: Templates for siteselective selfassembly. *Angew. Chem. Int. Ed.*, 51:10109–10113, 2012.

[149] L. Mishchenko, M. Khan, J. Aizenberg, and B. D. Hatton. Spatial control of condensation and freezing on superhydrophobic surfaces with hydrophilic patches. *Adv. Funct. Mater.*, 23:4577–4584, 2013.

[150] C. W. Lo, C. C. Wang, and M. C. Lu. Spatial control of heterogeneous nucleation on the superhydrophobic nanowire array. *Adv. Funct. Mater.*, 24:1211–1217, 2014.

[151] A. Ghosh, S. Beaini, B. J. Zhang, R. Ganguly, and C. M. Megaridis. Enhancing dropwise condensation through bioinspired wettability patterning. *Langmuir*, 30:13103–13115, 2014.

[152] Y. Zhao, D. J. Preston, Z. Lu, L. Zhang, J. Queeney, and E. N. Wang. Effects of millimetric geometric features on dropwise condensation under different vapor conditions. *Int. J. Heat Mass Transfer*, 119:931–938, 2018.

[153] P. Wolber and G. Warren. Bacterial ice-nucleation proteins. *Trends Biochem. Sci.*, pages 179–182, 1989.

[154] R. Pandey, K. Usui, R.A. Livingstone, S.A. Fischer, J. Pfaendtner, E.H.G. Backus, Y. Nagata, J. Frochlich-Nowoisky, L. Schmuser, S. Mauri, J.F. Scheel, D.A. Knopf, U. Poschl, M. Bonn, and T. Weidner. Ice-nucleating bacteria control the order and dynamics of interfacial water. *Sci. Adv.*, 2:e1501630, 2016.

[155] K.C. Failor, D.G. Schmale, B.A. Vinatzer, and C.L. Monteil. Ice nucleation active bacteria in precipitation are genetically diverse and nucleate ice by employing different mechanisms. *ISME J.*, 11:2740–2753, 2017.

[156] C.P. Garnham, R.L. Campbell, V.K. Walker, and P.L. Davies. Novel dimeric -helical model of an ice nucleation protein with bridged active sites. *BMC Struct. Biol.*, page 36, 2011.

[157] X. Chen, R. Ma, H. Zhou, X. Zhou, L. Che, S. Yao, and Z. Wang. Activating the microscale edge effect in a hierarchical surface for frosting suppression and defrosting promotion. *Sci. Rep.*, 3:2515, 2013.

[158] R. D. Deegan, O. Bakajin, T. F. Dupont, G. Huber, S. R. Nagel, and T. A. Witten. Capillary flow as the cuase of ring stains from dried liquid drops. *Nature*, 389:827–829, 1997.

[159] S. F. Ahmadi, S. Nath, C. M. Kingett, P. Yue, and J. B. Boreyko. How soap bubbles freeze. *Nat. Commun.*, 10:2531, 2019.

[160] P.-G. de Gennes and J. Badoz. *Fragile Objects: Soft Matter, Hard Science, and the Thrill of Discovery*. Copernicus, New York, NY, 1996.

[161] J. Plateau. *Experimental and theoretical statics of liquids subject to molecular forces only*. Gauthier-Villars, Paris, 1873.

[162] C. V. Boys. *Soap bubbles, their colours and the forces which mold them*. Courier Corporation, 1959.

[163] F. Behroozi. Soap bubbles in paintings: Art and science. *Am. J. Phys.*, 76:1087–1091, 2008.

[164] M. Blander and J.L. Katz. Bubble nucleation in liquids. *AIChE J.*, 21:833–848, 1975.

[165] L. Salkin, A. Schmit, P. Panizza, and L. Courbin. Generating soap bubbles by blowing on soap films. *Phys. Rev. Lett.*, 116:077801, 2016.

[166] P. Zhang and F. Y. Lv. A review of the recent advances in superhydrophobic surfaces and the emerging energy-related applications. *Energy*, 82:1068–1087, 2015.

[167] L. Champougny, M. Roché, W. Drenckhan, and E. Rio. Life and death of not so "bare" bubbles. *Soft Matter*, 12:5276–5284, 2016.

[168] F. Seychelles, F. Ingremeau, C. Pradere, and H. Kellay. From intermittent to nonintermittent behavior in two dimensional thermal convection in a soap bubble. *Phys. Rev. Lett.*, 105:264502, 2010.

[169] H. Lhuissier and E. Villermaux. Bursting bubble aerosols. *J. Fluid Mech.*, 696:5–44, 2012.

[170] G. Debrégeas, P.-G. de Gennes, and F. Brochard-Wyart. The life and death of "bare" viscous bubbles. *Science*, 279:1704–1707, 1998.

[171] T.-H. Hsu, S. Manakasettharn, J.A. Taylor, and T. Krupenkin. Bubbler: a novel ultra-high power density energy harvesting method based on reverse electrowetting. *Sci. Rep.*, 5:16537, 2015.

[172] J. Feng, M. Roché, D. Vigolo, L.N. Arnaudov, S.D. Stoyanov, T.D. Gurkov, G.G. Tsutsumanova, and H.A. Stone. Nanoemulsions obtained via bubble-bursting at a compound interface. *Nat. Phys.*, 10:606–612, 2014.

[173] J. Li, R.D. Sanderson, and E.P. Jacobs. Ultrasonic cleaning of nylon microfiltration membranes fouled by kraft paper mill effluent. *J. Memb. Sci.*, 205:247–257, 2002.

[174] Y.J. Chan, M.F. Chong, C.L. Law, and D.G. Hassell. A review on anaerobic–aerobic treatment of industrial and municipal wastewater. *Chem. Eng. J.*, 155:1–18, 2009.

[175] E. Esmaili, P. Shukla, J. D. Eifert, and S. Jung. Bubble impact on a tilted wall: Removing bacteria using bubbles. *Phys. Rev. Fluids*, 4:043603, 2019.

[176] V. J. Schaefer. The formation of ice crystals in the laboratory and the atmosphere. *Chem. Rev.*, 44:291–320, 1949.

[177] R. A. Stairs. Changes of drop-shapes on freezing. *Anal. Chem.*, 43:1535–1536, 1971.

[178] D. M. Anderson, M. G. Worster, and S. H. Davis. The case for a dynamic contact angle in containerless solidification. *J. Cryst. Growth*, 163(3):329–338, 1996.

[179] S. Wildeman, S. Sterl, C. Sun, and D. Lohse. Fast dynamics of water droplets freezing from the outside in. *Phys. Rev. Lett.*, 118:084101, 2017.

[180] Y. Zhong, A. M. Jacobi, and J. G. Georgiadis. Freezing front propagation on microgrooved substrates. *J. Thermophys. Heat Tr.*, 24:199–207, 2010.

[181] M. Schremb, J.M. Campbell, H.K. Christenson, and C. Tropea. Ice layer spreading along a solid substrate during solidification of supercooled water: experiments and modeling. *Langmuir*, 33:4870–4877, 2017.

[182] M. R. Moore, M. S. Mughal, and D. T. Papageorgiou. Ice formation within a thin film flowing over a flat plate. *J. Fluid Mech.*, 817:455–489, 2017.

[183] L. B. Lane. Freezing points of glycerol and its aqueous solutions. *Ind. Eng. Chem.*, 17:924–924, 1925.

[184] W.R. McEntee and K.J. Mysels. Bursting of soap films. i. an experimental study. *J. Phys. Chem.*, 73:3018–3028, 1969.

[185] C. Cohen, B. D. Texier, E. Reyssat, J.H. Snoeijer, D. Quéré, and C. Clanet. On the shape of giant soap bubbles. *Proc. Natl. Acad. Sci. U.S.A.*, 114:2515–2519, 2017.

[186] N. J. Alvarez, L. M. Walker, and S. L. Anna. A criterion to assess the impact of confined volumes on surfactant transport to liquid–fluid interfaces. *Soft Matter*, 8:8917–8925, 2012.

[187] K.J. Mysels. *Soap films: studies of their thinning and a bibliography*. Pergamon press, 1959.

[188] R. Bruinsma. Theory of hydrodynamic convection in soap films. *Physica A*, 216:59–76, 1995.

[189] N. Adami, S. Dorbolo, and H. Caps. Single thermal plume in locally heated vertical soap films. *Phys. Rev. E*, 84:046316, 2011.

[190] A. Dehaoui, B. Issenmann, and F. Caupin. Viscosity of deeply supercooled water and its coupling to molecular diffusion. *Proc. Natl. Acad. Sci. U.S.A.*, 112:12020–12025, 2015.

[191] M.A. Floriano and C.A. Angell. Surface tension and molar surface free energy and entropy of water to –27.2. degree. c. *J. Phys. Chem.*, 94:4199–4202, 1990.

[192] L. Keiser, H. Bense, P. Colinet, J. Bico, and E. Reyssat. Marangoni bursting: evaporation-induced emulsification of binary mixtures on a liquid layer. *Phys. Rev. Lett.*, 3:074504, 2017.

[193] H. Gao and H. Yao. Shape insensitive optimal adhesion of nanoscale fibrillar structures. *Proc. Natl. Acad. Sci. U.S.A.*, 101:7851–7856, 2004.

[194] W.S.B. Paterson. *The physics of glaciers*. Elsevier, 2016.

[195] M. Nauenberg. Theory and experiments on the ice–water front propagation in droplets freezing on a subzero surface. *Eur. J. Phys.*, 37:045102, 2016.

[196] K. E. Witt, S. F. Ahmadi, and J. B. Boreyko. Ice wicking. *Phys. Rev. Fluids*, 4:024002, 2019.

[197] V. C. Tsai and J. R. Rice. A model for turbulent hydraulic fracture and application to crack propagation at glacier beds. *J. Geophys. Res.*, 115:F03007, 2010.

[198] V. C. Tsai and J. R. Rice. Modeling turbulent hydraulic fracture near a free surface. *J. Appl. Mech.*, 79:031003, 2012.

[199] I. A. Buist and D. F. Dickens. Experimental spills of crude oil in pack ice. In *Proceedings of the 1987 International Oil Spill Conference*, 1987.

[200] D. F. Dickens. Behavior of oil spills in ice and implications for spill response. In *Proceedings of the Arctic Technology Conference*, 2011.

[201] M. Grabowski. *Responding to Oil Spills in the U.S. Arctic Marine Environment*. The National Academic Press, Washington DC, 2014.

[202] Z. Jin, H. Zhang, and Z. Yang. Experimental investigation of the impact and freezing processes of a water droplet on an ice surface. *Int. J. Heat Mass Transfer*, 109:716–724, 2017.

[203] M. Schremb, I. V. Roisman, and C. Tropea. Normal impact of supercooled water drops onto a smooth ice surface: experiments and modelling. *J. Fluid Mech.*, 835:1087–1107, 2018.

[204] T. S. Wong, S. H. Kang, S. K. Y. Tang, E. J. Smythe, B. D. Hatton, A. Grinthal, and J. Aizenberg. Bioinspired self-repairing slippery surfaces with pressure-stable omniphobicity. *Nature*, 477:443–447, 2011.

[205] A. Lafuma and D. Quéré. Slippery pre-suffused surfaces. *Europhys. Lett.*, 96:56001, 2011.

[206] R. Dou, J. Chen, Y. Zhang, X. Wang, D. Cui, Y. Song, L. Jiang, and J. Wang. Anti-icing coating with an aqueous lubricating layer. *ACS Appl. Mater. Interfaces*, 6:6998–7003, 2014.

[207] S. Hanninen and J. Sassi. Acute oil spills in arctic waters – oil combating in ice. Technical report, Research Council of Norway, 2010.

[208] Z. Xue, Y. Cao, N. Liu, L. Feng, and L. Jiang. Special wettable materials for oil/water separation. *J. Mater. Chem. A*, 2:2445–2460, 2014.

[209] E. C. Chen, J. C. K. Overall, and C. R. Phillips. Spreading of crude oil on an ice surface. *Can. J. Chem. Eng.*, 52:71–74, 1974.

[210] I. Cuesta, F. X. Grau, and F. Giralt. Numerical simulation of oil spills in a generalized domain. *Oil Chem. Pollut.*, 7:143–159, 1990.

[211] M. Afenyo, B. Veitch, and F. Khan. A state-of-the-art review of fate and transport of oil spills in open and ice-covered water. *Ocean Engineering*, 119:233–248, 2016.

[212] C. S. Lindenmeyer and B. Chalmers. Morphology of ice dendrites. *J. Chem. Phys.*, 45:2804–2806, 1966.

[213] S. H. Tirmizi and W. N. Gill. Effect of natural convection on growth velocity and morphology of dendritic ice crystals. *J. Cryst. Growth*, 85:488–502, 1987.

[214] W. Vedder and D. A. Vermilyea. Aluminum + water reaction. *Trans. Faraday Soc.*, 65:561–584, 1969.

[215] M. He, X. Zhou, X. Zeng, D. Cui, Q. Zhang, J. Chen, H. Li, J. Wang, Z. Cao, Y. Song, and L. Jiang. Hierarchically structured porous aluminum surfaces for high-efficient removal of condensed water. *Soft Matter*, 8:6680–6683, 2012.

[216] N. H. Fletcher. Structural aspects of the ice-water system. *Rep. Prog. Phys.*, 34(3):913–994, 1971.

[217] N. Fries and M. Dreyer. An analytic solution of capillary rise restrained by gravity. *J. Colloid Interface Sci.*, 320:259–263, 2008.

[218] F. J. Higuera, A. Medina, and A. Liñan. Capillary rise of a liquid between two vertical plates making a small angle. *Phys. Fluids*, 20:102102, 2008.

[219] A. Ponomarenko, D. Quéré, and C. Clanet. A universal law for capillary rise in corners. *J. Fluid Mech.*, 666:146–154, 2011.

[220] D. Deng, Y. Tang, J. Zeng, S. Yang, and H. Shao. Characterization of capillary rise dynamics in parallel micro v-grooves. *Int. J. Heat Mass Transfer*, 77:311–320, 2014.

[221] J. B. Boreyko, G. Polizos, P. G. Datskos, S. A. Sarles, and C. P. Collier. Air-stable droplet interface bilayers on oil-infused surfaces. *Proc. Natl. Acad. Sci. U.S.A.*, 111:7588–7593, 2014.

[222] P. B. Warren. Late stage kinetics for various wicking and spreading problems. *Phys. Rev. E*, 69:041601, 2004.

[223] E. Schmidt, W. Schurig, and W. Sellschopp. Versuche uber die kondensation von wasserdampf in film- and tropfenform. *Forsch. Ingenieurwes.*, 1:53–63, 1930.

[224] J. W. Rose. Dropwise condensation theory and experiment: a review. *Proc. Inst. Mech. Eng., Part A*, 216:115–128, 2002.

[225] J. Lienhard IV and J. Lienhard V. *A Heat Transfer Textbook*. Phlogiston, Cambridge, 3rd edition, 2003.

[226] J. W. Rose and L. R. Glicksman. Dropwise condensation − the distribution of drop sizes. *Int. J. Heat Mass Transfer*, 16:411–425, 1973.

[227] D. Quéré. Non-sticking drops. *Rep. Prog. Phys.*, 68:2495–2532, 2005.

[228] D. J. Preston, D. L. Mafra, N. Miljkovic, J. Kong, and E. N. Wang. Scalable graphene coatings for enhanced condensation heat transfer. *Nano Lett.*, 15:2902–2909, 2015.

[229] E. J. Le Fevre and J. W. Rose. A theory of heat transfer by dropwise condensation. In *Proceedings of the Third International Heat Transfer Conference*, pages 362–375, Chicago, IL, August 7–12 1966.

[230] I. Tanasawa. Critical size of departing drops. In *Proceedings of the Fifth International Heat Transfer Conference*, volume 7, page 188, Tokyo, Japan, September 3–7 1974.

[231] J. W. Rose. Some aspects of condensation heat transfer theory. *Int. Commun. Heat Mass*, 15:449–473, 1988.

[232] N. Miljkovic and E. N. Wang. Condensation heat transfer on superhydrophobic surfaces. *MRS Bull.*, 38:397–406, 2013.

[233] N. Miljkovic, R. Enright, Y. Nam, K. Lopez, N. Dou, J. Sack, and E. N. Wang. Jumping-droplet-enhanced condensation on scalable superhydrophobic nanostructured surfaces. *Nano Lett.*, 13:179–187, 2012.

[234] Y. Hou, M. Yu, X. Chen, Z. Wang, and S. Yao. Recurrent filmwise and dropwise condensation on a beetle mimetic surface. *ACS Nano*, 9:71–81, 2015.

[235] K. M. Wisdom, J. A. Watson, X. Qu, F. Liu, G. S. Watson, and C. H. Chen. Self-cleaning of superhydrophobic surfaces by self-propelled jumping condensate. *Proc. Natl. Acad. Sci. U.S.A.*, 110:7992–7997, 2013.

[236] G. S. Watson, M. Gellender, and J. A. Watson. Self-propulsion of dew drops on lotus leaves: a potential mechanism for self-cleaning. *Biofouling*, 30:427–434, 2014.

[237] G. S. Watson, L. Schwarzkopf, B. W. Cribb, S. Myhra, M. Gellender, and J. A. Watson. Removal mechanisms of dew via self-propulsion off the gecko skin. *J. Royal Soc. Interface*, 12:20141396, 2015.

[238] R. L. Chavez, F. Liu, J. J. Feng, and C. H. Chen. Capillary-inertial colloidal catapults upon drop coalescence. *Appl. Phys. Lett.*, 109:011601, 2016.

[239] Q. Zhang, M. He, J. Chen, J. Wang, Y. Song, and L. Jiang. Anti-icing surfaces based on enhanced self-propelled jumping of condensed water microdroplets. *Chem. Commun.*, 49:4516–4518, 2013.

[240] J. B. Boreyko, Y. Zhao, and C. H. Chen. Planar jumping-drop thermal diodes. *Appl. Phys. Lett.*, 99:234105, 2011.

[241] J. B. Boreyko and C. H. Chen. Vapor chambers with jumping-drop liquid return from superhydrophobic condensers. *Int. J. Heat Mass Transfer*, 61:409–418, 2013.

[242] J. Oh, P. Birbarah, T. Foulkes, S. L. Yin, M. Rentauskas, J. Neely, R. C. N. Pilawa-Podgurski, and N. Miljkovic. Jumping-droplet electronics hot-spot cooling. *Appl. Phys. Lett.*, 110:123107, 2017.

[243] K. F. Wiedenheft, H. A. Guo, X. Qu, J. B. Boreyko, F. Liu, K. Zhang, F. Eid, A. Choudhury, Z. Li, and C. H. Chen. Hotspot cooling with jumping-drop vapor chambers. *Appl. Phys. Lett.*, 110:141601, 2017.

[244] C. Dietz, K. Rykaczewski, A. G. Fedorov, and Y. Joshi. Visualization of droplet departure on a superhydrophobic surface and implications to heat transfer enhancement during dropwise condensation. *Appl. Phys. Lett.*, 97:033104, 2010.

[245] K. Rykaczewski and J. H. J. Scott. Methodology for imaging nano-to-microscale water condensation dynamics on complex nanostructures. *ACS Nano*, 5:5962–5968, 2011.

[246] K. Rykaczewski, J. H. J. Scott, S. Rajauria, J. Chinn, A. M. Chinn, and W. Jones. Three dimensional aspects of droplet coalescence during dropwise condensation on superhydrophobic surfaces. *Soft Matter*, 7:8749–8752, 2011.

[247] K. Rykaczewski. Microdroplet growth mechanism during water condensation on superhydrophobic surfaces. *Langmuir*, 28:7720–7729, 2012.

[248] E. Olceroglu, C. Y. Hsieh, M. M. Rahman, K. K. S. Lau, and M. McCarthy. Full-field dynamic characterization of superhydrophobic condensation on biotemplated nanostructured surfaces. *Langmuir*, 30:7556–7566, 2014.

[249] T. Liu, W. Sun, X. Li, X. Sun, and H. Ai. Growth modes of condensates on nano-textured surfaces and mechanism of partially wetted droplet formation. *Soft Matter*, 9:9807–9815, 2013.

[250] C. Lv, P. Hao, X. Zhang, and F. He. Dewetting transitions of dropwise condensation on nanotexture-enhanced superhydrophobic surfaces. *ACS Nano*, 9:12311–12319, 2015.

[251] F. C. Wang, F. Yang, and Y. P. Zhao. Size effect on the coalsecence-induced self-propelled droplet. *Appl. Phys. Lett.*, 98:053112, 2011.

[252] T. Q. Liu, W. Sun, X. Y. Sun, and H. R. Ai. Mechanism study of condensed drops jumping on super-hydrophobic surfaces. *Colloids Surf. A*, 414:366–374, 2012.

[253] C. Lv, P. Hao, Z. Yao, Y. Song, X. Zhang, and F. He. Condensation and jumping relay of droplets on lotus leaf. *Appl. Phys. Lett.*, 103:021601, 2013.

[254] B. Peng, S. Wang, Z. Lan, W. Xu, R. Wen, and X. Ma. Analysis of droplet jumping condensation with lattice boltzmann simulation of droplet coalescence. *Appl. Phys. Lett.*, 102:151601, 2013.

[255] Y. Nam, H. Kim, and S. Shin. Energy and hydrodynamic analyses of coalescence-induced jumping droplets. *Appl. Phys. Lett.*, 103:161601, 2013.

[256] F. Liu, G. Ghigliotti, J. J. Feng, and C. H. Chen. Self-propelled jumping upon drop coalescence on leidenfrost surfaces. *J. Fluid Mech.*, 752:22–38, 2014.

[257] F. Liu, G. Ghigliotti, J. J. Feng, and C. H. Chen. Numerical simulations of self-propelled jumping upon drop coalescence on non-wetting surfaces. *J. Fluid Mech.*, 752:39–65, 2014.

[258] R. Enright, N. Miljkovic, J. Sprittles, K. Nolan, R. Mitchell, and E. N. Wang. How coalescing droplets jump. *ACS Nano*, 8:10352–10362, 2014.

[259] K. Zhang, F. Liu, A. J. Williams, X. Qu, J. J. Feng, and C. H. Chen. Self-propelled droplet removal from hydrophobic fiber-based coalescers. *Phys. Rev. Lett.*, 115:074502, 2015.

[260] Q. Wang, X. Yao, H. Liu, D. Quere, and L. Jiang. Self-removal of condensed water on the legs of water striders. *Proc. Natl. Acad. Sci. U.S.A.*, 112:9247–9252, 2015.

[261] C. Lv, P. Hao, Z. Yao, and F. Niu. Departure of condensation droplets on superhydrophobic surfaces. *Langmuir*, 31:2414–2420, 2015.

[262] Y. Nam, D. Seo, C. Lee, and S. Shin. Droplet coalescence on water repellant surfaces. *Soft Matter*, 11:154–160, 2015.

[263] Y. Shi, G. H. Tang, and H. H. Xia. Investigation of coalescence-induced droplet jumping on superhydrophobic surfaces and liquid condensate adhesion on slit and plain fins. *Int. J. Heat Mass Transfer*, 88:445–455, 2015.

[264] M. K. Kim, H. Cha, P. Birbarah, S. Chavan, C. Zhong, Y. Xu, and N. Miljkovic. Enhanced jumping-droplet departure. *Langmuir*, 31:13452–13466, 2015.

[265] X. Chen, R. S. Patel, J. A. Weibel, and S. V. Garimella. Coalescence-induced jumping of multiple condensate droplets on hierarchical superhydrophobic surfaces. *Sci. Rep.*, 6:18649, 2016.

[266] H. Cha, J. M. Chun, J. Sotelo, and N. Miljkovic. Focal plane shift imaging for the analysis of dynamic wetting processes. *ACS Nano*, 10:8223–8232, 2016.

[267] A. Aili, H. Li, M. H. Alhosani, and T. Zhang. Unidirectional fast growth and forced jumping of stretched droplets on nanostructured microporous surfaces. *ACS Appl. Mater. Interfaces*, 8:21776–21786, 2016.

[268] X. Qu, J. B. Boreyko, F. Liu, R. L. Agapov, N. V. Lavrik, S. T. Retterer, J. J. Feng, C. P. Collier, and C. H. Chen. Self-propelled sweeping removal of dropwise condensate. *Appl. Phys. Lett.*, 106:221601, 2015.

[269] J. Liu, H. Guo, B. Zhang, S. Qiao, M. Shao, X. Zhang, X. Q. Feng, Q. Li, Y. Song, L. Jiang, and J. Wang. Guided self-propelled leaping of droplets on a micro-anisotropic superhydrophobic surface. *Angew. Chem. Int. Ed.*, 55:4265–4269, 2016.

[270] J. Cheng, A. Vandadi, and C. L. Chen. Condensation heat transfer on two-tier superhydrophobic surfaces. *Appl. Phys. Lett.*, 101:131909, 2012.

[271] R. Enright, N. Miljkovic, N. Dou, Y. Nam, and E. N. Wang. Condensation on superhydrophobic copper oxide nanostructures. *J. Heat Transfer*, 135:091304, 2013.

[272] N. Miljkovic, R. Enright, and E. N. Wang. Modeling and optimization of superhydrophobic condensation. *J. Heat Transfer*, 135:111004, 2013.

[273] J. Zhu, Y. Luo, J. Tian, J. Li, and X. Gao. Clustered ribbed-nanoneedle structured copper surfaces with high-efficiency dropwise condensation heat transfer performance. *ACS Appl. Mater. Interfaces*, 7:10660–10665, 2015.

[274] Y. Zhao, Y. Luo, J. Zhu, J. Li, and X. Gao. Copper-based ultrathin nickel nanocone films with high-efficiency dropwise condensation heat transfer performance. *ACS Appl. Mater. Interfaces*, 7:11719–11723, 2015.

[275] X. Chen, J. A. Weibel, and S. V. Garimella. Exploiting microscale roughness on hierarchical superhydrophobic copper surfaces for enhanced dropwise condensation. *Adv. Mater. Interfaces*, 2:1400480, 2015.

[276] E. Olceroglu and M. McCarthy. Self-organization of microscale condensate for delayed flooding of nanostructured superhydrophobic surfaces. *ACS Appl. Mater. Interfaces*, 8:5729–5736, 2016.

[277] S. Chavan, H. Cha, D. Orejon, K. Nawaz, N. Singla, Y. F. Yeung, D. Park, D. H. Kang, Y. Chang, Y. Takata, and N. Miljkovic. Heat transfer through a condensate droplet on hydrohpobic and nanostructured superhydrophobic surfaces. *Langmuir*, 32:7774–7787, 2016.

[278] P. Birbarah and N. Miljkovic. External convective jumping-droplet condensation on a flat plate. *Int. J. Heat Mass Transfer*, 107:74–88, 2017.

[279] N. Miljkovic, D. J. Preston, R. Enright, and E. N. Wang. Electrostatic charging of jumping droplets. *Nat. Commun.*, 4:2517, 2013.

[280] N. Miljkovic, D. J. Preston, R. Enright, and E. N. Wang. Electric-field-enhanced condensation on superhydrophobic nanostructured surfaces. *ACS Nano*, 7:11043–11054, 2013.

[281] N. Miljkovic, D. J. Preston, R. Enright, and E. N. Wang. Jumping-droplet electrostatic energy harvesting. *Appl. Phys. Lett.*, 105:013111, 2014.

[282] P. Birbarah, Z. Li, A. Pauls, and N. Miljkovic. A comprehensive model of electric-field-enhanced jumping-droplet condensation on superhydrophobic surfaces. *Langmuir*, 31:7885–7896, 2015.

[283] K. K. Lau, J. Bico, K. B. K. Teo, M. Chhowalla, G. A. J. Amaratunga, W. I. Milne, G. H. McKinley, and K. K. Gleason. Superhydrophobic carbon nanotube forests. *Nano Lett.*, 3:1701–1705, 2003.

[284] C. H. Chen, Q. Cai, C. Tsai, C. L. Chen, G. Xiong, Y. Yu, and Z. Ren. Dropwise condensation on superhydrophobic surfaces with two-tier roughness. *Appl. Phys. Lett.*, 90:173108, 2007.

[285] J. B. Boreyko, B. R. Srijanto, T. D. Nguyen, C. Vega, M. Fuentes-Cabrera, and C. P. Collier. Dynamic defrosting on nanostructured superhydrophobic surfaces. *Langmuir*, 29:9516–9524, 2013.

[286] H. Cha, C. Xu, J. Sotelo, J. M. Chun, Y. Yokoyama, R. Enright, and N. Miljkovic. Coalescence-induced nanodroplet jumping. *Phys. Rev. Fluids*, 1:064102, 2016.

[287] T. Mouterde, Gaëlle Lehoucq, Stéphane Xavier, A. Checco, C. T. Black, A. Rahman, T. Midavaine, C. Clanet, and D. Quéré. Antifogging abilities of model nanotextures. *Nat. Mater.*, 16:658–663, 2017.

[288] B. Pokroy, S. H. Kang, L. Mahadevan, and J. Aizenberg. Self-organization of a mesoscale bristle into ordered, hierarchical helical assemblies. *Science*, 323:237–240, 2009.

[289] Y. Liu, L. Moevius, X. Xu, T. Qian, J. M. Yeomans, and Z. Wang. Pancake bouncing on superhydrophobic surfaces. *Nat. Phys.*, 10:515–519, 2014.

[290] B. Zhang, X. Chen, J. Dobnikar, Z. Wang, and X. Zhang. Spontaneous wenzel to cassie dewetting transition on structured surfaces. *Phys. Rev. Fluids*, 1:073904, 2016.

[291] H. Jo, K. W. Hwang, D. Kim, M. Kiyofumi, H. S. Park, M. H. Kim, and H. S. Ahn. Loss of superhydrophobicity of hydrophobic micro/nano structures during condensation. *Sci. Rep.*, 5:9901, 2015.

[292] R. Wen, Q. Li, J. Wu, G. Wu, W. Wang, Y. Chen, X. Ma, D. Zhao, and R. Yang. Hydrophobic copper nanowires for enhancing condensation heat transfer. *Nano Energy*, 33:177–183, 2017.

[293] R. Wen, Z. Lan, B. Peng, W. Xu, R. Yang, and X. Ma. Wetting transition of condensed droplets on nanostructured superhydrophobic surfaces: coordination of surface properties and condensing conditions. *ACS Appl. Mater. Interfaces*, 9:13770–13777, 2017.

[294] S. Nath, S. F. Ahmadi, H. A. Gruszewski, S. Budhiraja, C. E. Bisbano, S. Jung, D. G. Schmale III, and J. B. Boreyko. 'sneezing' plants: pathogen transport via jumping-droplet condensation. *J. Royal Soc. Interface*, 16:20190243, 2019.

[295] R. Trostle. *Global agricultural supply and demand: factors contributing to the recent increase in food commodity prices*. DIANE Publishing, 2010.

[296] D.G. Schmale, S.D. Ross, T.L. Fetters, P. Tallapragada, A.K. Wood-Jones, and B. Dingus. Isolates of fusarium graminearum collected 40–320 meters above ground level cause fusarium head blight in wheat and produce trichothecene mycotoxins. *Aerobiologia*, 28:1–11, 2012.

[297] P. A. Paul, S. M. El-Allaf, P. E. Lipps, and L. V. Madden. Rain splash dispersal of gibberella zeae within wheat canopies in ohio. *Phytopathology*, 94:1342–1349, 2004.

[298] S. Kim, H. Park, H. A. Gruszewski, D. G. Schmale III, and S. Jung. Vortex-induced dispersal of a plant pathogen by raindrop impact. *Proc. Natl. Acad. Sci. U.S.A.*, page https://doi.org/10.1073/pnas.1820318116, 2019.

[299] A. K. Stosch, A. Solga, U. Steiner, E. C. Oerke, W. Barthlott, and Z. Cerman. Efficiency of self-cleaning properties in wheat (*Triticum aestivum* L.). *J. appl. Bot. food Qual*, 81:49–55, 2007.

[300] J. B. Boreyko and C. H. Chen. Self-propelled jumping drops on superhydrophobic surfaces. *Phys. Fluids*, 22:091110, 2010.

[301] D. E. Aylor. The role of intermittent wind in the dispersal of fungal pathogens. *Annu. Rev. Phytopathol.*, 28:73–92, 1990.

[302] K. Rykaczewski, J. Chinn, M. L. Walker, J. H. J. Scott, A. Chinn, and W. Jones. Dynamics of nanoparticle self-assembly into superhydrophobic liquid marbles during water condensation. *ACS Nano*, 5:9746–9754, 2011.

[303] T. Mouterde, T. V. Nguyen, H. Takahashi, C. Clanet Christophe, I. Shimoyama, and D. Quéré. How merging droplets jump off a superhydrophobic surface: Measurements and model. *Phys. Rev. Fluids*, 2:112001, 2017.

[304] P. Lecointre, T. Mouterde, A. Checco, C. T. Black, A. Rahman, C. Clanet, and D. Quéré. Ballistics of self-jumping microdroplets. *Phys. Rev. Fluids*, 4:013601, 2019.

[305] X. Chen, J. A. Weibel, and S. V. Garimella. Characterization of coalescence-induced droplet jumping height on hierarchical superhydrophobic surfaces. *ACS Omega*, 2:2883–2890, 2017.

[306] T. Meissner, D. Smith, and F. Wentz. A 10 year intercomparison between collocated special sensor microwave imager oceanic surface wind speed retrievals and global analyses. *J. Geophys. Res.-Oceans*, 106:11731–11742, 2001.

[307] D.J. McLaughlin, E.G. McLaughlin, K. Esser, and P.A. Lemke. *The Mycota: A Comprehensive Treatise on Fungi as Experimental Systems for Basic and Applied Research*. Springer, 2001.

[308] D. Quéré. Drops at rest on a tilted plane. *Langmuir*, 14:2213–2216, 1998.

[309] A. Pringle, S. N. Patek, M. Fischer, J. Stolze, and N. P. Money. The captured launch of a ballistospore. *Mycologia*, 97:866–871, 2005.

[310] X. Noblin, S. Yang, and J. Dumais. Surface tension propulsion of fungal spores. *J. Exp. Biol.*, 212:2835–2843, 2009.

[311] A. Buller. *Researches on Fungi, Vol. 1.* Longmans, Green, and Co., 1909.

[312] F. Liu, R. L. Chavez, S. N. Patek, A. Pringle, J. J. Feng, and C. H. Chen. Asymmetric drop coalescence launches fungal ballistospores with directionality. *J. Royal Soc. Interface*, 14(132):20170083, 2017.

[313] N.S. Berman. Drag reduction by polymers. *Annu. Rev. Fluid Mech.*, 10:47–64, 1978.

[314] G.D. Bixler and B. Bhushan. Fluid drag reduction with shark-skin riblet inspired microstructured surfaces. *Adv. Funct. Mater.*, 23:4507–4528, 2013.

[315] D. M. Bushnell and K. J. Moore. Drag reduction in nature. *Annu. Rev. Fluid Mech.*, 23:65–79, 1991.

[316] J. P. Rothstein. Slip on superhydrophobic surfaces. *Annu. Rev. Fluid Mech.*, 42:89–109, 2010.

[317] A. B. D. Cassie and S. Baxter. Wettability of porous surfaces. *T. Faraday Society*, 40:546–551, 1944.

[318] J. Ou, B. Perot, and J. P. Rothstein. Laminar drag reduction in microchannels using ultrahydrophobic surfaces. *Phys. Fluids*, 16:4635–4643, 2004.

[319] J. Ou and J. P. Rothstein. Direct velocity measurements of the flow past drag-reducing ultrahydrophobic surfaces. *Phys. Fluids*, 17:103606, 2005.

[320] C. H. Choi and C. J. Kim. Large slip of aqueous liquid flow over a nanoengineered superhydrophobic surface. *Phys. Rev. Lett.*, 96:066001, 2006.

[321] R. J. Daniello, N. E. Waterhouse, and J. P. Rothstein. Drag reduction in turbulent flows over superhydrophobic surfaces. *Phys. Fluids*, 21:085103, 2009.

[322] S. Srinivasan, J. A. Kleingartner, J. B. Gilbert, R. E. Cohen, A. J. B. Milne, and G. H. McKinley. Sustainable drag reduction in turbulent taylor-couette flows by depositing sprayable superhydrophobic surfaces. *Phys. Rev. Lett.*, 114:014501, 2015.

[323] F. Zhang, L. Zhao, H. Chen, S. Xu, D. G. Evans, and X. Duan. Corrosion resistance of superhydrophobic layered double hydroxide films on aluminum. *Angew. Chem. Int. Ed.*, 47:2466–2469, 2008.

[324] H. Liu, S. Szunerits, W. Xu, and R. Boukherroub. Preparation of superhydrophobic coatings on zinc as effective corrosion barriers. *ACS Appl. Mater. Interfaces*, 1:1150–1153, 2009.

[325] J. Genzer and K. Efimenko. Recent developments in superhydrophobic surfaces and their relevance to marine fouling: a review. *Biofouling*, 22:339–360, 2006.

[326] M. Ferrari, A. Benedetti, E. Santini, F. Ravera, L. Liggieri, E. Guzman, and F. Cirisano. Biofouling control by superhydrophobic surfaces in shallow euphotic seawater. *Colloids Surf. A*, 480:369–375, 2015.

[327] R. Poetes, K. Holtzmann, K. Franze, and U. Steiner. Metastable underwater superhydrophobicity. *Phys. Rev. Lett.*, 105:166104, 2010.

[328] M. S. Bobji, S. V. Kumar, A. Asthana, and R. N. Govardhan. Underwater sustainability of the "cassie" state of wetting. *Langmuir*, 25:12120–12126, 2009.

[329] P. Lv, Y. Xue, Y. Shi, H. Lin, and H. Duan. Metastable states and wetting transition of submerged superhydrophobic surfaces. *Phys. Rev. Lett.*, 112:196101, 2014.

[330] P. R. Jones, X. Hao, E. R. Cruz-Chu, K. Rykaczewski, K. Nandy, T. M. Schutzius, K. K. Varanasi, C. M. Megaridis, J. H. Walther, P. Koumoutsakos, H. D. Espinosa, and N. A. Patankar. Sustaining dry surfaces under water. *Sci. Rep.*, 5:12311, 2015.

[331] J. B. Boreyko and C. H. Chen. Restoring superhydrophobicity of lotus leaves with vibration-induced dewetting. *Phys. Rev. Lett.*, 103:174502, 2009.

[332] E. Bormashenko, Y. Bormashenko, T. Stein, G. Whyman, and E. Bormashenko. Why do pigeon feathers repel water? Hydrophobicity of pennae, Cassie-Baxter wetting hypothesis and Cassie-Wenzel capillarity-induced wetting transition. *J. Colloid Interface Sci.*, 311:212–216, 2007.

[333] S. Srinivasan, S. S. Chhatre, J. O. Guardado, K. C. Park, A. R. Parker, M. F. Rubner, G. H. McKinley, and R. E. Cohen. Quantification of feather structure, wettability and resistance to liquid penetration. *J. Royal Soc. Interface*, 11:20140287, 2014.

[334] C. Lee and C. J. Kim. Underwater restoration and retention of gases on superhydrophobic surfaces for drag reduction. *Phys. Rev. Lett.*, 106:014502, 2011.

[335] A. Balmert, H. F. Bohn, P. Ditsche-Kuru, and W. Barthlott. Dry under water: comparative morphology and functional aspects of air-retaining insect surfaces. *J. Morphol.*, 272:442–451, 2011.

[336] K. Anderson and A. Bows. Executing a scharnow turn: reconciling shipping emissions with international commitments on climate change. *Carbon Manag.*, 3:615–628, 2012.

[337] D. J. C. MacKay. *Sustainable Energy – Without the Hot Air*. UIT Cambridge Ltd., 2009.

[338] M. P. Schultz, J. A. Bendick, E. R. Holm, and W. M. Hertel. Economic impact of biofouling on a naval surface ship. *Biofouling*, 27:87–98, 2011.

[339] F.E. Fish. The myth and reality of gray's paradox: implication of dolphin drag reduction for technology. *Bioinsp. Biomim.*, 1:R17, 2006.

[340] J. Lovvorn, G. A. Liggins, M. H. Borstad, S. M. Calisal, and J. Mikkelsen. Hydrodynamic drag of diving birds: effects of body size, body shape and feathers at steady speeds. *J. Exp. Biol.*, 204:1547–1557, 2001.

[341] Y. Liu, X. Chen, and J. H. Xin. Hydrophobic duck feathers and their simulation on textile substrates for water repellent treatment. *Bioinsp. Biomim.*, 3:046007, 2008.

[342] P. R. Jones, A. T. Kirn, Y. D. Ma, T. D. Rich, and N. A. Patankar. The thermodynamics of restoring underwater superhydrophobicity. *Langmuir*, 33:2911–2919, 2017.